

MICROCAVITY LIGHT EMITTING DIODES IN THE VISIBLE RED AND NEAR INFRARED WAVELENGTH RANGE

THÈSE N° 3170 (2004)

PRÉSENTÉE À LA FACULTÉ SCIENCES DE BASE

Institut de photonique et d'électronique quantiques

SECTION DE PHYSIQUE

ÉCOLE POLYTECHNIQUE FÉDÉRALE DE LAUSANNE

POUR L'OBTENTION DU GRADE DE DOCTEUR ÈS SCIENCES

PAR

Reto JORAY

ingénieur en sciences des matériaux diplômé EPF
de nationalité suisse et originaire de Liesberg (BL)

acceptée sur proposition du jury:

Prof. M. Illegems, directeur de thèse
Prof. P. Heremans, rapporteur
Prof. Y. Leblebici, rapporteur
Dr R. Stanley, rapporteur
Dr K. Streubel, rapporteur

Lausanne, EPFL
2005

Acknowledgments

Never would I have been able to accomplish this work on my own. All this was only possible thanks to invaluable contributions of many people who contributed to my graduate education as teachers, colleagues or friends.

First of all I would like to thank my supervisor **Professor Marc Illegems**. It was him who offered me the opportunity to enter the field of optoelectronics, even though I didn't know much about this field beforehand. He gave me a lot of freedom in planning and carrying out the different research projects, but also the necessary guidance whenever critical questions arose. With his long experience of many decades in the field of III-V semiconductors, he was able to navigate this work through any storm or calm.

Then I would like to express my deepest gratitude to **Ross Stanley**, for introducing me to many secrets of microcavity LEDs and for supervising a large part of my work. I am especially grateful that he even continued to advise me after having left EPFL, in a way I never dared to hope for. There are definitely not many people out there in this world who know more than he does about this topic and I am very glad that I had the chance to work with him.

My appreciation goes as well to **Ursula Oesterle**, who taught me the basics of molecular beam epitaxy (MBE), a science of its own, for which I still have the greatest respect. Other than that I am thankful to her as well for guiding my first steps here at this institute. Working with her was a very valuable experience to me.

I am also indebted to **Jean-Francois Carlin**, who passed on to me part of his huge knowledge on semiconductor cleanroom processing techniques, without which I would never have been able to fabricate all these devices myself. In addition I would like to thank him for being there for me and always having a good answer or idea for any kind of question or problem I could come up with.

My overwhelming thanks go to **Hansjörg Bühlmann**, without whom I could never have accomplished the experimental part of this work. He helped me out on numerous occasions and on topics covering optics, mechanics, electronics or chemistry. His enormous wealth of knowledge and experience on topics so diverse is stunning and was very precious to me during this work.

There are many people at OSRAM Opto Semiconductors as well that I am very thankful to. First and foremost **Klaus Streubel**, who enabled this collaboration which gave my work a new and exciting perspective. He provided me with wafer structures and even fully processed devices and at the same time a lot of freedom in what to do with it. Furthermore working together with one of the leading companies in the field of LEDs was a very interesting and enriching experience for me. I am deeply indebted to **Wolfgang Schmid** and **Christian Karnutsch**, who acted as my direct contacts,

for all their contributions and explanations. Then I would like to thank as well Ralph Wirth, Rainer Butendeich, Arndt Jaeger and all the other persons at OSRAM who assisted in this work.

I owe a great deal to many other people in our institute and at EPFL as well. A special thanks to **Nicolas Leiser**, the person who keeps our cleanroom as well as our MBE running. Without his indefatigable efforts, all this High-Tech equipment would have permanently broken down a long time ago and the realization of all the MCLEDs treated in this thesis would probably not have been possible. In addition I would like to thank **Roger Rochat** for the many precious technical solutions he provided for my measurement set-ups. Many thanks to **Andrea Testa** for helping me keep my computer safe and running efficiently as well as with any other IT-related problem. I am grateful to **Christoph Zellweger** and **Julien Dorsaz** who helped me out on a number of occasions with technical and moral support. Then I would like to name the students who did a research project with me as well, Julien Dorsaz (before starting his Ph.D. in our group), Dany Chek-al-Kar and Christian Heinisch. It was a pleasant and probably as instructive experience for me as for them.

In addition many thanks to all the secretaries for their precious help, Corine Chiquet, Marleen David, Laurence Carlin, Claire-Lyse Rouiller, Denise Paroz, Lorena Sabin, Suada Hasanovic and Silvia Alvarez. I would like to thank as well all the other members of this institute who contribute to the knowledgeable and pleasant atmosphere which prevails in its premises. Just to name a few, all my office mates not mentioned previously already, Volker Wagner, Vlad Badilita, David Leuenberger and Barbara Wild; all the members of Andrea Fiore's group, including himself, Alexander Markus, Cyril Paranthoen, Val Zwiller, Blandine Alloing, Carl Zinoni, Marco Rossetti, Christelle Monat; plus many more, Ounsi El-Daïf, Lars Kappei, Andrea Dunbar, Eckard Deichsel, Alexei Sirbu, Vlad Iakovlev, Andrei Caliman, ... the list is endless.

Special thanks to all my friends for keeping me distracted from work and reminding me that there are other things in life. I am deeply grateful to those I was able to stay in contact with even through busy times, thanks for sticking around.

Thanks to my brothers as well for being there. And last but not least I would like to thank my parents for their never ending support and love during all those years of my studies, without which I would probably never have gotten that far.

Abstract

It was about 125 years ago that the light bulb was commercialized by Thomas Edison. No doubt a brilliant invention at the time, today its low power conversion efficiency is one of the reasons why lighting in the western world has such high energy consumption. Thus, the potential for saving energy is enormous in this area. The introduction of halogen, discharge and fluorescent lamps has lead to certain efficiency improvements, however more than half of the energy is still lost as heat.

Light-emitting diodes (LEDs) are very promising candidates for high efficiency light sources, with modern devices showing internal quantum efficiencies of virtually 100 %. However, due to the high refractive index of the commonly used semiconductor materials it is very difficult to have a large extraction efficiency; in a standard cubic geometry most of the internally emitted light is trapped inside the device due to total internal reflection.

Several methods have been developed in order to circumvent this problem, either by optimizing the device geometry in order to increase the escape cone or by incorporating a resonant structure in order to force the internal emission into the existing escape cone. The latter approach is called microcavity LED (MCLED) or resonant cavity LED (RCLED). In a MCLED the spontaneous internal emission is controlled by placing the emitter inside an optical cavity with a thickness of the order of its emitting wavelength. The resulting interference effects increase the part of the emission that can be extracted. Contrary to the other approaches this is possible without changing the device geometry and thus without additional costly back-end processing steps. The control of the far-field radiation pattern makes these devices particularly interesting for high brightness applications, which demand highly directional emitters, such as for printing, bar code reading, large area displays and optical communication.

The extraction efficiency of a MCLED is inversely proportional to the effective cavity length. An ideal cavity, allowing an extraction efficiency close to unity, consists of a low refractive index material and has an optical length of $\lambda/2$. In contrast to this, to obtain high internal quantum efficiencies it is necessary to use high index cavities with an optical length of at least λ . It should be noted, that the large penetration depth of the optical field in the semiconductor-based distributed Bragg reflectors (DBRs) leads to a significant increase of the effective cavity length and thus further reduces the achievable extraction efficiencies.

In this thesis novel concepts to reduce effective cavity lengths and therefore increase extraction efficiencies are implemented into standard MCLED structures. The phase-shift cavity principle whilst maintaining the electrical properties of a standard λ cavity achieves optical properties approaching that of a $\lambda/2$ cavity. The use of AlO_x instead of AlAs as the low refractive index component in the DBRs leads to smaller penetration

depths and a concomitant reduction of the effective cavity length. A similar effect can be obtained by combining a resonant cavity with a thin-film structure.

Thanks to these design improvements, the external quantum efficiency of different types of MCLEDs was increased. Near infrared emitting InGaAs/GaAs MCLEDs including a phase-shift cavity were realized, as both bottom and top emitting structures. The external quantum efficiencies achieved for emission into air were 18 and 19 %, respectively. With the additional incorporation of an oxide based bottom DBR, the efficiency of top emitting near infrared MCLEDs was further increased to 28 %. Red emitting AlGaInP-based structures are not compatible with the phase-shift cavity principle. However the beneficial effect of the implementation of an oxide DBR is greater at their wavelength rather than in the near infrared. Thus with preliminary red emitting GaInP/AlGaInP MCLEDs containing a bottom oxide DBR external quantum efficiencies of 12% could be achieved. Unfortunately, the incorporation of an oxide DBR significantly complicates the device design and the device fabrication. These problems can be avoided by combining the resonant cavity with a thin-film structure instead. Initial non-optimized red emitting thin-film MCLEDs were realized by OSRAM Opto Semiconductors and characterized in this work. They show external quantum efficiencies of 23 % and 18 % with and without encapsulation, respectively. It is assumed that a significant fraction of the high external quantum efficiency is due to a strong photon recycling effect in these devices.

Simulations presented in this thesis show that the theoretical limits for the MCLEDs discussed above are slightly higher than the values obtained, encouraging further device optimization. The thin-film MCLEDs seem to hold the biggest potential for high efficiency emission from MCLEDs, independent of the wavelength range of emission.

Résumé

La lampe à incandescence fut commercialisée par Thomas Edison il y a 125 ans de cela. Sans conteste une invention de génie à l'époque, elle est en partie responsable aujourd'hui de la consommation élevée en énergie pour l'illumination dans les pays occidentaux à cause de sa faible conversion de puissance. Donc ce secteur possède un énorme potentiel pour économiser de l'énergie. L'introduction des lampes halogènes, des lampes fluorescentes et des lampes à décharge a permis d'améliorer quelque peu l'efficacité de conversion, mais plus de la moitié de l'énergie produite est encore perdue sous forme de chaleur.

Les diodes électroluminescentes (DELs, ou encore LEDs) sont des candidats prometteurs comme sources de lumière à haute efficacité car les dispositifs modernes atteignent des efficacités quantiques internes proches de 100 %. Néanmoins, l'indice de réfraction élevé des semiconducteurs utilisés rend l'extraction de la lumière difficile car, pour une géométrie cubique, une grande partie de la lumière est confinée dans le dispositif à cause des réflexions totales à chaque interface.

De nombreuses méthodes ont été développées pour résoudre ce problème, soit en optimisant la géométrie du dispositif afin d'agrandir le cône d'extraction, soit en introduisant une cavité résonnante pour forcer l'émission de lumière dans le cône d'extraction déjà existant. La deuxième approche est appelée LED à microcavité (MCLED), ou également LED à cavité résonante (RCLED). Dans une MCLED, l'émission spontanée interne est contrôlée en plaçant l'émetteur dans une cavité optique dont l'épaisseur se rapproche de la longueur d'onde d'émission. Suite aux effets d'interférences, une plus grande partie de la lumière émise peut être extraite en redirigeant celle-ci dans le cône d'extraction. Contrairement aux autres approches, cela est possible sans changer la géométrie du dispositif et donc sans étapes de fabrication supplémentaires. Le contrôle de la forme de l'émission rend ces dispositifs particulièrement intéressants pour des applications de haute brillance demandant des émetteurs hautement directionnels, comme l'impression de documents, la lecture de code-barre, la fabrication d'écrans larges et la communication par fibres optiques.

L'efficacité d'extraction d'une MCLED est inversement proportionnelle à la longueur effective de la cavité. Une cavité idéale, permettant des efficacités d'extraction proche de l'unité, consiste en un matériau de bas indice de réfraction et d'une longueur optique de $\lambda/2$. Au contraire, des efficacités quantiques internes suffisamment hautes sont réalisables seulement avec des cavités à haut indice de réfraction et d'une longueur minimale de λ . De plus, la longueur de pénétration du champ optique dans les miroirs de Bragg semiconducteur (DBRs) mène à une augmentation significative de la longueur effective de la cavité et en conséquence une diminution de l'efficacité quantique de la MCLED.

Dans cette thèse, de nouveaux concepts sont appliqués aux MCLEDs standards afin de réduire la longueur effective de la cavité et d'augmenter ainsi l'efficacité quantique externe des dispositifs. Le principe de la "cavité déphasée" permet de conserver les propriétés d'injections électriques de la cavité λ tout en s'approchant des propriétés optiques favorables de la cavité $\lambda/2$. L'utilisation de l'oxyde d'aluminium AlO_x au lieu de l'AlAs comme couche à bas indice de réfraction dans les miroirs de Bragg permet de diminuer la longueur de pénétration dans le miroir et de réduire la longueur effective de la cavité. Une autre approche pour y parvenir est de combiner la MCLED avec une structure à couches minces.

Grâce à ces améliorations, l'efficacité quantique externe de divers type de MCLEDs fut améliorée. Des MCLEDs InGaAs/GaAs émettant dans l'infrarouge proche vers le haut ou à travers le substrat furent réalisées avec une cavité déphasée. Les efficacités quantiques externes sont respectivement de 18% et 19%. En remplaçant le DBR du bas par un DBR AlO_x , des efficacités de 28 % ont été mesurées pour des structures émettant vers le haut. Les structures émettant dans le rouge à base d'alliage d'AlGaInP ne sont pas compatibles avec le principe de la cavité déphasée, par contre les bénéfices de l'utilisation du DBR AlO_x sont plus prononcés que pour les structures infrarouges. Des MCLEDs GaInP/AlGaInP contenant un miroir AlO_x furent donc réalisées et atteignirent des efficacités quantiques externes de 12% malgré une incorporation du miroir difficile du point de vue du design et de la fabrication de la structure. Les problèmes liés à l' AlO_x peuvent être évités en combinant la structure MCLED standard avec une structure à couches minces. Des premières MCLEDs à couches minces émettant dans le rouge étaient réalisées par OSRAM Opto Semiconductors et caractérisées lors de cette thèse. Malgré leur detuning non optimisées, ces diodes montrent des efficacités de 23 % et 18 % avec et sans encapsulation. Il est probable que l'efficacité quantique externe élevée mesurée dans ses structures est liée à un effet important de recyclage de photons.

Des simulations effectuées dans le cadre de cette thèse montrent que les limites théoriques pour les structures à microcavité mentionnées ci-dessus sont légèrement supérieures aux valeurs mesurées, ce qui laisse entrevoir des possibilités d'optimisations. Les MCLEDs à couches minces semblent posséder le meilleur potentiel pour la réalisation de MCLEDs à haute efficacité, et ce indépendamment de la gamme de longueur d'onde d'émission.

Zusammenfassung

Die Glühlampe wurde vor etwa 125 Jahren durch Thomas Edison kommerzialisiert. Zweifellos eine geniale Erfindung zu dieser Zeit, ist die Glühlampe mit ihrem geringen Wirkungsgrad heute mitverantwortlich für den hohen Energieverbrauch für Beleuchtung in der westlichen Welt. In Anbetracht der niedrigen Effizienzen handelsüblicher Lichtquellen weist dieser Bereich ein enormes Energiesparpotential auf. Die Einführung von Halogen-, Entladungs- und Fluoreszenzlampen hat zu gewissen Effizienzverbesserungen geführt, wobei nach wie vor mehr als die Hälfte der Energie als Wärme verloren geht.

Leuchtdioden (englisch: light-emitting diodes (LEDs)) sind vielversprechende Kandidaten für hocheffiziente Lichtquellen, da moderne Bauteile eine interne Quanteneffizienz von nahezu 100 % aufweisen. Der hohe Brechungsindex der allgemein verwendeten Halbleitermaterialien macht es jedoch schwierig, dieses Licht auszukoppeln. Für eine gewöhnliche kubische Geometrie wird das meiste intern emittierte Licht durch Totalreflexion ins Innere des Bauteils zurückreflektiert.

Diverse Methoden wurden entwickelt, um dieses Problem zu umgehen. Diese basieren entweder auf der Optimierung der Bauteilgeometrie, um den Lichtauskopplungskegel zu vergrössern, oder auf der Implementation eines optischen Resonators, um die interne Emission bereits von vornherein in Richtungen zu konzentrieren, die nicht der Totalreflexion unterliegen. Der letztere Ansatz wird Microcavity LED (MCLED), oder auch Resonant Cavity LED (RCLED) genannt. In einer MCLED wird die spontane interne Emission kontrolliert indem der Emitter in einen optischen Resonator mit einer vertikalen Ausdehnung in derselben Grössenordnung wie die Emissionswellenlänge platziert wird. Dank der daraus folgenden Interferenzeffekte kann ein grösserer Anteil der Emission ausgekoppelt werden. Im Gegensatz zu den anderen Methoden erfordert dies keine Anpassung der Bauteilgeometrie und daher keine zusätzlichen, kostspieligen Endbearbeitungsschritte. Dank der Kontrolle über das Fernfeld sind diese Bauteile insbesondere für Anwendungen, welche eine gerichtete Emission verlangen, wie zum Beispiel Drucker, Strichcodelesegeräte, Grossbildschirme oder optische Kommunikation geeignet.

Die externe Quanteneffizienz einer MCLED ist umgekehrt proportional zur effektiven Resonatorlänge. Ein idealer Resonator mit einer Auskoppelleffizienz von nahezu eins besteht aus einem Material mit einem tiefen Brechungsindex und weist eine optische Länge von $\lambda/2$ auf. Zur Zeit können jedoch nur für Resonatoren mit einem hohen Brechungsindex und mit einer Länge von mindestens λ genügend hohe interne Quanteneffizienzen erreicht werden. Zusätzlich führt die hohe Penetrationstiefe des optischen Feldes in die aus Halbleitern aufgebauten, sogenannten Bragg-Spiegel zu einer erheblichen Zunahme der effektiven Resonatorlänge und somit zu einer weiteren Verringerung der erzielbaren Auskoppelleffizienzen.

In dieser Arbeit wurden neuartige Konzepte in klassische MCLED-Strukturen einbezogen, die geringere effektive Resonatorlängen und daher höhere Effizienzen ermöglichen. Das Prinzip der Phasenverschiebung ("phase-shift cavity") erlaubt es, die elektrischen Eigenschaften eines herkömmlichen λ -Resonators beizubehalten, bei gleichzeitiger Annäherung der optischen Eigenschaften an die eines $\lambda/2$ -Resonators. Der Einsatz von AlO_x statt AlAs als Komponente mit niedrigerem Brechungsindex in den Bragg-Spiegeln führt zu einer geringeren Penetrationstiefe und damit einer Verringerung der effektiven Resonatorlänge. Ein ähnlicher Effekt wird erreicht mit der Kombination des optischen Resonators mit einer Dünnschichtstruktur.

Dank dieser Verbesserungen des Bauteildesigns konnte die externe Quanteneffizienz von verschiedenen Typen von MCLEDs erhöht werden. Im nahen Infrarot emittierende InGaAs/GaAs MCLEDs mit einem Phase-shift Resonator wurden als nach unten oder oben emittierende Strukturen realisiert. Die erreichten externen Quanteneffizienzen für Emission in Luft entsprechen 18 und 19 %. Mit der zusätzlichen Implementation eines Oxid-Spiegels konnte die Effizienz von Oberflächen-emittierenden MCLEDs im nahen Infrarot auf 28 % erhöht werden. Strukturen basierend auf AlGaInP, die im roten Wellenlängenbereich emittieren, sind nicht kompatibel mit dem Phasenverschiebungsprinzip. Umgekehrt hat die Integration eines Oxid-Spiegels einen grösseren Effekt als im nahen Infrarot. Daher konnten mit rot emittierenden GaInP/AlGaInP MCLEDs mit einem unteren Oxid-DBR externe Quanteneffizienzen von 12 % erreicht werden. Die Eingliederung eines Oxid-Spiegels macht das Bauteildesign und dessen Herstellungsprozess jedoch massgeblich komplizierter. Diese Probleme können vermieden werden indem der optische Resonator stattdessen mit einer Dünnschichtstruktur kombiniert wird. Erste, nicht optimierte, rot emittierende Dünnschicht-MCLEDs wurden von OSRAM Opto Semiconductors hergestellt und als Teil dieser Arbeit charakterisiert. Diese Leuchtdioden weisen externe Quanteneffizienzen von 23 % mit und 18 % ohne Verkapselung auf. Es wird angenommen, dass ein beträchtlicher Anteil dieser hohen externen Quanteneffizienz von einem starken Photon Recycling-Effekt in diesen Bauteilen herrührt.

Im Rahmen dieser Arbeit durchgeführte Simulationen zeigen, dass das theoretische Limit für die oben erwähnten verschiedenen Typen von MCLEDs noch geringfügig höher liegt als die erreichten Werte. Dies macht eine weitere Bauteiloptimierung interessant. Dünnschicht-MCLEDs scheinen derzeit das grösste Potential als hocheffiziente MCLED zu haben, unabhängig von der Emissionswellenlänge.

Contents

Acknowledgments	i
Abstract	iii
Résumé	v
Zusammenfassung	vii
1 Introduction	1
1.1 Goals of this work	2
1.2 Thesis outline	3
2 High Efficiency LEDs	5
2.1 LED History	5
2.2 Applications for LEDs	9
2.3 LED Characteristics: Electrical Properties	12
2.3.1 Diode Current–Voltage Characteristic	12
2.3.2 Deviations from Ideal I–V Characteristic	13
2.4 Device Design Issues	15
2.4.1 Double Heterostructures	15
2.4.2 Quantum Wells	16
2.4.3 Separate Confinement Heterostructures	16
2.4.4 Carrier Loss Mechanisms	17
2.5 LED Characteristics: Optical Properties	19
2.5.1 Glossary of Radiometric and Photometric Units	19
2.5.2 Radiative and Non-radiative Recombination Mechanisms	23
2.5.3 Light Extraction Problem	25
2.6 Alternative Types of High Efficiency LEDs	30
2.6.1 Truncated Inverted Pyramid LEDs	32
2.6.2 Different Types of Thin–Film LEDs	33
2.7 Microcavity LEDs	36
2.7.1 Modification of Spontaneous Emission Pattern	37
2.7.2 Reflectors	43
2.7.3 Design Rules	48
2.7.4 State of the Art Semiconductor MCLEDs (Status 2001)	52
2.8 Novel Concepts	55
2.8.1 Phase-Shift Cavity	55

2.8.2	Oxide DBR	57
2.8.3	Omnidirectional Reflector (ODR)	59
2.8.4	Surface Plasmon Excitation	61
2.8.5	Substrate Structuring	62
3	Bottom Emitting MCLEDs at 970 nm	63
3.1	Introduction	63
3.2	Structure	64
3.3	Simulation	65
3.4	Fabrication	67
3.4.1	Cleaning	67
3.4.2	Lithography	67
3.4.3	Etching	67
3.4.4	Contacts	69
3.4.5	Current Confinement	70
3.4.6	Substrate Thinning	71
3.4.7	Anti-Reflection Coating	71
3.4.8	Fabrication Bottom Emitting MCLEDs	74
3.4.9	Current Confinement Methods	77
3.4.10	Samples after Front-Side Processing	78
3.4.11	Back-End Processing	80
3.5	Experimental Results	81
3.5.1	TLM Measurements	81
3.5.2	L-I-V Measurements	83
3.6	Discussion	91
3.6.1	Current-Voltage Characteristic	91
3.6.2	External Quantum Efficiency vs. Drive Current Density	93
3.6.3	Current Spreading Estimation	96
3.6.4	Maximum Efficiency after Back-End Processing	100
3.7	Conclusions	100
4	Top Emitting MCLEDs at 970 nm	101
4.1	Introduction	101
4.2	Structures	102
4.3	Simulation	104
4.4	Fabrication	107
4.4.1	Etching	107
4.4.2	Lateral Oxidation	108
4.4.3	Fabrication Semiconductor DBR Devices	110
4.4.4	Fabrication Oxide DBR Devices	115
4.5	Experimental Results	122
4.5.1	Characterization after Epitaxial Growth	122
4.5.2	Characterization of the Processed Devices	127
4.6	Discussion	147
4.6.1	Semiconductor DBR Devices	147
4.6.2	Oxide DBR Devices	148
4.7	Conclusions	153

5	Top Emitting MCLEDs at 650 nm	155
5.1	Introduction	155
5.2	Structure	157
5.3	Simulation	158
5.4	Fabrication	159
5.4.1	Etching	159
5.4.2	Contacts	160
5.4.3	Lateral Oxidation	161
5.4.4	Fabrication Red Emitting Oxide DBR MCLEDs	162
5.5	Experimental Results	170
5.5.1	Characterization after Epitaxial Growth	170
5.5.2	Characterization of the Processed Devices	172
5.6	Discussion	181
5.7	Conclusions	184
6	Thin-Film MCLEDs at 650 nm	185
6.1	Introduction	185
6.2	Structure	187
6.3	Simulation	188
6.4	Fabrication	189
6.5	Experimental Results	191
6.5.1	L-I-V Measurements	191
6.5.2	Far-Field Emission	193
6.5.3	Electroluminescence	195
6.6	Discussion	196
6.6.1	Cavity Thickness and Detuning	196
6.6.2	Photon Recycling and In-Plane Superluminescence	197
6.7	Conclusions	199
7	Conclusions and Perspectives	201
7.1	Summary of results	201
7.2	The Future of MCLEDs	204
A	Material Parameters	205
A.1	Bandgap Energy	205
A.1.1	The AlGaAs material system	206
A.1.2	The AlGaInP material system	207
A.2	Indices of refraction	208
B	Epitaxial Structures	209
C	Lithography Masks	219
C.1	Mask Substrate Emitting Devices	219
C.2	Masks Top Emitting Devices	220
C.2.1	Mask Semiconductor DBR Devices	220
C.2.2	Mask Oxide DBR Devices	221

D Detector Calibration	223
D.1 Large Area Photodiodes	223
D.2 Integrating Sphere	227
Bibliography	231
Curriculum Vitae	253
Publications	255

Chapter 1

Introduction

The understanding of the nature of light and the discovery of methods to produce light efficiently are amongst the most fascinating endeavors and the evolution of light sources over the centuries reflects the progress in science and technology. The main criteria for light emitters are their **energy conversion efficiency** and their **color rendition**. The latter describes the effect of the spectral characteristic of the light emitted by the source on the color appearance of the objects illuminated. The color rendition of a source is described with the **color-rendering index** (CRI), as defined by the International Commission on Illumination (CIE, Commission internationale d'Eclairage). The efficiency can be expressed either as the fraction of the electrical energy input that is transformed into optical energy (**wall-plug** or **power efficiency**) or more specifically for applications in the visible range as the fraction that is transformed into light in the visible range (**luminous efficiency**).

Taking into consideration that nearly 20 % of all electricity used in the Western society is used for lighting homes, buildings, factories, and streets, it is obvious that the energy savings potential is enormous in this sector. According to a recent U.S. Department of Energy analysis, lighting accounts for more than 40 % of the commercial sector electricity consumption in the United States, a total of 391 TWh/year [1]. Furthermore since in 2003 still about 60 % of the electricity production in the OECD (Organisation for Economic Co-operation and Development) comes from the burning of fossil fuels (70 % in the United States) [2], a reduced energy consumption would not only create huge economical but also environmental savings.

The invention of the battery allowed the production of electrical current, which, together with the development of vacuum techniques and the refinement of materials led to the realization of **incandescent lamps** in the 19th century. Despite successive improvements, including halogen gas fillings, the energy conversion efficiency of these light sources does not exceed 10 % and their luminous efficiency is limited to approximately 30 lm/W.

In the 20th century electric **discharge lamps** surpassed incandescent lamps in terms of luminous efficiency and values superior than 100 lm/W could be achieved with sodium lamps and the recent xenon metal halide lamps. However the lack of red light in their emission spectrum limits their color rendering properties and impedes their use for domestic applications. With low-pressure mercury **discharge fluorescent lamps** a significantly improved color rendering can be achieved and a wide range of color

temperatures are available today. Modern fluorescent lamps show energy conversion efficiencies up to 40 %.

Light-emitting diodes (LEDs) exist for more than fifty years but breakthroughs in efficiency mainly occurred in the last decade of the 20th century and it is more or less since the beginning of the 21st century that high performance LEDs are progressively replacing conventional light sources for more and more applications. LEDs are attractive due to their high efficiencies, their long lifetime, small size, robustness, flexibility, nearly instant start up and unique spectral characteristics. Today luminous efficiencies larger than 100 lm/W can be achieved with red emitting LEDs; for white LEDs the maximum values currently are of the order of 70 lm/W. However their high initial cost and their limitations for producing a warm white light still limit their use. Furthermore, their potential in terms of efficiency does not seem to be fully exploited yet. Therefore a lot of work still needs to be done in order to optimize the performance of LEDs, with one of the biggest challenges being the light extraction from the high refractive index LED material.

With the widespread use of efficient and long-lifetime LEDs enormous amounts of energy and money could be saved. It is estimated that by 2025 solid state lighting (based on LEDs) could reduce the global amount of electricity used for lighting by 50 % [3]; no other electricity consuming field has such a large energy-savings potential. In addition the fact that LEDs are mercury-free further reduces their overall life cycle impact on the environment and makes them more favorable in view of future environmental regulations.

1.1 Goals of this work

This work focuses on the optimization of one particular type of high-efficiency LED, the so-called microcavity LED (MCLED) or resonant cavity LED (RCLED). Different approaches are investigated in order to increase the extraction efficiency for this device type and to minimize its current consumption. This is done by optimizing the device design from an optical and electrical point of view.

Since the extraction efficiency of MCLEDs is inversely proportional to the effective cavity length, the limits for the overall efficiency can be pushed to higher values by decreasing the effective cavity length. This is achieved either by adapting the bandgap engineering within the cavity or by increasing the refractive index contrast in the surrounding distributed Bragg reflectors. Another important aspect that will be treated is the reduction of absorption losses.

An optimum current management requires a homogeneous current injection into the active region as well as a limitation of the lateral current spreading beyond the emission region. The homogeneity of the current distribution in the active region depends on the metal contact design and the conductivity of the intermediate semiconductor layers. A parasitic lateral current spreading can be avoided by increasing the resistance of some of the doped semiconductor layers between the contact and the active region either on the p-doped or on the n-doped side. From an electrical point of view a confinement on the p-side would be favorable, since the mobility of the holes is in general significantly lower than the mobility of the electrons. However, this may not be in agreement with the requirements for the optical design of the cavity.

1.2 Thesis outline

In chapter 2 the basic principles of a standard LED as well as its limitations in terms of efficiency are briefly reviewed. Furthermore, the different methods to increase the extraction efficiency are presented, with a detailed description of the microcavity LED. Finally different concepts for further enhancements of the MCLED performance are discussed.

Chapter 3 focusses on the design, realization and characterization of bottom emitting near infrared MCLEDs, including a phase-shift cavity structure, and on the impact of different current confinement schemes. The implementation of the phase-shift cavity principle is found to increase the extraction efficiency limit for microcavity-type devices. The effect of a recess etch and an oxide aperture on the parasitic lateral current spreading is compared.

In chapter 4 the phase-shift cavity principle is applied to top emitting near infrared MCLEDs. The effect of different top contact geometries on the current distribution in the active region is studied. Furthermore the beneficial effects as well as the problems related to the introduction of a high reflectivity oxide DBR are explored on the basis of supplementary characterization measurements.

Chapter 5 treats top emitting red MCLEDs with a high reflectivity oxide DBR. The results show that the potential efficiency increase but as well the related fabrication problems are more important in the red compared to the near infrared wavelength range.

Results on the first realization of red emitting thin-film MCLEDs, which corresponds to a combination of the microcavity principle with the thin-film technology, are presented in chapter 6. It is shown, that the performance of these devices is superior compared to standard red emitting MCLEDs. The effect of photon recycling and lateral in-plane superluminescence on the far-field radiation pattern of these devices is demonstrated.

Finally, the main conclusions and perspectives for the future of microcavity LEDs are given in chapter 7.

Chapter 2

High Efficiency LEDs

2.1 LED History

The observation of electroluminescence was mentioned for the first time in the literature nearly 100 years ago by Henry Joseph Round [4] in 1907. He noted that by touching silicon carbide (**SiC**) crystallites with electrodes a rectifying contact was formed and a yellowish light was emitted. However he did not pursue this discovery. In 1922 the light emission from a SiC diode was rediscovered and studied in detail by Losev [5]. His pioneering work on SiC emitters resulted in 16 papers and 4 patents on this topic [6]. Only in 1952 Lehovec et al. [7] finally established the theory of light-emitting diodes, based on Shockley's theory of p-n junctions [8].

Zincblende (**ZnS**) electroluminescence was discovered in 1936 by Destriau and was studied intensively in the 1950s but did not go very far [6].

In the beginning of the 1960s the first emitters based on the man-made III-V semiconductors were realized. The material systems were gallium phosphide (**GaP**), gallium arsenide (**GaAs**) and gallium arsenide phosphide (**GaAsP**) [9]. At that time the first commercial LEDs entered the market, a GaAsP red LED by General Electric and a GaAs infrared LED by Texas Instruments. In the late 1960s, Monsanto and Hewlett-Packard started the mass-production of low cost GaAsP red LEDs. The vapor-phase epitaxy (VPE) grown GaAsP emitters were soon joined by GaP devices, grown by liquid phase epitaxy (LPE) [10].

Since then, the luminous performance of visible LEDs showed an increase of nearly one order of magnitude per decade. The isoelectronic doping of GaP and GaAsP with optically active impurities in the 70s allowed a significant increase in performance. This led as well to an extension of the accessible color range and made possible the fabrication of green, orange and yellow emitters. In parallel the introduction of a simple and double heterostructure design led to drastic increases in injection efficiency by the confinement of carriers in the active region [11]. The aluminum gallium arsenide (**AlGaAs**) material system was the first material system suitable for high-brightness LED applications [9]. GaAs is a direct bandgap semiconductor and is lattice matched to AlAs, enabling the growth of high quality AlGaAs films on GaAs substrates. The LPE-grown, double heterostructure (DH) AlGaAs red LEDs introduced in the 80s were the first to outperform incandescent lamps with a red filter.

The introduction of more sophisticated growth techniques, metal organic vapor

phase epitaxy (MOVPE) [12] and molecular beam epitaxy (MBE) [13,14] in the 80s led to a further improved crystal quality and made possible the growth of new material systems. In 1990, Hewlett-Packard and Toshiba independently introduced LEDs based on aluminum gallium indium phosphide (**AlGaInP**). With the quaternary alloy $(\text{Al}_x\text{Ga}_{1-x})_{0.51}\text{In}_{0.49}\text{P}$ efficient double heterostructure LEDs emitting from the red to the yellow-green were made available, thanks to its large direct bandgap range [10]. The performance of AlGaInP devices was further increased by wafer bonding the epitaxial structure on a transparent GaP substrate (TS) and removing the absorbing GaAs substrate (AS), on which the structure was grown [15]. By further sawing the devices to a truncated-inverted-pyramid (TIP) chip geometry, record luminous efficiencies exceeding 100 lm/W for orange LEDs emitting around 610 nm were achieved by Lumileds in 1999 [16]. With the latest generation of their thin-film (TF) AlGaInP devices OSRAM Opto Semiconductors recently realized similar luminous efficiencies [17]. This technology is based on substrate removal and the formation of buried micro-reflectors, as will be discussed in detail later on.

In parallel another new material system evolved, based on gallium nitride (**GaN**). The first GaN p-n junction LEDs were fabricated in the beginning of the 1990s. Soon after that blue, yellow and green Indium Gallium Nitride (InGaN) based LEDs with high luminous efficiencies were realized.

Figure 2.1 shows the evolution of the luminous efficiency over time for high-brightness visible LEDs (definition luminous efficiency see section 2.5.1). The values are compared with the efficiencies of conventional light sources. It can be seen that LEDs already outperform incandescent lights and are approaching the efficiencies of fluorescent lamps. Similar to Moore's law for the performance increase of Si integrated circuits, an expo-

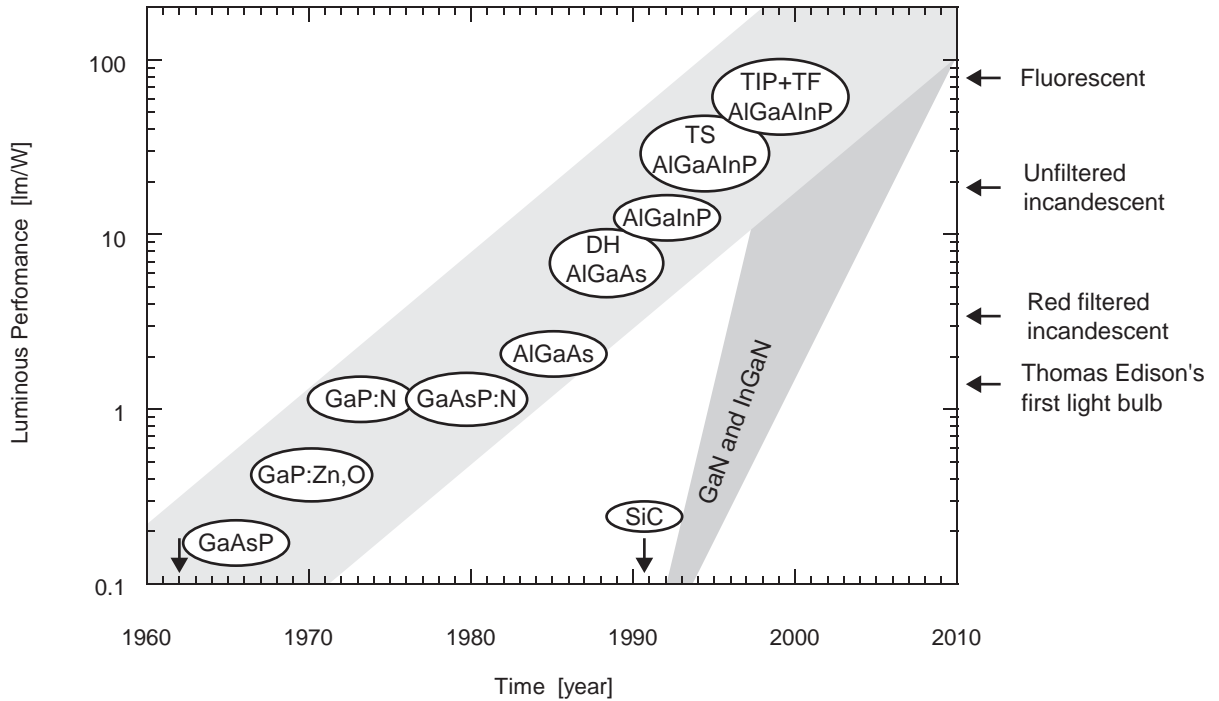


Figure 2.1: Luminous performance of visible LEDs versus time; compared with other light sources (based on [10])

nential increase in LED efficiency can be observed, with the LED luminous efficiency doubling every 4 years or increasing by nearly an order of magnitude per decade. For nitride-based LEDs however this rate has been much higher so far, the luminous efficiency increased by an order of magnitude approximately every three years.

Once high-performance LEDs were available over the entire visible spectral range, **white LEDs** started to appear on the market [18]. Three different approaches exist. One is to combine the output from two or three LED chips which can be blue and yellow, or more commonly red, green and blue (RGB-LED) [19]. If the powers of the three different LEDs are correctly balanced, this LED emits white light. Another possibility is to cover a blue LED with a phosphorous, which is excited by the blue light and emits over quite a broad spectrum (see figure 2.2) [9]. Together with the blue light from the LED this gives a white light, even if perceived as a cold white light. The third possibility is to excite the phosphor with an ultraviolet LED instead of a blue one. White LEDs progress very rapidly, currently luminous efficiencies up to 70 lm/W are available. Efficiencies as high as 200-300 lm/W are expected for the near future, which would establish LEDs as the most efficient light sources available. Ultraviolet LEDs are getting more and more common as well, as there are many other applications for them, apart from the phosphor excitation in white LEDs.

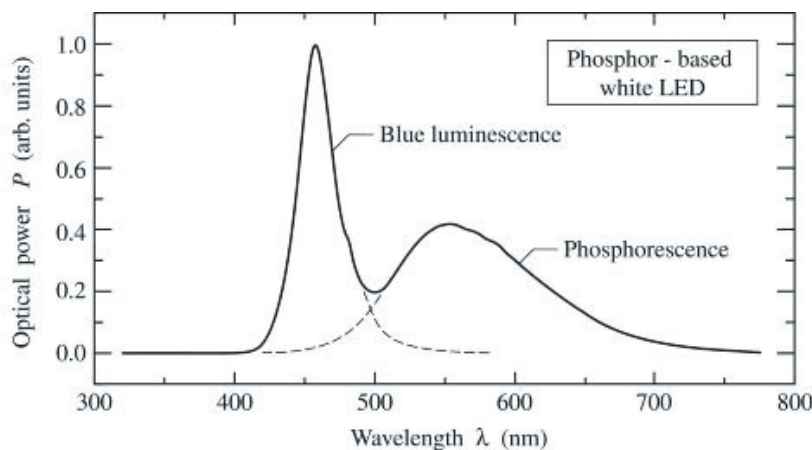


Figure 2.2: Emission of a commercial phosphor-based white LED manufactured by the Nichia Chemical Industries Corporation [9]

By the late 1960s, light-emitting diodes were fabricated based on more sophisticated SiC films [9,6]. However their conversion efficiencies were only 0.005 %. Only in the 1990s the blue SiC LEDs sold by Cree started to have a significant commercial success, but were soon displaced by nitride-based LEDs. Compared to the rapid advances in performance for LEDs from the III–V materials family, progress in SiC LEDs has been slow, due to the indirect bandgap and the more difficult materials technology. Today, except for applications at extreme high temperatures and voltages, the III–nitride materials have essentially superseded the SiC technology.

The **II–VI materials**, in contrast, exhibit very high luminous efficiencies covering a wide wavelength range. However, because of the difficulty to reproducibly achieve n- and p-doping and the lower chemical stability of these compounds, no major industrial

development of II–VI LED materials for electronic or optoelectronic applications has emerged, excepting specific usages such as far infrared detection.

Since the first observation of light emission in **organic LEDs** (OLEDs) at the end of the 1980s based on small molecules [20] and conjugated polymers [21], there has been a constant improvement in device performance. Nowadays OLED-based products have become competitive with existing technologies, especially in the area of flat panel displays [22]. In 2002 the external quantum efficiencies of polymer-based devices were typically of the order of 5%. In the near future, values up to 25% are expected. Different solutions for white OLEDs already exist as well.

2.2 Applications for LEDs

The initial GaAsP LEDs are used as status indicator lights on circuit boards and for numeric and alphanumeric displays since the late 60s. The displays were implemented in pocket calculators, digital wristwatches and telephone dial pads. Even in 2002 these applications still represent the largest LED chip market, as can be seen in figure 2.3. For near infrared LEDs there is a big market in IR transmitters, e.g. in remote controls. Other applications are scanning, printing and optical data storage systems. Red LEDs are used as well as transmitters for plastic optical fibers (POF), which are more and more often implemented in local area networks (LANs), e.g. in cars [23–25].

Once LEDs outperformed filtered incandescent lights they started to be used for traffic signal lighting and automotive lighting, the latter including indicator lighting within the vehicle as well as signal lighting on the exterior of the vehicle. In addition LEDs are now used for LCD backlighting and in large-area displays.

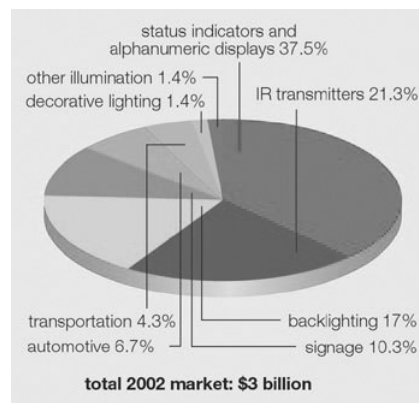


Figure 2.3: LED market by application in 2002 [17]

High-brightness (HB) LEDs show the highest growth rates, especially the white HB LEDs. Apart from general lighting, some of the fastest growing applications are expected to be the backlighting of color screens in mobile appliances and automotive headlights [26–28].

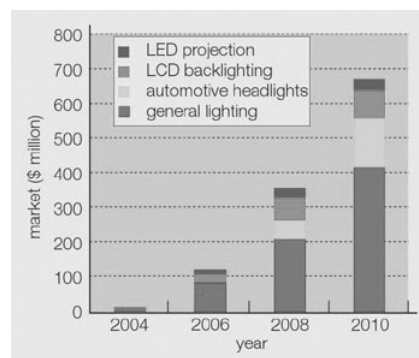


Figure 2.4: Market predictions for high-power white LEDs [28]

The range of applications for LEDs widens constantly. Due to their low power consumption they are interesting for illumination in any kind of mobile application, such as cellular phones, PDA's, laptops, flashlights, headlamps, highway signs; recently the first solar-powered devices were appearing on the market. There is even a Canadian humanitarian initiative, called "Light Up The World", whose goal is to furnish solar-powered lighting solutions based on white LEDs to people without electricity in third world countries [29].

Ultraviolet LEDs (UV LED) are expected to find many applications in various fields, e.g. chemical analysis, gas detection, air purification, water treatment, counterfeit detection (banknotes, passports or other official documents) and numerous medical applications.

The wide range of wavelengths and high power level available also lead to many applications in the medical field, such as the curing of dental composites with blue LEDs, medical diagnostic systems that measure the oxygen content of the blood or allow non-invasive imaging of the eye [30]; or the photodynamic therapy for the treatment of tumors [31].

Last but not least LEDs are even used by the NASA for farming. In the Advanced Astroculture experiment aboard the International Space Station soybeans are grown under LED light [32–34]. Plants require light at about 670 nm (red) for photosynthesis and a small amount at about 470 nm (blue) for development and for proper orientation in the absence of gravity. The intensity of the photon flux and the ratio of red to blue light may be continuously varied. The total photon flux of the light cap may be as large as several times full sunlight.



Figure 2.5: Advanced Astroculture facility on the Space Station for the growth of plants under LED illumination

Figures 2.6–2.9 show illustrations of several LED applications. The display for the NASDAQ-AMEX Marketsite Tower, installed in 2000, was the world's largest LED video display at the time [35]. It is approximately 40 meters high by 30 meters wide and contains 19 million LEDs.



Figure 2.6: LED traffic light



Figure 2.7: White LEDs in daytime running lights within headlamps (a); full LED headlamp prototype (b) [17]



Figure 2.8: LED display for the NASDAQ-AMEX Marketsite Tower in New York, USA



Figure 2.9: LEDs in architecture, examples from Kawasaki, Japan (left), Glasgow, UK (middle) and Athens, Greece (right) [36]

2.3 LED Characteristics: Electrical Properties

2.3.1 Diode Current–Voltage Characteristic

A light-emitting diode (LED) is basically a forward biased p–n or p–i–n junction diode. The p–i–n junction can be described as a p–n junction with a depletion layer that encompasses the entire intrinsic region [37]. Upon application of a bias voltage to a p–n junction, the voltage drop is concentrated over the depletion region.

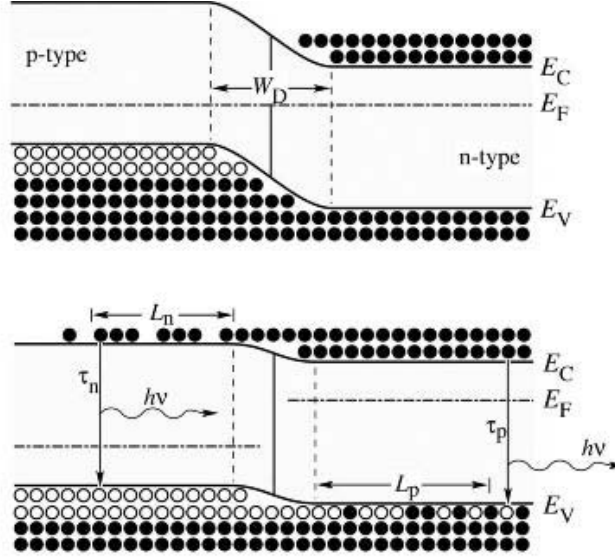


Figure 2.10: p–n homojunction under zero bias (top) and under forward bias (bottom) [9]

Electrons and holes are injected as minority carriers across the p–n junction and they recombine either by radiative or non-radiative recombination. The forward bias current is dominated by the minority charge diffusion current across the junction. Under forward bias the diffusion current consists in general of three components:

- J_{nd} minority carrier electron diffusion current density
- J_{pd} minority carrier hole diffusion current density
- J_{rec} non-radiative recombination current density in the depletion region

$$J_{nd} = eD_n \text{grad}n = \frac{eD_n n_{p0}}{L_n} \left[\exp\left(\frac{eV}{kT}\right) - 1 \right] \quad (2.1)$$

$$J_{pd} = eD_p \text{grad}p = \frac{eD_p p_{n0}}{L_p} \left[\exp\left(\frac{eV}{kT}\right) - 1 \right] \quad (2.2)$$

$$J_{rec} = \frac{en_i w}{2\tau_0} \left[\exp\left(\frac{eV}{2kT}\right) - 1 \right] \quad (2.3)$$

where e is the electron charge, k the Boltzmann constant, n and p are the electron and hole concentration, $D_{n,p}$ and $L_{n,p}$ the electron and hole diffusion constants and diffusion

lengths of electrons in the p-region and holes in the n-region, respectively. n_{p0} and p_{n0} represent the minority carrier concentration of electrons in the p-side and holes in the n-side at equilibrium, i.e. in the absence of an applied bias. n_i is the intrinsic carrier concentration, w is the width of the depletion region and τ_0 is the recombination time in the depletion region. The diffusion lengths are given by

$$L_n = \sqrt{D_n \tau_n} \quad \text{and} \quad L_p = \sqrt{D_p \tau_p} \quad (2.4)$$

where $\tau_{n,p}$ are the electron and hole minority carrier lifetimes, respectively.

The total forward current in the diode can therefore be written as

$$I = I_{0d} \left[\exp \left(\frac{eV}{kT} \right) - 1 \right] + I_{0\text{rec}} \left[\exp \left(\frac{eV}{2kT} \right) - 1 \right] \quad (2.5)$$

I_{0d} corresponds to the reverse saturation current and is equal to

$$I_{0d} = eA \left[\frac{D_n n_{p0}}{L_n} + \frac{D_p p_{n0}}{L_p} \right] \quad (2.6)$$

with A being the cross-sectional area of the diode. The expression for the forward current (2.5) is often simplified to

$$I = I_0 \left[\exp \left(\frac{eV}{n_{\text{ideal}} kT} \right) - 1 \right] \quad (2.7)$$

where n_{ideal} is the diode ideality factor. The current–voltage (I–V) characteristic of a p–n junction was first developed by Shockley [8] and the equation describing the I–V curve of a p–n junction diode is therefore referred to as the **Shockley equation**.

While radiative recombination leads to a current with $n_{\text{ideal}} = 1$, the non-radiative mechanisms lead to a contribution with $n_{\text{ideal}} = 2$. In reality the value often lies somewhere in between, depending on the relative importance of the two recombination mechanisms. At low biases the current is mainly of non-radiative nature which results in values of n close to 2. At higher injection levels the radiative recombination predominates and the ideality factor approaches unity.

2.3.2 Deviations from Ideal I–V Characteristic

A diode normally has unwanted or parasitic resistances in addition. The **series resistance** R_s , which is generally governed by the contact resistance, dominates at high voltages and causes the I–V characteristic to become linear. Channels that bypass the p–i–n junction like dislocations or surface imperfections cause leakage currents at very low bias voltages. This **shunt resistance** R_p is usually very high and is only noticeable close to the origin, where the diode resistance exceeds the parasitic parallel resistance. The expression for the I–V characteristic of a diode therefore needs to be modified taking into account these parasitic effects

$$I - \frac{V - R_s I}{R_p} = I_0 \left[\exp \left(\frac{e(V - R_s I)}{n_{\text{ideal}} kT} \right) - 1 \right] \quad (2.8)$$

Since the shunt resistance is generally very high it can be neglected for forward-biased p–n junctions. Hence equation (2.8) can be simplified to

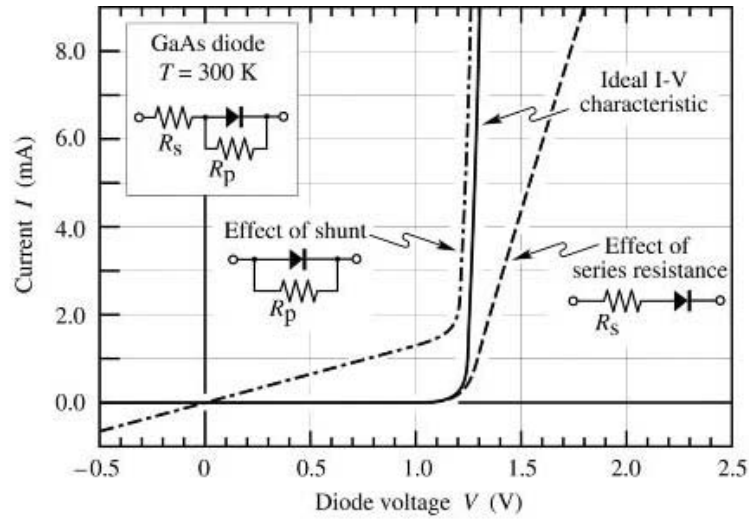


Figure 2.11: Effect of a series resistance and a parallel resistance (shunt) on the I-V characteristic of a p-n junction diode [9]

$$I = I_0 \left[\exp \left(\frac{e(V - R_s I)}{n_{\text{ideal}} k T} \right) - 1 \right] \quad (2.9)$$

2.4 Device Design Issues

Contrary to semiconductors used in purely electronic circuits, for LEDs it is desirable that all the injected carriers recombine in the active region to form photons. The **active region** is usually the lowest bandgap region within the depletion region of a p-i-n diode.

The carrier distribution in p-n **homojunctions**, i.e. p-n junctions consisting of a single semiconductor material, is governed by the carrier diffusion properties. In the absence of an external electric field, the minority carriers diffuse into the region with opposite conductivity with a mean distance corresponding to the diffusion length, L_n and L_p for electrons and holes, respectively (see figure 2.10). These values are typically of the order of several micrometers. This means that the minority carriers are distributed over a large region. The spontaneous radiative recombination rate R_{sp} is given by the bimolecular recombination equation (c.f. section 2.5.2)

$$R_{sp} = Bnp \quad (2.10)$$

which means that the rate is proportional to the carrier concentration in the active region (B is the radiative bimolecular recombination coefficient). However if the carriers are only limited by the diffusion their concentration will never be very high, not even for large current injection levels. The carriers therefore need to be confined by other means. In addition in a homojunction the emitted photons tend to be reabsorbed in the semiconductor before arriving at the surface.

2.4.1 Double Heterostructures

The efficiency of LEDs can be drastically improved with the use of a **heterojunction**, i.e. a junction between different semiconductor materials. By injecting the carriers from a larger bandgap semiconductor into a narrow bandgap active region they are confined to the low bandgap region as the band offsets act as barriers. Thus with this so-called **double heterostructure** (DH) higher carrier concentrations can be achieved, as is depicted schematically in figure 2.12. Furthermore the photons emitted are not absorbed in the wider bandgap confinement layers, as the photon energy is smaller than the bandgap of the barriers.

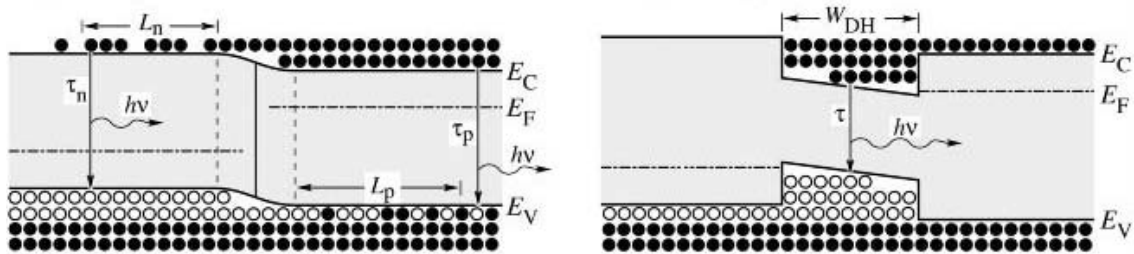


Figure 2.12: Free carrier distribution in a homojunction (left) and a heterojunction (right) under forward bias. In homojunctions carriers are distributed over the diffusion length whereas in heterojunctions they are confined to the well region with thickness W_{DH} [9].

2.4.2 Quantum Wells

A **quantum well** (QW) is a double heterojunction structure with a very thin ($\lesssim 50\text{nm}$) narrow bandgap layer. Under forward bias, approximately rectangular quantum wells appear in the conduction and valence band as shown schematically in figure 2.13. As the active layer thickness comes close to the De-Broglie wavelength (about 10 nm for semiconductor laser devices) quantum effects become apparent. The size quantization can be used to increase the emission energy. Due to their small thickness QWs can be strained by being lattice-mismatched without introducing any undesired defects. This further increases the accessible wavelength range compared to bulk emission. The thickness reduction leads to high carrier densities. As a result, the carrier lifetime for radiative recombination is reduced and the radiative efficiency is increased. In addition due to the reduced active region thickness the re-absorption of emitted photons is drastically reduced.

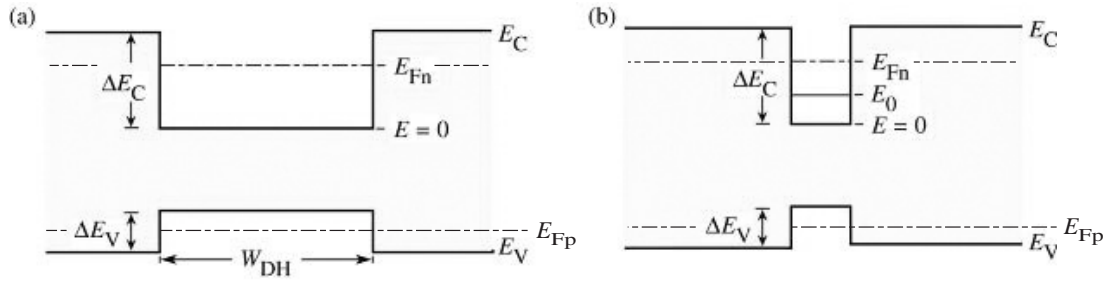


Figure 2.13: Fermi level (E_{Fn}) and subband level (E_0) in a double heterostructure (a) and a quantum well structure (b) at high injection levels [9]

However quantum wells are saturated at lower injection levels compared to bulk active regions and hence for high power devices multi quantum well (MQW) structures are employed. In that case the barriers between the different wells need to be sufficiently transparent, i.e. low or thin, in order to allow for efficient transport between the wells and to ensure a homogeneous carrier distribution.

2.4.3 Separate Confinement Heterostructures

The lower bandgap region in a double heterostructure usually also has a higher index of refraction. Therefore not only the carriers but the photons as well are confined to the narrow bandgap active region and the structure acts like a transverse dielectric optical waveguide or a vertical optical cavity. However with the use of a quantum well this optical confinement effect is sacrificed. Therefore different heterostructures are used for the electrical and the optical confinement. Such **separate confinement heterostructures** (SCH) consist of thin quantum well carrier-confining active regions and a surrounding intermediate bandgap separate photon confinement region. By a grading of the index in the outer heterobarriers the overlap between the optical standing wave and the quantum well regions can be further improved, this configuration being called **graded index separate confinement heterostructure** (GRINSCH).

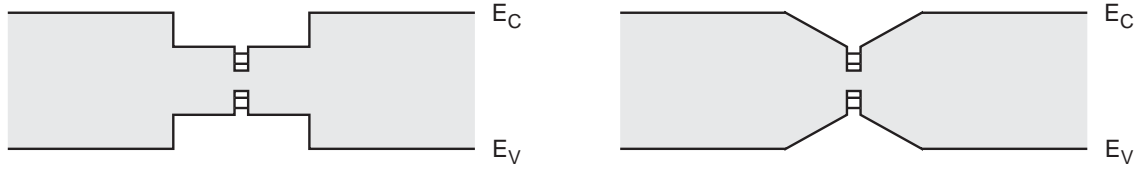


Figure 2.14: Transverse band structure for two different separate confinement heterostructures (SCHs): standard SCH (left) and graded index SCH (GRINSCH) (right). The electric field (photons) is confined by the outer step or graded heterostructure; the central quantum well confines the electrons.

2.4.4 Carrier Loss Mechanisms

Carrier Leakage in Double Heterostructures

Ideally the injected carriers are confined to the active region by the barrier layers adjoining the active region. This way a high carrier concentration is attained resulting in a high radiative efficiency. For an efficient confinement the barriers must be much larger than the thermal energy of the carriers, which is equal to kT . However, the energy distribution of the free carriers in the active region is given by the Fermi–Dirac distribution. Thus a certain fraction of the carriers has a higher energy than the barriers. These carriers can diffuse into the barrier layers and recombine there instead of in the active region.

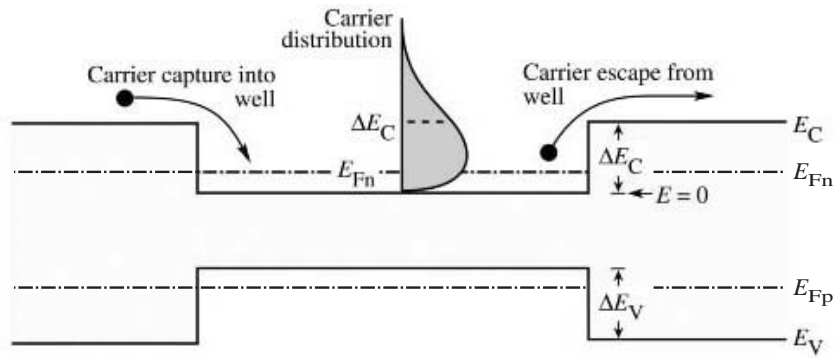


Figure 2.15: Carrier capture and escape in a double heterostructure. Also shown is the energy distribution of the free carriers in the active layer [9].

For the AlGaAs/GaAs and the InGaAs/AlGaAs material system the barriers are relatively high, but in case of GaInP/AlGaInP they are significantly lower, both for electrons and holes (see table 5.1 for a comparison). This results in significantly higher leakage currents for this material system.

As the carrier energy distribution strongly depends on the temperature, the carrier leakage increases exponentially with temperature [38].

Carrier Overflow in Double Heterostructures

At high injection levels carrier start to spill over from the active region into the confinement region. With increasing injection current density the carrier concentration in the active region increases and the Fermi energy rises. For sufficiently high current densities, the Fermi energy will rise to the top of the barrier. At that point the active region is flooded with carriers and a further increase in injection current density will not increase the carrier concentration in the active region. As a result the optical intensity saturates.

The problem of carrier overflow is more severe in QW structures. Hunt et al. [39] showed that the saturation level of the optical intensity is proportional to the number of quantum wells in a LED. Therefore carrier overflow in high-current devices can be avoided by employing either thick DH active regions, multi quantum well (MQW) structures or a large injection area, which means a large contact size.

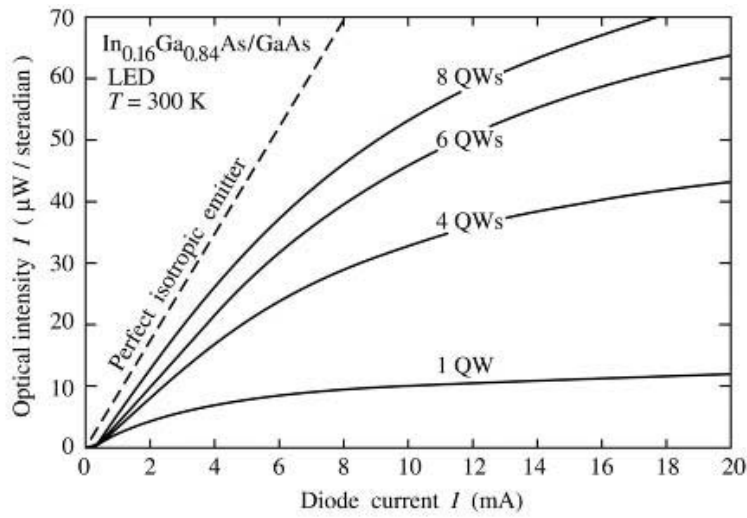


Figure 2.16: Optical intensity emitted by $\text{In}_{0.16}\text{Ga}_{0.84}\text{As/GaAs}$ LEDs with active regions consisting of 1, 4, 6 and 8 QWs and theoretical intensity of a perfect isotropic emitter (dashed line) [39]

2.5 LED Characteristics: Optical Properties

Luminescence can be defined as the non-thermal conversion of energy into light, as compared to **incandescence**, which is the emission of light by thermal radiation. If excited to higher energy levels by an external source of energy, a luminescent radiator decays to lower energy levels by emitting optical radiation [37]. Luminescent radiators are classified according to the source of excitation energy. **Cathodoluminescence** is caused by electrons that collide with the atoms of a target. **Photoluminescence** is caused by energetic optical photons. **Electroluminescence** results from energy provided by an applied electrical field. An important example of electroluminescence is **injection electroluminescence**, which occurs when electric current is injected into a forward-biased semiconductor junction diode. As injected electrons from the conduction band recombine with injected holes from the valence band, photons are emitted. This is the radiation process taking place in light-emitting diodes (LEDs).

Singh [40] defines a **light-emitting diode** as follows: “The basic LED is a p–n junction which is forward biased to inject electrons and holes into the p- and n-sides respectively. The injected minority charge from the n- and p-sides recombines with the majority charge in the depletion region or the neutral region. In direct band semiconductors, this recombination leads to light emission since radiative recombination dominates in high quality materials. In indirect gap materials, the light emission efficiency is quite poor and most of the recombination paths are non-radiative which generate heat rather than light.”

The color of the emitted light is defined by the energy of the emitted photons, which is approximately equal to the energy bandgap of the semiconductor material in the active region of the LED, since the injected electrons and holes are described by quasi-Fermi distribution functions.

2.5.1 Glossary of Radiometric and Photometric Units

The physical properties of electromagnetic radiation are characterized by **radiometric units**. To characterize visible light and the color sensation by the human eye, however, **photometric units**, which take into account the sensitivity of the human eye, are used.

Radiometric Units

The following definitions for radiometric units are based on the conventions by Saleh and Teich [37]. The total electron flux $\Phi_{\text{el}}^{\text{tot}}$, i.e. the number of electrons per second injected in the device, corresponds simply to the injected current I , divided by the electron charge e

$$\Phi_{\text{el}}^{\text{tot}} = \frac{I}{e} \quad (2.11)$$

The **injection efficiency** η_{inj} takes into account that not all the injected carriers recombine in the active region and is defined as the ratio of the electron flux injected into the active region, $\Phi_{\text{el}}^{\text{int}}$, to the total electron flux injected in the device, $\Phi_{\text{el}}^{\text{tot}}$,

$$\eta_{\text{inj}} = \frac{\Phi_{\text{el}}^{\text{int}}}{\Phi_{\text{el}}^{\text{tot}}} \quad (2.12)$$

The **radiative efficiency** η_{rad} corresponds to the fraction of the injected electron flux, $\Phi_{\text{el}}^{\text{int}}$, that is converted into a photon flux $\Phi_{\text{opt}}^{\text{int}}$ in the active region

$$\eta_{\text{rad}} = \frac{\Phi_{\text{opt}}^{\text{int}}}{\Phi_{\text{el}}^{\text{int}}} \quad (2.13)$$

The **internal quantum efficiency** η_{int} accounts for injection losses as well as losses due to non-radiative recombination in the active region and corresponds therefore to the ratio of the photon flux generated in the active region, $\Phi_{\text{opt}}^{\text{int}}$, to the total electron flux, $\Phi_{\text{el}}^{\text{tot}}$,

$$\eta_{\text{int}} = \frac{\Phi_{\text{opt}}^{\text{int}}}{\Phi_{\text{el}}^{\text{tot}}} = \eta_{\text{inj}}\eta_{\text{rad}} \quad (2.14)$$

The photon flux generated in the active region is radiated uniformly in all directions, however due to re-absorption in the semiconductor and internal reflection at the interface semiconductor–air only a fraction of the light can escape the semiconductor. This characteristic is described with the **extraction efficiency** η_{extr} , which relates the output photon flux $\Phi_{\text{opt}}^{\text{out}}$ to the internal photon flux $\Phi_{\text{opt}}^{\text{int}}$

$$\eta_{\text{extr}} = \frac{\Phi_{\text{opt}}^{\text{out}}}{\Phi_{\text{opt}}^{\text{int}}} \quad (2.15)$$

The **external quantum efficiency** η_{ext} accommodates all losses and is defined as the ratio of the output photon flux $\Phi_{\text{opt}}^{\text{out}}$ to the total electron flux $\Phi_{\text{el}}^{\text{tot}}$

$$\eta_{\text{ext}} = \frac{\Phi_{\text{opt}}^{\text{out}}}{\Phi_{\text{el}}^{\text{tot}}} = \eta_{\text{int}}\eta_{\text{extr}} = \eta_{\text{inj}}\eta_{\text{rad}}\eta_{\text{extr}} \quad (2.16)$$

Each photon has an energy of $h\nu$, therefore the optical output power of a LED, P_{opt} , is related to the output photon flux in the following way

$$P_{\text{opt}} = h\nu\Phi_{\text{opt}}^{\text{out}} \quad (2.17)$$

The expression for the external quantum efficiency (2.16) can therefore be rewritten as

$$\eta_{\text{ext}} = \frac{e}{h\nu} \frac{P_{\text{opt}}}{I} \quad (2.18)$$

Another measure of performance for LEDs is the **power efficiency** or **wall-plug efficiency** η_{wp} . It corresponds to a power conversion efficiency and is defined as the ratio of the optical output power P_{opt} to the applied electrical power P_{el}

$$\eta_{\text{wp}} = \frac{P_{\text{opt}}}{P_{\text{el}}} = \frac{P_{\text{opt}}}{VI} \quad (2.19)$$

where V is the voltage drop across the device. The external quantum efficiency and the wall-plug efficiency are related as follows

$$\eta_{\text{wp}} = \eta_{\text{ext}} \frac{h\nu}{eV} \quad (2.20)$$

As the total applied electrical power includes the electrical power dissipated as heat through the series resistance of the device, eV is normally greater than $h\nu$ (which corresponds to the bandgap energy) and hence η_{wp} is normally smaller than η_{ext} .

The different efficiencies are related in the following way. The internal quantum efficiency corresponds to the product of the injection efficiency and the radiative efficiency

$$\eta_{\text{int}} = \eta_{\text{inj}} \eta_{\text{rad}} \quad (2.21)$$

The external quantum efficiency is the product of the the internal quantum efficiency and the extraction efficiency. It includes therefore the injection efficiency, the radiative efficiency and the extraction efficiency.

$$\eta_{\text{ext}} = \eta_{\text{int}} \eta_{\text{extr}} = \eta_{\text{inj}} \eta_{\text{rad}} \eta_{\text{extr}} \quad (2.22)$$

The **brightness** (or **radiance**) corresponds to the wavelength-integrated emitted power per unit area and unit solid angle [41] and can be defined as

$$B(\theta) = \frac{dP_{\text{opt}}(\theta)}{dA d\Omega} \quad (2.23)$$

Brightness is an important factor for MCLEDs, as several applications demand a high directionality and a high brightness. In microcavities brightness and directionality are closely related due to the unavoidable angle-wavelength dispersion of cavity modes (see section 2.7.1).

Photometric Units

For visible LEDs photometric units are used to characterize the device performance. They are weighted according to the sensitivity of the human eye. A standard eye sensitivity function, $V(\lambda)$, as defined by the International Commission on Illumination (CIE, Commission internationale d'Eclairage), allows the conversion between radiometric and photometric units (figure 2.17). It can be seen that the human eye has its peak sensitivity in the green at 555 nm.

The luminous flux represents the optical output power of a source as perceived by the human eye. It is expressed in units of **lumen** (lm), which is defined as follows: “A monochromatic light source emitting an optical power of (1/683) Watt at 555 nm has a luminous flux of 1 lumen (lm)”.

The luminous flux Φ_{lum} can therefore be obtained from the radiometric optical power as follows

$$\Phi_{\text{lum}} = 683 \int V(\lambda) P_{\text{opt}}(\lambda) d\lambda \quad [\text{lm}] \quad (2.24)$$

where $P_{\text{opt}}(\lambda)$ is the power spectral density, i.e. the optical power emitted (in W) per unit wavelength and the prefactor 683 lm/W is a normalization factor.

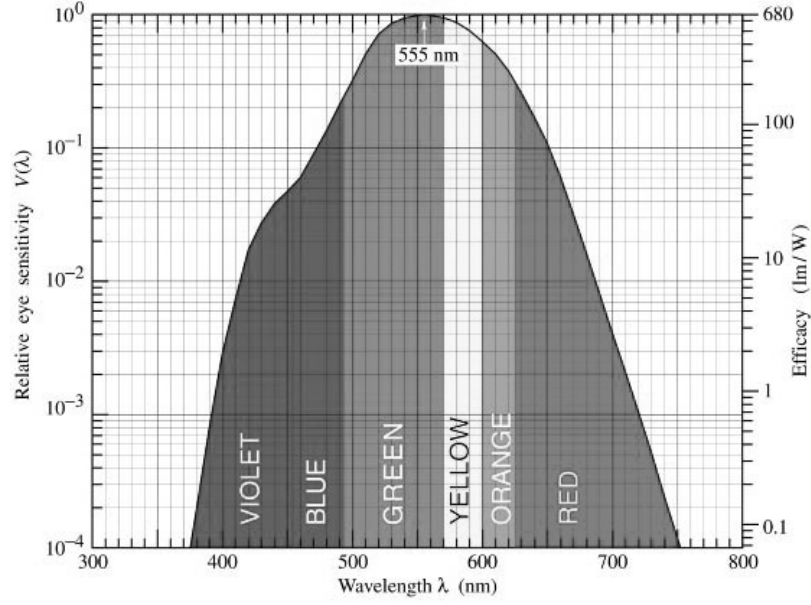


Figure 2.17: Eye sensitivity function $V(\lambda)$ (left ordinate) and corresponding luminous efficacy (right ordinate), according to CIE standards [9]

The **luminous efficacy** of optical radiation ζ_{lum} is the conversion efficiency from optical power to luminous flux.

$$\zeta_{\text{lum}} = \frac{\Phi_{\text{lum}}}{P_{\text{opt}}} = 683 \frac{\int V(\lambda) P_{\text{opt}}(\lambda) d\lambda}{\int P_{\text{opt}}(\lambda) d\lambda} \quad [\text{lm/W}] \quad (2.25)$$

The **luminous efficiency** η_{lum} of a light source is defined as the ratio of the luminous flux of the light source, Φ_{lum} , to the electrical input power P_{el} .

$$\eta_{\text{lum}} = \frac{\Phi_{\text{lum}}}{P_{\text{el}}} = \frac{\Phi_{\text{lum}}}{VI} \quad [\text{lm/W}] \quad (2.26)$$

The luminous efficiency and the luminous efficacy can be related via the wall-plug efficiency (see (2.19))

$$\eta_{\text{lum}} = \zeta_{\text{lum}} \eta_{\text{wp}} \quad (2.27)$$

2.5.2 Radiative and Non-radiative Recombination Mechanisms

Consider a forward biased p-i-n junction with a single quantum well of thickness t_{qw} and volume V_{qw} in the center of a nominally undoped intrinsic region. The electron density in the quantum well can then be described by the following rate equation [42,43]

$$\frac{dN}{dt} = G - R - R_l \quad (2.28)$$

where G is the rate of injected electrons, R the rate of recombining electrons per unit volume in the active region, neglecting photon recycling, and R_l the **carrier leakage rate**. The carrier leakage rate includes vertical carrier spill-over out of the active region and lateral diffusion out of the cavity region.

The generation rate G corresponds to the fraction of the current being injected into the active region,

$$G = \frac{\eta_{inj} I}{e V_{qw}} \quad (2.29)$$

with I being the applied current and η_{inj} the injection efficiency. The recombination rate is the sum of the **radiative recombination rate**, R_{rad} and the **non-radiative recombination rate** R_{nr} . For lasers the **stimulated recombination rate** R_{st} would have to be considered as well, but can usually be neglected for LED structures.

$$R = R_{rad} + R_{nr} + R_{st} \quad (2.30)$$

Under steady-state conditions ($dn/dt = 0$)

$$\frac{\eta_{inj} I}{e V_{qw}} = R_{rad} + R_{nr} + R_l \quad (2.31)$$

The radiative efficiency η_{rad} is defined as the ratio of the number of photons generated in the active region per unit time per unit volume to the number of electrons injected in the active region per unit time per unit volume. Thus it can be written as

$$\eta_{rad} = \frac{R_{rad}}{R_{rad} + R_{nr} + R_l} \quad (2.32)$$

The **band-to-band radiative recombination rate** R_{rad} is

$$R_{rad} = Bnp = Bn^2 \quad (2.33)$$

where n and p are the electron and hole concentrations in the active region, respectively. At high injection levels charge neutrality requires $n = p$ in the active region. B is the radiative bimolecular recombination coefficient and is of the order of 10^{-10} cm³/s for InGaAs/GaAs structures [44,45].

The **non-radiative recombination rate** R_{nr} includes deep-level defect and impurity recombination in the depletion layer, surface and interface recombination and Auger recombination, which can be an important mechanism at very high injection levels.

$$R_{nr} = An + Cn^3 \quad (2.34)$$

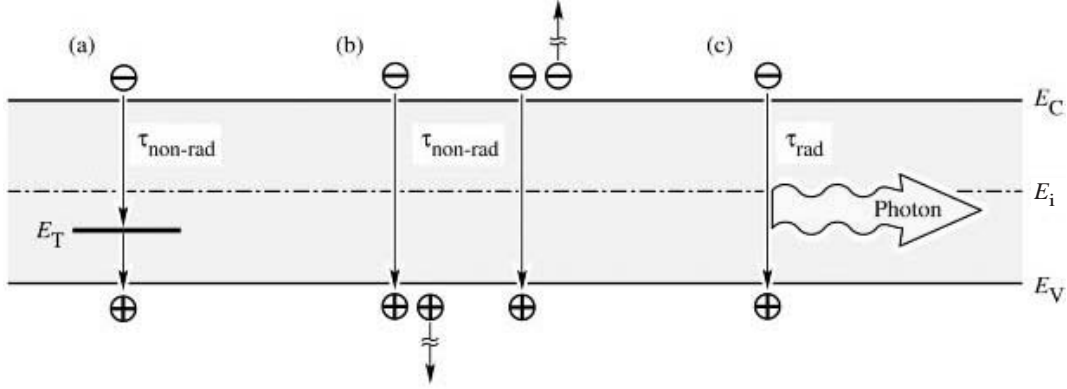


Figure 2.18: Band diagram illustrating recombination mechanisms: via a deep level (a), via an Auger process (b) and radiative recombination (c) [9]

A corresponds to the non-radiative recombination coefficient (in units of $[s^{-1}]$) and C to the Auger coefficient. Typical values for C are 10^{-28} - 10^{-29} cm^6/s for III-V semiconductors [9]. For InGaAs/GaAs devices at room temperature the Auger recombination can be neglected [44].

In the GaAs/AlGaAs and InGaAs/GaAs systems **surface recombination** can be quite severe for small devices [46,47,43]. Assuming a uniform carrier distribution over the whole mesa the non-radiative recombination coefficient can be expressed as [43]

$$A = A_0 + \frac{a_s \nu_s}{V_{qw}} = A_0 + \frac{4\nu_s}{d} \quad (2.35)$$

where A_0 stands for defect and impurity recombination, a_s is the exposed quantum well surface area, V_{qw} the volume of the active region, ν_s the surface recombination velocity and d the device diameter. For strained InGaAs/GaAs quantum well lasers the surface recombination velocity has been found to be of the order of 2×10^5 cm/s [48–50].

Expression (2.32) for the radiative efficiency can therefore be rewritten in the following way for InGaAs/GaAs LEDs:

$$\eta_{\text{rad}} = \frac{Bn^2}{Bn^2 + An + R_l} \quad (2.36)$$

with A including surface and interface recombination. The deep-level defect and impurity recombination in the depletion layer can be minimized with the use of high purity and low defect density substrates and epitaxial structures. With an appropriate device design the injection efficiency η_{inj} and the carrier density in the active region can be maximized and the carrier leakage rate can be minimized at the same time. With all these measures internal quantum efficiencies close to unity are possible in modern devices. The external quantum efficiencies of LEDs are therefore essentially limited by their extraction efficiencies.

2.5.3 Light Extraction Problem

The extraction efficiency is defined as the fraction of the light generated in the active region which is extracted out of the device. It depends on the optical properties of the device, on its layer structure and on its geometry. Limiting factors are **re-absorption** in the semiconductor and **internal reflection** at the interface semiconductor–air. In addition for top emitting devices the extraction efficiency can be significantly reduced by **shadowing** of the emission by the top contact. Therefore the extraction efficiency can be expressed as the product of an absorption factor γ_{abs} , a reflection factor γ_{refl} , and a shadowing factor γ_{sh}

$$\eta_{\text{extr}} = \gamma_{\text{abs}} \gamma_{\text{refl}} \gamma_{\text{sh}} \quad (2.37)$$

The amount of re-absorption depends on the layer structure and can usually be minimized by using materials with a bandgap energy larger than the photon energy or by limiting their thicknesses. The top contact shadowing depends on the device design, often there exists a trade-off between improved current spreading and reduced extraction for a more dense top contact pattern.

In case of an isotropic internal emission of the active region, the amount of reflection at the interface semiconductor–air is dictated by the device geometry and by the refractive index of the semiconductor layer at the interface. Due to the high refractive index of most semiconductors, **total internal reflection** (TIR) at the interface semiconductor–air drastically limits their extraction efficiency. In the following the limits for γ_{refl} for different device geometries are estimated. Since γ_{abs} and γ_{sh} are assumed to be equal to unity, $\eta_{\text{extr}} \approx \gamma_{\text{refl}}$.

The Light Escape Cone

At the interface semiconductor – outside medium, an incident ray is split into two, a reflected ray and a refracted (or transmitted) ray. The transmitted ray obeys **Snell's law of refraction**

$$n_{\text{int}} \sin \theta_{\text{int}} = n_{\text{ext}} \sin \theta_{\text{ext}} \quad (2.38)$$

where n_{int} and θ_{int} are the refractive index and the incident angle from the normal in the high index semiconductor, n_{ext} is the refractive index of the low index outside medium (typically air) and θ_{ext} the angle of the refracted beam in the outside medium. Total internal reflection occurs for $\theta_{\text{int}} \geq \theta_c$, with θ_c being the **critical angle of total internal reflection**

$$\theta_c = \arcsin \left(\frac{n_{\text{ext}}}{n_{\text{int}}} \right) \quad (2.39)$$

for which $\theta_{\text{ext}} = 90^\circ$. For larger angles of incidence, $\theta_{\text{int}} > \theta_c$, θ_{ext} becomes complex and the entire electromagnetic energy is reflected back, apart from an evanescent wave in the low index material which decreases exponentially away from the interface [40]. The critical angle defines the light escape cone in the semiconductor. The critical solid angle Ω_c corresponding to θ_c is

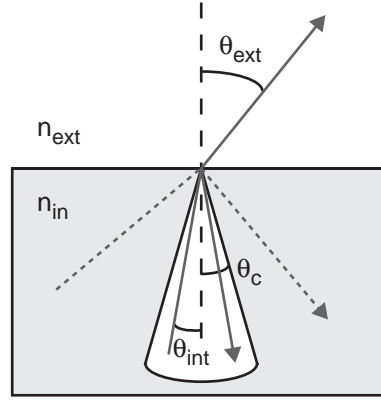


Figure 2.19: Transmission and reflection at the interface semiconductor–air; θ_c corresponds to the critical angle of total internal reflection, defining the light escape cone

$$\Omega_c = 2\pi(1 - \cos \theta_c) \quad (2.40)$$

while the total solid angle is 4π .

For $\theta_{\text{int}} \leq \theta_c$ the reflected and transmitted intensities of a ray are equal to

$$I_t = TI_i = (1 - R)I_i \quad (2.41)$$

$$I_r = RI_i \quad (2.42)$$

where I_i , I_t and I_r are the intensities of the incident, transmitted and reflected ray, respectively. T is the power transmission coefficient and R the Fresnel power reflection coefficient. In case of TE polarization R is equal to

$$R = \left(\frac{n_{\text{int}} \cos \theta_{\text{int}} - n_{\text{ext}} \cos \theta_{\text{ext}}}{n_{\text{int}} \cos \theta_{\text{int}} + n_{\text{ext}} \cos \theta_{\text{ext}}} \right)^2 \quad (2.43)$$

For normal incidence ($\theta_i = 0$) this expression simplifies to

$$R_0 = \left(\frac{n_{\text{int}} - n_{\text{ext}}}{n_{\text{int}} + n_{\text{ext}}} \right)^2 \quad (2.44)$$

Assuming an isotropic internal emission and $R \approx R_0$ for all angles $\theta \leq \theta_c$, the fraction of the light emitted in a semiconductor that can be extracted through the top surface is therefore given by

$$\gamma_{\text{refl}} \approx \frac{2\pi(1 - \cos \theta_c)}{4\pi} (1 - R_0) \quad (2.45)$$

For the interface GaAs–air, this leads to an extraction efficiency between 1 and 2 % only. By encapsulating the LED in a hemispherical epoxy dome with a refractive index of approximately 1.5 the light extraction can be significantly enhanced [51]. Due to the larger index of the outside medium, the critical angle is increased and the reflection at normal incidence is reduced. The critical angle for the interface epoxy–air is large due to the small index difference. If the LED is placed at the center of the hemispherical

epoxy dome, all the light rays hit the interface epoxy–air at normal incidence and the device shows a quasi-isotropic emission. Alternatively the LED can be placed at the Weierstrass point, i.e. at a distance of r_s/n_{epoxy} below the center of the sphere with radius r_s , which leads to a directional emission [52]. This geometry is called a **Weierstrass sphere**.

Thus extraction efficiencies between 3 and 4% can be achieved with an epoxy dome. The different numerical values for GaAs are summarized in table 2.1 and table 2.2 for emission into air and epoxy, respectively. The values are calculated at the two wavelengths of interest for this work, 650 and 970 nm.

Table 2.1: Extraction properties for interface GaAs–air at 650 and 970 nm

Wavelength [nm]	n_{GaAs}	n_{air}	θ_c [°]	$\Omega_c/4\pi$ [%]	R_0 [%]	γ_{refl} [%]
650	3.83	1	15.2	1.7	34	1.1
970	3.52	1	16.5	2.1	31	1.4

Table 2.2: Extraction properties for interface GaAs–epoxy at 650 and 970 nm

Wavelength [nm]	n_{GaAs}	n_{epoxy}	θ_c [°]	$\Omega_c/4\pi$ [%]	R_0 [%]	γ_{refl} [%]
650	3.83	1.5	23.1	4.0	19	3.2
970	3.52	1.5	25.2	4.8	16	4.0

The reflection at the interface epoxy–air is about 4% for normal incidence. By taking this into account the extraction efficiencies for devices encapsulated in a hemispherical epoxy dome diminish slightly to 3.1 and 3.8% at 650 and 970nm, respectively. Even with an epoxy dome the maximum attainable extraction efficiencies are therefore extremely low for planar structures with a single facet emission.

Optimization Standard Geometry

The standard LED geometry is a rectangular parallelepiped, fabricated by cleaving the wafer along its crystallographic axes. The active region is assumed to be close to the surface and the substrate absorbing, due to the fact that it has a lower bandgap than the active region. Such a device has a total of six light escape cones, two of them perpendicular to the wafer surface and four of them parallel to it. The light emitted into the bottom escape cone is entirely absorbed in the substrate. Apart from a small area close to the edges, the emission in the bottom part of the four in-plane escape cones is absorbed in the substrate too, as well as a large amount of the top part, which is totally internally reflected at the top surface and redirected towards the substrate. The light in the top escape cone is in part obstructed by the top contact. Thus the extraction efficiency of this device geometry is very low, as its reflection factor is close to the value calculated above for a single escape cone. Its external quantum efficiency can be expressed as

$$\eta_{\text{ext}} = \eta_{\text{int}} \gamma_{\text{refl}} \gamma_{\text{sh}} \quad (2.46)$$

Even for an internal efficiency of 100 % and no shadowing, the theoretically achievable external quantum efficiency for this geometry is smaller than 2 % for emission into air and below 4 % for emission into epoxy.

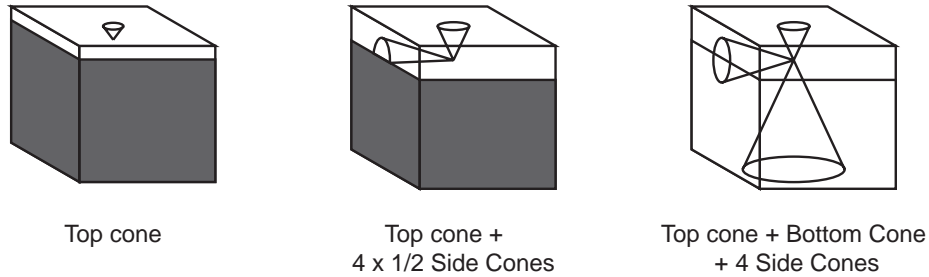


Figure 2.20: Simplified schematic illustration of light extraction for various LED designs based on a standard rectangular parallelepiped; absorbing substrate with thin window layer (left), absorbing substrate with thick window layer (middle) and transparent substrate with thick window layer (right). To simplify matters only one of the four side cones is shown. [53]

A first approach to increase the extraction efficiency of the standard LED structure is to add a thick window layer on top of the epitaxial structure. This window layer needs to be optically transparent and electrically conductive. With increasing thickness of this layer the extraction of the top part of the four in-plane escape cones increases until the entire half-cones are extracted, as depicted schematically in figure 2.20. In addition the shadowing of the light in the top escape cone by the top contact can be reduced thanks to an improved current spreading. With this device design the extraction efficiency can therefore be increased by a factor of 3, as in addition to the top cone four more half cones can be extracted.

In order to extract all cones, a transparent substrate needs to be used in addition. The bottom escape cone can then either be extracted via the substrate side or reflected

to the top by a bottom mirror. With this design a near 6-fold increase in extraction efficiency can be achieved. The maximum achievable extraction efficiencies are summarized in table 2.3. These are simplified approximations that do not take into account internal absorption or multiple pass reflection effects such as photon recycling. The actual limits might be a few percent higher [53]. The shadowing by the top contact is not included either in these estimations.

Table 2.3: Extraction improvements for standard LED geometry (neglecting absorption, shadowing and multiple pass reflection effects)

Design	Extracted cones	$\gamma_{\text{ref}}(\text{air})$ [%]	$\gamma_{\text{ref}}(\text{epoxy})$ [%]
standard geometry	1	1-2	3-4
thick window layer	3	3-6	9-12
transparent substrate	6	6-12	18-24

For a cylindrical shape the four in-plane escape cones are replaced by an escape ring. Therefore cylindrical LEDs show higher extraction efficiencies than comparable cubic LEDs. However they can only be fabricated by etching and not by cleaving.

Optimum Device Geometries

The ideal device geometry would be a sphere with a point source as active region in the center of the LED, or a hemisphere with a perfect bottom mirror [52]. No total internal reflection would occur in such a device as all the rays are incident at a normal angle at the interface semiconductor–air. However, unless the sphere is coated with an anti-reflection coating, the rays would still undergo Fresnel reflection at this interface. Comparable extraction efficiencies can be expected from Weierstrass spheres, truncated ellipsoids and truncated cones, in case of the latter for an optimum apex half-angle of $\beta_m = (\pi/2 - \theta_c)/2$ [52].

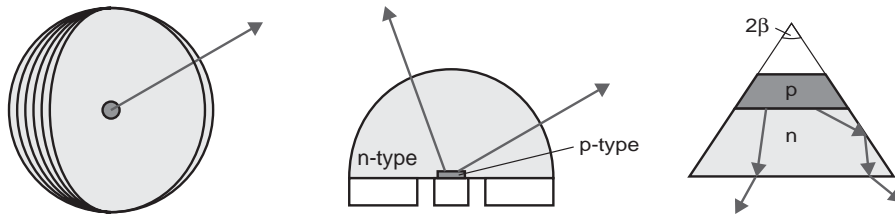


Figure 2.21: Cross-section schematics of ideal geometries; sphere with point source (left), hemisphere (middle) and a truncated cone (right)

The problem of light extraction had been realized already in the very beginning of LEDs in the 1960s. Hemispherical shapes [54] and truncated cones [55] had been demonstrated to improve the extraction efficiency over conventional cubic or cylindrical designs. However these device geometries are not very compatible with semiconductor fabrication technologies, optimized for planar processes in view of the flat substrates used in epitaxial growth and were therefore not developed further for a long time.

2.6 Alternative Types of High Efficiency LEDs

The evolution of high efficiency LEDs can be divided into three eras. First of all the device design was optimized [11]. Thanks to the introduction of double heterostructures, quantum wells and separate confinement heterostructures the injection efficiencies in modern devices can often be assumed to be close to 100 %. With the evolution of the growth methods the crystal quality was constantly optimized, leading to drastically improved radiative efficiencies. Together with the increased carrier densities in the active regions and the reduced leakage rates, internal quantum efficiencies close to unity could be achieved. The problem of light extraction, finally, was realized already in the 1960s [52,54,55] but was not addressed until the 1990s.

The evolution of the extraction efficiency can be shown by means of the chronological improvements of the external quantum efficiency for AlGaInP LEDs by Hewlett-Packard (now Lumileds), which follows the approaches presented in section 2.5.3 [53]. In agreement with the simple model the implementation of a thick GaP window layer led to a three-fold increase in efficiency. By transferring the epitaxial structure on a transparent GaP substrate values of the order of 20 % could be achieved. The increase from 24 to 32 % is due to an improved device design, the double heterostructure being replaced by a separate confinement heterostructure (SCH) with multiple quantum wells (MQWs) as active region. This leads to an increased internal quantum efficiency as well as an increased extraction efficiency due to a reduced re-absorption in the thinner active region [56]. Figure 2.22 contains pictures of the amber DH LED with a thick GaP window layer and the DH LED with a transparent GaP substrate.

Table 2.4: Chronological external quantum efficiency improvements for AlGaInP LEDs

Year	Design	$\eta_{\text{ext}}(\text{epoxy})$ [%]	Ref.
1990	standard LED	≈ 2	[57]
1992	thick GaP window layer	≈ 6	[58]
1994	transparent GaP substrate	17.6	[15]
1996	idem	23.7	[59]
1999	idem + MQW	32.0	[56]

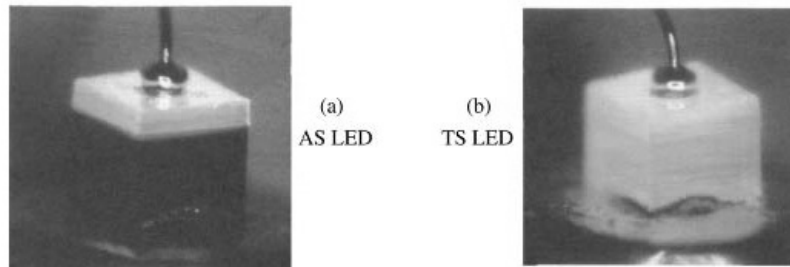


Figure 2.22: Two different generations of amber AlGaInP LEDs by Hewlett-Packard (now Lumileds): absorbing GaAs substrate (AS) LED with thick GaP window layer (a); and wafer-bonded transparent GaP substrate (TS) LED (b) [9]

The value of 32 % published by Gardner et al. [56] probably represents an ultimate limit to the external quantum efficiency achievable with a rectangular parallelepiped device geometry. In an ideal structure with an internal quantum efficiency of unity and with zero internal optical losses, even for a cubic geometry all the light would be eventually coupled out, after a sufficient number of internal reflection and re-absorption and re-emission steps [60]. However in reality $\eta_{\text{int}} < 100\%$ and the internal optical losses, including the finite mirror reflectivity, re-absorption in the active region and free-carrier absorption are non-negligible and the probability of the light being absorbed in the device increases with the number of internal reflections. For AlGaInP LEDs, a tradeoff exists between active layer re-absorption and electron confinement, which results in an optimum active layer thickness [56]. Hence in order to further optimize the extraction efficiency the number of internal reflections before extraction, corresponding to the **mean photon path length for extraction**, needs to be reduced. This can be done either by modifying the device geometry in order to increase the light escape cones; or by altering the internal emission spectrum in order to force the emission into the existing vertical escape cones of the standard planar geometry.

As shown in section 2.5.3 the ideal geometry would be a hemisphere or a Weierstrass sphere, depending on whether a uniform or directed emission is desired [52]. However until today the fabrication of such device geometries is difficult due to technological limitations. More feasible geometries have been realized and led to drastic increases in external quantum efficiency, such as truncated inverted pyramids [16] and radial outcoupling tapers [61]. The substrate-less thin-film LEDs, for which the extraction is optimized either by a surface roughening or by the implementation of pyramidal dice geometries, represent an alternative successful approach [62,63].

In parallel to these geometrical approaches another type of LEDs was developed by modifying the spontaneous emission pattern while retaining a planar geometry [64]. By placing the active region inside an optical cavity the emission intensity in the vertical escape cones can be increased by means of interference effects. This type of light-emitting diode is hence called resonant cavity LED (RCLED) or microcavity LED (MCLED).

In the following the different types of high efficiency LEDs will be briefly introduced and then the theory of MCLEDs will be presented. Detailed reviews for high efficiency AlGaInP LEDs were written by Streubel [65] and Gessmann and Schubert [66].

2.6.1 Truncated Inverted Pyramid LEDs

AlGaInP LEDs are generally grown on GaAs substrates, although GaAs is absorbing in the visible wavelength range, making it impossible to couple out light efficiently through the substrate. In the 1990s Hewlett-Packard (now Lumileds Lighting) continuously increased the extraction efficiency of AlGaInP LEDs by optimizing the device design for an optimal light outcoupling.

The implementation of a thick transparent GaP window layer and the wafer bonding of the epitaxial structure to a transparent GaP substrate lead to a drastic improvement in extraction efficiency. However in these structures the extraction is still limited to the six light escape cones of a rectangular parallelepiped. It was realized already in the 1960's that hemispherical-domed LEDs as well as truncated cones would have optimum extraction properties (see section 2.5.3) [52,54,55], however these solutions were considered as not very practical due to the high costs associated with the chip shaping. Finally in 1999 Krames et al. [16] presented the realization of a practical shaped AlGaInP/GaP LED chip with a **truncated inverted pyramid (TIP)** geometry. The TIP geometry reduces the mean photon path length for extraction. This leads to a reduction of the internal optical losses and therefore to an increased external quantum efficiency [60].

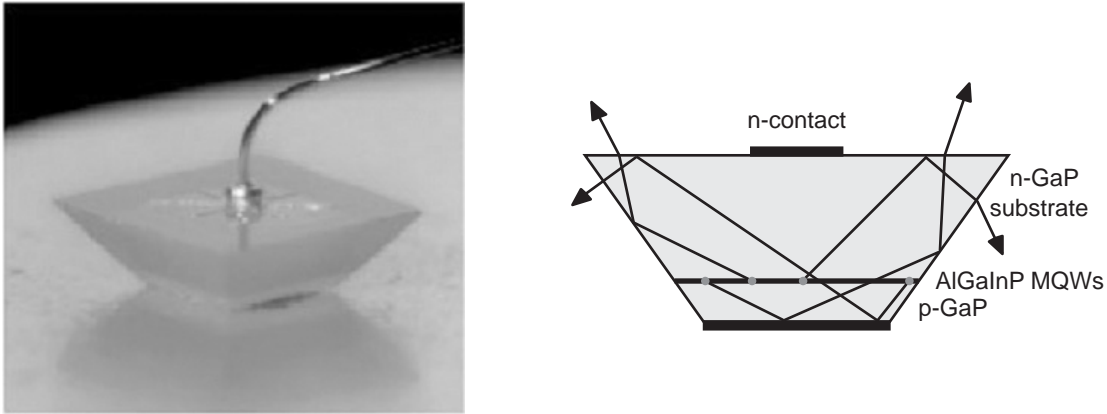


Figure 2.23: Geometry of the truncated inverted pyramid (TIP) AlGaInP/GaP LED. Photomicrograph of a TIP LED under forward bias (left); schematic cross-section illustrating the enhanced light extraction (right)

TIP devices are sawn with a beveled dicing blade to provide chip sidewall angles of 35° with respect to the vertical. With red-emitting TIP LEDs ($\lambda_p \sim 650$ nm) record external quantum efficiencies of 32.6 % for emission into air and 55 % for emission into epoxy (60.9% under pulsed operation) were achieved [16]. These devices show luminous efficiencies exceeding 100 lm/W.

2.6.2 Different Types of Thin-Film LEDs

By placing the epitaxially grown structure on a highly reflective mirror instead of wafer bonding it to a transparent substrate the stringent process parameters related to semiconductor-to-semiconductor wafer bonding such as ultraflat surfaces, crystallographic orientation matching and high bonding temperature can be omitted.

In 1993 Schnitzer et al. [60] presented optically pumped thin films with an external quantum efficiency of 72 %. They are floated off their substrates by the **epitaxial lift-off** technique (ELO) [67] and are van der Waals bonded by surface tension forces onto dielectric coated gold mirrors. In this structure photons which were initially emitted outside of the escape cone, are redirected by internal reflection, re-absorbed and partially re-emitted in the active region (this mechanism is called photon recycling, see section 2.7.3 as well). However for this approach the external quantum efficiency is very susceptible to internal optical losses and to slight degradations of the internal quantum efficiency as the mean photon path length for extraction is extremely high.

Surface-Textured Thin-Film LEDs

A more practical approach for the angular randomization of the totally reflected light is to scatter it from textured semiconductor surfaces, making the extraction less susceptible to the material quality and internal optical losses. Experiments had shown that a surface texture on the scale of half an optical wavelength produces complete internal angular randomization of light rays in a semiconductor film [68]. The first realization of an electrically pumped surface-textured thin-film LED (also called non-resonant cavity LED (NRC-LED)) led to an external quantum efficiency of approximately 30% [69]. The surface texturing is done by depositing polystyrene spheres on the surface and using them as an etch mask for ion-beam etching, a process called **natural lithography** [70]. The substrate is removed by ELO and the thin film is van der Waals bonded onto large area dielectric coated Au mirrors.

Windisch et al. optimized the surface-textured thin-film LED design for 850 nm devices and demonstrated external quantum efficiencies of 46 % and 54 % for unencapsulated and encapsulated devices, respectively [71,72]. The LED employs an oxide current confinement aperture to prevent the generation of light under the top contact. In order to extract as well some of the light in the laterally guided modes, not only the mesa top surface but as well the area between mesa and bottom contact are roughened. Similar red-emitting devices ($\lambda_p \sim 650$ nm) resulted in efficiencies of 24 % and 31 % before and after encapsulation, respectively [73]. Yet in all these devices the ratio of active area to total chip area is reduced, leading to a relatively inefficient material use.

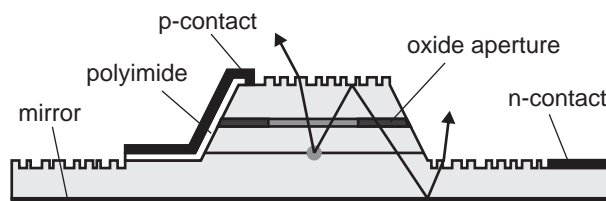


Figure 2.24: Schematic cross-section of the surface-textured thin-film LED with metallic back mirror and roughened surface

Structured Thin-Film LEDs

Another approach for an efficient outcoupling of internally trapped light is the structuring of the backside facing the rear reflector in regular patterns of geometrical structures. The geometries that have been used to shape dies in order to enhance the light extraction, as shown previously, can in general be scaled down as well and still demonstrate their beneficial effect. This has been shown for top emitting AlGaInP LEDs with a bottom reflector on an absorbing GaAs substrate by OSRAM Opto Semiconductors [74,75]. These so-called **micro-reflectors** can be buried at the bonded interface of a thin-film LED as well. After being covered with an insulator and a metal mirror, these structures can then be soldered to a carrier wafer with an intermediate metal layer [76,65]. Contrary to van der Waals bonded structures, conductive interfaces are created with metal bonding that can be used as p-contact, leading to low forward voltages. The current is then injected through small openings in the dielectric layer at the top of the micro-reflectors. Preliminary 650 nm **buried micro-reflector** (BMR) thin-film LEDs showed a maximum wall-plug efficiency of 23.6 % [65], however much higher efficiencies can be expected from this type of thin-film LED.

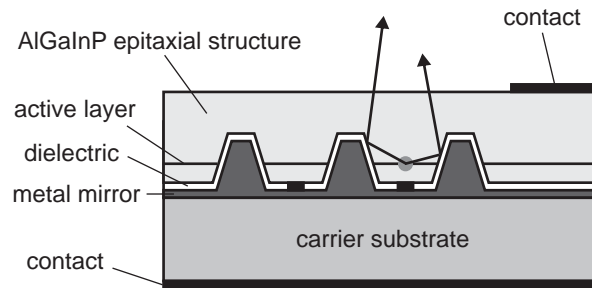


Figure 2.25: Schematic cross-section of a thin-film BMR LED with one possible design of buried micro-reflectors [65]

Structured Thin-Film LEDs with Surface Texturing

BMR thin-film LEDs with in addition a surface texturing as presented in the previous section have been realized. The achieved efficiencies are similar to the ones of standard surface-textured LEDs, 42 % and 51 % before and after encapsulation, respectively, for the GaAs/AlGaAs 870 nm devices and 28 % for un-encapsulated GaInP/AlGaInP 650nm LEDs [72]. However the former technology has the advantage that it can be easily upgraded to a wafer-scale process, being compatible with 4 inch wafer technologies. The design of the red structured thin-film LEDs including a surface texturing was further improved. With an epitaxial structure geometry similar to truncated pyramids and a partially conductive mirror an external quantum efficiency of 35% was achieved without encapsulation [73]. With a further optimized design 40 % were reached for encapsulated devices [62]. With the latest generation of their thin-film AlGaInP devices OSRAM Opto Semiconductors recently realized similar luminous efficiencies as Lumileds with their TIPLEDs [17].

Tapered LEDs

The concept of the tapered LED is similar to the one of the TIP LED. Light generated in a small center active region not falling in the escape cone is redirected to the bottom surface at an outer radial tapered output coupler [61]. The taper has the shape of a shallow truncated cone and is covered with an insulator and a gold mirror. The fabrication of these devices is less cost-intensive than for the TIP LEDs, however the mean photon path length for extraction is estimated to be longer, leading to slightly lower efficiencies.

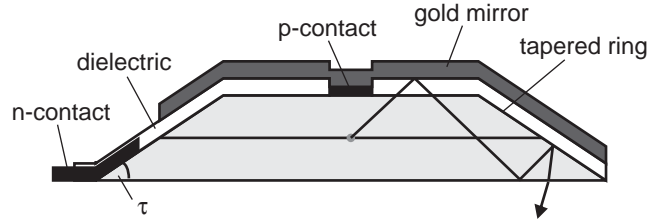


Figure 2.26: Geometry of the tapered LED, schematic cross-section illustrating the enhanced light extraction

In order for light with any initial direction to be coupled out, the taper angle τ needs to be equal or smaller than the critical angle for total internal reflection, θ_c , and the azimuthal wave vector component is kept small by choosing appropriate device dimensions in order to avoid guided modes.

The taper is fabricated by photoresist reflow and mask shape transfer using ion beam etching. After the contact deposition, the structure is covered with polyimide and the gold mirror is evaporated on top. The cover metal thickness is increased galvanically and the substrate is removed by wet etching. Figure 2.27 shows a scanning electron microscope (SEM) picture of the geometry after dry etching.

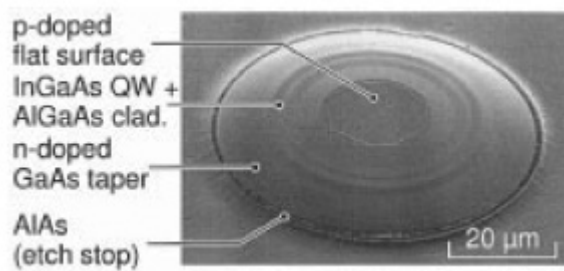


Figure 2.27: SEM viewgraph of structured semiconductor after etching [61]

Near infrared tapered LEDs with InGaAs QWs emitting at 980 nm show external quantum efficiencies close to 40 % for emission into air and 52 % for emission into epoxy [77,61]. With preliminary GaInP/AlGaInP red-emitting devices ($\lambda_p \sim 650$ nm) based on the same technology an efficiency into air of 13 % was achieved [61].

2.7 Microcavity LEDs

A **Microcavity LED** (MCLED), also known as **Resonant Cavity LED** (RCLED), is a light-emitting diode, for which the light-emitting active region is placed in an optical cavity with a thickness of the order of the wavelength of emission [78]. The optical cavity is in resonance with the internal emission, resulting in a modification of the spontaneous emission process, such that the internal emission is no longer isotropic. This results in an increased directionality and brightness and a higher spectral purity of the LED emission spectrum. If the cavity is properly tuned, the alteration of the intrinsic emission spectrum leads to an increase of the power emitted within the escape cone, leading to a higher extraction efficiency.

Microcavity structures have been demonstrated with different active media and different geometries [79–81]. The first microcavity structure made of small metallic spheres was proposed by Purcell in 1946 for emission frequencies in the radio frequency regime [82]. In 1980 Kunz and Lukosz observed for the first time a change of the spontaneous emission rate for an emitter placed in an optical cavity [83,84]. They studied the changes in fluorescent lifetimes of Eu^{3+} ions induced by a variation of their optical environment. In the 1980s and 1990s microcavity structures have been realized with different kind of emission media, including organic dyes [85,86], semiconductors [87,88], rare-earth doped silica [89] and organic polymers [90,91]. Clear changes in spontaneous emission were demonstrated, including the modification of spectral, spatial and temporal emission characteristics.

The first current-injected resonant cavity light-emitting diode was realized in 1992 by Schubert et al. [64] in the GaAs material system and in 1993 by Nakayama et al. with organic polymers [90].

The simplest cavity design consists of two coplanar mirrors surrounding the active region. The first study of optical cavities with coplanar reflectors by Fabry and Perot dates back to 1899 [92]. Even though in their case the cavity lengths were significantly longer than the wavelength of the incident light, this type of optical resonator is called **Fabry–Perot cavity** ever since.

In case of the structures described in this thesis with electron-hole pair recombination and rather low reflection coefficients, the total emission and hence the spontaneous lifetimes are only weakly affected. This regime is called **weak coupling** regime, to be distinguished from the situation of Rabi vacuum field splitting in the **strong coupling** regime [93,94].

In the following the theory of spontaneous emission from microcavities will be briefly described, more detailed analysis were written for example by Benisty et al. [95–97], Neyts [98], Wasey and Barnes [99], Delbeke et al. [100] and Baets et al. [101]. Furthermore the PhD thesis of Royo [42] and Ochoa [102] contain elaborate essays on MCLEDs.

2.7.1 Modification of Spontaneous Emission Pattern

Transmission of a Fabry–Perot Cavity

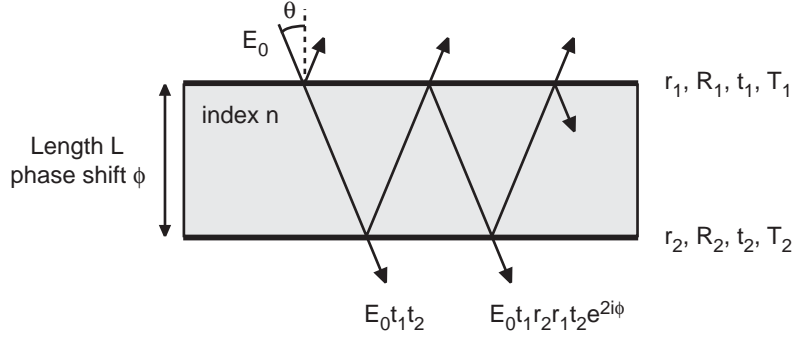


Figure 2.28: Schematic cavity of index n , limited by two mirrors

Consider a Fabry–Perot cavity with a refractive index n , surrounded by two plane-parallel, semi-transparent mirrors. In a simplified scalar approach, the transmitted electric far field of a plane wave of monochromatic light which is incident upon the first mirror at an angle θ from the normal is [103,41]

$$E_t = E_0 t_1 t_2 [1 + r_1 r_2 e^{2i\phi} + (r_1 r_2 e^{2i\phi})^2 + \dots + (r_1 r_2 e^{2i\phi})^{2n}] \quad (2.47)$$

$$= E_0 \frac{t_1 t_2}{1 - r_1 r_2 e^{2i\phi}} \quad (2.48)$$

where E_t is the transmitted electric field, E_0 is the dipole far field without cavity, and t_i and r_i are the field transmission and reflection coefficients, respectively. 2ϕ corresponds to the **cavity round-trip phase shift** and is equal to

$$2\phi = 2kL \cos \theta \quad (2.49)$$

with L being the cavity length, k the amplitude of the wavevector in the cavity with refractive index n , $k = 2\pi n/\lambda$, and θ the angle of incidence. Phase changes at the reflectors are neglected. The maxima of the transmittance occur if the condition of constructive interference is fulfilled, i.e.

$$2\phi(\lambda, \theta) = 2\pi m \quad (2.50)$$

with m a positive integer. This leads to the following power transmission coefficient for a Fabry–Perot cavity

$$T_{FP} = \frac{|E_t|^2}{|E_0|^2} = \frac{T_1 T_2}{1 + R_1 R_2 - 2\sqrt{R_1 R_2} \cos(2\phi)} \quad (2.51)$$

where T_i and R_i are the power transmission and reflection coefficients, $T_i = |t_i|^2$, $R_i = |r_i|^2$ and $R + T = 1$ for lossless mirrors. This factor defines the resonant modes of the cavity and is called **cavity enhancement factor** or **Airy factor** $A'(2\phi)$.

Transmission In Case of a Source Inside a Fabry–Perot Cavity

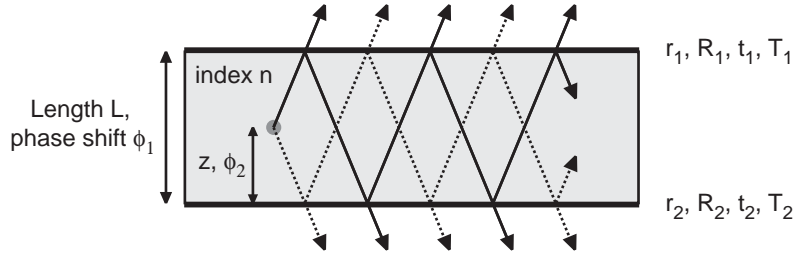


Figure 2.29: Schematic cavity of index n , limited by two mirrors, with an emitter inside the cavity emitting two series of waves

If the point source is located within the cavity, the transmission through the top mirror corresponds to the transmission through the cavity with an external source, T_{FP} , except for the term T_2 , multiplied with an additional factor ζ taking into account the additional set of waves emitted downwards by the source (dotted lines).

$$T_{\text{top}} = A(2\phi_1^{\text{eff}}) \times \zeta(\phi_2^{\text{eff}}) = \frac{T_{FP} \times \zeta}{T_2} = \frac{T_1 |1 + r_2 e^{2i\phi_2^{\text{eff}}}|^2}{|1 - r_1 r_2 e^{2i\phi_1^{\text{eff}}}|^2} \quad (2.52)$$

$$= \frac{T_1 (1 + R_2 + 2\sqrt{R_2} \cos(2\phi_2^{\text{eff}}))}{1 + R_1 R_2 - 2\sqrt{R_1 R_2} \cos(2\phi_1^{\text{eff}})} \quad (2.53)$$

with $\phi_1 = kL \cos \theta$ and $\phi_2 = kz \cos \theta$. The phase changes at the reflectors can be included by introducing **effective phase shifts**,

$$2\phi_1^{\text{eff}}(\lambda, \theta) = 2\phi_1 - \arg(r_1) - \arg(r_2) \quad (2.54)$$

$$2\phi_2^{\text{eff}}(\lambda, \theta) = 2\phi_2 - \arg(r_2) \quad (2.55)$$

$\zeta(\phi_2^{\text{eff}})$ is called the **standing wave factor** and expresses the dependence of the emitted intensity on the position of the source. Transmission is high in a particular direction if the source is located at an antinode of the standing wave field.

The Airy factor $A(2\phi_1^{\text{eff}})$ differs slightly from the case of an external source. The Airy function is periodic with period π in ϕ_1^{eff} . Its maxima define the resonant modes of the cavity and obey the phase condition $2\phi_1^{\text{eff}}(\lambda, \theta) = 2m\pi$ with m a positive or negative integer. In case of a perfect resonator, $|r_1 r_2| = 1$, the optical modes represent singularities. For $|r_1 r_2| < 1$ the optical mode density is no longer a Dirac distribution, the resonant peaks caused by the Airy factor have a finite width. The full-width half-maximum (FWHM) $\delta\phi_1^{\text{eff}}$ is inversely proportional to the cavity **fineness** F , defined as

$$F = \frac{\Delta\phi_1^{\text{eff}}}{\delta\phi_1^{\text{eff}}} = \frac{\pi}{\delta\phi_1^{\text{eff}}} \quad (2.56)$$

where $\Delta\phi_1^{\text{eff}}$ is the separation between two adjacent resonances, which is equal to π . $\Delta\phi$ and $\delta\phi$ are illustrated in figure 2.30.

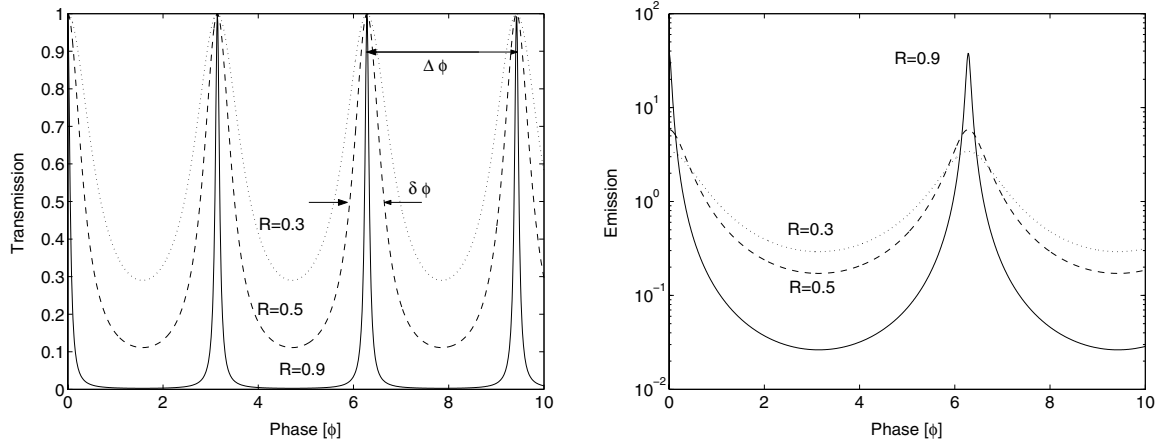


Figure 2.30: Normalized Airy factor (left) and Emission from a Fabry-Perot cavity (right, semilogarithmic plot) for the simplified case $R_1 = R_2 = R$ and $z = L/2$ and for different reflectivities R (0.9, 0.5 and 0.3).

Expression (2.53) describes the emission properties of a Fabry-Perot cavity. For the simplified case $R_1 = R_2 = R$, $z = L/2$ and ideal mirrors ($\phi = \phi_1 = \phi_1^{\text{eff}} = 2\phi_2^{\text{eff}}$) it reduces to

$$T'_{\text{top}} = \frac{T(1 + R + 2\sqrt{R}\cos\phi)}{1 + R^2 - 2R\cos 2\phi} \quad (2.57)$$

The Airy factor $A(2\phi)$ for emission from within the cavity and the top transmission of a Fabry-Perot cavity $T'_{\text{top}}(\phi)$ for this simplified case are depicted in figure 2.30 for different values of R . For isotropic emitters the top transmission is equal to the top emission, $I'_{\text{FP}} = T'_{\text{top}}$. It can be seen that only the even modes are excited ($2\phi(\lambda, \theta) = 2\pi m$, m even) for this source position and the corresponding standing wave factor $\zeta(\phi)$. The absolute values of the maxima and minima depend strongly on the mirror reflectivity, they can be expressed as ($R = |r|^2$)

$$I'_{\text{max}} = \frac{1+r}{1-r} \quad \text{and} \quad I'_{\text{min}} = \frac{1-r}{1+r} \quad (2.58)$$

The **cavity order** m_c corresponds to the number of resonances. Resonances of the Airy function are 2π -periodic with respect to $2\phi_1^{\text{eff}}$ and hence are also periodic with $k_z = k\cos\theta$. Let k_0 be the wavevector associated to a given wavelength in the source spectrum. The number of resonances is limited since $2\pi \leq 2k_0L$ and $2\pi = 2k_0L$ at normal incidence. Hence the cavity order is given by

$$m_c = \text{integer} \left[\frac{2\phi_1^{\text{eff}}(\lambda, \theta = 0)}{2\pi} \right] = \text{integer} \left[\frac{2nL}{\lambda} \right] \quad (2.59)$$

As a consequence of $2\pi = 2k_0L\cos\theta$ there are m_c resonant angles θ_i with equally spaced $\cos\theta_i$. In the following the resonant angle closest to the normal will be denoted θ_0 , for which we have

$$2\phi(\theta_0) = 2\pi m_c = 2k_0\cos\theta_0L \quad (2.60)$$

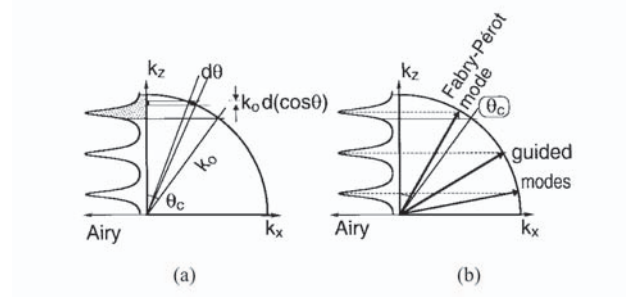


Figure 2.31: Plot in k -space depicting cavity modes, critical angle, monochromatic emission, and the Airy function (z -axis normal to the cavity). Emission from the micro-cavity is essentially proportional to the shaded area below the Airy function (a); at angles above θ_c , there is a guided mode at each Airy peak, at a discrete angle (b) [95]

Among θ_i 's, resonances with angles smaller than θ_c are extracted, whereas the resonant angles larger than θ_c correspond to leaky modes and guided modes. In the k_x - k_z plane a monochromatic source defines a quarter-circle of radius $k = k_0$ (a finite spectral linewidth would be accounted for by replacing the circle with an annulus). As a first approximation the source is assumed to be isotropic. Light emission within $d\theta$ is basically proportional to the product $\text{Airy} \times d\Omega$. The light that may be extracted corresponds to the part emitted in the escape window, at angles θ smaller than θ_c . Thus the amount of extracted light is measured by the area under the Airy function between boundaries $k_z = k_0$ and $k_z = k_0 \cos \theta_c$, corresponding to the shaded area in figure 2.31 (a). The extraction efficiency decreases therefore with the number of resonant modes, as each mode carries roughly the same amount of power. In case of ideal mirrors ($\arg(r_i) = 0$) the cavity order describes the cavity length in units of half-wavelength, $\lambda/2n$. However for real mirrors the penetration of the field into the mirrors has to be considered as well (see section 2.7.2).

Frequently the cavity **quality factor** Q is used instead of the finesse F . It is defined as the ratio of the transmission peak frequency to the peak width. For small variations it can be linked to the finesse via the cavity order [100]

$$Q = \frac{\phi_1^{\text{eff}}}{\delta\phi_1^{\text{eff}}} \approx m_c F \quad (2.61)$$

Source Terms for Electrical Dipoles

In the weak coupling regime the spontaneous emission of electron-hole pairs can be adequately represented by electrical dipoles [104]. An electrical dipole can be decomposed into a **horizontal electrical dipole** (dipole moment in the $(x-y)$ plane) and a **vertical electrical dipole** (dipole moment along the z -axis). In bulk semiconductor material the dipoles can have any orientation, in unstrained QWs however there is a strong preference for emission through horizontal dipoles. Furthermore, if a compressive strain is added to the QW, a strong enhancement of radiation through horizontal dipoles is realized, while tensile strain enhances vertical dipoles [105]. As all the structures discussed in this thesis contain compressively strained QWs, the contribution of the vertical dipoles is neglected in the following. Thus the total emitted intensity $I(\theta)$ can be decomposed into contributions from **TE-emitting** (transverse electric or s) and **TM-emitting** (transverse magnetic or p) horizontal dipoles (h)

$$I_{FP}(\theta) = I_{FP}^{h,s}(\theta) + I_{FP}^{h,p}(\theta) \quad (2.62)$$

The emitted intensity $I_{FP}^{\text{pol}}(\theta)$ can then be expressed as a function of the source's downwards and upwards propagating plane wave components $A_{\downarrow}^{\text{pol}}$ and $A_{\uparrow}^{\text{pol}}$ ($\text{pol} = s, p$).

$$I_{FP}^{\text{pol}}(\theta) = \frac{T_1 |A_{\uparrow}^{\text{pol}} + A_{\downarrow}^{\text{pol}} r_2 e^{2i\phi_2^{\text{eff}}}|^2}{|1 - r_1 r_2 e^{2i\phi_1^{\text{eff}}}|^2} \quad (2.63)$$

The extraction efficiency of the layer structure can then be expressed as

$$\eta_{\text{extr}} = \frac{I_{\text{extr}}}{I_{\text{tot}}} = \frac{\int_0^{\theta_c} I(\theta) \sin \theta d\theta}{\int_0^{\pi} I(\theta) \sin \theta d\theta} \quad (2.64)$$

Equation (2.64) has to be solved numerically, approximating the integral by a discrete summation. If the cavity finesse is high ($R_1 R_2 \rightarrow 1$) the Airy function can be approximated by a Dirac distribution and the area under the resonance peak is the same for all modes. Hence the extraction efficiency is translated to a ratio of discrete sums. If there is only one mode in the extraction cone and the antinode factors of the excited modes are all equal to 1 [95], η_{extr} is given by

$$\eta_{\text{extr}} = \frac{\sum_{i, \theta < \theta_c} \zeta_i}{\sum_i \zeta_i} \approx \frac{1}{m_c} \quad (2.65)$$

In case only the even modes are excited (determined by the position of the source), only half of the cavity resonances would have to be considered and the above estimate would have to be multiplied with a factor 2.

Exact calculations can be done with standard transfer-matrix techniques in order to describe the extraction properties of the layer structure. The dipole emission is included simply as additive source terms [97].

$$\begin{pmatrix} E_{0\uparrow} \\ E_{0\downarrow} \end{pmatrix} = M_a \begin{pmatrix} E_{10\uparrow} \\ E_{10\downarrow} + A_{\downarrow} \end{pmatrix} \quad \text{and} \quad M_b \begin{pmatrix} E_{12\uparrow} + A_{\uparrow} \\ E_{12\downarrow} \end{pmatrix} = \begin{pmatrix} E_{2\uparrow} \\ E_{2\downarrow} \end{pmatrix} \quad (2.66)$$

E_0 and E_2 correspond to the bottom and top outside field, respectively, E_{1i} describe the internal fields, and M_a and M_b the optical properties of the bottom and the top mirror, respectively. In the case of internal emission only obviously $E_{0\uparrow} = 0$ and $E_{2\downarrow} = 0$.

Purcell Effect

The impact of the cavity on the total power emitted by the dipole can be expressed as a change in radiative electron-hole recombination rate and hence the lifetime

$$F_p = \frac{\frac{1}{\tau}}{\frac{1}{\tau_0}} = \frac{\text{emitted dipole power in cavity}}{\text{emitted dipole power in bulk}} \quad (2.67)$$

where F_p is the **Purcell factor** and τ and τ_0 are the radiative lifetimes with and without cavity, respectively. The change of the carrier lifetime due to the presence a cavity is known as the Purcell effect [82]. Purcell derived the spontaneous emission enhancement factor for three-dimensional cavities by noting that a single (quasi-) mode occupies a spectral bandwidth ν/Q within a cavity volume V . Normalizing the resulting cavity-enhanced mode density per unit volume to the mode density of free space gives

$$F_p = \frac{3}{4\pi^2} \left(\frac{\lambda}{n} \right)^3 \frac{Q}{V} \quad (2.68)$$

where the refractive index n is a modern addition to this expression to account for emission within dielectrics [81].

With a planar cavity having a mirror separation larger than $\lambda/2$ ($m_c > 1$), the potential increase or decrease in the spontaneous emission rate is at most a factor of 3 or 2, respectively (see figure 2.32) [79,106]. More drastic changes can however be expected in two or three dimensionally confined cavities. Significantly higher enhancement factors have been observed for three-dimensionally confined cavities with a small volume, such as quantum dots in pillar microcavities ($F_p = 5$) or microdisks ($F_p = 15$) [107].

High Purcell factors can be achieved for planar structures by coupling to surface plasmon modes (see section 2.8.4).

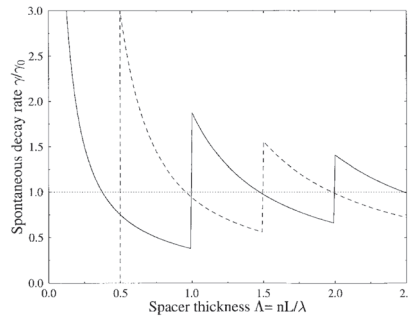


Figure 2.32: Estimation of the modification of the spontaneous emission decay rate relative to the free space value (γ/γ_0) for a horizontal dipole placed in the center of a planar microcavity with ideal mirrors, as a function of the spacer thickness; for $r = +1$ (solid line) and for $r = -1$, corresponding to perfect metallic mirrors (dashed line) [106].

2.7.2 Reflectors

Different types of reflectors are used in MCLEDs, metallic reflectors, distributed Bragg reflectors (DBRs) and hybrid metal–DBR reflectors. **Metal mirrors** typically show reasonably high reflectivities over a large spectral range, covering the near infrared regime and a large part of the visible range. In addition they show a constant reflectivity independent of the incident angle. However, unless the thickness of the metal is very thin, metallic reflectors are absorbing. Therefore their transmittance is near zero and they cannot be used as outcoupling mirrors. The phase change upon reflection at metal mirrors is negative, related to their complex refractive index. In order to compensate for this effect an additional **phase-matching layer** with an appropriate thickness needs to be added.

DBRs are described in detail in the following subsection. They consist of multilayer quarter wave stacks of either epitaxial semiconductor layers or subsequently deposited dielectric layers. With DBRs the reflectivity can be tuned via the number of DBR pairs and high efficiencies close to 100 % can be achieved with negligible absorption losses, if all the layers are transparent. Hence DBRs can be grown epitaxially and made conductive by doping. The main drawback of DBRs is that they display only a narrow band of high reflectivity in the spectral and angular regime. Due to the partial penetration of the optical wave in the reflector the use of DBRs leads to a significantly increased effective cavity length and cavity order. At normal incidence and for the central wavelength λ_{Bragg} , the phase change upon reflection is zero for a DBR.

With **hybrid reflectors** consisting of a metal mirror and a DBR the high DBR reflectivity and its low absorption losses can be coupled with the large spectral and angular reflectivity band of the metal.

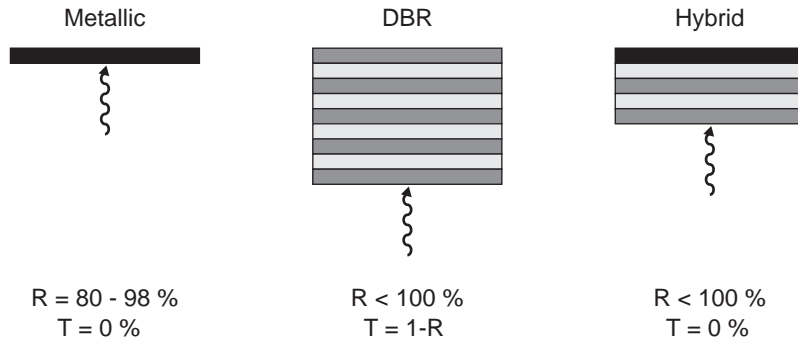


Figure 2.33: Schematic representation of different types of reflectors: metallic reflector (left), distributed Bragg reflector (middle) and hybrid reflector (right) [9]

The spectral and angular reflection properties around 980 nm of a GaAs/Au interface, a GaAs/air interface and a 15.5 pair GaAs/AlAs DBR centered at 980 nm are compared in figure 2.34. At normal incidence the GaAs/air interface shows a reflectivity of approximately 30 % and for incidence angles $\theta > \theta_c$ ($\approx 17^\circ$) the reflectivity rises to unity due to total internal reflection. Hence the interface GaAs/air can be used as weak outcoupling mirror on its own or in combination with a DBR with a small number of pairs.

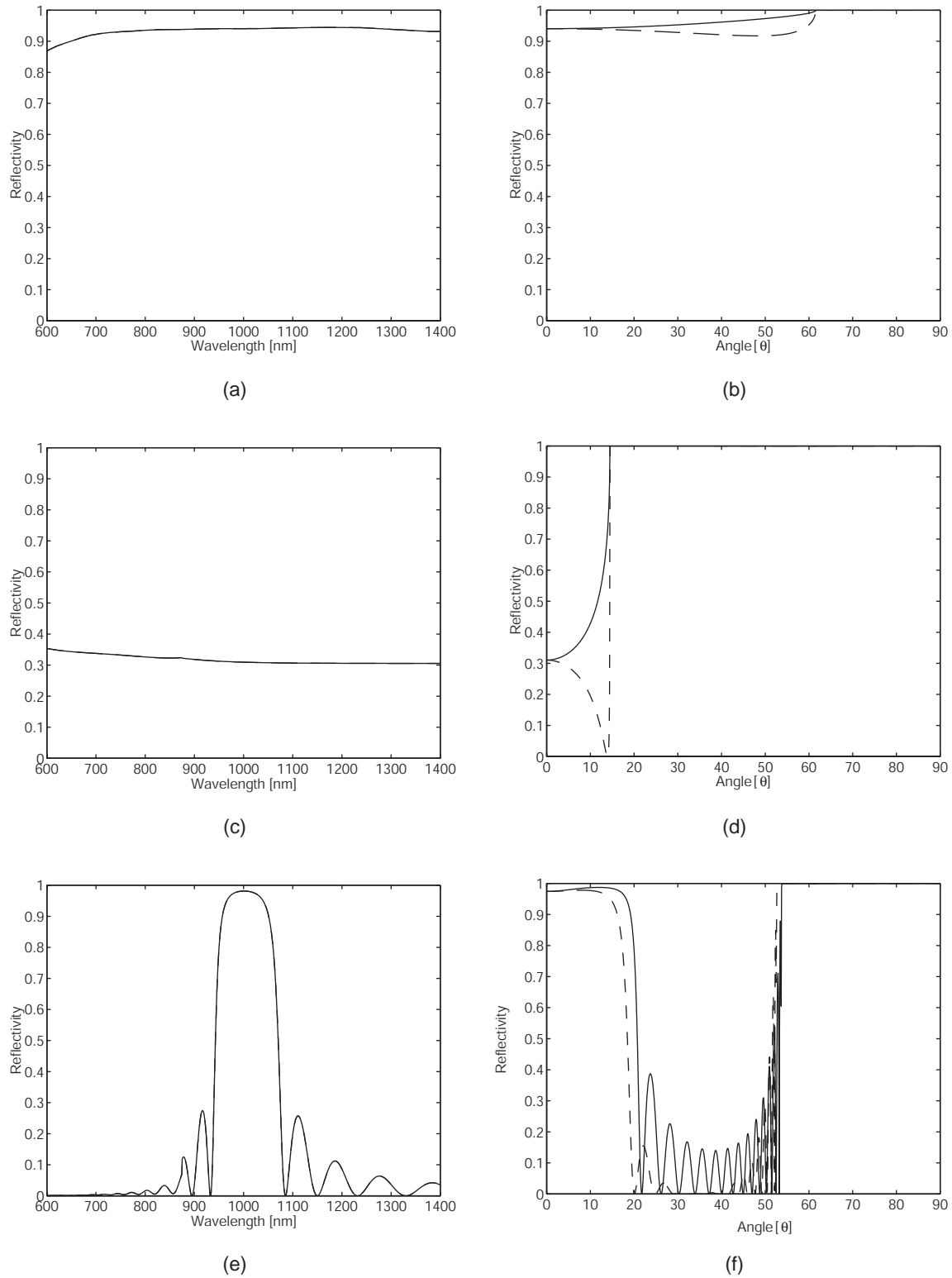


Figure 2.34: Reflectivity as a function of wavelength (left) and incident angle (right) around 980 nm, TE polarization (solid line) and TM polarization (dashed line); GaAs/Au interface (a)-(b); GaAs/air interface (c)-(d); and 15.5 pair GaAs/AlAs DBR centered at 980 nm (f)-(g)

Distributed Bragg Reflector (DBR)

Distributed Bragg Reflectors (DBRs) are periodic multilayer structures with a unit cell of two dielectric layers, consisting of alternating layers of low (n_l) and high (n_h) refractive index material with an optical thickness of a quarter wave for the designed wavelength λ_{Bragg} ($d_i = \lambda_{\text{Bragg}}/4n_i$ ($i = h, l$)) [108,109]. Their key parameter is the refractive index difference $\Delta n/n_{\text{eff}}$ where $\Delta n = n_h - n_l$ and n_{eff} is the effective refractive index of the mirror [110]

$$n_{\text{eff}} = 2 \left(\frac{1}{n_l} + \frac{1}{n_h} \right)^{-1} \quad (2.69)$$

Attainable Δn values are dictated by epitaxial or deposition constraints inherent to the material systems. The values for common material systems for transparent DBRs at the wavelengths of interest for this thesis, 970 and 650 nm, are listed in table 2.5.

Table 2.5: Refractive index contrasts of common DBR material systems

DBR type	λ [nm]	n_h	n_l	Δn	n_{eff}	$\Delta n/n_{\text{eff}}$
GaAs/AlAs	970	3.52	2.95	0.57	3.21	0.18
Al _{0.5} Ga _{0.5} As/AlAs	650	3.476	3.095	0.38	3.27	0.12
(Al _{0.2} Ga _{0.8}) _{0.5} In _{0.5} P/AlInP	650	3.446	3.175	0.27	3.30	0.08

DBR mirrors capitalize on successive reflections at dielectric interfaces. For quarter wave layer optical thicknesses, phases from such waves are separated by $\phi_c = 2\pi$ at their central (nominal) wavelength λ_{Bragg} . Multiple reflections at the interfaces of the DBR and constructive interference of the multiple reflected waves increase the reflectivity with increasing number of pairs. The optical properties of DBRs can be calculated with the transfer-matrix formalism [111].

$$\begin{pmatrix} E_{b\uparrow} \\ E_{b\downarrow} \end{pmatrix} = m \begin{pmatrix} E_{a\uparrow} \\ E_{a\downarrow} \end{pmatrix} \quad (2.70)$$

Consider a finite DBR consisting of p pairs sandwiched between two media, a substrate and an outside medium with refractive indices n_s and n_o , respectively. Its reflectivity at its central wavelength λ_{Bragg} and for normal incidence is then given by [95,111]

$$R_0 = R_0(p) = \left[\frac{1 - \frac{n_s}{n_o} \left(\frac{n_l}{n_h} \right)^{2p}}{1 + \frac{n_s}{n_o} \left(\frac{n_l}{n_h} \right)^{2p}} \right]^2 \quad (2.71)$$

If the center wavelength lies at oblique incidence, the n_i 's are to be replaced with e.g. $n_i \cos \theta_i$ in case of TE-waves. The high-reflectivity band is called **stopband**. Beyond the stopband, DBRs are no longer mirrors and allow propagative photon states called leaky modes (see further below). The width of the spectral stopband scales with the refractive index difference $\Delta n/n_{\text{eff}}$ and is approximately given by [112]

$$\Delta\lambda_{\text{stopband}} = \frac{2\lambda_{\text{Bragg}}\Delta n}{\pi n_{\text{eff}}} \quad (2.72)$$

The angular stopband can be estimated from (2.72) and (2.49) to be [113]

$$\Delta\theta_{\text{stopband}} = \pm \sqrt{\frac{2\Delta\lambda_{\text{stopband}}}{\lambda_{\text{Bragg}}}} = \pm 2\sqrt{\frac{\Delta n}{\pi n_{\text{eff}}}} \quad (2.73)$$

When compared to a localized mirror (metal, single interface) with a well-defined phase change determined by dielectric constants, a DBR mirror gives an angle and wavelength-dependent phase change at the first DBR interface due to the changes of partial beams reflecting on successive interfaces. Across the angular stopband the phase essentially evolves linearly, just as would do a wave reflecting at an imaginary perfect mirror placed at some location inside the DBR. This is taken into account by defining a **penetration length** L_p , which is equal to the difference between the position of the first DBR interface and the location of this imaginary perfect mirror and can be quantitatively expressed as [95]

$$L_p = \frac{\lambda_{\text{Bragg}}}{2} \frac{n_l}{2n_{\text{eff}}\Delta n} \quad (2.74)$$

This penetration length leads to an increased cavity order and affects therefore all the properties related to it, including the extraction efficiency. Hence an **effective cavity order** m_c^{eff} is defined as the sum of the bare cavity order plus the cavity order increases Δm_c for the bottom and the top mirror [95]

$$m_c^{\text{eff}} = m_0 + \sum_{i=1,2} \Delta m_{c,i} \quad (2.75)$$

$$\Delta m_c = \frac{n_h n_l}{2n_{\text{eff}}\Delta n} \approx \frac{n}{2\Delta n} \quad (2.76)$$

$$m_c^{\text{eff}}(2 \text{ DBRs}) = m_0 + 2\frac{n_h n_l}{2n_{\text{eff}}\Delta n} \approx m_0 + \frac{n}{\Delta n} \quad (2.77)$$

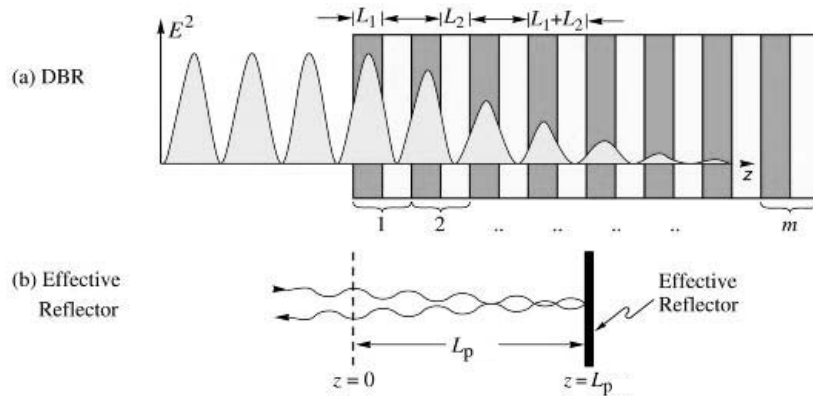


Figure 2.35: Illustration of the DBR penetration length. DBR and schematic penetration of the optical wave in the reflector (a); ideal mirror displaced from the first DBR interface by the penetration length L_p [9].

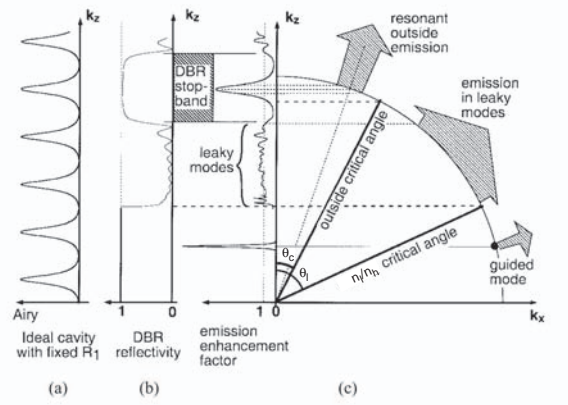


Figure 2.36: Same plot as figure 2.31 for the case of a DBR as high reflectivity bottom reflector. Comb-like Airy function of an ideal cavity with constant reflectivities (a); DBR reflectivity with the stopband, the low reflectivity region for lower k_z and the total reflection at the interface of the first low index DBR layer above the critical angle θ_l (b); modified Airy function with the extracted FP peak, the leaky modes and the guided modes (c) [95]

For typical refractive index differences in common DBRs, this cavity order increase can be significantly larger than the bare cavity order itself. This leads to significantly reduced maximum achievable efficiencies for DBR-bounded MCLEDs.

When a DBR with a moderate refractive index difference is used on a high-index substrate, its limited angular stopband allows light to escape towards the substrate at oblique angles larger than θ_c , referred to as **leaky modes**. In this region no cavity modes appear as this light is not reflected and is eventually absorbed in the substrate. Therefore the emission into leaky modes is essentially lost for extraction.

At even larger angles $\theta > \theta_l$, there is again a unit reflectivity due to total internal reflection at the interface of the first low index DBR layer, according to Snell's law $\sin \theta_l = n_l/n_h$. In this area the cavity acts as a lateral waveguide and the light is reflected back and forth until it is either extracted laterally or reabsorbed. These modes are called **guided modes**. This contribution is not entirely lost to extraction, part of it can be extracted via re-absorption in the active layer and re-emission into the escape window, denoted as **photon recycling** (discussed in detail later on).

2.7.3 Design Rules

The basic structure of a MCLED consists of a cavity with length L , surrounded by two reflectors, a back reflector with reflectivity R_2 and an outcoupling reflector with reflectivity R_1 . An active layer is located in the cavity, preferably at the antinode location of the standing optical wave of the cavity. For simplicity R_2 is considered as unity in the following, since the reflectivity of the back mirror should be as high as possible in order to minimize reflection losses. For the reflectivity R_1 of the outcoupling mirror on the other hand a trade-off exists between increasing extraction and increasing losses, as will be seen in the following subsection.

Outcoupling Mirror Reflectivity

The optimum outcoupling mirror reflectivity R_1^{opt} corresponds to the case where the extracted Airy peak is squeezed reasonably well into the escape window $[k_0, k_0 \cos \theta_c]$. Increasing the reflectivity leads to an only marginally increased extraction but can on the other hand cause significant absorption losses due to the increased number of round-trips. By imposing that the Airy factor at the escape window edges ($\theta = 0$ and $\theta = \theta_c$) needs to be only 10 % of its peak value, the following condition can be found for R_1^{opt} in the case of a lossless cavity [95]

$$R_1^{\text{opt}} = 1 - \frac{m_c}{n^2} \quad (2.78)$$

which is of the order of 80 % for a cavity of order 2 and a refractive index of 3.5 and is decreasing with increasing cavity order. In the case of significant losses in the cavity, another criterion for R_1 is that extraction losses must be always higher than dispersive losses. Otherwise a further increase of R_1 only leads to an increased directionality. For a detailed estimation the natural spectral width of the source needs to be considered as well. In case of a very broad emission not all the wavelengths can be extracted and another limiting factor for R_1 evolves.

Cavity Order

Equation (2.65) indicates that the extraction efficiency is inversely proportional to the cavity order. Hence as a general rule the cavity order and therefore the cavity length should be kept as small as possible. However, as seen in section 2.7.2, in case of DBRs with moderate refractive index differences the penetration of the optical standing wave into the reflector leads to a significantly increased effective cavity length.

For optical purposes it would be ideal to use a $\lambda/2$ cavity with order $m_c = 1$. This cavity would have a single extractable Fabry-Perot mode, leading to very high efficiencies. However λ cavities are generally used in practical applications for different reasons [100]. In case of a cavity with one or two metal mirrors, the use of a $\lambda/2$ cavity would imply that the active layer is very close to the metal, which can result in considerable losses due to non-radiative energy transfer from the dipole to the absorptive metal [114]. Moreover a λ cavity is preferable from a technological point of view, independent if metal or dielectric reflectors are used. A metal mirror requires a heavily doped contact layer with a thickness of several tens of nanometers to ensure good electrical contact. When insulating dielectric mirrors are used, thick (usually $\lambda/4$) and highly conductive

lateral current injection layers are needed. Quantum wells are typically sandwiched in graded index separate confinement heterostructures (GRINSCH) with a total thickness of the order of $\lambda/2$.

The effective cavity order m_c^{eff} of a λ cavity with $m_0 = 2$ can be minimized by using either a metallic back mirror or a DBR back mirror with a high refractive index difference.

Cavity Tuning

In order to obtain the largest area under the Airy function, the peak resonant angle θ_0 should be centered in the escape window by symmetrizing phases at window edges $2\phi(0)$ and $2\phi(\theta_c)$, which leads to the following approximation for θ_0

$$\theta_0 \approx \frac{n_{\text{ext}}}{\sqrt{2}n_{\text{int}}} \quad (2.79)$$

which leads to an outside angle peak at 45° . This is achieved with a **detuning** δ of the Fabry-Perot wavelength of the cavity, λ_{FP} , versus the wavelength of emission of the source λ_s

$$\delta = \lambda_s - \lambda_{FP} \quad (2.80)$$

whereas λ_{FP} is related to the cavity thickness L and its order m_c in the following way (see equation (2.59))

$$\lambda_{FP} = \frac{2nL}{m_c} \quad (2.81)$$

The optimum detuning in order to fulfill (2.79) is then [115,102]

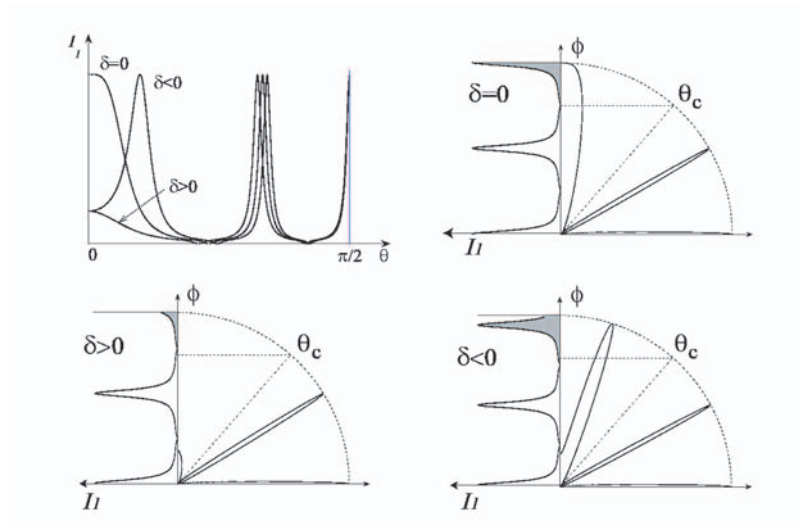


Figure 2.37: Angular plot depicting mode positions as a function of detuning δ (top left); plots in k-space for zero detuning, $\delta = 0$, (top right); positive detuning, $\delta > 0$, (bottom left); and negative detuning, $\delta < 0$, (bottom right) [102]

$$\delta_{\text{opt}} \approx -\frac{\lambda_s n_{\text{ext}}^2}{4n_{\text{int}}^2} \quad (2.82)$$

As can be seen in figure 2.37 the area under the Airy function within the escape window increases for $\delta < 0$. The optimal detuning, as defined in equation (2.81), is negative. For a positive detuning $\delta > 0$ the area and hence the extraction efficiency rapidly decrease.

Optimizing the detuning for a maximum extraction efficiency is leading to a non-directional emission (see figure 2.38). Therefore the MCLED has to be optimized specifically for the application needs, either maximum extraction efficiency or maximum brightness (e.g. for coupling into a fiber).

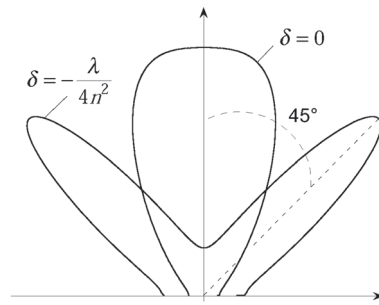


Figure 2.38: Angular emission diagram for a MCLED with detuning zero $\delta = 0$ and a directional emission, and for a MCLED with optimal detuning for emission into air, $\delta_{\text{opt}} \approx -\lambda_s/4n^2$, leading to an external emission angle of 45° [102]

Photon Recycling

Photons emitted into guided modes can still be extracted if they are re-absorbed in the active layer and re-emitted into the escape cone subsequently. This effect is called **photon recycling** and can lead to a significant increase of the external quantum efficiency for large area MCLEDs. QW-based devices normally do not show this effect, except if the photons are emitted into modes that show an increased overlap with the QWs, as is the case for laterally propagating modes in MCLEDs [116]. Photon recycling can be modeled as an increase of the external quantum efficiency by a photon recycling factor F_{PR} , defined as [100]

$$F_{\text{PR}} = \frac{1}{1 - g\eta_{\text{int}}} \quad (2.83)$$

where g is the re-absorption factor corresponding to the percentage of internally generated photons being recycled. This value depends on the fraction of the photons emitted into the guided modes that are re-absorbed before escaping the structure laterally, i.e. on the characteristic absorption length of the layer structure and the device dimensions. The **characteristic absorption length** is a function of the absorption coefficient of the active layer, which varies with carrier density, and the overlap between the internal field and the active layer. Typical values are of the order of $100 \mu\text{m}$ [101]. It can be estimated that 90% of the photons in guided modes are re-absorbed over this distance for

a QW absorption coefficient of 10^3 cm^{-1} [117]. This implies that the photon recycling effect is strongly size-dependent and is pronounced only for large area devices.

The amount of photon recycling increases with the guided mode fraction and is therefore high for DBRs with a large refractive index difference Δn and metal mirror structures, as well as for thin-film LEDs. For a reasonable internal quantum efficiency of the order of 80 % or higher and a high guided mode fraction of 80 %, photon recycling factors significantly higher than unity can therefore be expected for large devices. Experimentally an increase in external quantum efficiency by a factor of 1.4 has been shown by increasing the diameter from $85 \mu\text{m}$ to 1.5 mm for asymmetric DBR/cavity/metal structures [118].

Saturation

At high injection levels the optical power of MCLEDs tends to saturate. This is caused by several effects. With increasing current density the intrinsic emission spectrum broadens, leading to a decreased overlap between the cavity resonance and the emission spectrum and therefore a decreased extraction efficiency.

At even higher injection levels thermal effects come into play [101]. Non-radiative recombination and ohmic heating by the series resistance lead to a temperature increase of the active region. This leads to a decrease of the internal quantum efficiency and a decrease of the detuning away from the optimal value. The latter effect is related to the fact that the temperature shift of the emission wavelength due to its decreasing bandgap energy is much more important than the shift of the cavity resonance wavelength due to the temperature dependence of the refractive indices.

Furthermore carrier spill-over and current crowding can lead to a reduced injection efficiency at high carrier density. The occurrence of lateral in-plane gain finally cancels any photon recycling.

2.7.4 State of the Art Semiconductor MCLEDs (Status 2001)

The first Microcavity LED by Schubert et al. [64] is based on GaAs/AlGaAs and shows an emission peak at 862 nm. The top emitting device consists of an asymmetric DBR/cavity/metal mirror structure, where the DBR is made of AlAs/Al_{0.14}Ga_{0.86}As periods and the thin transparent metal reflector of silver (Ag) or silver in combination with cadmium tin oxide (Ag/CdSnO_x). Since then MCLEDs were realized in different material systems, covering a large range of emission wavelengths [9,100,101]. In the following a brief overview will be given on the state of the art of electrically injected MCLEDs, divided into different wavelength ranges, from the visible to the infrared. For each range typical fields of application, material systems and efficiencies are listed.

400-500 nm

InGaN/GaN-based MCLEDs are under development. However due the low index of GaN ($n \approx 2.5$), the light extraction is less of a problem than for the other material systems. In addition the lattice mismatch between GaN and AlN limits the maximum achievable refractive index contrast and therefore the realization of high reflectivity DBRs as well. Furthermore the lack of a simple epitaxial lift-off technique prevents the realization of short cavity metal-bound structures so far.

650 nm

Apart from lighting applications, 650 nm emitting devices are commercially important for plastic optical fiber (POF) based communication. The material system of choice for the cavity is AlGaInP, in combination with AlGaAs DBRs and current spreading and current injection layers. Due to several limiting factors the attainable efficiencies in the red are lower than for near-IR MCLEDs, as discussed in chapter 5. With red MCLEDs wall-plug efficiencies η_{wp} of 10 % and external quantum efficiencies η_{ext} of 9.6 % were shown for $300 \times 300 \mu\text{m}^2$ devices [119]. Due their low forward voltages the external quantum efficiencies are slightly smaller than the wall-plug efficiencies. The structure consists of a λ -cavity with 5 compressively strained GaInP QWs, a 34 period Al_{0.5}Ga_{0.5}As/Al_{0.95}Ga_{0.05}As bottom DBR and a 6 period top DBR.

850-880 nm

The target applications of 850-880 nm devices are Ethernet data links, remote controls and infrared communication as regulated by the Infrared Data Association (IrDA). This is mainly due to the availability of low-cost Si-based detectors in this wavelength range. The obvious material system for this region is GaAs/AlGaAs. An external quantum efficiency η_{ext} of 14.6% was achieved with an 850nm top emitting device [120]. It consists of a λ -cavity surrounded by two DBRs, the bottom mirror a 20 pair Al_{0.15}Ga_{0.85}As/AlAs DBR, the top one a 1.5 pair Al_{0.15}Ga_{0.85}As/AlAs DBR. The current is confined with an oxide aperture of $180 \mu\text{m}$ in diameter. With another structure emitting at 880 nm and an emission window of $80 \mu\text{m}$ an efficiency $\eta_{ext}^{\text{epoxy}}$ of 16 % was demonstrated after encapsulation. The λ -cavity was sandwiched between a 20 pair bottom DBR and a 5-7 pair top DBR, both consisting of Al_{0.2}Ga_{0.8}As/Al_{0.9}Ga_{0.1}As [121].

980 nm

Even though no large scale application exists so far for 980 nm near infrared devices the availability of high quality InGaAs/GaAs strained QWs makes these devices ideal for the proof of principle of new concepts. The InGaAs active material is used in conjunction with the GaAs/AlGaAs material system. Compared to higher bandgap emitters, this combination has the advantage that the GaAs substrate is transparent in the emission wavelength range. Hence highly efficient bottom emitting devices have been realized. With an asymmetric GaAs/AlAs DBR/ λ -cavity/Au mirror structure efficiencies η_{ext} of 17 and 23 % were shown for 85 μm and 1.5 mm diameter devices, respectively [118]. The active region consists of three strained InGaAs QWs and the increase in efficiency with device size is attributed to an increased photon recycling.

Top emitting monolithic devices with three InGaAs QWs and GaAs/AlAs DBRs with 15.5 pairs at the bottom and three pairs at the top, including $\text{Al}_{0.5}\text{Ga}_{0.5}\text{As}$ grading layers, led to a maximum efficiency η_{ext} of 10 % [122,123]. With the use of a 6.5 pair high index contrast GaAs/ AlO_x bottom DBR and a single period SiO_2/ZnSe dielectric top DBR, a differential quantum efficiency $\eta_{\text{ext}}^{\text{diff}}$ of 27 % could be demonstrated for top-emitting devices, corresponding to a maximum absolute external quantum efficiency of approximately 23 % [124]. The device contains a λ -cavity, a tunnel contact junction and an aperture of 6 μm only.

1300-1550 nm

Silica optical fibers show attenuation minima around 1300 and 1550 nm and therefore these two wavelengths are the pre-eminent communication windows for telecom (see for example [9]). The principal material system is InGaAsP/InP. In addition to the broader intrinsic emission spectrum of long-wavelength devices, the low refractive index contrasts limit the maximum efficiency of long-wavelength MCLEDs, similar to the case of vertical cavity surface emitting lasers (VCSELs).

Bottom emitting 1300 nm large diameter devices (2 mm) with a peak quantum efficiency η_{ext} of 9 % are reported using an asymmetric DBR/ λ -cavity/Au mirror structure with three strained $\text{InGa}_{0.12}\text{As}_{0.56}\text{P}$ QWs [125]. The DBR consists of 5.5 pairs of $\text{InGa}_{0.23}\text{As}_{0.50}\text{P}/\text{InP}$.

An InP-based MCLED of 85 μm in diameter emitting at 1550 nm with a 6.8 % external quantum efficiency is cited in [126]. The device is bottom emitting, using an asymmetric DBR/cavity/Au mirror structure. The active region consists of three $\text{In}_{0.84}\text{Ga}_{0.16}\text{As}_{0.74}\text{P}_{0.26}$ QWs and the outcoupling DBR of 12 pairs of $\text{InGa}_{0.38}\text{As}_{0.82}\text{P}/\text{InP}$.

Mid-IR

The main use for mid infrared emitters is gas detection. Several types of mercury cadmium telluride (HgCdTe) based MCLEDs have been realized with emission wavelengths at 3.3, 3.7, 4.2 and 4.7 μm adapted for the detection of different gases [127–130]. The structures are grown on cadmium zinc telluride (CaZnTe) substrates and the dielectric DBRs are made of zinc sulfide (ZnS) and yttrium fluoride (YF_3).

Other Types of MCLEDs

Thin-film MCLEDs surrounded by two metal mirrors have been realized at 870 nm with a GaAs/AlGaAs-based cavity by Wilkinson et al. [131] and with InP/InGaAsP emitting at 1550 nm by Corbett et al. [132]. Another interesting device is the broadly tunable GaAs/AlGaAs-based MCLED by Larson et al. [133]. The top mirror consists of a deformable membrane whose position is controlled via electrostatic forces. This allows a wavelength tuning of nearly 40 nm from 930 to 970 nm.

Overview of Maximum External Quantum Efficiencies

The maximum external quantum efficiencies published before 2001 are listed in table 2.6 and plotted as a function of emission wavelength in figure 2.39.

Table 2.6: Overview experimental results of MCLEDs for different wavelengths

Wavelength [nm]	material system	type	η_{ext} [%]	diameter [μm]	Ref.
650	AlGaInP/AlGaAs	top	9.6	300	[119]
650	AlGaInP/AlGaAs	top	≈ 12	700	[65]
850	GaAs/AlGaAs	top	14.6	180	[120]
880	GaAs/AlGaAs	top	16 (epoxy)	80	[121]
970	InGaAs/AlGaAs	top	10	400	[123]
980	InGaAs/GaAs/AlO _x + dielectric top DBR	top	≈ 23 27 (diff.)	6	[124]
995	InGaAs/AlGaAs	bottom	17	85	[118]
995	InGaAs/AlGaAs	bottom	23	1.5 mm	[118]
1300	InGaAsP/InP	bottom	9	2 mm	[125]
1550	InGaAsP/InP	bottom	6.8	85	[126]

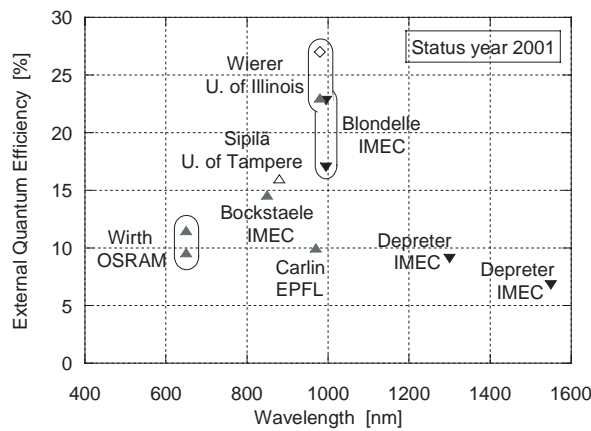


Figure 2.39: Maximum external quantum efficiency of MCLEDs vs. emission wavelength for top emitting (Δ) and bottom emitting (∇) devices, for emission into air (solid) and epoxy (empty); differential external quantum efficiency into air (\diamond).

2.8 Novel Concepts

2.8.1 Phase-Shift Cavity

Generally MCLEDs comprise a λ cavity, consisting of a high refractive index (low bandgap) material. For optical purposes a $\lambda/2$ low index cavity would be preferable, due to the reduced cavity order and the absence of guided modes. However this design is not practical for technical reasons. An efficient electrical injection demands a low bandgap active layer (high refractive index). In addition, in the InGaAs/AlGaAs material system, defects associated with the low index AlAs layers would lower the internal quantum efficiency.

A standard resonant cavity is formed between two reflectors by introducing a phase shift equal to a multiple of π , translating to an optical cavity length equal to an integral times $\lambda/2$. From distributed feedback laser theory it is known that this is not the only way to induce Fabry-Perot modes. An alternative approach to achieve the same effect is to place two $\lambda/8$ low index phase-shift layers around a $\lambda/4$ high refractive index layer containing the active region, thereby forming a virtual $\lambda/2$ cavity [134]. This structure is called a **phase-shift cavity** and approaches the optical properties of a $\lambda/2$ low index cavity while keeping the preferential practical aspects of a λ high index cavity. A phase-shift cavity shows an effective cavity length decreased by one and a reduced coupling to guided modes, allowing significantly higher extraction efficiencies.

In figure 2.40 a standard λ high index cavity, a $\lambda/2$ low index cavity and a $\lambda/8$ phase-shift cavity surrounded by two DBRs consisting of $\lambda/4$ layers are depicted. The optical properties of these different cavity designs are simulated for the case of the AlGaAs system by assuming $n_h = 3.5$ for GaAs and $n_l = 2.9$ for AlAs.

Figure 2.41 (a) shows the optical field of the Fabry-Perot mode as a function of position for the three different designs. The field has a maximum at the center of the cavity in each case and falls off more or less rapidly. The penetration of the optical field is minimum for the $\lambda/2$ low index cavity and the $\lambda/8$ phase-shift cavity shows a significant improvement compared to the standard λ high index cavity.

The optical fields of the guided mode are compared in figure 2.41 (b). Since the $\lambda/2$ low index cavity has no guided mode it was replaced with a $\lambda/2$ high index cavity. It is

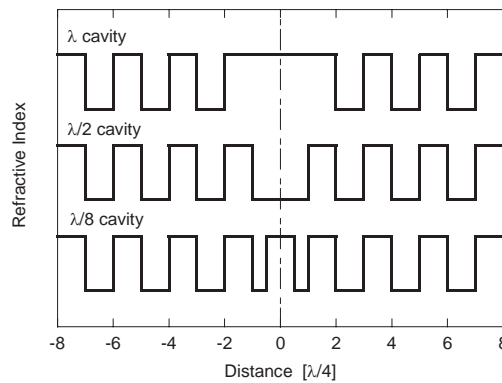


Figure 2.40: Three different cavity structures; a λ high index cavity, a $\lambda/2$ low index cavity and a $\lambda/8$ phase-shift cavity, all surrounded by $\lambda/4$ layers representing two DBRs. The dashed line denotes the source position [134]

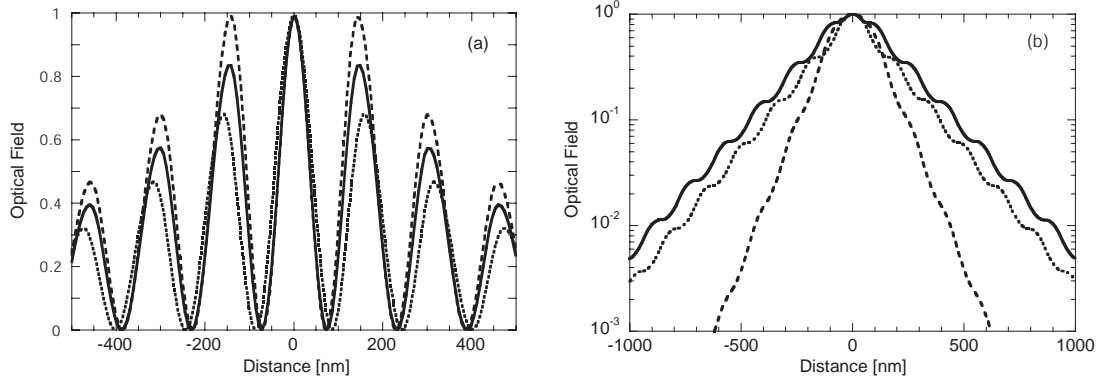


Figure 2.41: Optical fields of the Fabry-Perot mode (a) and the guided mode (b) as a function of position for a λ high index cavity (dashed line), a $\lambda/2$ cavity (dotted line) and a $\lambda/8$ phase-shift cavity (solid line). In (b) the $\lambda/2$ low index cavity is replaced by a $\lambda/2$ high index cavity as the former has no guided mode [134]

obvious that the λ high index cavity has the most confined guided mode, while the $\lambda/8$ phase-shift cavity is significantly less confined. The results of the numerical calculations are listed in table 2.7. It can be seen that a $\lambda/8$ phase-shift cavity shows a significantly increased emission into the Fabry-Perot mode compared to a standard λ high index cavity, with a concomitant reduction of the guided mode fraction. If the difference in refractive index of the medium confining the source is taken into account, the relative extraction efficiency of the $\lambda/2$ low index cavity reduces to 30 % after normalization with the factor $n_l/n_h = 0.83$.

Table 2.7: Calculated fractions of emission into Fabry-Perot modes and guided modes

cavity design	f_{FP} [%]	f_{guided} [%]
λ high index	20	36
$\lambda/2$ low index	36 (30)	-
$\lambda/8$ phase-shift	28	28

Furthermore it can be shown that the phase-shift cavity leads to a significant reduction of metal absorption losses for metal-bound structures [135].

Bottom emitting and top emitting near infrared MCLEDs comprising phase-shift cavities are presented in chapters 3 and 4.

2.8.2 Oxide DBR

It has been shown in section 2.7.2 that the properties of a DBR mainly depend on the refractive index difference $\Delta n/n_{\text{eff}}$ between its two constituents. Unfortunately the range of refractive indices accessible with epitaxially grown materials is very limited (see table 2.5). With dielectric DBRs high index contrast are possible, however only by paying the high price of a more complicated design and fabrication. In the 1990s a method was found which allows to significantly decrease the refractive index of the low index high aluminum content constituent. Dallesasse et al. discovered that high Al-content $\text{Al}_x\text{Ga}_{1-x}\text{As}$ layers can be selectively oxidized at elevated temperatures, producing a mechanically stable oxide [136,137] which shows good insulating properties and a low refractive index of approximately 1.6 [138–141]. With this technique GaAs/ AlO_x DBRs can be formed with a drastically reduced number of DBR pairs necessary to achieve a certain reflectivity [139,142]. In addition so-called oxide DBRs show a significantly larger spectral and angular stopband and a drastically reduced penetration length, allowing smaller effective cavity lengths and therefore higher extraction efficiencies (see [95,96] for detailed calculations).

Figures 2.42 and 2.43 illustrate the difference in spectral and angular stopband width between a 15.5 pair GaAs/AlAs DBR and a 3.5 pair GaAs/ AlO_x DBR, both centered at 980nm. The intensity jump at 870nm of the simulated curve is related to the absorption band edge of GaAs. Evanescent coupling with the substrate may cause an extension of the low reflectivity region to angles larger than θ_l , the angle for total internal reflection at the first DBR interface.

The cavity order increase Δm_c related to the penetration depth of a DBR can be estimated according to equation (2.76)

$$\Delta m_c \approx \frac{n}{2\Delta n} \quad (2.84)$$

Hence by replacing AlAs with AlO_x Δn can be increased from 0.57 (at 980 nm) to 1.9, leading to a 70 % reduction in Δm_c (compare with table 2.5). At 650 nm the reduction is even 80 %. More detailed calculations show that the angular penetration depth L_p^θ is minimal for $n_l \approx \sqrt{n_h}$ [100]. With a value of 1.6 the refractive index of the AlO_x is thus quite close to the optimum value.

In addition the increase of the guided mode fraction at the expense of the leaky mode fraction leads to a higher degree of photon recycling, allowing an even higher external quantum efficiency (see section 2.7.3 for details).

However the implementation of an oxide DBR complicates the design and device fabrication. Since oxide DBRs are insulating, they need to be used in combination with a lateral intracavity contact, whereby care must be taken to ensure that the conductivity of the current injection layer is not reduced by the oxidation process. In addition the vertical contraction of the layers during oxidation has to be taken into account (see section 4.4.2).

MCLEDs with a high reflectivity oxide bottom DBR are treated in chapters 4 and 5 for the case of near infrared emitting InGaAs/AlGaAs structures and red emitting AlGaInP/AlGaAs structures, respectively.

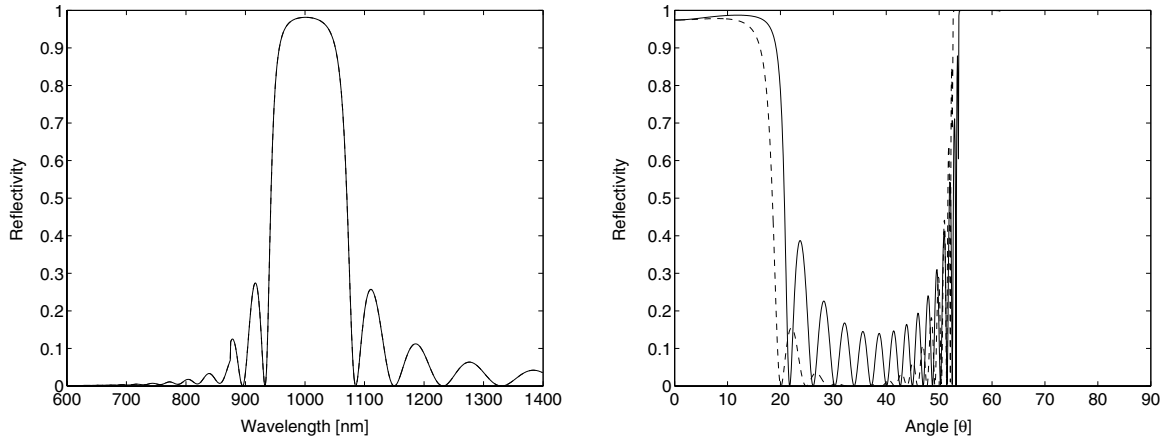


Figure 2.42: Spectral stopband (left) and angular stopband (right) around 980 nm of a 15.5 pair GaAs/AlAs DBR with $\lambda_{\text{Bragg}} = 980$ nm; TE polarization (solid line) and TM polarization (dashed line)

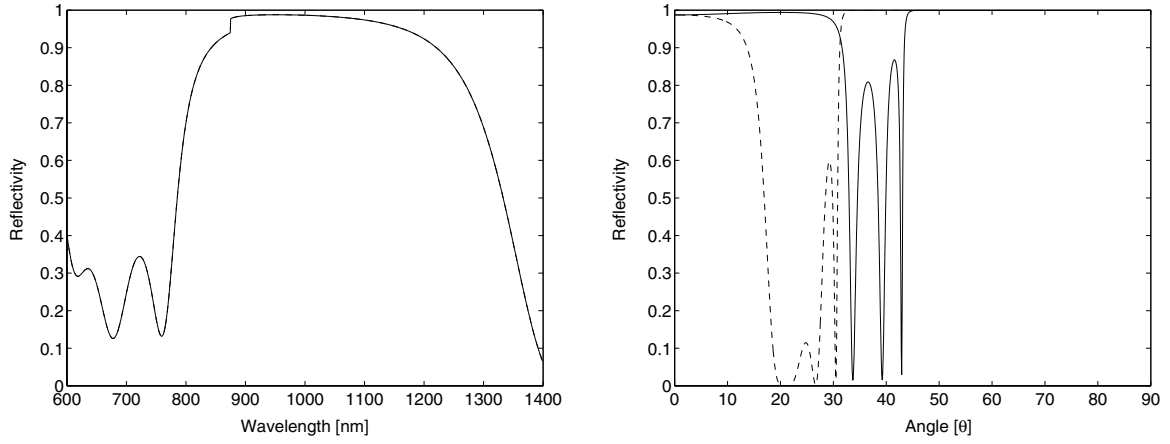


Figure 2.43: Spectral stopband (left) and angular stopband (right) around 980 nm of a 3.5 pair GaAs/AlO_x DBR with $\lambda_{\text{Bragg}} = 980$ nm; TE polarization (solid line) and TM polarization (dashed line). Intensity jump at the absorption band edge of GaAs at 870 nm. The reflectivity drop between 30 and 50° for TE polarization is related to losses caused by an evanescent coupling with the substrate

2.8.3 Omnidirectional Reflector (ODR)

Metal mirrors typically show a reflectivity below 100 %. Adding an intermediate low refractive index layer can lead to an increase of a few percent. Omnidirectional reflectors (ODRs) consist of the underlying semiconductor material (refractive index n_s), a quarter-wave low refractive index layer (n_l) and a metal layer with a complex refractive index $N_m = n_m + ik_m$ [143]. They can be made electrically conductive by perforating the low index dielectric layer with an array of metallic micro-contacts (typically AuZn), as depicted schematically in figure 2.44.



Figure 2.44: Schematic perspective view of an ODR with metallic micro-contacts [66]

For a thickness of the low index layer of $\lambda_0/(4n_l)$ the reflectivity of the triple-layer ODR at normal incidence is given by [143]

$$R = \frac{[(n_s - n_l)(n_l + n_m) + (n_s + n_l)k_m]^2 + [(n_s - n_l)k_m + (n_s + n_l)(n_l - n_m)]^2}{[(n_s + n_l)(n_l + n_m) + (n_s - n_l)k_m]^2 + [(n_s + n_l)k_m + (n_s - n_l)(n_l - n_m)]^2} \quad (2.85)$$

For an AlGaInP/SiO₂/Ag structure at 630 nm the reflectivity at normal incidence can thus be estimated to be $R_{\text{ODR}} > 98\%$, compared to a value of about 96 % for the structure without the dielectric layer. Figure 2.45 shows the superior spectral and angular reflection properties of ODRs compared to an AlGaInP/AlInP DBR. As a result, ODRs show a much larger reflectivity averaged over all angles of incidence [66]

$$\overline{R}(\lambda) = \frac{1}{2\pi} \int_0^{\pi/2} R(\lambda, \theta) 2\pi \sin \theta d\theta \quad (2.86)$$

For example for an AlGaInP/SiO₂/Ag ODR at 630 nm $\overline{R} > 0.98$ whereas it is only ≈ 0.5 for a 35 pair (Al_{0.3}Ga_{0.7})_{0.5}In_{0.5}P/Al_{0.51}In_{0.49}P DBR.

ODRs are interesting for MCLEDs as they show low penetration depths. Furthermore they lead to a significant reduction of the leaky mode fraction in favor of guided modes, leading to an increased amount of photon recycling and therefore a higher external quantum efficiency. This effect is particularly pronounced in thin-film LEDs with ODRs, where the substrate is removed by epitaxial lift-off and the thin-film acts as a waveguide structure. Enhancement factors significantly larger than unity can be expected due to photon recycling for such a device (see section 2.7.3).

Thin-film MCLEDs with a bottom ODR have been realized by OSRAM Opto-Semiconductors and are discussed in chapter 6.

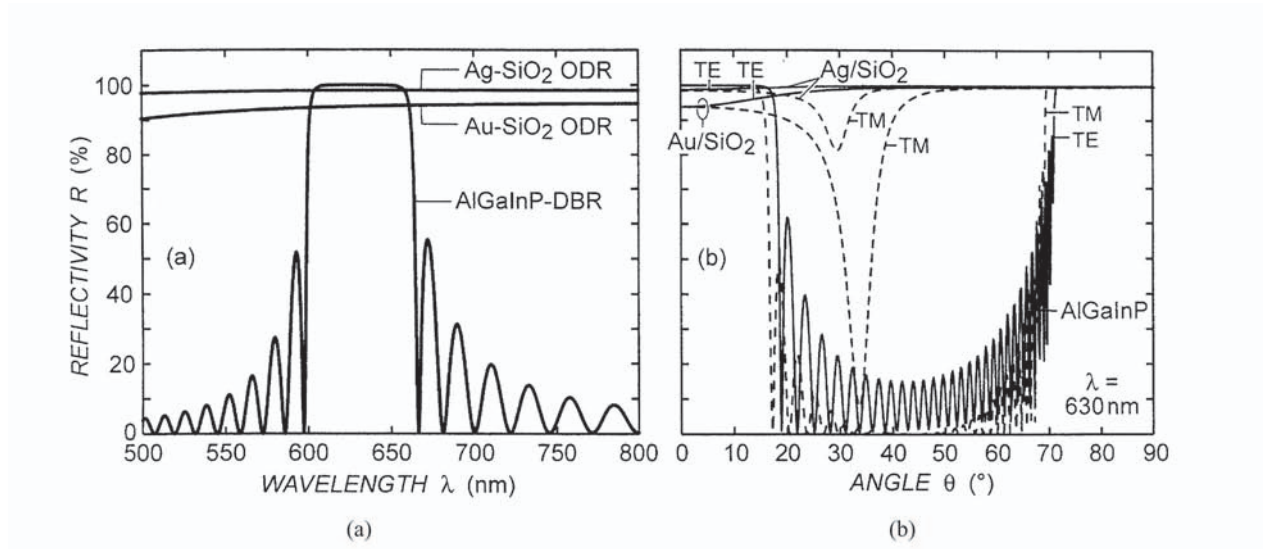


Figure 2.45: Calculated reflectivity versus wavelength (a) and versus angle of incidence (b) for two ODRs and a DBR with a Bragg wavelength of 980 nm. The external medium is GaP. The transparent AlGaInP DBR consists of 35 pairs of $(\text{Al}_{0.3}\text{Ga}_{0.7})_{0.5}\text{In}_{0.5}\text{P}/\text{Al}_{0.51}\text{In}_{0.49}\text{P}$. The ODRs comprise a 500 nm thick metal layer of either Ag or Au covered by a quarter wave layer of SiO₂. The solid and dashed lines correspond to TE- and TM-polarized waves, respectively [143]

2.8.4 Surface Plasmon Excitation

As seen in section 2.7.1, the spontaneous emission of electron-hole pairs can be represented by electrical dipoles [104]. The dipole emission has near-field and far-field components. The far-field component propagates as plane waves while the near-field is made up of evanescent waves which are quite intense. Generally the methods to increase the LED extraction efficiency focus on the extraction of the plane wave components. An alternative approach would be to convert the evanescent waves into plane waves via coupling to surface plasmon modes.

Surface plasmons are waves that propagate along the surface of a conductor [144]. The interaction between the free charges at the metal surface and electromagnetic radiation results in surface plasmons having greater momentum, or equivalently, a greater in-plane wavevector k_{SP} compared to “free” photons in the semiconductor, i.e. $k_{SP} > nk_0$. This increased momentum (in-plane wavevector) means that SP modes are non-radiative, they are bound to the interface between the metal and the dielectric. SPs may however be coupled to radiation by prism coupling or Bragg scattering [145–148]. For the latter the metal layer needs to be structured with a wavelength-scale periodic microstructure [149]. Barnes [146] proposed the use of a periodic array of holes or a periodic array of metallic particles for an efficient coupling to radiation.

Purcell enhancement factors of approximately 55 have been demonstrated for an InGaN/GaN QW placed in the vicinity of a thin silver layer [150]. Vučković et al. [151] estimated the extraction efficiencies of metal-clad surface plasmon enhanced LEDs with a periodic pattern on one side to be as high as 37 %, with Purcell factors of up to 4.5.

The light extraction enhancement for the case of near infrared InGaAs/AlGaAs-based LEDs with gold particles deposited on the top surface was assessed [152]. Simulations of a dipole embedded in GaAs ($n = 3.6$) in the vicinity of a gold layer (100 nm thick) with air on the opposite side show that for distances below 100 nm the emission originating from evanescent waves starts to become important. In case of metal particles, the resonance frequency of the collective electron oscillation is essentially determined by the dielectric properties of the metal and the surrounding medium, the particle size and the particle shape [153]. Rayleigh-Mie scattering theory predicts an optical gold particle diameter of 300 nm for an efficient scattering and outcoupling of light centered at 970 nm [152].

Electrically injected LEDs with a single InGaAs QW surrounded by a squeezed GRINSCH-like AlGaAs confinement region with a distance QW–surface of only 40 nm were successfully fabricated. Non-radiative recombination at the GaAs–air interface as well as the diffusion of the gold from the Ti/Au top contact into the QW had to be inhibited. Gold particles with a diameter of 250 nm and 20 nm were deposited on the surface of the emission area of these LEDs. However no noticeable increase in light output was measured. It is assumed that a small air gap between the surface and the particles reduces the coupling to gold surface plasmon modes to virtually zero. Calculations confirm that an air gap of 2 nm is sufficient to diminish the coupling by an order of magnitude [152]. Further extensive studies would be necessary in order to develop appropriate test structures. Due to time constraints this idea was not elaborated.

2.8.5 Substrate Structuring

The light extraction of bottom emitting devices or top emitting ones with a thick window layer can be further enhanced by structuring the surface at the extraction side, thereby enlarging θ_c , the critical angle of total internal reflection. Different geometries have been proposed, such as microlenses or cones [9]. Microlenses act in addition as optical lenses to collimate the light and can significantly improve the device's directionality, e.g. leading to an improved fiber coupling efficiency. Monolithically integrated microlenses are interesting due to their high refractive index and the redundancy of an emitter-lens alignment. Figure 2.46 shows a commercial communication LED with a monolithically integrated microlens.

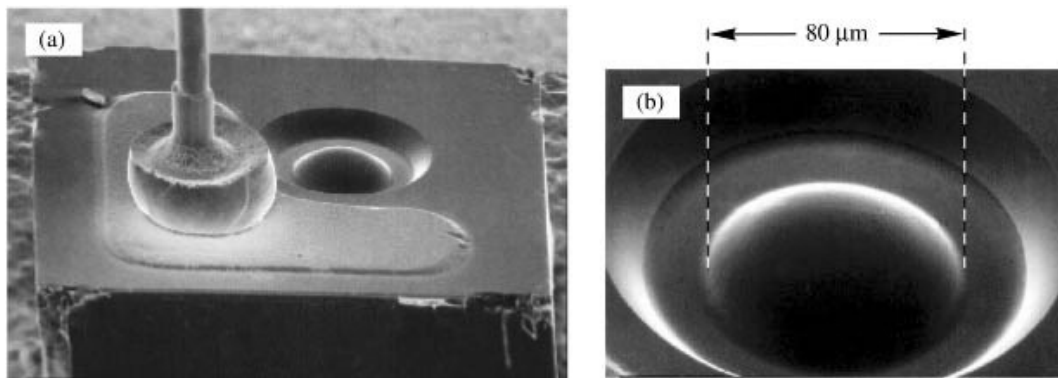


Figure 2.46: Commercial communication LED chip with integrated lens (a). Detailed picture of the lens etched by a photochemical process into the GaAs substrate (b) (AT&T ODL product line, 1995) [9]

Cones with sidewalls steep enough for an increased light outcoupling are difficult to fabricate. The realization of microlenses with an appropriate geometry for small LEDs on the other hand is much more straightforward. Several etching methods have been proposed for the fabrication of GaAs or InP microlenses. The **mask shape transfer method** is based on the transfer of a lens-like shape by dry etching, the lens is formed by photoresist reflow [154–156]. The **photoelectrochemical etching method** exploits the light intensity dependence of the etch rate [157]. Miscellaneous wet etching solutions have been presented as well. One consists of a negative profiling of the substrate by wet etching, followed by an epitaxial overgrowth and substrate removal [158,159]. Another principle is based on the edge effect of diffusion-limited etchants, i.e. an increased etch rate near the mask edge. Different etching systems of this type have been published, a sulfuric acid solution [159], a hydrobromic acid solution [160] and a mixed solution of hydrochloric acid, acetic acid and hydrogen peroxide [161].

Wet etching tests were carried out in order to realize larger microlenses in GaAs substrates with the hydrobromic acid solution proposed in [160]. For the bottom emitting near infrared MCLEDs discussed in chapter 3 the diameters of the microlenses would have to be increased to several hundreds of microns in order to achieve a significant enhancement of their external quantum efficiency. The achieved curvatures are not significant enough and therefore this idea was not pursued further.

Chapter 3

Bottom Emitting MCLEDs at 970 nm

3.1 Introduction

Bottom emitting MCLEDs represent the simplest MCLED configuration. The structure consists of a high reflectivity top mirror, the cavity with the active region and a low reflectivity outcoupling mirror. The bottom reflector consists of a semiconductor DBR, the top reflector of a metal mirror. Gold is the preferential mirror metal as it has a high reflectivity in the near infrared and a high electrical conductivity, thanks to which it can be used at the same time as top contact. In the infrared wavelength regime the GaAs substrate is transparent, which allows to couple out the light through the substrate. In order to minimize free carrier absorption losses, the substrate is generally thinned down by mechanical and chemical polishing and an anti-reflection coating (ARC) is deposited on the backside.

In this chapter a particular type of bottom emitting MCLEDs is studied, characterized by a short $\lambda/8$ phase-shift cavity, as described in section 2.8.1. Devices of this type with a gold top mirror were fabricated and analyzed. The holes are injected vertically in the p^+ -GaAs contact layer and the p-GaAs current spreading layer, whereas the electrons are injected horizontally through an n-GaAs intracavity contact layer in the bottom DBR. Thanks to the high reflectivity at all angles of the metal mirror and its low penetration depth, high external quantum efficiencies can be achieved with this type of MCLED. The influence of two different current confinement methods on the device performance is studied. The current is confined laterally either by a recess etch of the top p-doped GaAs layers beyond the metal mirror or by forming an oxide aperture on the n-side, between the intracavity contact layer and the active region.

3.2 Structure

The structure consists of a 3.5 pair bottom DBR, a phase-shift cavity and a top metal mirror. The cavity region is made up of a single $\text{In}_{0.16}\text{Ga}_{0.84}\text{As}$ quantum well (QW) and squeezed GRINSCH-like confinement regions. The top metal mirror is deposited on the highly doped p^+ -contact layer by e-beam evaporation. It is used as well as the top contact. The bottom DBR shows a reflectivity of approximately 70 % in the normal direction. Its low index layer closest to the cavity contains a higher percentage of aluminum than the ones underneath and can be used to form a current confinement aperture by selective lateral wet oxidation. The electrons are injected laterally via an n-intracavity contact in the bottom DBR. The n-contact is deposited on the GaAs high index layer below the oxide aperture layer, after the mesa definition.

The structure was designed by Ross Stanley and grown by molecular beam epitaxy (MBE) by the author, under the supervision of Ursula Oesterle. It is labelled S1892. The bottom DBR comprises 3.5 pairs of silicon-doped GaAs/ $\text{Al}_{0.93}\text{Ga}_{0.07}\text{As}$. GaAs corresponds to the high index material and $\text{Al}_{0.93}\text{Ga}_{0.07}\text{As}$ to the low index material. The top low index layer contains 98 % of aluminum. The cavity region comprises a three-step confinement profile ($\text{Al}_{0.93}\text{Ga}_{0.07}\text{As}$ – $\text{Al}_{0.50}\text{Ga}_{0.50}\text{As}$ – $\text{Al}_{0.10}\text{Ga}_{0.90}\text{As}$) and a single $\text{In}_{0.16}\text{Ga}_{0.84}\text{As}$ QW embedded in GaAs. On top a beryllium-doped GaAs current spreading layer and a highly beryllium-doped GaAs contact layer are grown. The refractive index profile of the structure is displayed in figure 3.1, the detailed structure can be found in appendix B.

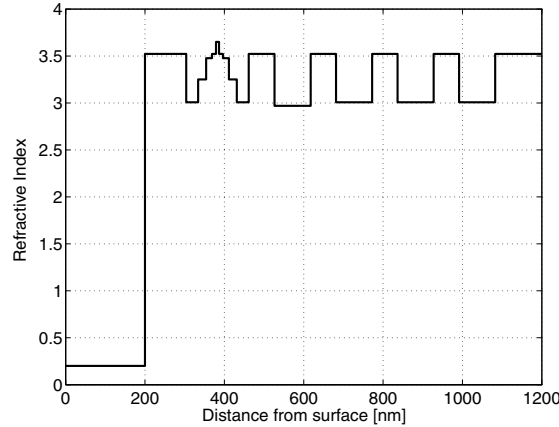


Figure 3.1: Refractive index profile of structure S1892

3.3 Simulation

The light extraction properties of the structure are calculated with a transfer-matrix based simulation program developed in-house, called “TEM_14”. It is based on the now standard methods using a plane wave expansion of an electrical dipole emitter inside a multilayer structure [84,97,98] and the standard electric field transfer matrices [111]. This approach is complete in that all near field and far field terms of the dipole are automatically included. The dipole approximation is widely used for calculating light emission from semiconductors. The calculation of the refractive index of AlGaAs is based on the data by Adachi [162] and the refractive index of gold is estimated to be $0.2 + 6i$ around 970 nm (see for example Palik et al. [163]).

The reflectivity as well as the spectral and angular emission characteristics of a cavity can be modelled with this program. For the determination of the emission properties of a structure the intrinsic emission spectrum needs to be included. The fractions emitted in extracted resonant modes, in leaky modes and in guided modes as a function of wavelength are calculated according to equation (2.64) for the extracted part. The transition from leaky modes to guided modes is determined by θ_l , the angle for total internal reflection at the first DBR interface, or the limit of evanescent coupling.

$$\eta_{\text{extr}}(\lambda) = \frac{\int_0^{\theta_c} I(\theta) \sin \theta d\theta}{\int_0^{\pi} I(\theta) \sin \theta d\theta} \quad (3.1)$$

The values obtained for the extraction efficiency $\eta_{\text{extr}}(\lambda)$ are then multiplied with the intrinsic emission spectrum $r_{\text{spont}}(\lambda)$ and integrated over all wavelengths, in order to take into account the polychromatic emission. The result corresponds to the theoretical external quantum efficiency η_{ext} of the structure for a typical emission spectrum.

$$\eta_{\text{ext}} = \frac{\int_0^{\infty} \eta_{\text{extr}}(\lambda) r_{\text{spont}}(\lambda) d\lambda}{\int_0^{\infty} r_{\text{spont}}(\lambda) d\lambda} \quad (3.2)$$

Ideally the intrinsic emission spectrum should be measured for every structure individually in order to take into account variations due to growth condition fluctuations. There are nondestructive ways of extracting the QW emission spectrum from a MCLED at a certain current level (edge emission electroluminescence, deconvolution of angle-resolved measurements [164]) but to simplify matters for the calculations mentioned in this thesis a typical QW emission spectrum measured at a characteristic current level was used. It originates from a bare QW structure grown around the same time as the structures used.

The extraction efficiencies of structure S1892, calculated for monochromatic emission, can be found in figure 3.2 as a function of wavelength. The QW emission spectrum used for the integration is displayed as well. Table 3.1 shows the distribution of the emission in the different modes at 970 nm, for emission into air and epoxy.

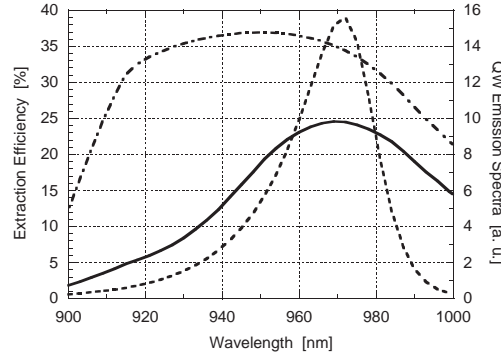


Figure 3.2: Simulated extraction efficiency of structure S1892; emission into air (solid line) and epoxy (dash-dot line) plus intrinsic emission spectrum (dashed line)

Table 3.1: Fractions of emission in the various kinds of modes for structure S1892 at 970nm, for emission into air and epoxy

	extracted [%]	leaky [%]	guided [%]
air	28	41	27
epoxy	39	33	25

The external quantum efficiencies attained by integration of the extraction efficiency spectrum with the QW electroluminescence spectrum are listed in table 3.2. An efficiency of 21 % for emission into air and 34 % for emission into epoxy is predicted. By depositing an appropriate anti-reflection coating (ARC) these values can be increased to 24 % and 36 %.

Table 3.2: Theoretical external quantum efficiencies of structure S1892 for emission into air and epoxy; without and with ARC

	$\eta_{\text{ext}}(\text{air})$ [%]	$\eta_{\text{ext}}(\text{epoxy})$ [%]
without ARC	21	34
with ARC	24	36

3.4 Fabrication

The fabrication of bottom emitting MCLEDs comprises the device isolation by the mesa etching to the n-intracavity contact layer and the deposition of the metal contacts and the top metal mirror. All process steps mentioned in chapters 3–5 have been carried out in the cleanroom facilities of the institute.

3.4.1 Cleaning

Cleaning operations are performed prior to major processing steps. Before every lithography, the samples are rinsed with acetone and isopropanol. Prior to an etching or deposition, thin films of resist left in developed areas are removed by oxygen plasma ashing, followed by a deoxidation step. The deoxidation is done immediately before loading the samples in the e-beam evaporator in order to guarantee a good adhesion of the metallizations.

3.4.2 Lithography

All photoresist patterning has been done by contact printing with a Karl Suss MJB3 UV400. The photoresist used is AZ 5214 E by Clariant, in conjunction with the developer MF-319 from Shipley. The AZ 5214 E is a positive photoresist and can be used for contrast inversion. A contrast inversion leads to an undercut resist profile, which simplifies the metal patterning by lift-off. Instead of patterning the metal by wet etching, in GaAs processes the metal is generally deposited on the resist mask and then the resist is dissolved by a solvent, which causes the metal on top of it to “lift off”. Typical solvents for the lift-off process are acetone and NMP (N-Methyl-pyrrolidone).

3.4.3 Etching

Surface Deoxidation

GaAs is known to oxidize in air at room temperature. This native oxide layer is generally between 10 and 50 Å thick [165]. The electrical properties and the reliability of GaAs-based devices depend on the removal of the native oxide. In addition, the photoresist seems to adhere better on a freshly etched semiconductor surface. Commonly used chemicals for oxide removal are diluted hydrochloric acid (HCl) [166–168], diluted ammonium hydroxide (NH₄OH) and hydrofluoric acid (HF) [169]. A diluted hydrochloric acid solution containing 16 weight percent (w/o) of HCl was used for deoxidation during the fabrication of all near infrared MCLEDs discussed in this thesis.

Selective Wet Mesa Etch

Two steps can be distinguished in the etching of semiconductor materials. First the semiconductor is oxidized and then the oxidation products are dissolved. The oxidizing agent is generally a strong oxidant like hydrogen peroxide (H₂O₂). The dissolving agent consists of an acid or a base.

As the n-intracavity contact layer is quite thin (approximately 100 nm), its exposure needs to be done with a selective etching method. For the Al_xGa_{1-x}As material system

several wet etching solutions have been found that preferentially etch either low or high aluminum content layers. Selective dry etching has been demonstrated as well but seems to be more difficult to set up [170–172].

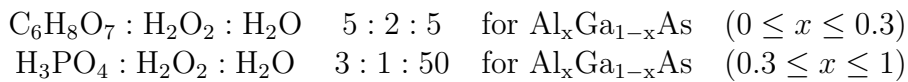
A frequently used etchant for $\text{Al}_x\text{Ga}_{1-x}\text{As}$ consists of phosphoric acid (H_3PO_4), hydrogen peroxide (H_2O_2) and water [173]. The selectivity of this solution depends on the phosphoric acid concentration. Concentrated solutions are nonselective, whereas diluted solutions display a preferential etching of AlAs with a selectivity versus GaAs of approximately 20 [174].

HCl was found to dissolve $\text{Al}_x\text{Ga}_{1-x}\text{As}$ if $x > 0.3$ with an etch rate that increases with aluminum content [175]. Selectivities above 100 have been reported.

The ammonium hydroxide/hydrogen peroxide ($\text{NH}_4\text{OH} : \text{H}_2\text{O}_2$) system is a common etchant for GaAs and low aluminum content $\text{Al}_x\text{Ga}_{1-x}\text{As}$ [176]. Its selectivity can be controlled by adjusting the pH value. Selectivities well above 100 have been achieved [177,178].

The citric acid/hydrogen peroxide/water system ($\text{C}_6\text{H}_8\text{O}_7 : \text{H}_2\text{O}_2 : \text{H}_2\text{O}$) has been known for quite a while already [179]. However its high selectivity for GaAs has only been discovered around 1990 [172,180,181]. Its selectivity between GaAs and $\text{Al}_x\text{Ga}_{1-x}\text{As}$ drastically depends on the $\text{C}_6\text{H}_8\text{O}_7 : \text{H}_2\text{O}_2$ ratio [172,180–185].

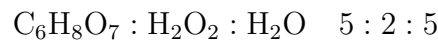
The high Al-content $\text{Al}_x\text{Ga}_{1-x}\text{As}$ layers in the structures used in this thesis consist of superlattices of AlAs and GaAs layers with a corresponding thickness ratio. Hence the selective etchant for these layers may not be too selective, otherwise the digital alloys would not be etched at all. The system of choice is therefore the diluted phosphoric acid solution. The citric acid solution is the preferential low Al-content $\text{Al}_x\text{Ga}_{1-x}\text{As}$ etchant since it shows higher selectivities than the ammonium hydroxide solution. In addition it proofed to etch low indium content $\text{In}_x\text{Ga}_{1-x}\text{As}$, which is present in the quantum well, with a similar rate as GaAs [181]. Consequently the low aluminum content $\text{Al}_x\text{Ga}_{1-x}\text{As}$ layers have been selectively etched with a citric acid ($\text{C}_6\text{H}_8\text{O}_7$) solution and the high Al-content layers with a diluted phosphoric acid (H_3PO_4) solution, as proposed by Bacher and Harris [174].



The citric acid solution is prepared by dissolution of 25 g of anhydrous citric acid in de-ionized water (DI H_2O) and stirring it for one hour. Just before etching 9 ml of H_2O_2 (30 w/o) are added. The phosphoric acid solution consists of 100 ml DI H_2O , 6 ml H_3PO_4 (ortho-phosphoric acid, 85 w/o) and 2 ml H_2O_2 (30 w/o).

Selective Wet Recess Etch

The selective removal of the top p-doped GaAs layers is accomplished with the same highly selective citric acid etchant as used for the mesa etching.



3.4.4 Contacts

The purpose of an ohmic contact on a semiconductor is to allow electrical current to flow through the semiconductor. An ideal contact should show a linear I–V characteristic, a minimal parasitic resistance, a long lifetime and a good temperature stability.

N-Contact

The use of an n-intracavity contact allows to have all electrical connections on the top surface. Furthermore the bottom DBR conductivity does not have to be optimized.

However implementing an intracavity contact in a cavity which should be as small as possible is not simple at all. The thickness of the contact layer after mesa etching needs to be large enough in order not to be entirely depleted and its conductivity needs to be high enough to allow an efficient injection of the carriers and keep the series resistance and Joule heating low.

Silicon is used for n-doping in the near infrared emitting structures treated in this thesis. The maximum achievable activated donor density in bulk GaAs is limited to approximately $5 \times 10^{18} \text{ cm}^{-3}$ [186], which is insufficient for an ohmic contact formation. This problem can be overcome by using alloyed contacts. The gold–germanium–nickel system was introduced by Braslau et al. [187] in 1967 and has become the preferred choice for contacting n-type GaAs.

Gold and germanium form an eutectic alloy that melts at 360°C for a composition of 88 w/o Au and 12 w/o Ge. The Au–Ge phase diagram is shown in figure 3.3. The germanium is used to highly dope the surface layer [165]. During the alloying process it diffuses into the GaAs cap layer and acts as a dopant. This allows to increase the doping level above 10^{19} cm^{-3} . Nickel is believed to act as a wetting agent and prevent the AuGe alloy from “balling up” during alloying [189,190]. In addition it seems to enhance the diffusion of the Ge into the GaAs. The Ni : Ge ratio appears to be critical and has been studied in detail [191,192]. It was found in addition that a first Ni layer deposited

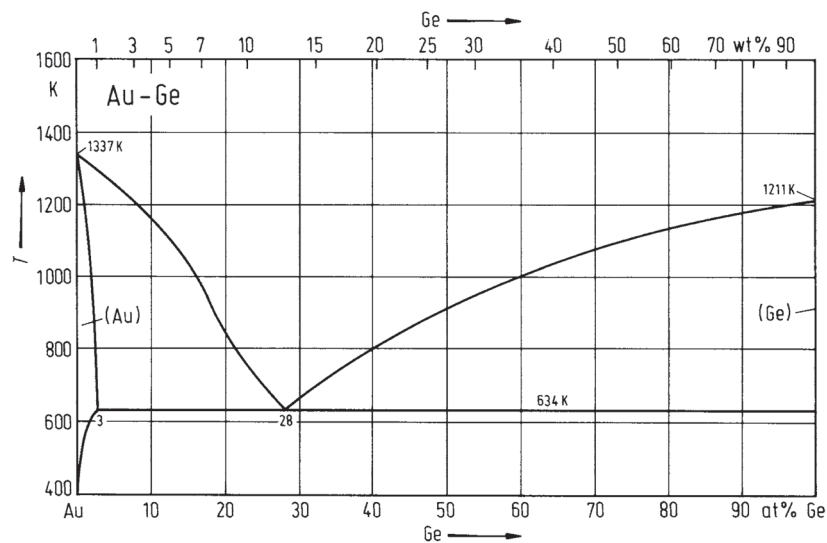


Figure 3.3: Phase diagram Au-Ge [188]

on the GaAs improves the wetting and adhesion to GaAs as well as the uniformity of the interface after alloying [193]. A thick gold overcoating results in an improved surface morphology and a reduced sheet resistance of the metallization, which simplifies a reproducible device probing [165]. The following five layer metallization was used as contact to n-GaAs in accordance with Lee et al. [194]:

$$\text{Ni/Ge/Au/Ni/Au} \quad 10/25/50/20/100 \text{ nm}$$

After e-beam deposition of the different layers and lift-off the contacts are annealed on an alloy stage. The temperature is ramped up to 380 °C with a rate of 5 °C/min and lowered again with no dwell time. The alloying is performed in the presence of forming gas, consisting of 92 vol% of nitrogen and 8 vol% of hydrogen.

P-Contact

In the case of the bottom emitting MCLED treated in this chapter, the p-contact is used as top mirror simultaneously. Hence no alloyed contact can be used since otherwise the increased interface roughness would lead to a low mirror reflectivity. By p-doping with beryllium levels high enough for the formation of ohmic contacts can be achieved. This enables the use of non-alloyed p-contact metallizations. Gold is the material of choice for this application, as it shows a high reflectivity in the near infrared and a high electrical conductivity. Furthermore it displayed a reasonably good adhesion and a low contact resistivity to p-GaAs. Figure 3.4 shows the typical reflectivity spectrum of a commercial gold mirror.

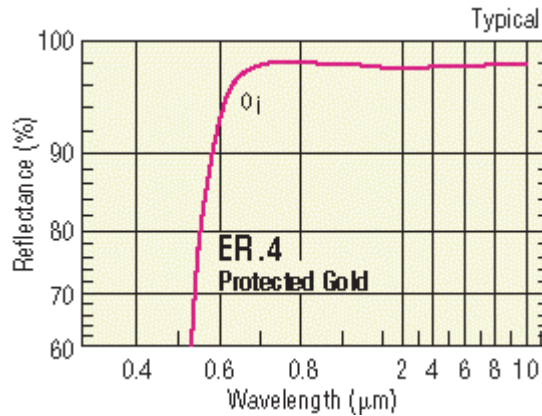


Figure 3.4: Typical reflectance versus wavelength of protected gold mirrors (by Newport)

3.4.5 Current Confinement

Additional steps can be performed for lateral current confinement. Confining the current minimizes the radiative recombination outside the cavity and the non-radiative surface recombination at the mesa sidewalls. This can be achieved by significantly increasing the resistivity of an injection layer beyond the designated emission area either on the p- or on the n-side. A confinement of the holes is more effective due to their lower mobility

but is often difficult for high efficiency MCLEDs as the cavity length should be kept as small as possible.

There are three standard current confinement methods [195]. A recess can be formed by selectively etching away a layer. The selective oxidation of a high Al-content layer allows to create an oxide aperture. The third possibility is the formation of a current aperture by proton implantation. The effect of the first two will be compared in this chapter. Etching away a layer in a structure can lead to stability problems and is therefore not trivial, however selectively removing the top p-doped GaAs layers is a very convenient and effective method to confine the holes in the mentioned structure. Lateral wet oxidation is an elegant method to form a buried current aperture, but the issues of strain and interface recombination need to be addressed.

3.4.6 Substrate Thinning

The absorption losses in the substrate are minimized by thinning down the substrate to a minimum thickness that still guarantees the mechanical stability of the sample. This is done by mechanical and chemical polishing. 2" GaAs wafers typically have a thickness of 350 μm . The free carrier absorption of n-doped GaAs substrates with a carrier concentration of typically $2 \times 10^{18} \text{ cm}^{-3}$ is of the order of 20 cm^{-1} [196]. The attenuation increases exponentially with thickness [37]:

$$\frac{P(z)}{P(0)} = e^{-\alpha z} \quad (3.3)$$

where $P(z)$ is the power at a traversed distance z and α the absorption coefficient. By reducing the substrate thickness from 350 to 150 μm the light extraction can be increased by roughly 30 %:

$$1 - e^{-\alpha d} = 0.33 \quad (3.4)$$

for an absorption coefficient $\alpha = 20 \text{ cm}^{-1}$ and a reduced distance $d = 200 \mu\text{m}$.

3.4.7 Anti-Reflection Coating

The Fresnel reflection at the semiconductor–air interface can be reduced with an anti-reflection coating (ARC). For normal incidence, the reflection coefficient is given by

$$r_{s\text{-air}} = \frac{n_s - n_{\text{air}}}{n_s + n_{\text{air}}} \quad (3.5)$$

where n_s and n_{air} are the refractive indices of the semiconductor and air, respectively.

For the case of a GaAs–air interface at 970nm, the reflectance, which corresponds to the square of the reflection coefficient, is approximately 31 %. With the proper coating of thin dielectric layers this reflection can be reduced or even eliminated. A single homogenous layer is the first and simplest ARC and probably still the most widely used. As depicted in figure 3.5, the reflection coefficient of a single homogeneous and isotropic layer sandwiched between two semi-infinite media can be found by summing the amplitudes of successive reflections and refractions, called Airy summation [112].

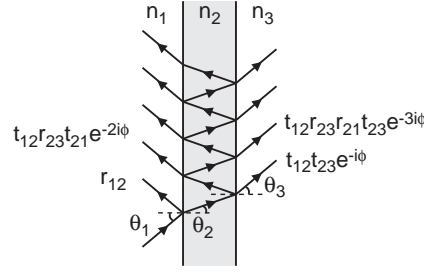


Figure 3.5: Airy summation for a thin homogeneous layer of dielectric material

$$r_{123} = \frac{r_{12} + r_{23}e^{-2i\phi}}{1 + r_{12}r_{23}e^{-2i\phi}} \quad (3.6)$$

r_{12} and r_{23} are the reflection coefficients of the first and the second interface, respectively. The factor $e^{-2i\phi}$ takes into account the phase difference due to the geometric path difference between successive rays. The parameter ϕ is given by

$$\phi = \frac{2\pi}{\lambda} n_2 d \cos \theta_2 \quad (3.7)$$

and is proportional to the thickness d and the index n_2 of the intermediate layer.

Therefore the reflection is zero when the denominator in equation (3.6) is equal to zero. The refractive indices of dielectric materials are real numbers, as well as r_{12} and r_{23} . For the case $n_1 < n_2 < n_3$, r_{12} and r_{23} are negative. Thus the phase shift $e^{-2i\phi}$ must be equal to -1 , which means $\phi = (2k + 1)\pi$ with k being an integer. This is the case for

$$d_{\text{ARC}} = \frac{\lambda}{4n_2} \quad (3.8)$$

In addition the magnitudes of r_{12} and r_{23} must be equal. For the case of a phase change of -1 the expression for the reflection coefficient can be rewritten as

$$r_{123} = \frac{n_1 n_3 - n_2^2}{n_1 n_3 + n_2^2} \quad (3.9)$$

which leads to the condition

$$n_2 = \sqrt{n_1 n_3} \quad (3.10)$$

Hence the ideal ARC should have an optical thickness of $\lambda/4$ and a refractive index which corresponds to the square root of the indices of the two adjacent layers. The optimal index of an ARC for a GaAs–air interface is therefore 1.88. The ideal values for ARCs at 970 nm for the two interfaces GaAs–air and GaAs–epoxy are summarized in table 3.3. Table 3.4 shows the refractive indices around $1 \mu\text{m}$ of several dielectrics commonly used as ARCs (after Palik et al. [163]). It can be seen that amorphous silicon monoxide (SiO) has an appropriate index for the interface GaAs–air in the near infrared regime.

Table 3.3: Optimal thickness and refractive index of ARCs at 970 nm

Interface	n_{ARC}	d_{ARC} [nm]
GaAs–air	1.88	129
GaAs–epoxy	2.30	105

Table 3.4: Refractive index at 1 μm of common dielectrics used as ARCs [163]

Dielectric material	Refractive index
SiO_2 (amorphous)	1.45
$\alpha\text{-SiO}_2$ (crystalline)	1.54
$\alpha\text{-Al}_2\text{O}_3$ (crystalline)	1.76
SiO (amorphous)	1.87
Si_3N_4 (amorphous)	2.00
ZnS (cubic)	2.29

3.4.8 Fabrication Bottom Emitting MCLEDs

The main processing steps are:

- Mesa Etch
- N-Contact Deposition
- Top Mirror and P-Contact Deposition
- Current Confinement
- Back-end Processing

The different steps are described in detail in the following part and are illustrated with schematic cross-sections and top views in figures 3.6–3.11. The effect of different current confinement methods on the electrical and optical properties is studied. The deployed methods are a recess etch on the p-side for one sample and an oxide aperture on the n-side for another. The recess is formed by selective wet etching of the top p-doped GaAs layers at the exterior of the top p-contact. The p-contact can thereby be used as etch mask. The oxide aperture is formed by selective lateral oxidation of the $\text{Al}_{0.98}\text{Ga}_{0.02}\text{As}$ layer below the active region after this layer has been exposed by the mesa etching. The lateral wet oxidation process is explained in detail in section 4.4.2. Hence three different samples were fabricated, labelled *S1892 A*, *S1892 B* and *S1892 C*. The first one comprises no current confinement at all, the second one a recess etch on the p-side and the third one an oxide aperture on the n-side. The recess is etched after the p-contact deposition, whereas the lateral wet oxidation is done after the mesa etching. Below the fabrication of devices without any current confinement is presented, followed by the illustration of the different current confinement methods.

The mask set used features circular devices with diameters ranging from 50 to 400 μm . The individual mask layers are illustrated in appendix C. During the n-contact annealing the sample *S1892 C* delaminated at the oxidation front of the current aperture. The contraction of the oxidized layer lead to high mechanical stresses and unequal thermal expansions, which caused the rupture. The sample was processed again (*S1892 C2*) with a different mask set, the same as for the semiconductor DBR devices presented in section 4.4. The advantage of this mask set is that the necessary oxidation depth is much smaller and therefore the stresses introduced are lower. However the disadvantage is that the devices on this sample have a squared geometry, which makes it difficult to compare the results with the devices on the other samples. The diameters of the mesas, the top p-contacts and the oxide aperture diameters in case of sample *S1892 C2* are compared for the different samples and device sizes in table 3.6.

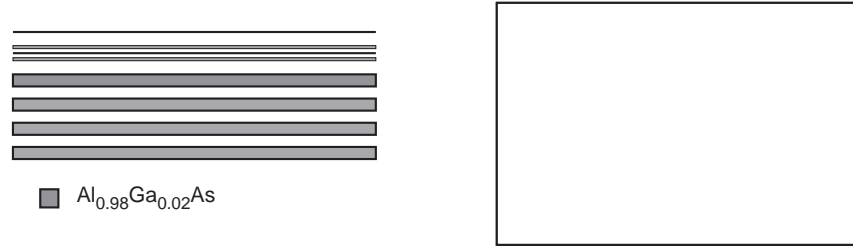


Figure 3.6: Schematic layer structure after growth

Mesa Etch

- i. Surface cleaning
- ii. Lithography
- iii. Surface deoxidation with diluted HCl
- iv. Selective wet etching of circular mesas of varying diameter; through cavity, down to n-GaAs intracavity contact layer. Citric acid solution for low Al-content layers and diluted phosphoric acid solution for high Al-content layers.

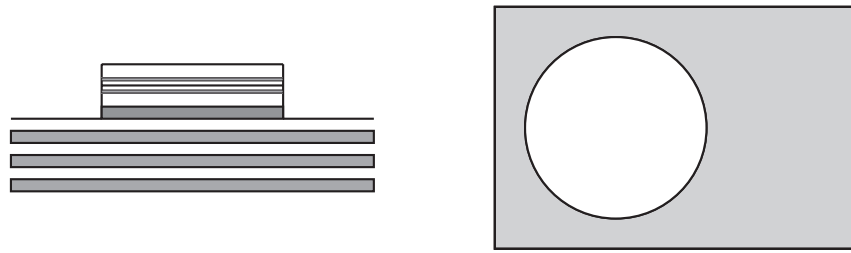


Figure 3.7: Mesa etch

N-Contact Deposition

- i. Lithography
- ii. Surface deoxidation with diluted HCl
- iii. E-beam evaporation n-contact layer sequence:

Ni/Ge/Au/Ni/Au 10/25/50/20/100 nm

- iv. Lift-off in acetone
- v. N-contact alloying at 380 °C in forming gas atmosphere (ramps 5 °C/min)

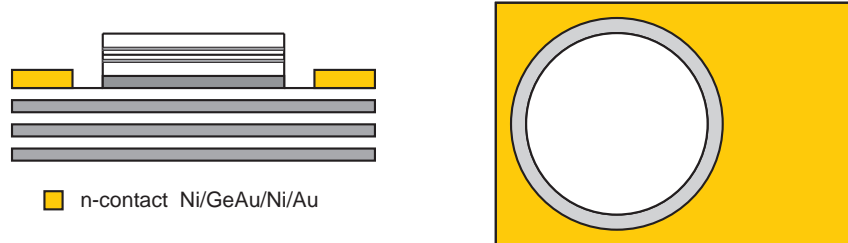


Figure 3.8: N-contact deposition

Top Mirror and P-Contact Deposition

- i. Lithography
- ii. Surface deoxidation with diluted HCl
- iii. E-beam evaporation p-contact: Au 200 nm
- iv. Lift-off in acetone
- v. No alloying

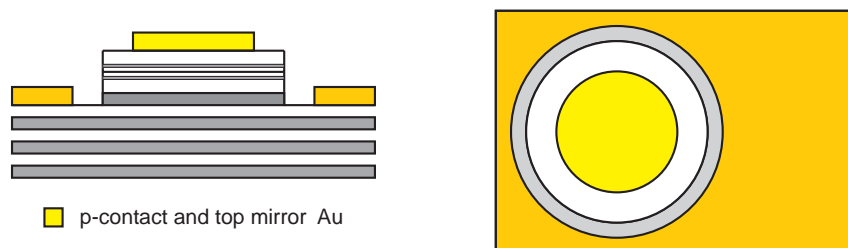


Figure 3.9: Top mirror and p-contact deposition

3.4.9 Current Confinement Methods

Recess Etch (after top mirror and p-contact deposition)

- i. Lithography
- ii. Surface deoxidation with diluted HCl
- iii. Selective wet etching of ring-shaped recess down to p- $\text{Al}_{0.93}\text{Ga}_{0.07}\text{As}$ GRINSCH layer. Removal of p-doped GaAs layers with citric acid solution.

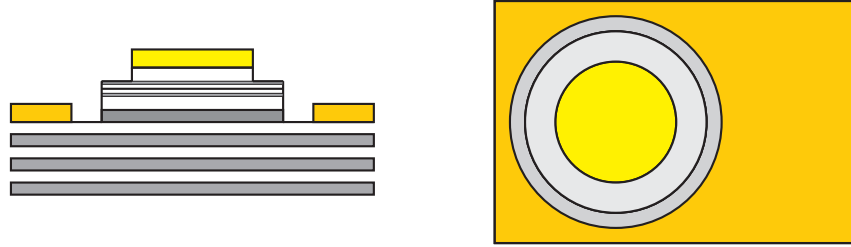


Figure 3.10: Recess etch

Selective Lateral Oxidation (after mesa etch)

Lateral wet oxidation of exposed $\text{Al}_{0.98}\text{Ga}_{0.02}\text{As}$ layer until diameter oxide aperture equal or slightly smaller than diameter p-contact.

Table 3.5: Oxidation parameters S1892 C and S1892 C2

Sample	Temperature [°C]	Time [min]	Oxidation depth [μm]
S1892 C	450	28	75
S1892 C2	400	36	12

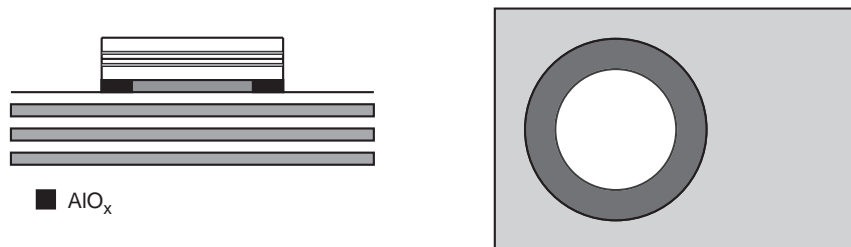


Figure 3.11: Lateral wet oxidation current confinement layer

3.4.10 Samples after Front-Side Processing

Optical Microscope Pictures

Figures 3.12 and 3.13 show optical microscope pictures of the different samples taken after front-side processing. The picture of sample S1892 C was taken after the n-contact annealing, the delamination at the oxidation front is obvious. Sample S1892 C2 on the other hand shows no signs of degradation. It can be seen that the recess etch ring on the devices from sample S1892 B shows an increased roughness. It is assumed that this is due to the surface oxidation of the $\text{Al}_{0.93}\text{Ga}_{0.07}\text{As}$ layer after being exposed to air.

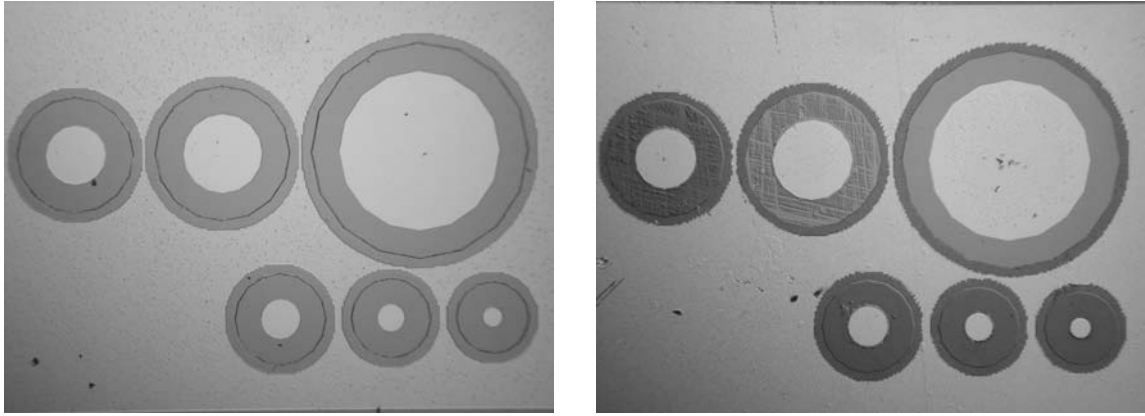


Figure 3.12: Samples S1892 A (left) and S1892 B with recess (right); top row 400, 200 and 150 μm diameter devices, bottom row 100, 70 and 50 μm diameter devices

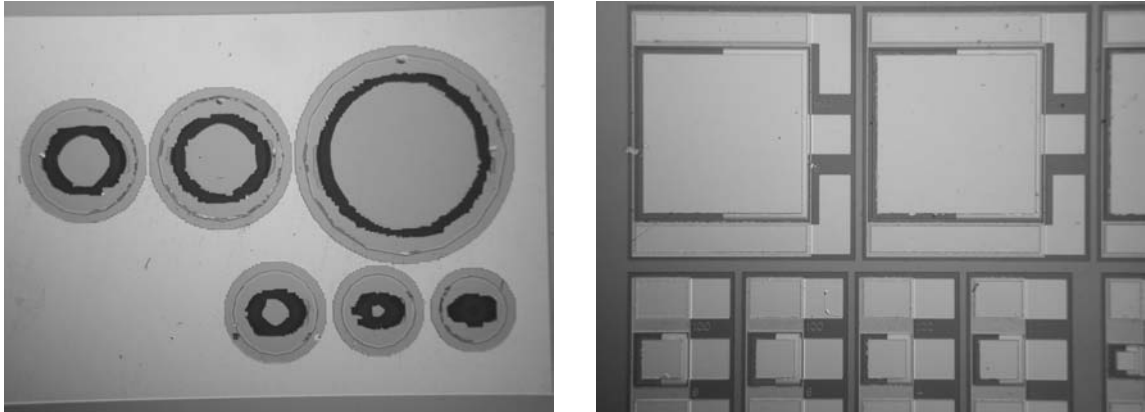


Figure 3.13: Samples S1892 C after n-contact annealing (left) and S1892 C2 after processing (right); S1892 C2 different mask set with reduced oxidation depth

SEM Pictures

The samples were analyzed with a Philips XL 30 FEG scanning electron microscope (SEM). Figure 3.14 shows cross-sections of structure S1892 after mesa etching at the left side and the sample S1892 C2 after front-side processing. The high aluminum content layers oxidize in air and therefore become isolating and appear darker in the SEM pictures. The $\text{Al}_{0.93}\text{Ga}_{0.07}\text{As}$ bottom DBR layers, the $\text{Al}_{0.98}\text{Ga}_{0.02}\text{As}$ oxidation layer and the $\text{Al}_{0.93}\text{Ga}_{0.07}\text{As}$ GRINSCH layers can be identified. Apparently the underetch of the $\text{Al}_x\text{Ga}_{1-x}\text{As}$ layers is more important than for the GaAs layers. On the right side the p-contact, the polyimide isolation layer and the oxidation front can be seen. The layer was oxidized from the right and the oxidation stopped about 1 micron before reaching the p-contact edge in case of the shown device.

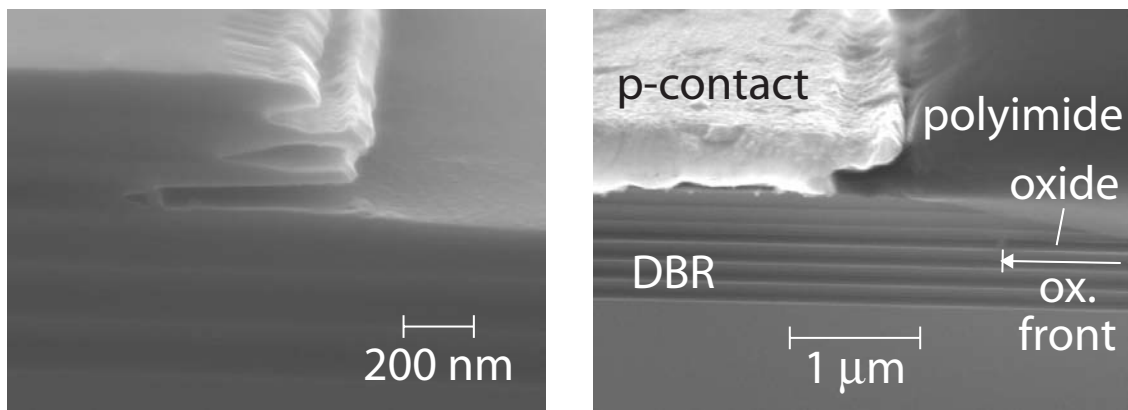


Figure 3.14: SEM pictures after mesa etching (left) and S1892 C2 after processing (right)

Device Dimensions

Table 3.6 summarizes the device dimensions for the different samples. The oxide aperture diameters have been determined with an optical microscope using a high bandpass filter, which blocks light below 665nm in order to increase the contrast between oxidized and un-oxidized areas.

Table 3.6: Mesa, p-contact and oxide aperture diameters of the different devices

S1892 A, S1892 B		S1892 C2		
circular		square		
mesa [μm]	p-contact [μm]	mesa [μm]	p-contact [μm]	oxide aperture [μm]
540	400	420	400	396
350	200	220	200	196
300	150			
240	100	120	100	96
210	70			
190	50	70	50	46

3.4.11 Back-End Processing

The additional back-end processing steps are:

- Substrate Thinning
- Anti-Reflection Coating Deposition

After the front-side processing the devices from sample S1892 B showed very promising results (see section 3.5.2). The processing was continued by reducing the substrate thickness by lapping to $150 - 200 \mu\text{m}$. As demonstrated previously this reduces the free carrier absorption losses by approximately 30 %. Finally a SiO anti-reflection coating was deposited on the substrate side to eliminate the Fresnel reflection at the GaAs-air interface. In addition a second sample, named *S1892 B2*, was processed the same way.

Substrate Thinning

- i. Lapping with carborundum slurry, mesh # 600 and 1000
- ii. Lapping with diamond polish paste, grit size 10, 3, 1 and $0.25 \mu\text{m}$

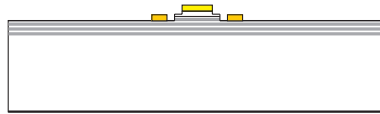
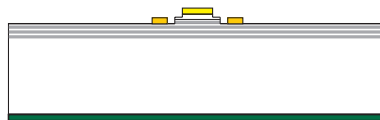


Figure 3.15: Substrate thinning

Anti-Reflection Coating Deposition

- i. Surface deoxidation with diluted HCl
- ii. Evaporation anti-reflection coating: SiO 130 nm



■ ARC SiO

Figure 3.16: Anti-reflection coating deposition

3.5 Experimental Results

3.5.1 TLM Measurements

Ohmic contacts to semiconductor devices are obtained by alloying a metal film stack to a highly doped cap layer. The electron transfer from the metal to the semiconductor then takes place by tunneling.

A convenient way to determine simultaneously the contact resistance of planar ohmic contacts and the sheet resistance of the highly doped cap layer is given by the **transmission line model** (TLM). The method was originally proposed by Shockley [197] and developed independently by Murrmann and Widmann [198–200] and Berger [201].

To obtain the measurement geometry, rectangular contact pads of length L and width W are aligned with increasing distances $d_1, d_2, d_3 \dots$. The pattern is isolated to restrict current flow between the two contact pads (figure 3.17).

The I–V characteristics of adjacent contacts are determined for the different contact spacings. The resistance between two contacts is then given by the two contact resistances plus the resistance of the semiconductor layer between the two contacts.

$$R = \left. \frac{\delta U}{\delta I} \right|_{U=0} = 2R_c + R_{sh}d/W \quad (3.11)$$

The values of the contact resistance R_c and the sheet resistance R_{sh} are then obtained from plots of the measured resistance R as a function of spacing d . The intercept with the ordinate yields $2R_c$ and the slope of the straight line equals R_{sh}/W . The contact resistivity can be derived by the TL-model in the following way:

$$\rho_c = \frac{(R_c W)^2}{R_{sh}} \quad (3.12)$$

Ideally, for all contact resistance measurements the contacts would have to show purely ohmic I–V characteristics; this up to the device's maximum current level. The TLM method closely approaches the operating conditions of surface devices, having lateral current escape from the contact to the semiconductor, such as Field Effect Transistors (FETs) or High Electron Mobility Transistors (HEMTs). In the ideal case the

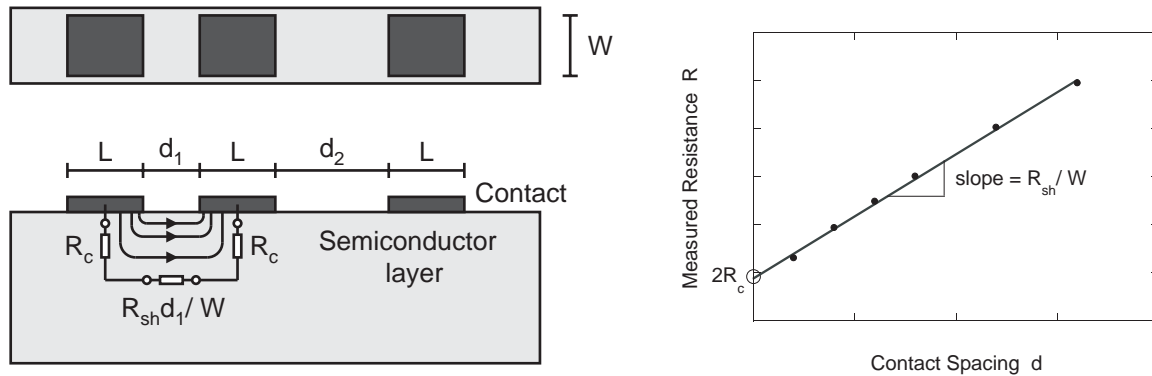


Figure 3.17: Schematic TLM test structure and plot of contact to contact resistance R as a function of spacing d to obtain contact resistance R_c and sheet resistance R_{sh}

TLM method also leads to good values of ρ_c for bulk devices, where the current escapes rather perpendicularly from the contact into the semiconductor (diodes, bipolars, lasers). More elaborate models have been developed, taking into account a modified sheet resistance under the contact area, current crowding effects at the metal–cap layer boundary, etc. [202–205].

In the case of alloyed germanium-gold contacts on n-type GaAs significant inter-diffusion occurs at the semiconductor–metal interface [206,207]. In addition for the MCLED structures with n-intracavity contact layers the underlying n-GaAs layer is quite thin (below 100 nm) and might therefore be entirely depleted, which would lead to a Schottky-type behavior. Effectively it was not possible to determine the sheet resistance and the contact resistivity of the Ni/AuGe/Ni/Au n-contacts in this manner since a non-ohmic behavior was measured for these contacts. The measurements of the p-contacts on the other hand lead to reasonable results.

Square test patterns are used with dimensions slightly varying between the two different mask sets. In case of samples S1892 A and S1892 B the contact areas are $100 \times 120 \mu\text{m}^2$, with contact spacings of 5, 10, 15, 20 and $30 \mu\text{m}$. The contact areas for sample S1892 C are $100 \times 100 \mu\text{m}^2$, with contact spacings of 2, 4, 6, 8, 12 and $16 \mu\text{m}$. The measurements are carried out by means of an HP4156A Semiconductor Parameter Analyzer. The I–V characteristics for the different contact spacings are recorded with a four point probe set-up. Two probes serve for applying a voltage and sweeping it over a certain range while the other two are used to measure the resulting current.

Table 3.7 shows the sheet resistances R_{sh} and contact resistivities ρ_c of the p-contacts of the different samples obtained from the TLM measurements. As the p-doped GaAs layers between the TLM contact pads were etched away during the recess etch, it was not possible to determine the characteristics of this sample. Reasonable contact resistivities were found for the other two samples, confirming the good electrical properties of the non-alloyed gold p-contact.

Table 3.7: Contact parameters p-contacts

Sample	Confinement	R_{sh} [Ω/\square]	ρ_c [Ωcm^2]
S1892 A	-	870	2.0×10^{-4}
S1892 B	recess	-	-
S1892 C	oxide	2000	2.0×10^{-4}

3.5.2 L–I–V Measurements

The characteristics of devices from the different samples after the front-side processing are compared. For the devices with recess etch the results after the substrate thinning and anti-reflection coating deposition will be shown as well.

The devices are characterized by detailed light, current and voltage (L–I–V) measurements. The set-up consists of a calibrated large area silicon photodiode (Hamamatsu S1337-1010BR) and a HP 4145A Semiconductor Parameter Analyzer which is used as DC voltage source, current monitor and photocurrent monitor simultaneously (see figure 3.18). All measurements are taken in cw (continuous wave) mode and at room temperature. The device is contacted with two probe needles connected via coaxial cables. A voltage is applied to the diode and is varied over a certain range while the resulting diode forward current and the photocurrent generated in the photodiode are recorded. The photodiode is biased at 0 V in order to minimize its dark current.

Bottom emitting devices are measured simply by placing them either on a glass microscope slide on the photodiode or directly on the photodiode. As the surface of the photodiode of 1 cm² is large compared to the device sizes, it is assumed that all the emitted light is captured by the photodiode if the device is centered on it.

The external quantum efficiency η_{ext} is defined as the ratio of the externally emitted photon flux, $\Phi_{\text{opt}}^{\text{out}}$, to the total injected electron flux, $\Phi_{\text{el}}^{\text{tot}}$ (see section 2.5.1)

$$\eta_{\text{ext}} = \frac{\Phi_{\text{opt}}^{\text{out}}}{\Phi_{\text{el}}^{\text{tot}}} = \frac{e}{h\nu} \frac{P_{\text{opt}}}{I} \quad (3.13)$$

where $h\nu$ denotes the energy of the emitted photons, e the electron charge, P_{opt} the

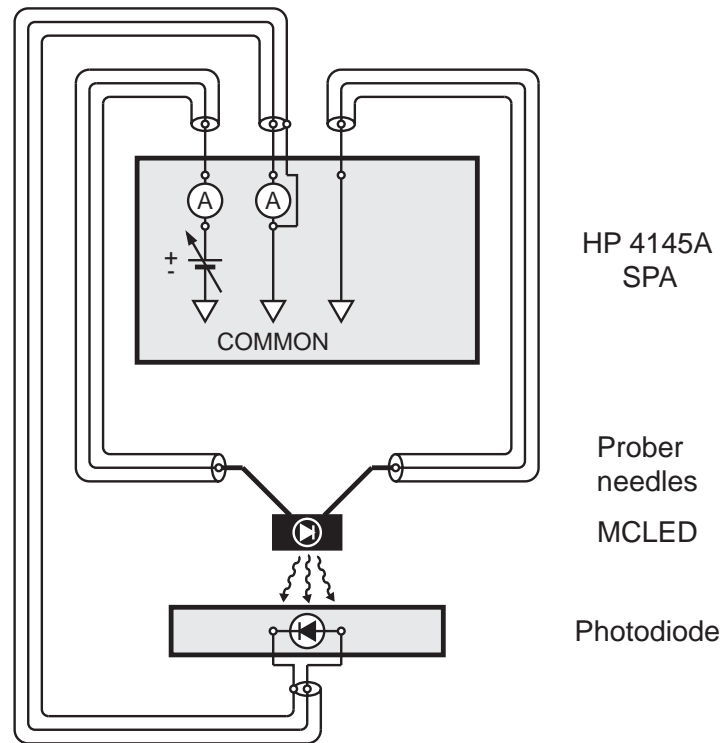


Figure 3.18: Schematic representation electrical circuit L–I–V measurement set-up

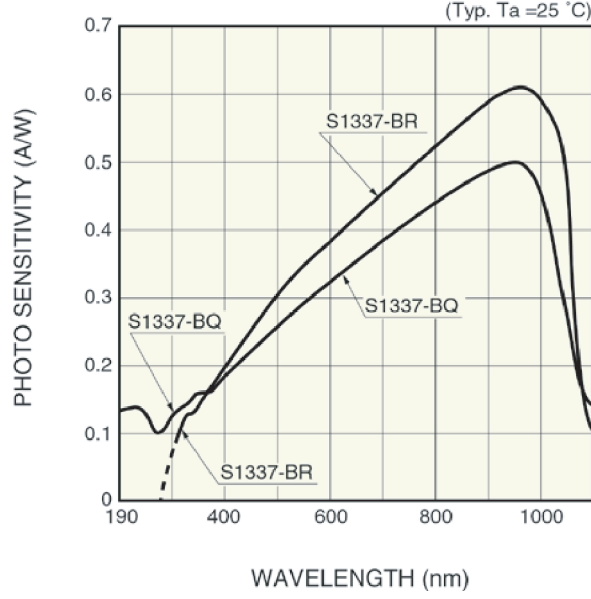


Figure 3.19: Typical spectral response large area photodiodes by Hamamatsu

optical output power and I the injected current [37]. The measured external quantum efficiency is therefore calculated as follows:

$$\eta_{\text{ext}} = \frac{\lambda[\mu\text{m}]}{1.24} \frac{I_{PD}}{R_{PD}I_F} \quad (3.14)$$

R_{PD} corresponds to the photo sensitivity of the photodiode, which is expressed in units of A/W. The typical spectral response of the photodiodes S1337-1010BR and S1337-1010BQ given by Hamamatsu is shown in figure 3.19. The photodiodes S1337-1010BQ have a quartz window instead of a resin coating and show therefore an increased sensitivity below 400nm but a reduced sensitivity for longer wavelengths. All the measurements were carried out with a photodiode S1337-1010BR, which had been calibrated by the Swiss Federal Office of Metrology and Accreditation (METAS). The calibration results are listed in appendix D.1.

The external quantum efficiency of the photodetector, which corresponds to the product $1.24R_{PD}/\lambda[\mu\text{m}]$, is equal to 0.786 at 970nm. As the detector quantum efficiency is more or less constant in this wavelength regime this value is used for the device efficiency calculation. The detector efficiency is assumed to be independent of the angle of incidence.

$$\eta_{\text{ext}} = \frac{1}{0.786} \frac{I_{PD}}{I_F} \quad (3.15)$$

Since the LED characteristics at low current densities are representative for the electrical and optical quality of the device, the current density–voltage curves are plotted on a semilogarithmic scale ($\log(J)$ –V) and the external quantum efficiency is plotted versus the logarithm of the current density (η_{ext} – $\log(J)$). The representation as a function of current density instead of the current allows to compare the curves for the different device sizes.

L–I–V Measurements after Front-Side Processing

Figures 3.20–3.22 show the measured current density–voltage (J – V) characteristics and external quantum efficiencies as a function of drive current density (η_{ext} – J) for MCLEDs of varying diameter and with the different current confinement methods. The measurements have been carried out by placing the samples on pyrex microscope slides with a thickness of 0.8 mm. The reduction in light output due to the microscope slide is estimated to be of the order of 10 %. For the current density calculation the area of current flow is assumed to be equal to the top p-contact area in case of the devices with no current confinement or a recess etch and equal to the oxide aperture area in case of the devices with an oxide aperture. The maximum efficiencies as well as the current densities at maximum efficiency are summarized in tables 3.8– 3.10 for the different device types.

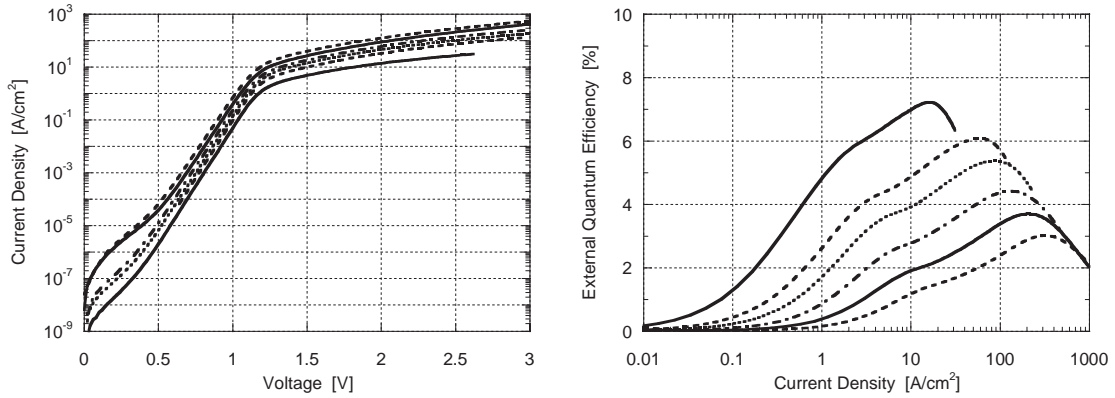


Figure 3.20: J – V characteristic and external quantum efficiency vs. drive current density of MCLEDs without confinement from sample S1892 A; diameters 400, 200, 150, 100, 70 and 50 μm (solid, dashed, dotted, dash-dot, solid and dashed line)

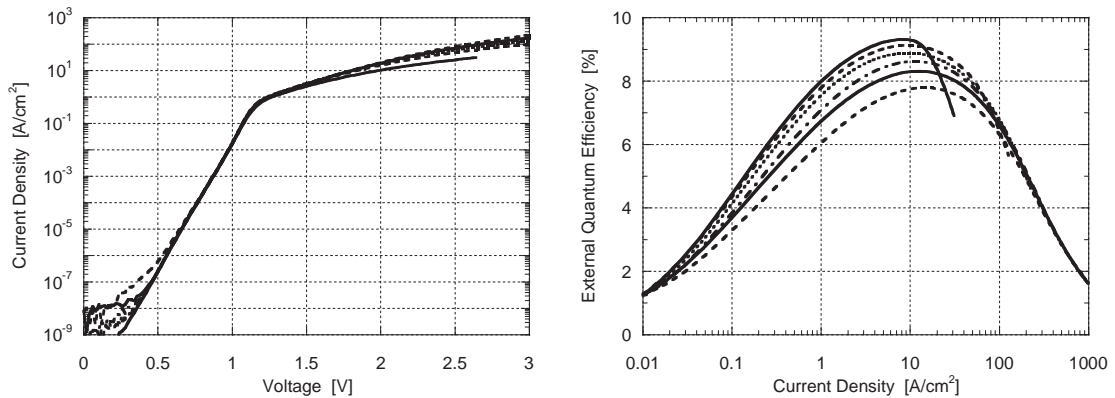


Figure 3.21: J – V characteristic and external quantum efficiency vs. drive current density of MCLEDs with recess etch from sample S1892 B; diameters 400, 200, 150, 100, 70 and 50 μm (solid, dashed, dotted, dash-dot, solid and dashed line)

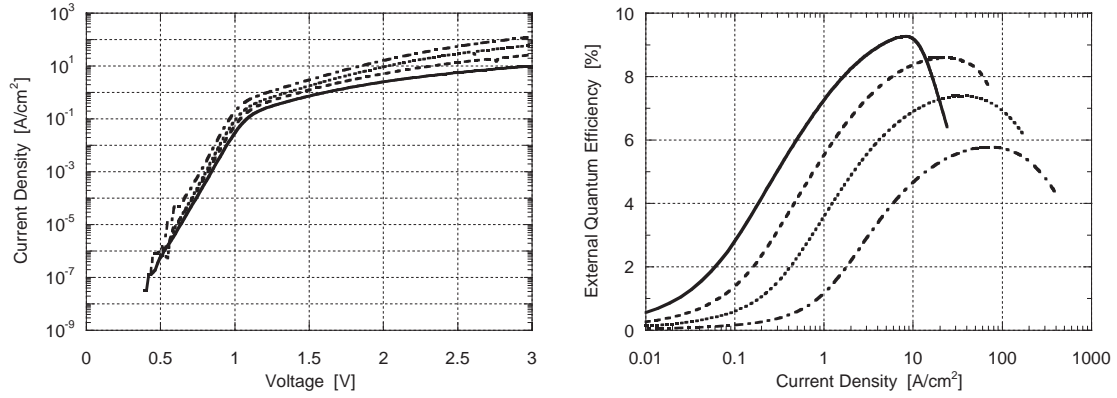


Figure 3.22: J–V characteristic and external quantum efficiency vs. drive current density of MCLEDs with oxide aperture from sample S1892 C2; diameters 400, 200, 100 and 50 μm (solid, dashed, dotted and dash-dot line)

Table 3.8: Maximum external quantum efficiencies and corresponding current densities for devices without confinement (sample S1892 A)

Diameter [μm]	$\eta_{\text{ext,max}}$ [%]	$J(\eta_{\text{ext,max}})$ [A/cm²]
400	7.2	16
200	6.1	60
150	5.4	85
100	4.4	131
70	3.7	206
50	3.0	325

Table 3.9: Maximum external quantum efficiencies and corresponding current densities for devices with recess etch (sample S1892 B)

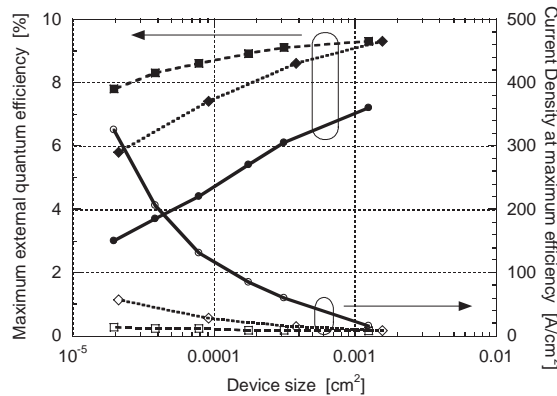
Diameter [μm]	$\eta_{\text{ext,max}}$ [%]	$J(\eta_{\text{ext,max}})$ [A/cm²]
400	9.3	8.0
200	9.1	9.0
150	8.9	9.0
100	8.6	12
70	8.3	12
50	7.8	14

Table 3.10: Maximum external quantum efficiencies and corresponding current densities for devices with oxide aperture (sample S1892 C2)

Diameter [μm]	$\eta_{\text{ext,max}}$ [%]	$J(\eta_{\text{ext,max}})$ [A/cm ²]
396	9.3	8.3
196	8.6	15
96	7.4	28
46	5.8	57

In case of sample S1892 A without any current confinement the J–V curves for the different device diameters differ significantly. The current density at maximum efficiency increases significantly with decreasing device size, which indicates that the current flow is not restricted to the p-contact area. The ratio of the mesa size to the p-contact area is larger for the smaller devices, therefore the current spreading is more important and the total current or the apparent current density increases to a greater extent. The J–V curves of the devices with recess etch on the other hand coincide over a large voltage range. At low voltage levels leakage currents dominate and above the turn-on voltage series resistances govern the current flow. The implementation of an oxide aperture leads to an improved overlap of the different curves as well, however to a lesser extent than the recess etch.

The implementation of a recess on the p-side allows to efficiently confine the current to the cavity region, leading to a significant increase in external quantum efficiency and reduced drive current densities. In addition the reduction in efficiency and the increase in current density with decreasing device size has become less important. With an oxide aperture on the n-side high efficiencies can be achieved for the largest devices as well, yet the beneficial effect is lower for the small devices. Figure 3.23 illustrates the decrease of the maximum external quantum efficiency with device size and the effect on the current density at maximum efficiency for the different current confinement methods.

**Figure 3.23:** Maximum external quantum efficiency (solid symbols) and current density at maximum efficiency (empty symbols) as a function of p-contact area for the different current confinement methods; no current confinement (solid line), recess etch (dashed line) and oxide aperture (dotted line)

L–I–V Measurements after Back–End Processing

The device characteristics of the MCLEDs with recess etch have been remeasured after substrate thinning and deposition of the anti-reflection coating. For these measurements the sample was placed directly on the photodiode in order to avoid the 10 % reduction in light output due to the microscope slide. The photodiode had been calibrated by METAS, the Swiss Federal Office of Metrology and Accreditation, prior to the measurements (data see appendix D.1). The curves for sample S1892 B1 and S1892 B2 are shown in figures 3.24 and 3.25, the maximum efficiencies are listed in table 3.11.

The increase due to the substrate thinning corresponds to the predicted 33 % (see equation (3.4)). The ARC leads to an increase of 15 % for sample S1892 B1 in average, and about 20 % for sample S1892 B2. Hence slightly higher values are measured after the back-end processing for the devices on the latter sample, with the exception of the 400 μm diameter devices, which consistently show a significantly lower efficiency than the other devices. This phenomenon could originate from a bad adhesion of the top mirror for the largest devices.

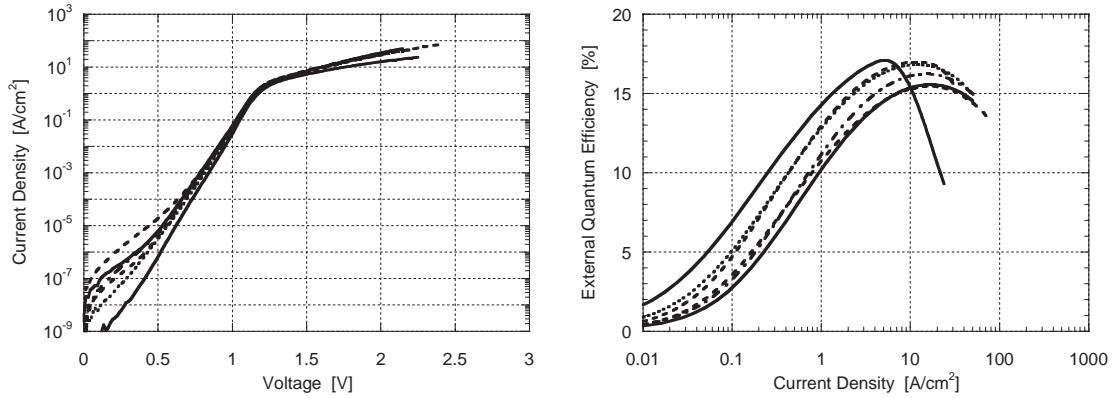


Figure 3.24: J–V characteristic and external quantum efficiency vs. drive current density of MCLEDs from sample S1892 B1 after backend processing; diameters 400, 200, 150, 100, 70 and 50 μm (solid, dashed, dotted, dash-dot, solid and dashed line)

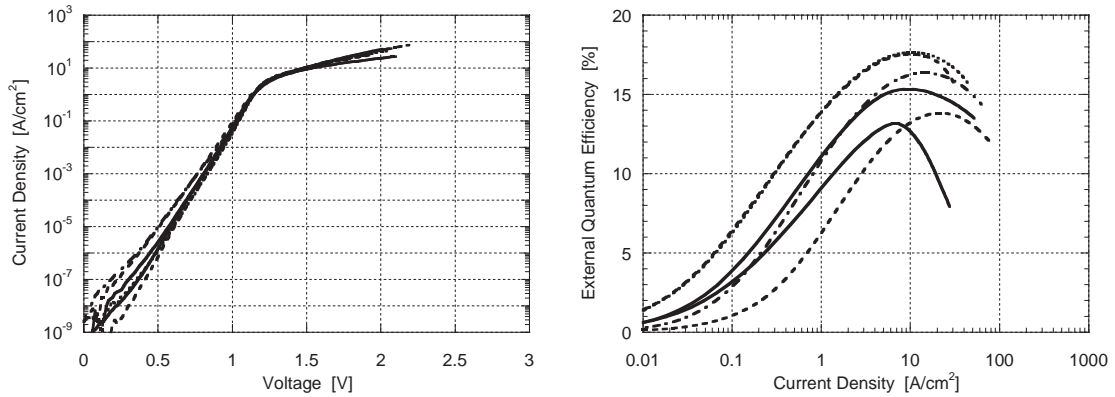


Figure 3.25: J–V characteristic and external quantum efficiency vs. drive current density of MCLEDs from sample S1892 B2 after backend processing; diameters 400, 200, 150, 100, 70 and 50 μm (solid, dashed, dotted, dash-dot, solid and dashed line)

Table 3.11: Maximum external quantum efficiencies for devices with recess etch from samples S1892 B1 and S1892 B2 after back-end processing

Diameter [μm]	S1892 B1 [%]	S1892 B2 [%]
400	17.1	13.2
200	17.0	17.5
150	16.8	17.7
100	16.2	16.4
70	15.6	15.3
50	15.7	13.8

External quantum efficiencies up to 18% have been measured for sample S1892 B2 at very low current densities around 10 A/cm^2 . Compared to the results before the back-end processing (see figure 3.21), the performance of the smallest devices deteriorated. They might have been damaged with the prober needles during the measurements.

The emission into epoxy is simulated by immersing the backside of the sample and the detector in glycerol. Anhydrous glycerol has a refractive index of 1.4746 at 589 nm and 20°C [208], similar to the refractive index of epoxy of 1.5. However with increasing water content this value is decreasing towards 1.33, which reduces the beneficial effect of the glycerol. The ARC is not adapted to an emission in a medium with refractive index of 1.5 but simulations show that the difference in efficiency is marginal. This configuration corresponds to the emission into the epoxy dome but does not take into account the reflection at the epoxy–air interface corresponding to 4%. Figures 3.26 and 3.27 show the results of the measurements in glycerol. The maximum external quantum efficiencies measured are compiled in table 3.12. In addition the values corrected by 4% for the presence of an epoxy–air interface are listed. Efficiencies between 26 and 27% were measured for the 200 and 150 μm diameter devices, corresponding to 25 – 26%, if corrected for the presence of an epoxy–air interface.

Table 3.12: Maximum external quantum efficiencies for devices with recess etch from samples S1892 B1 and S1892 B2 after back-end processing for emission into glycerol; measured values and values reduced by 4% in order to take into account the reflection at the interface epoxy–air

Diameter [μm]	S1892 B1		S1892 B2	
	Measurements [%]	Corrected [%]	Measurements [%]	Corrected [%]
400	25.2	24.2	22.1	21.2
200	26.1	25.1	26.6	25.5
150	25.9	24.9	26.3	25.2
100	24.9	23.9	23.5	22.6
70	19.6	18.8	21.0	20.2
50	21.0	20.1	18.0	17.3

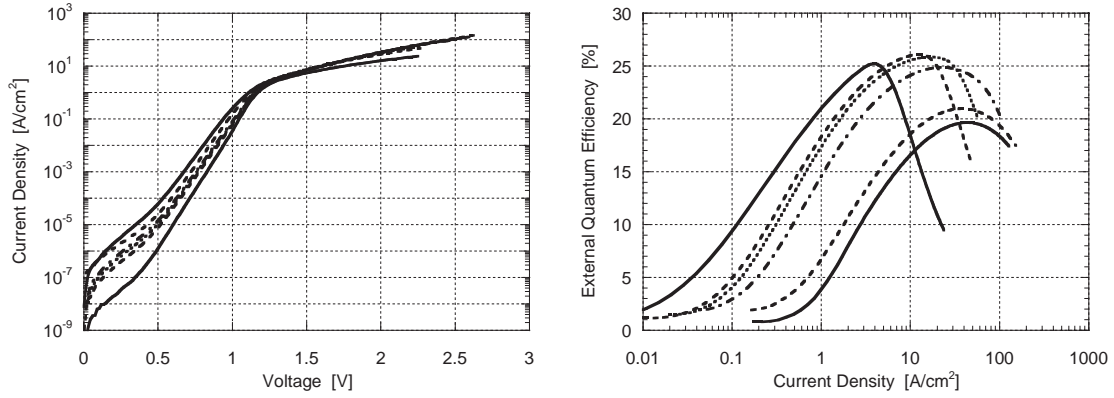


Figure 3.26: J–V characteristic and uncorrected external quantum efficiency vs. drive current density of MCLEDs from sample S1892 B1 after back–end processing, immersed in glycerol; diameters 400, 200, 150, 100, 70 and 50 μm (solid, dashed, dotted, dash-dot, solid and dashed line)

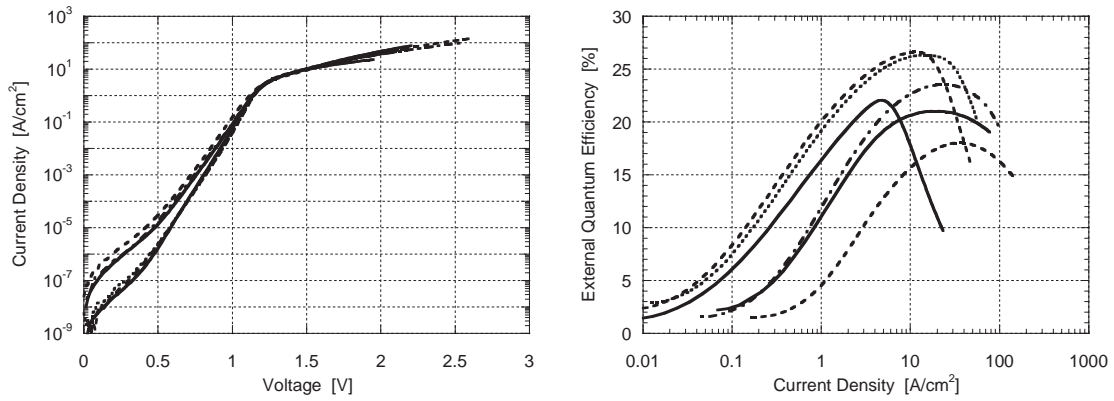


Figure 3.27: J–V characteristic and uncorrected external quantum efficiency vs. drive current density of MCLEDs from sample S1892 B2 after back–end processing, immersed in glycerol; diameters 400, 200, 150, 100, 70 and 50 μm (solid, dashed, dotted, dash-dot, solid and dashed line)

The maximum efficiencies are summarized in table 3.13 together with the simulation results. Record high values have been achieved and the theoretical values indicate that efficiencies above 20% for emission into air and 30% for emission into epoxy are possible.

Table 3.13: Maximum external quantum efficiencies of SE MCLEDs emitting at 970 nm

Sample	Simulation		Measurements	
	air [%]	epoxy [%]	air [%]	glycerol [%]
S1892 B1	24	36	17	≈ 25
S1892 B2	24	36	18	≈ 26

3.6 Discussion

Light generated from regions not directly underneath the top mirror is not subject to cavity effects, the bottom emission in this region can be assumed to be zero. By limiting the device current to the region under the top mirror the amount of radiative recombination beyond the cavity region can be drastically reduced. Hence higher external quantum efficiencies and lower current densities are achieved. As the mesa to cavity area ratio increases with decreasing device size, this effect is more pronounced for smaller devices. Both current confinement methods lead to significantly improved device performances, however the oxide aperture has a reduced effect on the smaller devices. This can be due to different reasons. Generally a confinement of the electrons is less effective than a hole confinement, as the hole mobility is significantly smaller than the electron mobility. In addition the oxide is further away from the active region, with a doped GaAs layer in between. Hence the lateral diffusion of the electrons between aperture and QW is not negligible.

Furthermore the oxide layer is comparably thick and no Al-content grading is incorporated. Therefore it is possible that due to the lateral oxidation strain and non-radiative defects are introduced at the oxidation front, which would lead to an increased non-radiative recombination at the oxide-semiconductor interface. The recombination at heterostructure interfaces is known to occur mainly at misfit dislocations [209]. This effect will be discussed in more detail in the following.

3.6.1 Current–Voltage Characteristic

As derived in section 2.3, the I–V characteristic of a LED can be written as

$$I = I_0 \left[\exp \left(\frac{e(V - R_s I)}{n_{\text{ideal}} k T} \right) - 1 \right] \quad (3.16)$$

I_0 corresponds to the reverse saturation current, n_{ideal} is the ideality factor of the diode and R_s the series resistance. In the case of the MCLEDs described in this thesis the regime with $n_{\text{ideal}} = 1$ is masked by the effect of the series resistance R_s which dominates at high voltages and causes the I–V characteristic to become linear.

Solving equation (3.16) for V yields

$$V = R_s I + \frac{n_{\text{ideal}} k T}{e} \ln \left(\frac{I}{I_0} + 1 \right) \quad (3.17)$$

This expression allows to fit $V(I)$ in order to determine the parameters R_s , I_0 and n_{ideal} at low biases. The fit parameters for 200 μm MCLEDs from the different samples are depicted in table 3.14. Figures 3.28–3.29 show the corresponding graphs. The model describes well the rise at low biases but differs from the measurements at voltages exceeding turn-on, where the curve is governed by the series resistance. This deviation is related to the fact that the I–V curves have been recorded by 2-point probe measurements. This configuration is accurate at low bias but not at high bias, as the diode resistance falls below the internal resistance of the ampere meter. In that regime the voltage drop over the diode and the ampere meter is measured, which results in a more pronounced roll-over at high voltage levels. In order to measure the voltage drop over

Table 3.14: Fit parameters I–V characteristic for 200 μm MCLEDs

Sample	R_s [Ω]	I_0 [A]	n_{ideal}
S1892 A	40	5.0×10^{-14}	1.90
S1892 B	40	1.0×10^{-15}	1.72
S1892 C2	200	5.0×10^{-15}	1.75

the diode only and determine the contact resistance correctly 4-point probe measurements would have to be carried out in addition. However this configuration has the disadvantage that at low voltage levels the current flows through the voltmeter connected in parallel. In addition the contacts might not be perfectly ohmic, which would mean that their I–V characteristic is not linear and hence would not correspond to the simulation.

The device without current confinement shows an ideality factor n_{ideal} of 1.9, whereas for the other two devices a slope between 1.7 and 1.75 was found. This implies that

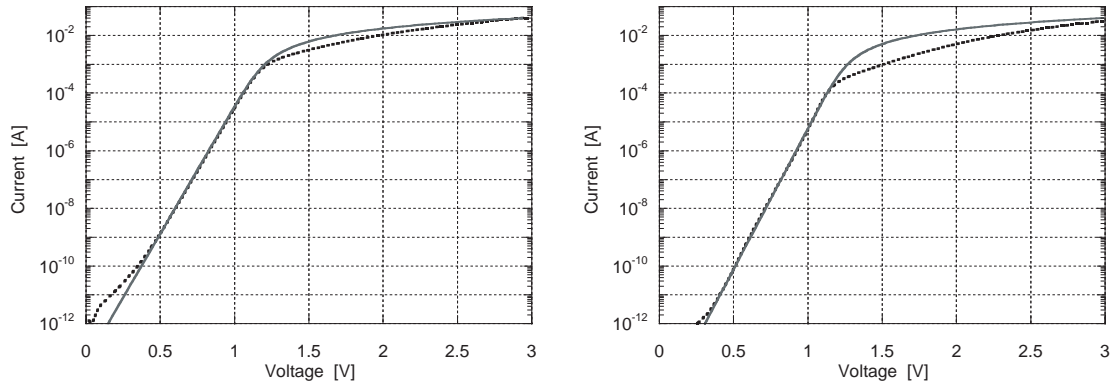


Figure 3.28: Comparison between measurement (dotted line) and simulation (solid line) of the I–V characteristic of a 200 μm MCLED without current confinement from sample S1892 A (left) and with recess etch from sample S1892 B (right)

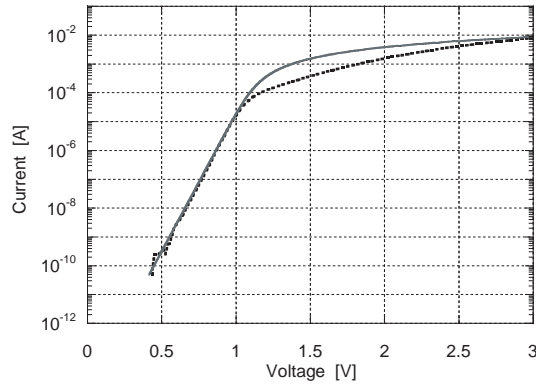


Figure 3.29: Comparison between measurement (dotted line) and simulation (solid line) of the I–V characteristic of a 200 μm MCLED with oxide aperture from sample S1892 C2 (left)

the relative amount of non-radiative recombination in this voltage range is reduced by confining the current laterally. Henry et al. [46,47] showed that the current contribution with $n_{\text{ideal}} = 2$ is mainly due to surface recombination. Hence a decrease in the ideality factor can be explained by a reduced current spreading to and reduced surface recombination at the mesa sidewalls.

3.6.2 External Quantum Efficiency vs. Drive Current Density

In section 2.5.2 the generation and recombination mechanisms in an active region are described, neglecting photon recycling. The equilibrium under steady-state conditions was found to be

$$\frac{\eta_{\text{inj}} I}{e V_{qw}} = R_{sp} + R_{nr} + R_l \quad (3.18)$$

which leads to the following expression for the radiative efficiency

$$\eta_{\text{rad}} = \frac{B n^2}{B n^2 + A n + R_l} \quad (3.19)$$

For the following derivation the injection efficiency η_{inj} is assumed to be 100 %, in which case the internal quantum efficiency η_{int} is equal to the radiative efficiency. In order to express the internal quantum efficiency as a function of current density equation (3.18) can be transformed to

$$\frac{J}{e t_{qw}} = B n^2 + A n + R_l \quad (3.20)$$

If the carrier leakage is assumed to be negligible ($R_l \approx 0$) this quadratic expression can be solved for n and inserted in equation (3.19), which gives

$$\eta_{\text{int}}(J) = 1 + \frac{J_0}{J} \left(1 - \sqrt{1 + \frac{2J}{J_0}} \right) \quad (3.21)$$

with

$$J_0 = \frac{e t_{qw}}{2} \frac{A^2}{B} \quad (3.22)$$

At high carrier densities the function (3.21) saturates to one since the radiative recombination rate $\propto n^2$ dominates. The smaller J_0 , the faster $\eta_{\text{int}}(J)$ converges to one. The radiative recombination coefficient B can be assumed to be constant for a certain material system, whereas A , the non-radiative recombination coefficient, depends on the device geometry, since it includes surface and interface recombination as shown previously. Hence by determining J_0 for different device types the relative extent of A can be compared.

The roll-over of the efficiency at high current densities can have numerous origins. Carrier spill-over and current crowding can lead to a reduced injection efficiency. The extraction efficiency is decreased by a spectral broadening of the emission spectrum, a shift of the detuning caused by Joule heating, or at very high current densities due to the occurrence of lateral in-plane gain. This behavior can be described with the

following empirical function $\eta_{\text{sat}}(J)$ which corresponds to the product of the injection efficiency η_{inj} and the extraction efficiency η_{extr}

$$\eta_{\text{sat}}(J) = \eta_{\text{inj}}(J)\eta_{\text{extr}}(J) = \frac{1}{1 + \frac{J}{J_{\text{sat}}}} \quad (3.23)$$

where J_{sat} corresponds to a phenomenological saturation current density. The higher J_{sat} , the slower the function decreases. Thus the model expression for the external quantum efficiency $\eta_{\text{ext}}(J)$ corresponds to

$$\eta_{\text{ext}}(J) = \eta_{\text{int}}(J)\eta_{\text{sat}}(J) = \frac{\eta_0}{1 + \frac{J}{J_{\text{sat}}}} \left[1 + \frac{J_0}{J} \left(1 - \sqrt{1 + \frac{2J}{J_0}} \right) \right] \quad (3.24)$$

where η_0 is a fitting parameter which, ideally, should be equal to the theoretically calculated extraction efficiency as given by table 3.2.

The measured external quantum efficiency versus drive current density curves of 200 μm MCLEDs from the different samples have been fitted with expression (3.24). As

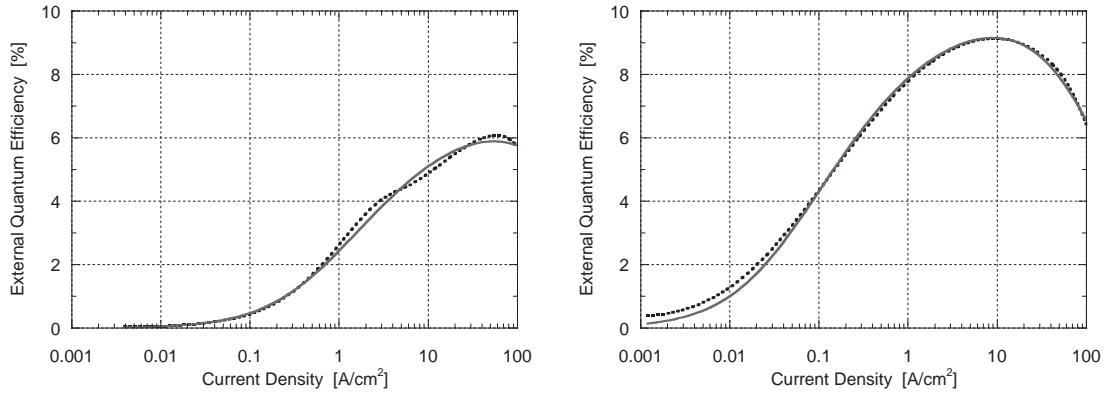


Figure 3.30: Comparison between measurement (dotted line) and simulation (solid line) of the external quantum efficiency vs. drive current density of a 200 μm MCLED without current confinement from sample S1892 A (left) and with recess etch from sample S1892 B (right)

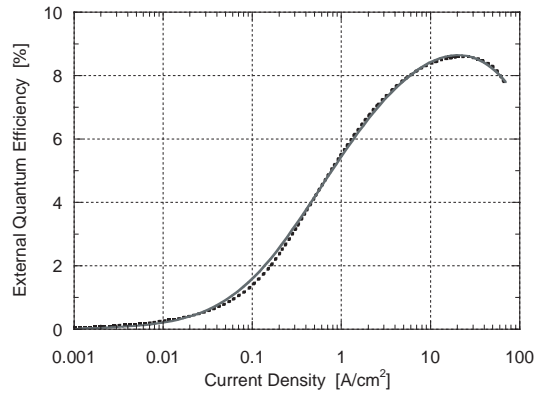


Figure 3.31: Comparison between measurement (dotted line) and simulation (solid line) of the external quantum efficiency vs. drive current density of a 200 μm MCLED with oxide aperture from sample S1892 C2

Table 3.15: Fit parameters external quantum efficiency versus drive current density for 200 μm MCLEDs

Sample	η_0 [%]	J_{sat} [A/cm ²]	J_0 [A/cm ²]	A [s ⁻¹]
S1892 A	8	620	0.71	3.4×10^7
S1892 B	11	170	0.04	8.5×10^6
S1892 C2	11	240	0.25	2.0×10^7

can be seen in figures 3.30–3.31 this simple model fits the measurements surprisingly well. The fit parameters are summarized in table 3.15. Assuming a radiative recombination coefficient B of $10^{-10} \text{ cm}^3/\text{s}$, the non-radiative recombination coefficient A can be estimated. The deduced values of A are added to table 3.15. Obviously the surface recombination at the mesa sidewalls and hence the values of J_0 and A can be significantly reduced with the incorporation of a recess etch. The oxide aperture improves the device performance as well, but the effect is smaller than for the recess etch.

Taking into account the dependence of A on the device diameter due to surface recombination (see equation (2.35) in section 2.5.2) the size dependence of J_0 can be described as

$$J_0 = \frac{et_{qw}}{2} \frac{A_0^2}{B} \left[1 + \frac{4\nu_s}{A_0 d} \right]^2 \quad (3.25)$$

Thus from the plot of the values for J_0 against the inverse device diameter estimates of the non-radiative recombination rate due to deep-level defect and impurity recombination A_0 and of the surface and interface recombination velocity can be found. The values for the devices without current confinement could not be fitted, the results for the devices with recess etch and oxide aperture are shown in table 3.16. Again a value of $10^{-10} \text{ cm}^3/\text{s}$ was assumed for B . The values of the 400 μm diameter devices have not been considered for this estimation.

Table 3.16: Fit parameters J_0 versus device diameter

Sample	$\frac{et_{qw}}{2} \frac{A_0^2}{B}$ [A/cm ²]	$\frac{\nu_s}{A_0}$ [μm]	A_0 [s ⁻¹]	ν_s [cm/s]
S1892 A	-	-	-	-
S1892 B	0.034	4.9	7.5×10^6	3.7×10^3
S1892 C2	0.020	102	5.8×10^6	5.9×10^4

Forming an oxide aperture apparently leaves the value for A_0 unchanged, however the surface and interface recombination velocity is increased by an order of magnitude. The latter values are lower than previously published surface recombination velocities [48–50]. The value for sample S1892 C2 is close to the estimate of the oxide-semiconductor interface recombination velocity of $3 \times 10^4 \text{ cm/s}$ found by Kash et al. [210]. This implies that the formation of an oxide aperture leads to an increased interface re-

combination velocity and therefore an increased size dependence of A and ultimately to a reduction in external quantum efficiency compared to a recess etch.

High interface recombination rates at the oxide-semiconductor interface in the vicinity of an InGaAs quantum well have been observed in several photoluminescence studies [210–213]. Ochoa [102] already designated this effect as the main cause for the linear decrease of the internal quantum efficiency with device diameter observed for his MCLED structures. Kash et al. [210] demonstrated the beneficial effect of graded interface layers. By grading the aluminum content between the oxidation layer and the surrounding GaAs layers, the oxidation can be impeded from reaching the GaAs interface and the low interface recombination rate is preserved. This allows lower non-radiative recombination rates than for apertures formed by proton implantation, as the implantation process inevitably leads to the formation of defects. Oxide-confined vertical cavity surface emitting lasers (VCSELs) with record performances have been demonstrated [195]. In 1997 oxide-confined VCSELs showed the lowest threshold current [142] and threshold voltage [214] and the highest power conversion efficiency [215] and small-signal modulation bandwidth [216]. The structure presented in this thesis on the other hand does not contain a grading in aluminum content, which might be the reason for the difference in performance. Due to time constraints this comparison could not be repeated with a structure with an appropriate interface grading.

3.6.3 Current Spreading Estimation

A method has been defined to assess the current spreading quantitatively. Current spreading affects the L–I–V characteristics in different ways. On one hand it leads to an increased area of current flow, which can be noted by a shift of the J–V and $\eta_{\text{ext}}\text{--}J$ curves to higher current densities. This effect is more pronounced for smaller devices. In addition non-radiative recombination outside the cavity leads to a reduction in external quantum efficiency as these photons cannot be extracted on the substrate side. Again this reduction is more important for smaller device sizes.

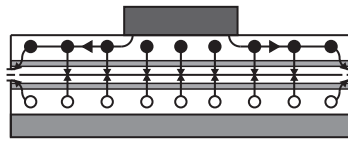


Figure 3.32: Schematic illustration of current spreading and surface recombination for a device without lateral current confinement

If the current spreads over the whole mesa and reaches the mesa sidewalls then both effects described above are aggravated by surface recombination at the mesa sidewalls. Surface recombination can be modelled as an additional current spreading, as it drains the regions close to the surface and causes an increased lateral current flow. Assuming again an injection efficiency of unity, the effect on the efficiency can be demonstrated by simplifying the expression for the internal quantum efficiency as a function of carrier density in the active region (3.19) to

$$\eta_{\text{int}} = \frac{1}{1 + \frac{A}{Bn}} \quad (3.26)$$

Hence the internal quantum efficiency scales inversely with the non-radiative recombination coefficient and decreases with decreasing device size, if surface recombination at the mesa sidewalls is the dominant non-radiative recombination mechanism.

Effect of Current Spreading on Current Density

The area of current flow is estimated by recalculating the current densities with an area larger than the p-contact surface:

$$S' = \pi(r_p + \Delta r_{cs})^2 \quad (3.27)$$

where S' is the apparent device area, r_p the p-contact radius and Δr_{cs} the increase in radius due to the current spreading. As the difference in radius between the mesa and the p-contact is similar for all device sizes (see table 3.6), Δr_{cs} is assumed to be independent of device size. The value that leads to the best match of the apparent current densities for the different device sizes is determined by the least square method.

$$J_1 \left(\frac{S_1}{S'_1} \right) = J_2 \left(\frac{S_2}{S'_2} \right) \quad (3.28)$$

This is done for the current densities at maximum efficiency and for the J–V curves at a voltage of 0.7 V. Since at low bias the diode resistance is much more important compared to the resistivity of the p-doped layers the current spreading is expected to be more pronounced than at higher current levels. The values of the 400 μm diameter devices have been excluded from the normalization of the current densities at maximum efficiency as the roll-over seems to be governed by another mechanism than for the smaller devices. This is evident from the different slope of the efficiency decrease after the roll-over in figures 3.20–3.22. It is presumed that for the largest devices the efficiency is limited by the onset of lateral in-plane gain, whereas for smaller devices the roll-over is rather caused by spectral broadening and current crowding. Table 3.17 shows the values found for the different device types.

Table 3.17: Current spreading estimation by current density normalization

Sample	Δr_{cs}	
	$\eta_{\text{ext,max}}$ [μm]	0.7 V [μm]
S1892 A	79	207
S1892 B	9	2
S1892 C2	39	25

The large values of Δr_{cs} found for the devices without current confinement indicate that surface recombination significantly affects the performance of these devices. The recess etch seems to confine the current very well, whereas the oxide aperture is not as effective.

Effect of Current Spreading on Maximum Efficiency

The decrease of the external quantum efficiency with decreasing device size seems to be dominated by the increasing fraction of radiative recombination outside the cavity region due to a relative increase in current spreading. The maximum external quantum efficiencies for the different device sizes are normalized assuming a repartition of the current between the cavity area and the mesa area outside the cavity depending on the amount of current spreading. This translates to a weighting of the efficiency between the efficiency inside and outside the cavity (η_{in} and η_{out} , respectively). These two values are assumed to be constant, as well as Δr_{cs} . Again the efficiencies of the 400 μm diameter devices have been excluded from the normalization. The maximum external efficiency as a function of device size and current spreading can therefore be described as

$$\eta_{\text{ext},i} = \eta_{\text{in}} \frac{S_{\text{in},i}}{S_{\text{tot},i}} + \eta_{\text{out}} \frac{S_{\text{out},i}}{S_{\text{tot},i}} \quad (3.29)$$

Outside the cavity the top mirror is missing but the bottom DBR is reflecting the light to the top. Therefore the bottom emission in this area is zero and $\eta_{\text{out}} = 0$. Thus the expression for the maximum external quantum efficiency becomes

$$\eta_{\text{ext},i} = \eta_{\text{in}} \frac{r_{p,i}^2}{(r_{p,i} + \Delta r_{cs})^2} \quad (3.30)$$

As the efficiency inside the cavity η_{in} is assumed to be independent of device size, Δr_{cs} can be determined by solving equation (3.30) for η_{in} and matching the values for the different device sizes with the least-square method.

$$\eta_{\text{in}} = \eta_{\text{ext},i} \frac{(r_{p,i} + \Delta r_{cs})^2}{r_{p,i}^2} = \text{constant} \quad (3.31)$$

The results are shown in table 3.18. They show the same trend as the estimates for the apparent current density at maximum efficiency in table 3.17, a significant current spreading for the devices with no confinement, nearly no current spreading in presence of a recess etch and a reduced improvement with the oxide aperture.

Table 3.18: Current spreading estimation by maximum efficiency normalization

Sample	Δr_{cs} [μm]
S1892 A	16
S1892 B	3
S1892 C2	7

Figures 3.33–3.35 show the normalized curves for the three different kind of structures. As the values of the 400 μm diameter devices have been excluded from the maximum efficiency normalization and from the current density at maximum efficiency normalization their normalized values do not match with the others.

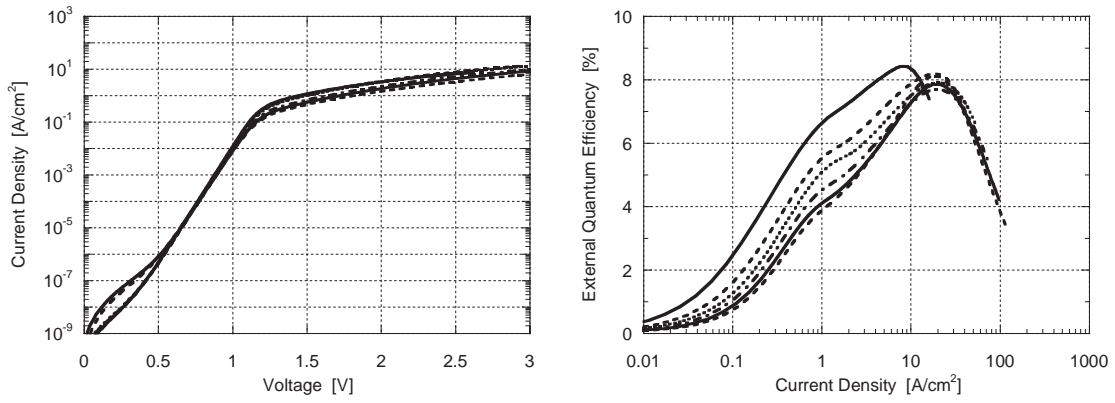


Figure 3.33: Normalized J–V characteristic and normalized external quantum efficiency vs. normalized drive current density of MCLEDs from sample S1892 A; diameters 400, 200, 150, 100, 70 and 50 μm (solid, dashed, dotted, dash-dot, solid and dashed line)

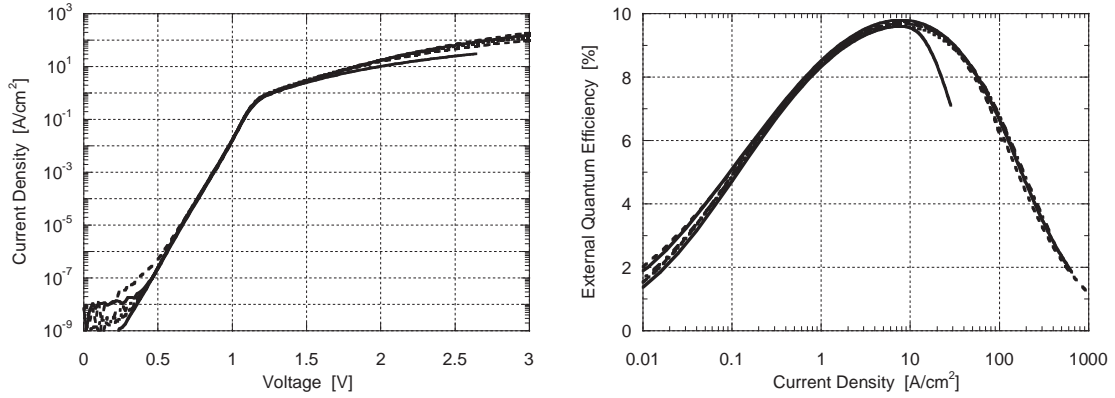


Figure 3.34: Normalized J–V characteristic and normalized external quantum efficiency vs. normalized drive current density of MCLEDs from sample S1892 B; diameters 400, 200, 150, 100, 70 and 50 μm (solid, dashed, dotted, dash-dot, solid and dashed line)

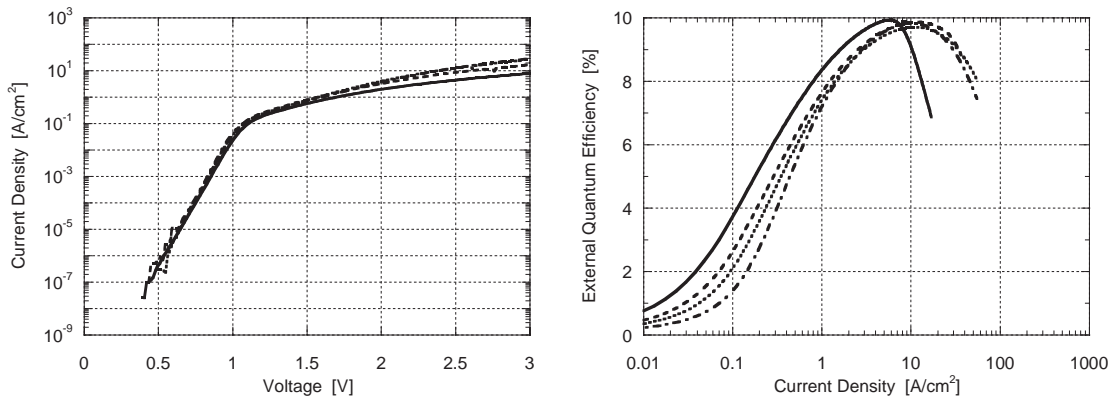


Figure 3.35: Normalized J–V characteristic and normalized external quantum efficiency vs. normalized drive current density of MCLEDs from sample S1892 C2; diameters 400, 200, 100 and 50 μm (solid, dashed, dotted and dash-dot line)

3.6.4 Maximum Efficiency after Back–End Processing

The values after back–end processing of the MCLEDs with recess etch demonstrate that with this type of devices external quantum efficiencies of 18 % for emission into air and 24 % for emission into glycerol can be achieved at very low current densities of about 10 A/cm². Apart from the 23 % external quantum efficiency reported for large area devices (contact diameter 1.5 mm) by Blondelle et al. [118], these 18 % represent the highest external quantum efficiency for emission into air ever presented for bottom emitting MCLEDs. So far the record value published for smaller devices is 17 % from the same group for the same device type but a diameter of only 85 μm [118]. The increase of efficiency with device size is ascribed to photon recycling in the large area devices [117].

With a further optimization of the device type presented in this work, especially the substrate thinning and the ARC deposition, efficiencies above 20 % for emission into air and 30 % for emission into epoxy should be achievable for small devices. Simulations for the structure with a proper anti-reflection coating show maximum efficiencies of 24 and 36 % for emission into air and epoxy, respectively.

3.7 Conclusions

Bottom emitting near infrared MCLEDs with record efficiencies for small devices have been fabricated. The structure incorporates a phase-shift cavity, a top gold mirror, which is used at the same time as top contact and a bottom DBR with a weak reflectivity. Electrons are injected laterally via an n-intracavity contact and the holes are injected through the top contact. The current is confined laterally by a recess etch on the top p-side. Large devices with an oxide aperture on the n-side show a similar performance, however in the present case this method is less effective for smaller devices due to the fact that the interfaces of the oxidation layer are not graded. With an interface grading the increase of the non-radiative interface recombination rate at the oxide-semiconductor interface could be avoided.

With this type of device including a recess etch on the p-side, a thinned substrate and an anti-reflection coating adapted for emission into air an external quantum efficiency of 18% for emission into air and 24% for emission into glycerol were achieved at a very low current density of 10 A/cm². Simulations show that with a further device optimization values above 20 % into air and 30 % into epoxy are possible. An oxide aperture with an appropriate interface grading should lead to similar device performances.

Chapter 4

Top Emitting MCLEDs at 970 nm

4.1 Introduction

Top emitting near infrared InGaAs/GaAs-based MCLEDs with a short $\lambda/8$ phase-shift cavity, as described in section 2.8.1, were fabricated and analyzed. All the structures feature an asymmetric cavity with a high reflectivity DBR as bottom reflector and the interface GaAs–air as top reflector. The bottom mirror consists either of an all semiconductor DBR or a semiconductor/oxide DBR. The first one typically contains GaAs/AlAs layer pairs, the second one GaAs/ AlO_x layer pairs. As demonstrated in section 2.8.2 and depicted for example by Nelson et al. [217], an oxide DBR shows a significantly higher refractive index contrast, which leads to a reduced penetration depth of the optical field and therefore a shorter effective cavity length. This means that higher extraction efficiencies can be achieved with this type of reflector. However, the implementation of an oxide DBR involves a more critical design and fabrication. This is related to the properties of the oxide. The shrinkage of the layers during the oxidation has to be taken in consideration. In addition the refractive index of the oxide is not known as precisely as for semiconductors.

Contrary to bottom emitting devices the substrate does not affect the emission for top emitting MCLEDs. Nevertheless the light extraction proves to be more challenging. The current has to be injected uniformly over the whole device surface but at the same time the shadowing of the emission by the top contact should be as small as possible. The standard top contact geometry is thus either simply a contact ring at the edge of the device or in addition a grid of thin metal wires evenly distributed over the device surface. On one hand a grid leads to a more homogeneous current injection, on the other hand the shadowing of the emitted light by the contact becomes more important as well. The two approaches will be compared for the different structures in this chapter.

The contact shadowing by the outer contact ring can be averted by limiting the emission to an area smaller than the contact aperture. This is achieved by confining the current either on the p-doped or on the n-doped side. Proton implantation, selective lateral oxidation or the introduction of air posts are the generally used current confinement techniques. The semiconductor DBR devices presented in this chapter contain oxide current apertures, the oxide DBR devices a recess on the top p-side.

4.2 Structures

The top emitting structures presented in this chapter were designed by Ross Stanley and grown by the author, under the supervision of Ursula Oesterle. They all contain a highly reflective bottom DBR. The phase-shift cavity contains a single $\text{In}_{0.16}\text{Ga}_{0.84}\text{As}$ quantum well and squeezed GRINSCH-like confinement regions. The concept of the phase-shift cavity is presented in detail in section 2.8.1. The top mirror consists either simply of the interface GaAs–air or has an additional DBR pair. The reflectivity of the bottom reflector is approximately 99 % in the normal direction. In case of the top reflector the values are 44 and 31 %, with and without a DBR pair, respectively.

Five different structures were grown by MBE, named S1904, S1905, S1907, S1908 and S1910. They differ in the composition of the bottom and the top mirror and are either optimized for emission into air or epoxy. The $\text{Al}_x\text{Ga}_{1-x}\text{As}$ layers are grown as digital alloys, called superlattices as well [195,218]. They consist of AlAs layers with GaAs layers sandwiched in between. The aluminum content is adjusted via the thickness ratio. Digital alloys are known to show similar optical and electrical properties as real alloys as well as a similar etching and oxidation behavior.

S1904 and S1910 are intended to be used with a GaAs/ $\text{Al}_{0.98}\text{Ga}_{0.02}\text{As}$ semiconductor bottom DBR; S1905, S1907 and S1908 on the other hand with a GaAs/ AlO_x semiconductor/oxide bottom DBR. Due to the small refractive index difference ($\Delta n = 0.55$) in the semiconductor DBRs a high number of pairs is necessary in order to achieve the desired reflectivity of 99 %. With an oxide DBR 3.5 DBR pairs are sufficient, as the index contrast between GaAs and AlO_x corresponds to 1.9 (details see section 2.7.2 and section 2.8.2).

Structures S1905, S1907 and S1910 are optimized for emission into air, S1904 and S1908 for emission into epoxy. The mirror compositions of the different structures are presented in table 4.1, the detailed structures can be found in appendix B. The top reflector of the structure S1904 contains an additional GaAs/ $\text{Al}_{0.98}\text{Ga}_{0.02}\text{As}$ pair, the one of the structures S1907 and S1908 includes a GaAs/ $\text{Al}_{0.90}\text{Ga}_{0.10}\text{As}$ pair. The structure S1908 comprises as well an extra GaAs/ $\text{Al}_{0.90}\text{Ga}_{0.10}\text{As}$ pair in the bottom DBR, on top of the oxide layers. The refractive index profiles of the different structures are displayed in figures 4.1–4.3.

Table 4.1: Mirror composition top emitting MCLED structures emitting at 980 nm

Structure	Bottom DBR			Top DBR		
	pairs	n_h	n_l	pairs	n_h	n_l
S1904	16.5	GaAs	$\text{Al}_{0.98}\text{Ga}_{0.02}\text{As}$	1	GaAs	$\text{Al}_{0.98}\text{Ga}_{0.02}\text{As}$
S1910	15.5	GaAs	$\text{Al}_{0.98}\text{Ga}_{0.02}\text{As}$	0	GaAs	air
S1905	3.5	GaAs	AlO_x	0	GaAs	air
S1907	3.5	GaAs	AlO_x	1	GaAs	$\text{Al}_{0.90}\text{Ga}_{0.10}\text{As}$
S1908	3.5	GaAs	AlO_x	1	GaAs	$\text{Al}_{0.90}\text{Ga}_{0.10}\text{As}$
	+1	GaAs	$\text{Al}_{0.90}\text{Ga}_{0.10}\text{As}$			

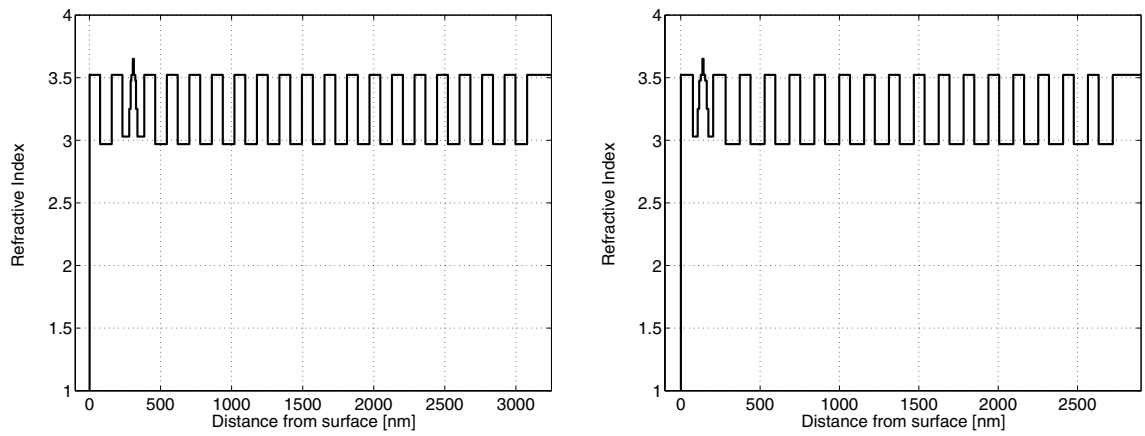


Figure 4.1: Refractive index profile of structure S1904 (left) and S1910 (right)

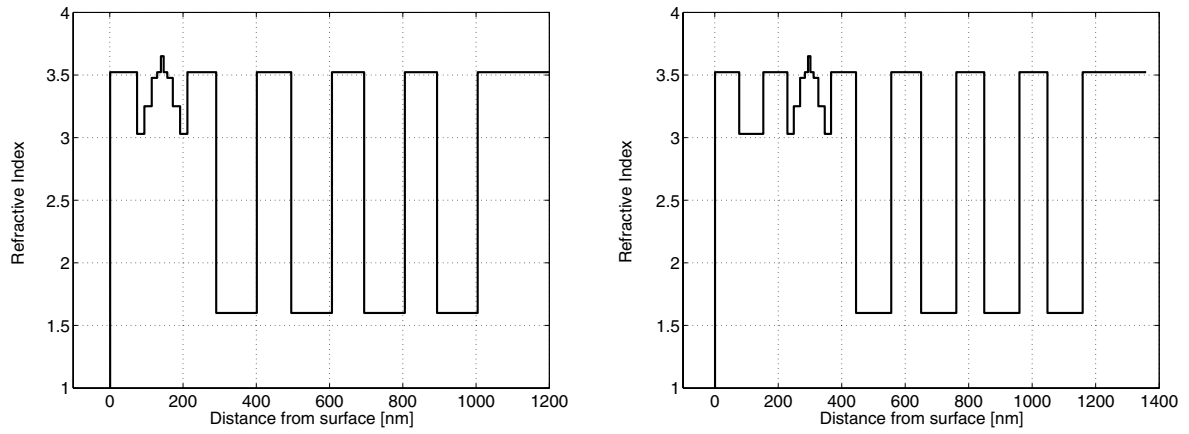


Figure 4.2: Refractive index profile of structure S1905 (left) and S1907 (right)

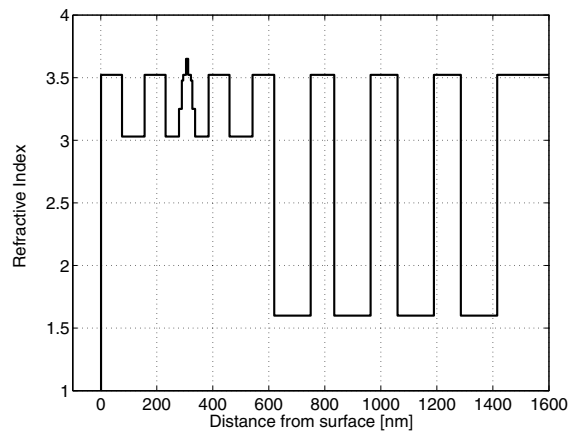


Figure 4.3: Refractive index profile of structure S1908

4.3 Simulation

The light extraction properties of the structure are calculated with the simulation program described in section 3.3. The calculation of the refractive index of AlGaAs is based on the data by Adachi [162]. The refractive index of AlO_x is assumed to be 1.6 over the whole wavelength range of interest [138–141] and the vertical contraction during the oxidation is estimated to be 8 % [219,140,141].

The extraction efficiencies of the different structures, calculated for monochromatic emission, can be found in figures 4.4–4.6 as a function of wavelength. The QW emission spectrum used for the integration is displayed in every figure as well. It can be seen that for the structures optimized for emission into air the maximum extraction efficiency into air is centered around the peak of the intrinsic emission. The structures for emission into epoxy on the other hand have a larger detuning, which means an increased cavity length. Therefore the peak for emission into air is red-shifted with respect to the intrinsic emission, but the emission into epoxy is centered on the intrinsic emission peak. This explains why structures optimized for emission into epoxy show low extraction efficiencies for emission into air.

Tables 4.2 and 4.3 show the distribution of the emission in the various modes for the different structures at 970 nm, for emission into air and epoxy, respectively. Note that the guided mode fractions are significantly higher with the use of an oxide DBR. The internal angular emission profiles at 970nm of structures S1910 and S1905 are compared in figure 4.7.

Table 4.2: Fractions of emission in the various kinds of modes for the different structures at 970 nm and for emission into air

	extracted [%]	leaky [%]	guided [%]
S1904	8	78	14
S1910	28	56	15
S1905	31	25	43
S1907	34	21	45
S1908	18	52	29

Table 4.3: Fractions of emission in the various kinds of modes for the different structures at 970 nm and for emission into epoxy

	extracted [%]	leaky [%]	guided [%]
S1904	35	52	11
S1910	32	50	17
S1905	33	21	44
S1907	35	17	46
S1908	39	30	29

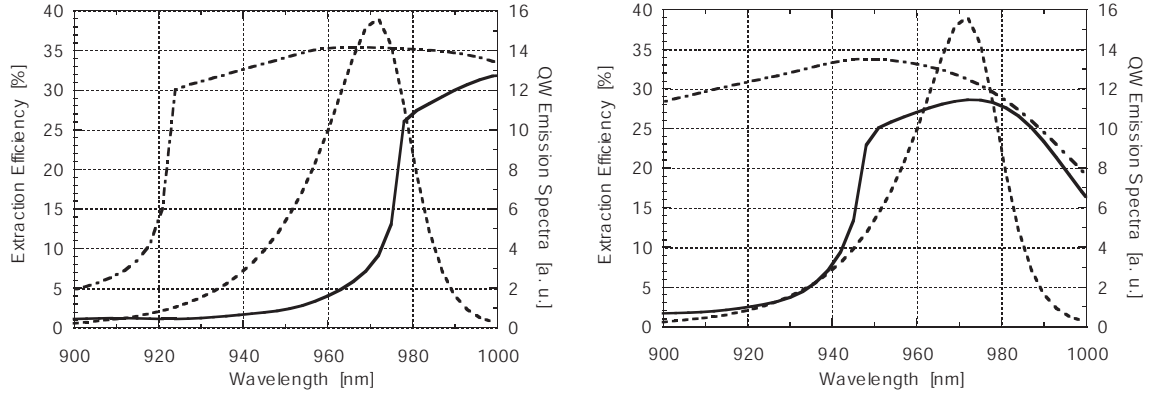


Figure 4.4: Simulated extraction efficiency for structure S1904 (left) and S1910 (right); emission into air (solid line) and epoxy (dash-dot line) plus intrinsic emission spectrum (dashed line)

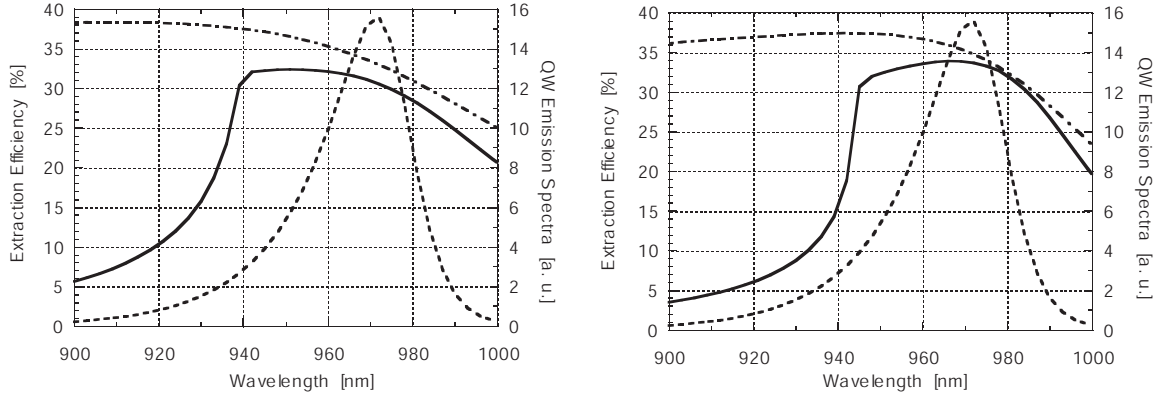


Figure 4.5: Simulated extraction efficiency for structure S1905 (left) and S1907 (right); emission into air (solid line) and epoxy (dash-dot line) plus intrinsic emission spectrum (dashed line)

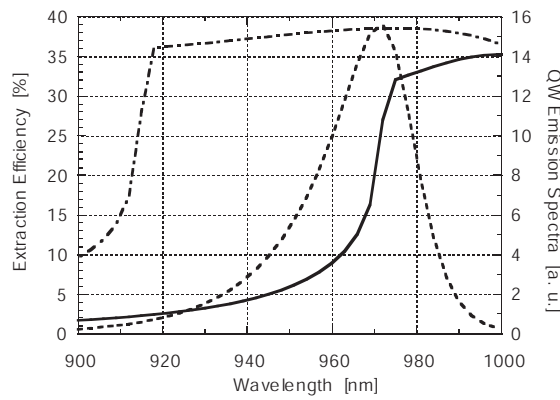


Figure 4.6: Simulated extraction efficiency for structure S1908; emission into air (solid line) and epoxy (dash-dot line) plus intrinsic emission spectrum (dashed line)

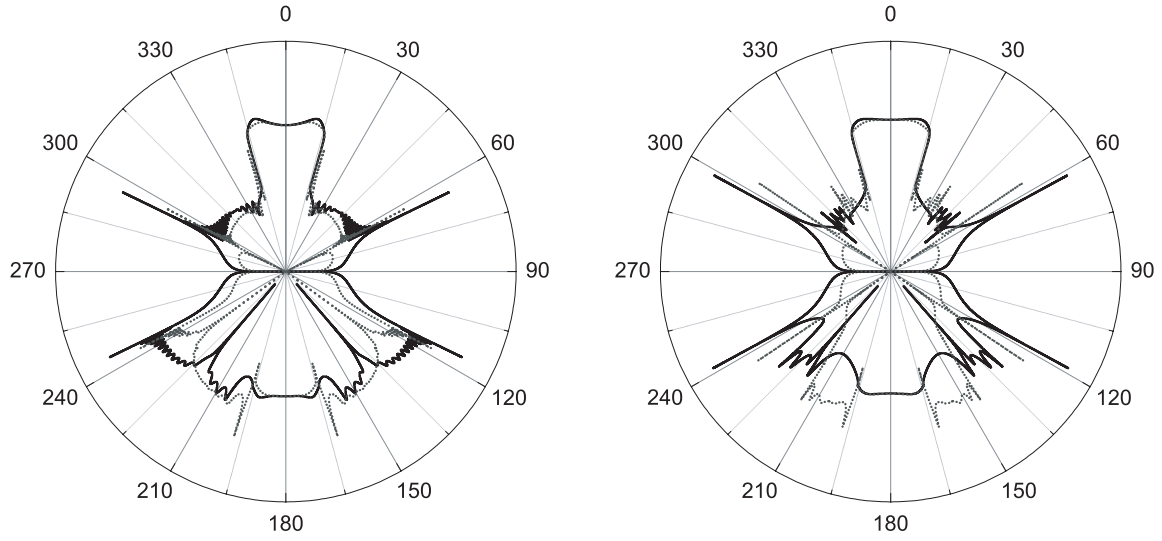


Figure 4.7: Simulated internal angular intensity profile (logarithmic intensity scale) at 970 nm for emission into air for structure S1910 (left) and S1905 (right); TE polarization (solid line) and TM polarization (dotted line)

The external quantum efficiencies attained by integration of the extraction efficiency spectrum with the QW electroluminescence spectrum are listed in table 4.4.

Table 4.4: Theoretical external quantum efficiencies TE MCLEDs emitting at 970 nm

Structure	$\eta_{\text{ext}}(\text{air})$ [%]	$\eta_{\text{ext}}(\text{epoxy})$ [%]
S1904	10	34
S1910	24	31
S1905	29	34
S1907	30	35
S1908	18	38

The simulations of the reflectivity spectra as well as the angular and spectral emission properties of the different structures are shown in section 4.5 together with the measurement results.

4.4 Fabrication

The main part of the device processing is the same as for the fabrication of bottom emitting near infrared MCLEDs: mesa definition, contact deposition and current confinement. For top emitting devices a dielectric coating and large contact pads need to be deposited in addition in order to be able to contact the thin p-contact ring. Polyimide is used as a dielectric. It has a low dielectric constant of 3.5 and can be easily applied via spin-coating. The patterning is done by etching it directly with the photoresist developer. In case of the oxide DBR structures the p-contact was deposited directly on the dielectric and therefore no additional step for the contact pad deposition was necessary.

The fabrication of the oxide DBR devices includes in addition the oxidation of the bottom DBR. Prior to the selective lateral wet oxidation of the high aluminum content bottom DBR layers they need to be exposed by etching deep trenches around the emission area.

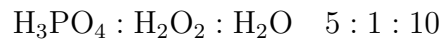
In case of the semiconductor DBR devices the injected current is confined laterally by oxide apertures. S1910 contains an oxide aperture on the n-side, S1904 an oxide aperture on each side of the quantum well. The layers are selectively oxidized after having been uncovered during the mesa etching. The oxide DBR device fabrication includes a recess etch of the top p-doped layers (down to the top p-Al_{0.90}Ga_{0.10}As GRINSCH layer) for current confinement.

Since the fabrication is different for the semiconductor DBR structures and the oxide DBR structures different mask sets are used for the two types. The semiconductor DBR devices have a square geometry with emission aperture diameters ranging from 50 to 400 μm . The oxide DBR devices are circular with diameters varying between 50 and 350 μm . Detailed mask set illustrations can be found in appendix C.

4.4.1 Etching

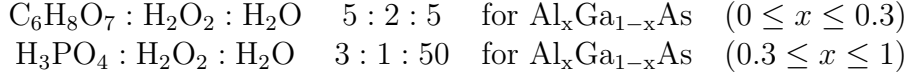
Non-Selective Wet Oxidation Trench Etch

The trenches for the exposure of the high Al-content layers in the bottom DBR for lateral oxidation are etched with a concentrated phosphoric acid (H₃PO₄) solution. This etchant is nonselective between GaAs and AlAs, it shows a high etch rate of approximately 1 $\mu\text{m}/\text{min}$ and provides well defined profiles with a limited underetch rate [173,220]. 10 ml H₃PO₄ (ortho-phosphoric acid, 85 w/o) and 2 ml H₂O₂ (30 w/o) are added to 20 ml DI H₂O.



Selective Wet Mesa Etch

For the definition of the mesas and the uncovering of the n-contact layer the selective wet etch system presented in section 3.4.3 is used. The low aluminum content Al_xGa_{1-x}As layers are selectively etched with a citric acid (C₆H₈O₇) solution and the high Al-content layers with a diluted phosphoric acid (H₃PO₄) solution.



The citric acid solution is prepared by dissolution of 25 g of anhydrous citric acid in DI H₂O and stirring it for one hour. Just before etching 9 ml of H₂O₂ (30 w/o) are added. The phosphoric acid solution consists of 100 ml DI H₂O, 6 ml H₃PO₄ (ortho-phosphoric acid, 85 w/o) and 2 ml H₂O₂ (30 w/o).

Selective Wet Recess Etch

The removal of the top p-doped AlGaAs layers is accomplished with the same selective solutions as for the mesa etching.

4.4.2 Lateral Oxidation

Dallesasse et al. discovered in 1990 that the wet oxidation of high Al-content AlGaAs layers at elevated temperatures produces a mechanically stable oxide [136,137]. It shows good insulating properties and a low refractive index of approximately 1.6 [138–141]. The microstructure of this oxide was found to be an amorphous solid solution of (Al_xGa_{1-x})₂O₃ [221]. Since the oxide has a more dense crystal lattice the AlGaAs layers contract in thickness during the oxidation. This can cause significant stresses, especially at the oxidation front, and can even lead to delamination of parts of the structure. However this problem could be diminished by using high Al-content AlGaAs instead of AlAs and by grading the Al-content at the interfaces [222–224].

The aluminum oxide (AlO_x) has been introduced successfully in vertical cavity surface emitting lasers (VCSELs) as buried oxide aperture for efficient electrical and optical confinement, which leads to decreased threshold currents and voltages [225]. The oxide is used as well to fabricate high index contrast DBRs composed of GaAs/AlO_x layer stacks [139,142]. These oxide-based DBRs exhibit a high reflectivity and a wide bandwidth from only a few pairs (see section 2.8.2).

The principle is the following: The high Al-content layers are exposed to water vapor transported in an inert gas within an elevated temperature environment (350 – 500 °C). The vapor is supplied by bubbling nitrogen gas through a flask of deionized water, which is immersed within a constant temperature bath of silicon oil maintained at 84 °C. The gas is then directed through heated tubes into the 2-in-diameter quartz tube furnace. The furnace is kept at the desired oxidation temperature and the tubes are heated to 150 °C to avoid condensation. The sample is placed in a quartz boat, which is maneuvered on quartz rails.

As for the oxidation of silicon, the time dependence of the oxidation depth d_{ox} can be expressed as [226]

$$d_{ox}^2 + Ad_{ox} = Bt \quad (4.1)$$

B depends on the diffusion constant of the reactants and B/A on the interfacial reaction rate. The temperature dependence of the oxidation rate follows an Arrhenius law. It varies strongly with the gas flow rate, the bath temperature and the oven temperature. A careful control of these parameters is necessary in order to guarantee a stable and

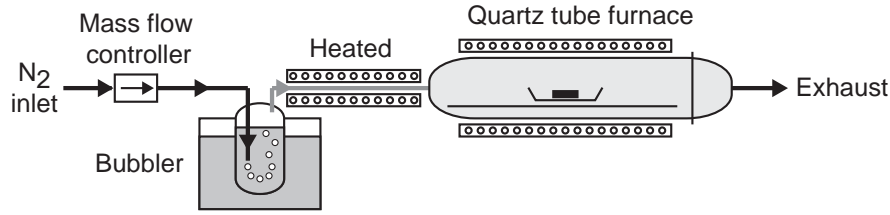
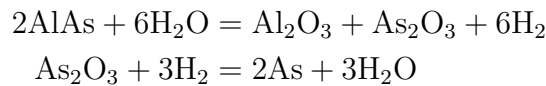


Figure 4.8: Schematic diagram oxidation system

reproducible oxidation process. In addition the oxidation rate strongly depends on the aluminum content and is therefore highly selective for high Al-content layers. Down to a minimal thickness the rate is independent of the layer thickness, below that value it rapidly decreases with decreasing thickness. Overviews on the oxidation process have been presented by Choquette et al. [221], Geib et al. [227], and Brunner [228].

Raman spectroscopy measurements revealed the presence of arsenic oxide (As_2O_3) and arsenic (As) as intermediates in the wet oxidation process [229,230]. The following mechanism has therefore been proposed:



The reactions are thermodynamically favorable at room temperature (negative Gibbs free energy). Replacing Al with $\text{Al}_x\text{Ga}_{1-x}\text{As}$ will make the first reaction less favorable since the Gibbs free energy of the first reaction with GaAs is slightly positive. The As could be removed from the oxidized film either as gaseous As or as arsine (As_2H_3).

The vertical contraction during oxidation depends on the Al-content, experimentally determined values are 12 – 13 % for AlAs [231] and 6.7 % for $\text{Al}_{0.92}\text{Ga}_{0.08}\text{As}$ [232]. By using $\text{Al}_{0.98}\text{Ga}_{0.02}\text{As}$ layers together with a linear grading of the Al-content at the interfaces the induced strain can be drastically reduced. This significantly reduces the risk of delamination during subsequent annealing steps. GaAs/AlAs digital alloys commonly used during MBE growth show similar oxidation rates and stabilities compared to $\text{Al}_x\text{Ga}_{1-x}\text{As}$ layers of the same concentration [233].

After having determined the optimal oxidation time for achieving the desired oxidation depth, the corresponding layers are exposed by etching and should then be oxidized immediately, in order to avoid the formation of a native oxide layer at the surface, which might inhibit the oxidation process.

When mirror layers are oxidized over long distances, the parasitic oxidation of lower Al-content layers has to be taken into consideration, even if their oxidation rate is several orders of magnitude lower. This can limit the maximum possible mirror oxidation time.

4.4.3 Fabrication Semiconductor DBR Devices

The main processing steps are:

- Mesa Etch
- Lateral Oxidation of Current Confinement Layer
- N-Contact Deposition
- P-Contact Deposition
- Dielectric Coating
- Contact Pad Deposition

The different steps are described in detail below and are illustrated with schematic cross-sections and top views in figures 4.9–4.15. In order to study the influence of the p-contact composition on the device characteristics, the structures S1904 and S1910 were processed in two different ways. The samples labelled *S1904 na* and *S1910 na* have a non-alloyed gold (Au) p-contact, the ones labelled *S1904 a* and *S1910 a* an alloyed Ti/Pt/Au contact. The first part of the processing is exactly the same for both types as they were processed as one piece. Before the p-contact deposition the samples were cleaved in half and then processed separately. However after the alloying step for the devices with alloyed contacts the same steps were carried out on both sample types.

Gold is the standard contact material for bottom emitting devices and has shown reasonable contact resistivities. Alloyed Ti/Pt/Au contacts to p-GaAs are known to show ohmic behavior and low specific contact resistances [234–237]. The titanium (Ti) acts as adhesion layer and the platinum (Pt) as diffusion barrier. Auger electron spectroscopy results showed that no metal intermixing takes place with Ti/Pt/Au contacts, whereas in the absence of a diffusion barrier Au is known to diffuse into the semiconductor and form deep spikes several 100 nm deep [237].

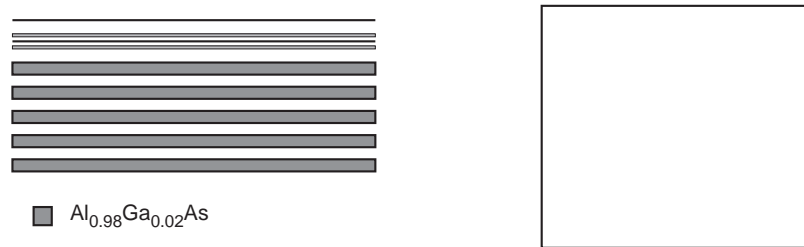


Figure 4.9: Schematic layer structure after growth

Mesa Etch

- i. Surface cleaning
- ii. Lithography
- iii. Surface deoxidation with diluted HCl
- iv. Selective wet etching of square mesas of varying diameter; through cavity, down to n-GaAs intracavity contact layer. Citric acid solution for low Al-content layers and diluted phosphoric acid solution for high Al-content layers.

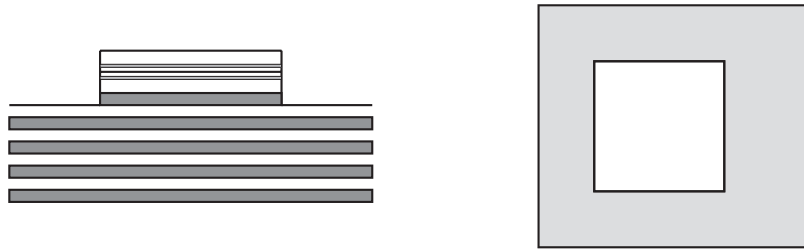


Figure 4.10: Mesa etch

Selective Lateral Oxidation

Lateral wet oxidation of exposed $\text{Al}_{0.98}\text{Ga}_{0.02}\text{As}$ layer(s) until the diameter of the oxide aperture is equal or slightly smaller than the inner diameter of the p-contact ring.

Table 4.5: Oxidation parameters S1904, S1910

Structure	Temperature [°C]	Time [min]	Oxidation depth [μm]
S1904	400	28	11
S1910	400	27	14

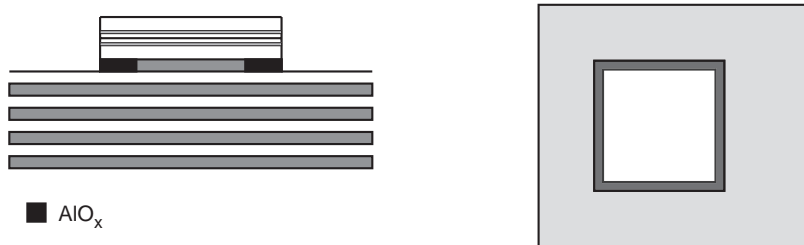


Figure 4.11: Lateral wet oxidation of current confinement layer

N-Contact Deposition

- i. Lithography
- ii. Surface deoxidation with diluted HCl
- iii. E-beam evaporation n-contact layer sequence:

Ni/Ge/Au/Ni/Au 10/25/50/20/100 nm

- iv. Lift-off in acetone
- v. N-contact alloying at 380 °C in forming gas atmosphere (ramps 5 °C/min)

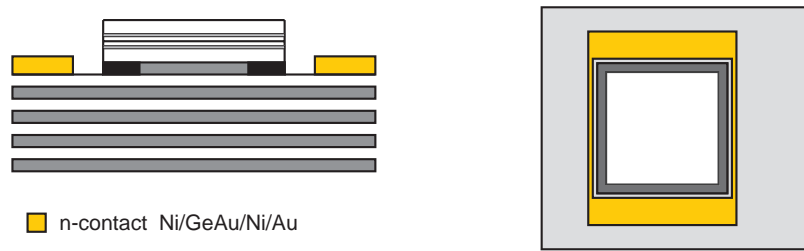


Figure 4.12: N-contact deposition

P-Contact Deposition

- i. Lithography
- ii. Surface deoxidation with diluted HCl
- iii. E-beam evaporation p-contact layer sequence:

S1904 na, S1910 na: Au 200 nm
S1904 a, S1910 a: Ti/Pt/Au 20/38/150 nm

- iv. Lift-off in acetone
- v. S1904 a and 1910 a only: p-contact alloying at 380 °C in forming gas atmosphere (ramps 5 °C/min)



Figure 4.13: P-contact deposition, shown without (left) and with grid (right)

Dielectric Coating

- i. Polyimide spinning (thickness $1\ \mu\text{m}$)
- ii. Polyimide soft bake
- iii. Lithography
- iv. Polyimide etching
- v. Polyimide curing at $250\ ^\circ\text{C}$ for 2 h in air (ramps $5\ ^\circ\text{C}/\text{min}$)

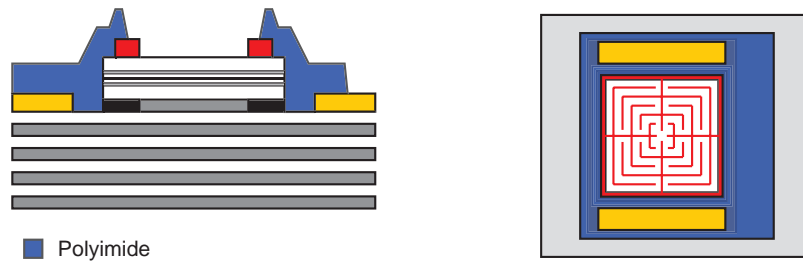


Figure 4.14: Dielectric coating with polyimide

Contact Pad Deposition

- i. Lithography
- ii. Surface deoxidation with diluted HCl
- iii. E-beam evaporation contact pad layer sequence: Ti/Au 10/250 nm
- iv. Lift-off in acetone
- v. No alloying

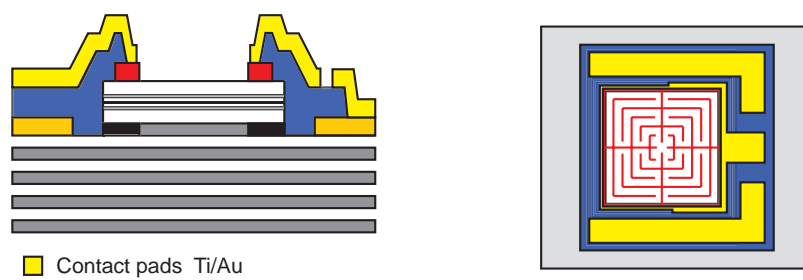


Figure 4.15: Contact pad deposition

Final Samples

Figures 4.16 and 4.17 show the different samples after processing. The pictures were taken after the samples have been measured, thus scratches from the prober needles are visible on the contact pads. Samples S1904 a and S1910 na show some signs of contact pad delamination, which appeared after the measurements. The pictures show 400 and 100 μm devices without and with a p-contact grid.

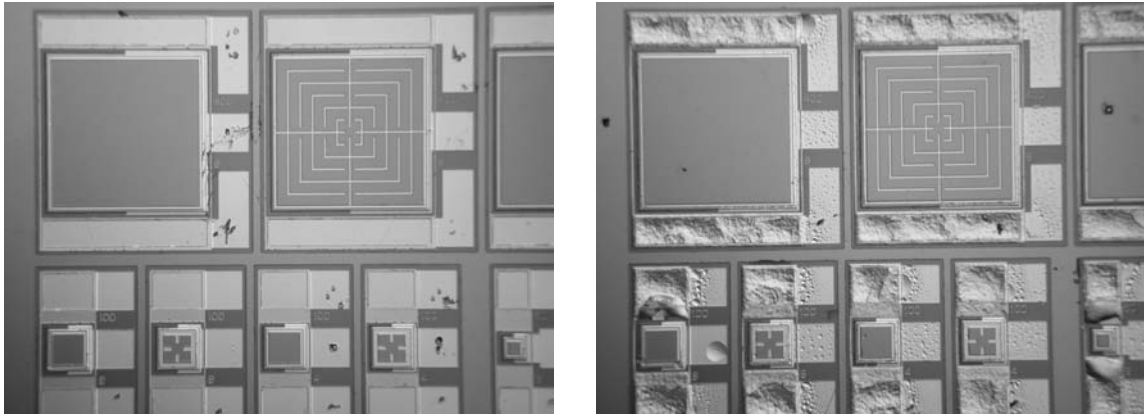


Figure 4.16: Samples S1904 na (left) and S1904 a (right); top row 400 μm devices, bottom row 100 μm devices, both without and with p-contact grid

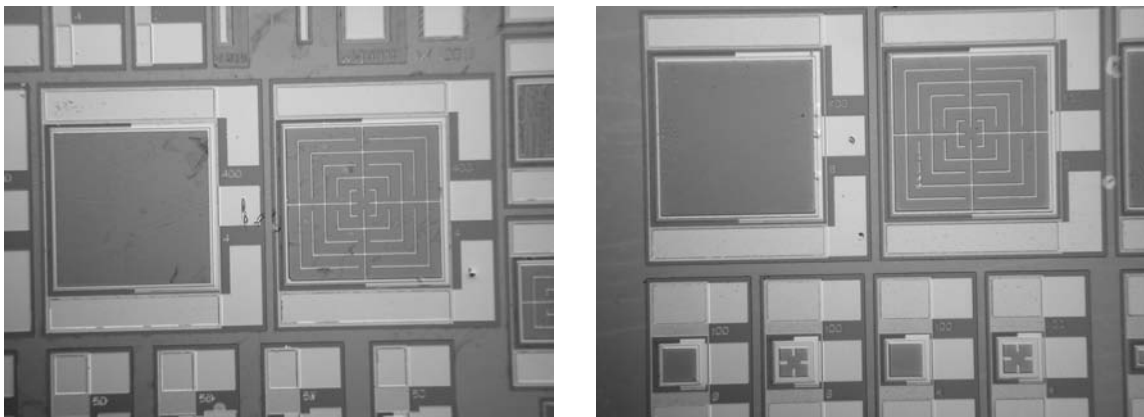


Figure 4.17: Samples S1910 na (left) and S1910 a (right); 400 μm devices without and with p-contact grid

4.4.4 Fabrication Oxide DBR Devices

The main processing steps are:

- Trench Etch for DBR Oxidation
- Lateral Oxidation of Low Index DBR Layers
- Mesa Etch
- Recess Etch
- N-Contact Deposition
- Dielectric Coating
- P-Contact Deposition

The different steps are described in detail below and are illustrated with schematic cross-sections and top views in figures 4.18–4.25. All three structures were processed several times. The first processing run of structure S1905, labelled *S1905 A*, was carried out by Maxime Rattier with a different mask set, and characterized by Ross Stanley. For the sake of completeness the fabrication and the external quantum efficiency results of this sample are listed as well. Four attempts were made to process the structures S1907 and S1908. The first one had to be aborted, since the surface was completely oxidized after the mirror oxidation. For the second one the oxidation time was reduced in order to alleviate the surface oxidation. This way working devices could be fabricated, but the samples, labelled *S1907 B* and *S1908 B*, show a varying density of circular dots on the surface. These defects seem to be oxidized spots with a hole in the middle, from which the oxidation started. Before the processing no defects were visible. Therefore a surface protection layer was deposited before the oxidation during the third run in order to protect the surface, very similar to the fabrication AlGaInP-based devices emitting at 650 nm presented in section 5.4. However, due to the strain introduced by the surface protection layer the whole structure delaminated during the oxidation. A fourth run was carried out with the shortest possible oxidation times to oxidize completely the 200 μm devices. These samples are labelled *S1907 D* and *S1908 D* and they show no surface oxidation at all. Together with these two samples the structure S1905 was processed once more, named *S1905 D*. Only the procedure for the successful processing runs B and D is described below.

Different p-contact compositions were chosen. In order to avoid additional stress caused by a second heat treatment after the mirror oxidation, the p-contacts were not alloyed. Sample S1905 A has a simple gold contact only. Since tests indicated that titanium is blocking the diffusion of gold similarly to platinum, a Ti/Au contact was used for samples S1907 B and S1908 B. For samples S1905D, S1907 D and S1908 D a non-alloyed Ti/Pt/Au contact was chosen [234,235]. Yet all samples have a standard alloyed Ni/Ge/Au/Ni/Au n-contact.

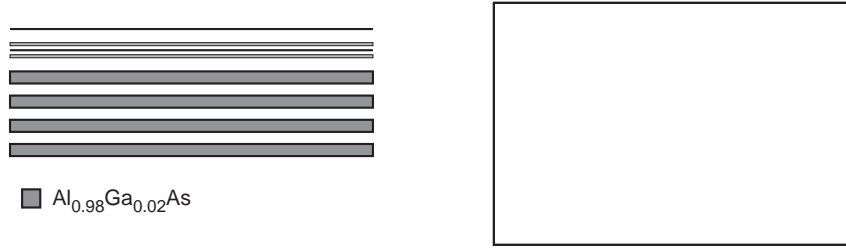


Figure 4.18: Schematic layer structure after growth

Trench Etch for DBR Oxidation

- i. Surface cleaning
- ii. Lithography
- iii. Surface deoxidation with diluted HCl
- iv. Non-selective wet etching of trenches with concentrated phosphoric acid solution

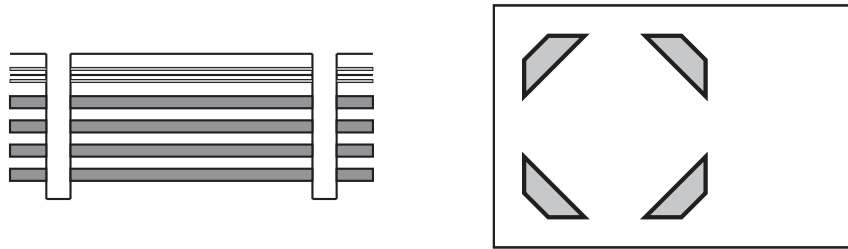


Figure 4.19: Trench etch for lateral oxidation of low index DBR layers

Lateral Oxidation of Low Index DBR Layers

The lateral wet oxidation of the exposed $\text{Al}_{0.98}\text{Ga}_{0.02}\text{As}$ layers in the bottom DBR was carried out until the DBR under the emission area was completely oxidized. The concomitant partial oxidation of the $\text{Al}_{0.90}\text{Ga}_{0.10}\text{As}$ GRINSCH layers is inevitable and needs to be limited to outside the emission area.

Table 4.6: Oxidation parameters oxide DBR samples

Sample	Temperature [°C]	Time [min]	Oxidation depth [μm]	Aperture 350 μm devices [μm]
S1905 A	450	120	250	completely oxidized
S1905 D	450	90	140	110 – 120
S1907 B	450	150	200	completely oxidized
S1907 D	450	105	170	50 – 70
S1908 B	450	136	200	completely oxidized
S1908 D	450	90	160	40 – 50

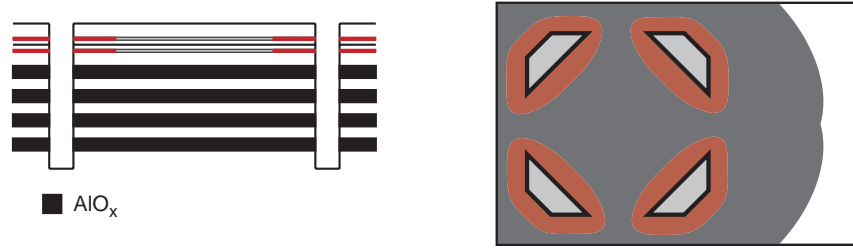


Figure 4.20: Lateral wet oxidation of low index DBR layers (parasitic oxidation of high Al-content GRINSCH layers schematically indicated in red)

Mesa Etch

- i. Lithography
- ii. Surface deoxidation with diluted HCl
- iii. Selective wet etching of circular mesas of varying diameter; through cavity, down to n-GaAs intracavity contact layer. Citric acid solution for low Al-content layers and diluted phosphoric acid solution for high Al-content layers.

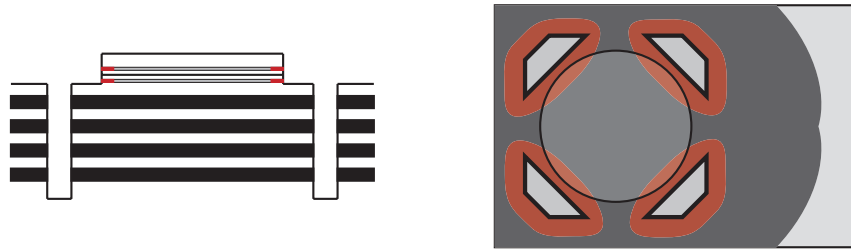


Figure 4.21: Mesa etch

Recess Etch

- i. Lithography
- ii. Surface deoxidation with diluted HCl
- iii. Selective wet etching of ring-shaped recess; down to p-Al_{0.90}Ga_{0.10}As GRINSCH layer (removal of p-doped GaAs layers, and top DBR pair for S1907 and S1908). Citric acid solution for low Al-content layers and diluted phosphoric acid solution for high Al-content layers.

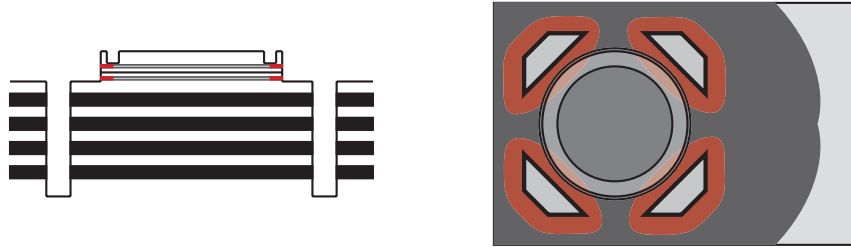


Figure 4.22: Recess etch

N-Contact Deposition

- i. Lithography
- ii. Surface deoxidation with diluted HCl
- iii. E-beam evaporation n-contact layer sequence:

Ni/Ge/Au/Ni/Au 10/25/50/20/100 nm

- iv. Lift-off in acetone or NMP (N-Methyl-2-pyrrolidone)
- v. N-contact alloying at 380 °C in forming gas atmosphere (ramps 5 °C/min)

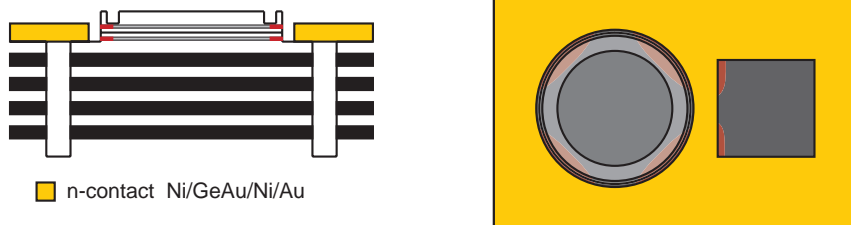


Figure 4.23: N-contact deposition

Dielectric Coating

- i. Polyimide spinning (thickness 1 μm)
- ii. Polyimide soft bake
- iii. Lithography
- iv. Polyimide etching
- v. Polyimide curing at 250 °C for 2 h in air (ramps 5 °C/min)

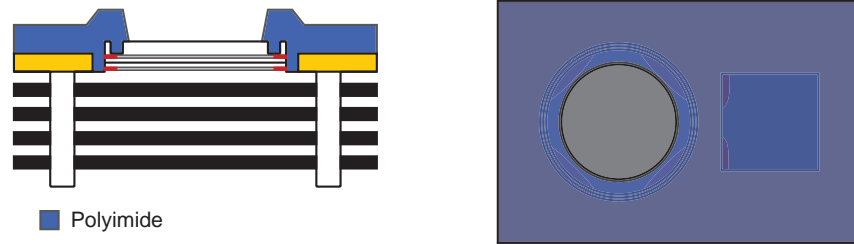


Figure 4.24: Dielectric coating with polyimide

P-Contact Deposition

- i. Lithography
- ii. Surface deoxidation with diluted HCl
- iii. E-beam evaporation p-contact layer sequence:

S1905 A:	Au	200 nm
S1907 B, S1908 B:	Ti/Au	10/250 nm
S1905 D, S1907 D, S1908 D:	Ti/Pt/Au	20/38/200 nm

- iv. Lift-off in acetone or NMP (N-Methyl-2-pyrrolidone)
- v. No alloying

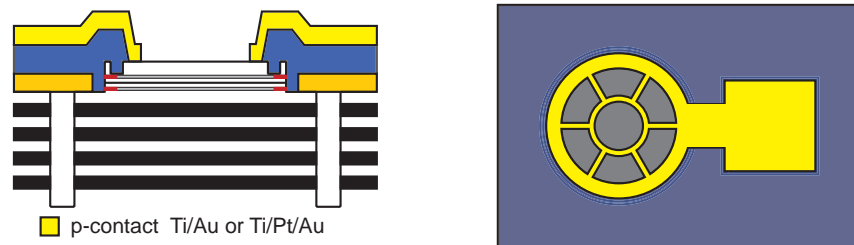


Figure 4.25: P-contact deposition, shown without (left) and with grid (right)

Final Samples

Figure 4.26 shows 350 μm devices of samples S1905 A and S1905 D. A different mask set was used for sample S1905 A. On the newer mask set used for the other samples the oxidation trenches are circular for the largest devices and consist of four trapezoidal or triangular openings for the smaller devices.

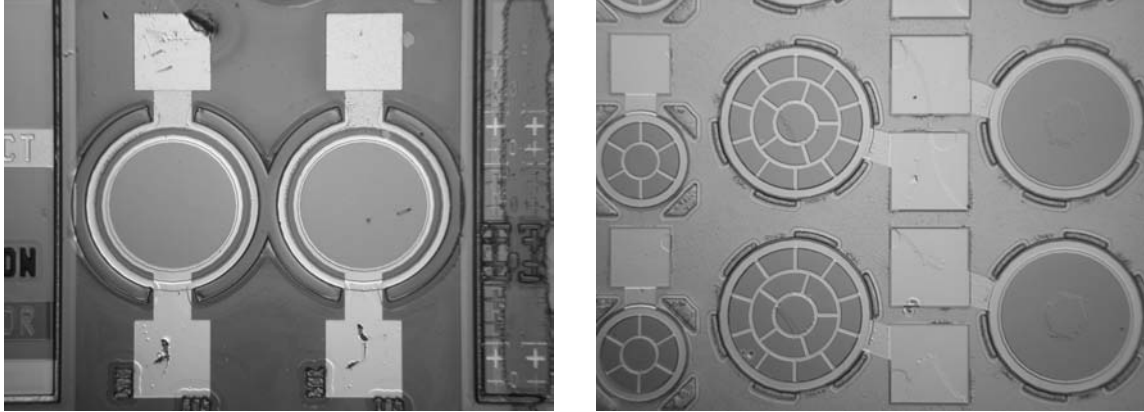


Figure 4.26: 350 μm devices of samples S1905 A (left) and S1905 D (right), in the latter case without and with p-contact grid plus 200 μm devices with grid

Defects appeared on the samples S1907 B and S1908 B during the lateral oxidation of the bottom DBR. Figures 4.27 and 4.28 show the samples after recess etch and after processing. On both samples the defect density varies to a great extent. Nevertheless some nearly defect-free areas can be found. The parasitic oxidation of the high Al-content GRINSCH layers is distinguishable around the oxidation trenches.

By reducing the oxidation time for samples S1905 D, S1907 D and S1908 D the emergence of defects could be avoided entirely. However the mirrors of the 350 μm devices are not completely oxidized on these samples.

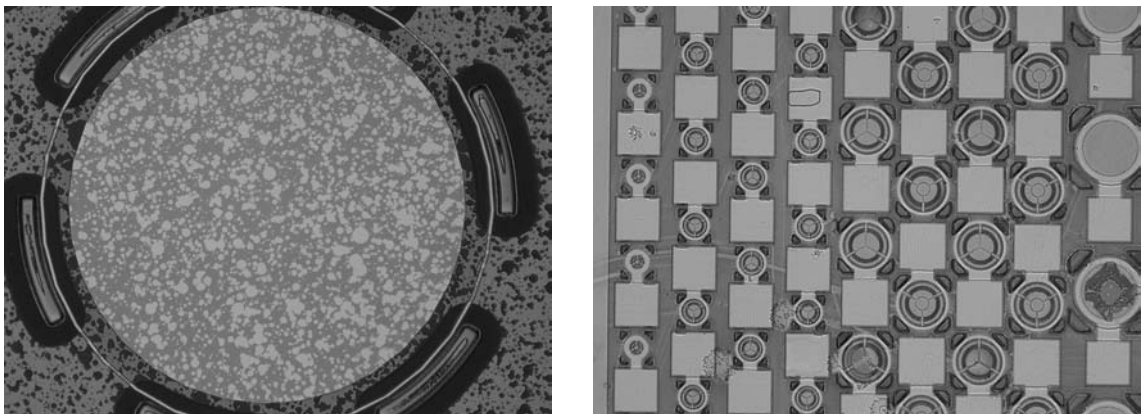


Figure 4.27: Sample S1907 B: 350 μm mesa with high defect density after recess etch (left); area with low defect density after processing (right), device sizes ranging from 20 to 200 μm

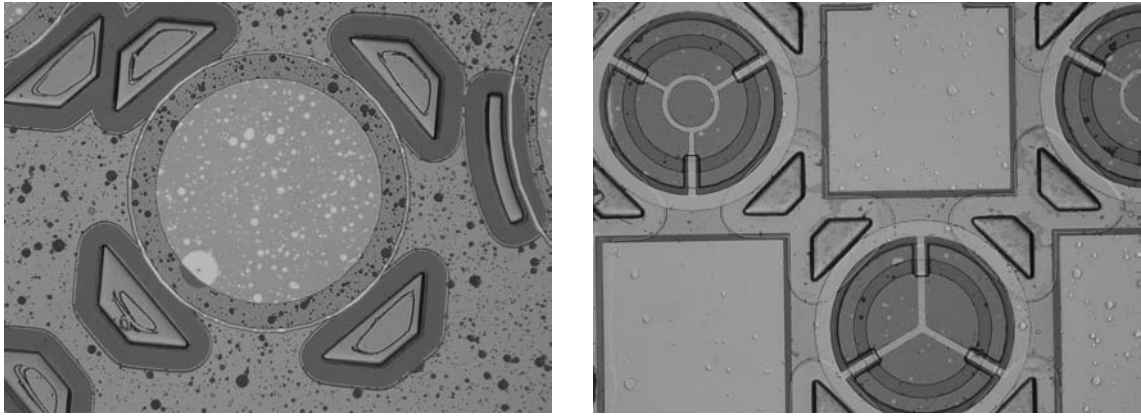


Figure 4.28: Sample S1908 B: 200 μm mesa with high defect density after recess etch (left); 200 μm devices with low defect density after processing (right)

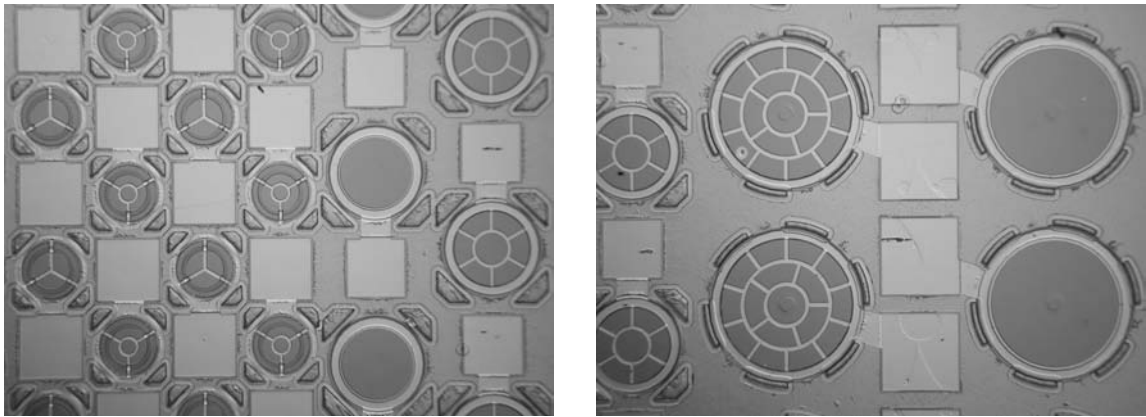


Figure 4.29: Sample S1907 D: 100, 200 and 350 μm devices; the first size with two different kind of grids, the latter two each without and with p-contact grid

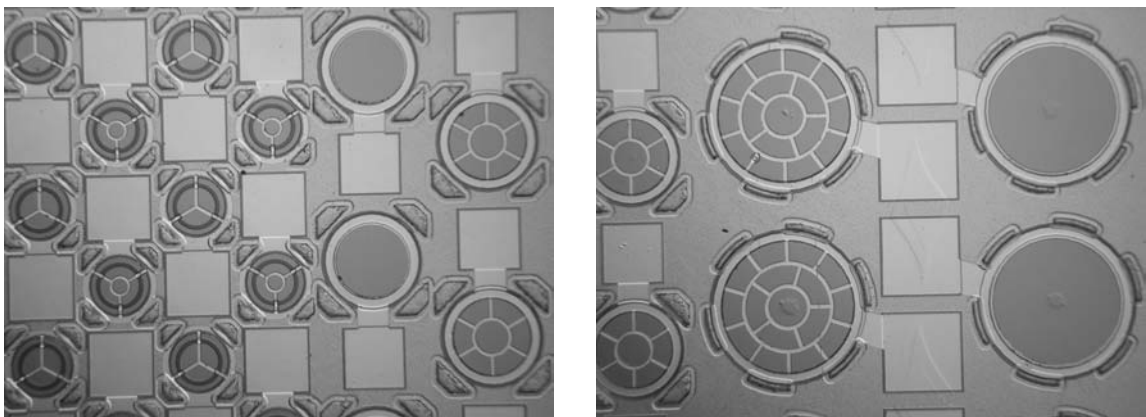


Figure 4.30: Sample S1908 D: 100, 200 and 350 μm devices; the first size with two different kind of grids, the latter two each without and with p-contact grid

4.5 Experimental Results

4.5.1 Characterization after Epitaxial Growth

After growth the structures are characterized in order to check whether they correspond to the structure as designed. This is done by photoluminescence and reflectivity measurements.

Photoluminescence

Photoluminescence is used to check the emission wavelength of the InGaAs quantum well and to evaluate its quality. The 532 nm line of a frequency-doubled Nd:YAG laser is used as excitation source together with a Spex Compudrive CD2 spectrometer and a silicon photodiode as detector.

Figure 4.31 shows the photoluminescence spectra of structures S1907 and S1910 after growth, representative for all the structures. The quantum well emission is centered around 970 nm, except for the structure S1910, for which the emission is blue-shifted by about 5 nm. The measured photoluminescence maxima are listed in table 4.7. In case of the semiconductor DBR structures the QW emission is influenced by the cavity, whereas for the oxide DBR structures the emission spectrum should not be significantly affected since the reflectivity of the bottom DBR before oxidation is low.

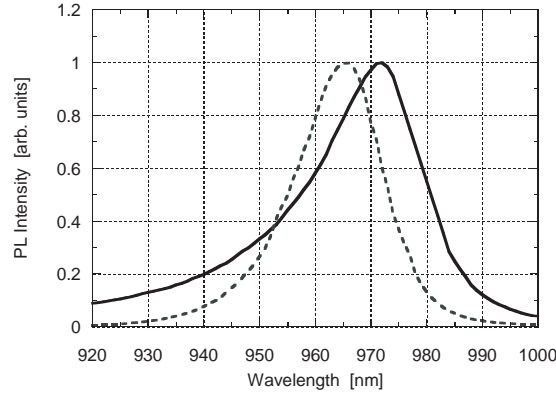


Figure 4.31: Photoluminescence spectra of structure S1907 (solid line) and S1910 (dashed line) after growth

Table 4.7: Measured QW emission wavelengths

Structure	peak [nm]
S1904	969
S1910	965
S1905	970
S1907	972
S1908	969

Reflectivity

Reflectivity measurements are essential in analyzing the optical properties of DBR mirrors and Fabry-Perot cavities [238]. In combination with a simulation tool the reflectivity spectrum allows to estimate thickness and compositional deviations from the nominal layer structure. Thus reflectivity measurements are a powerful means of quality control of the structures after epitaxial growth as well as after device processing.

The reflectivity set-up is shown in figures 4.32 and figure 4.33. The measurements are carried out at normal incidence and room temperature. The emission of a white light source (1) is coupled into an optical fiber. The white light is focussed by means of a microscope objective (2) and filtered with a low bandpass filter (3) in order to block the second order spectrum of the short wavelength part of the emission spectrum (below 600 – 700 nm). With the aid of a cubic beam splitter (4) the light beam is halved and directed on a gold reference mirror (6) and on the sample (8). In both cases the light is focused on the surface with a microscope objective (5,7). The reflected light is coupled into an optical fiber and analyzed with a Jobin Yvon 1000M spectrometer (10) and a photodetector (11).

By blocking the beam directed on the sample the reference spectrum of the reflection of the white light from the gold mirror can be recorded. The reflectivity spectrum of the sample can then be deduced by acquiring the reflection of the white light from the sample and dividing this spectrum by the reference spectrum. To simplify matters, unprocessed samples were often measured without the collection lenses (5 and 7). This way the resulting spectrum corresponds to an average over the area of the spot size of several millimeters in diameter. For the reflectivity measurements of processed devices the spot was aligned on the device by imaging it with a CCD camera placed behind the sample (details see section 4.5.2).

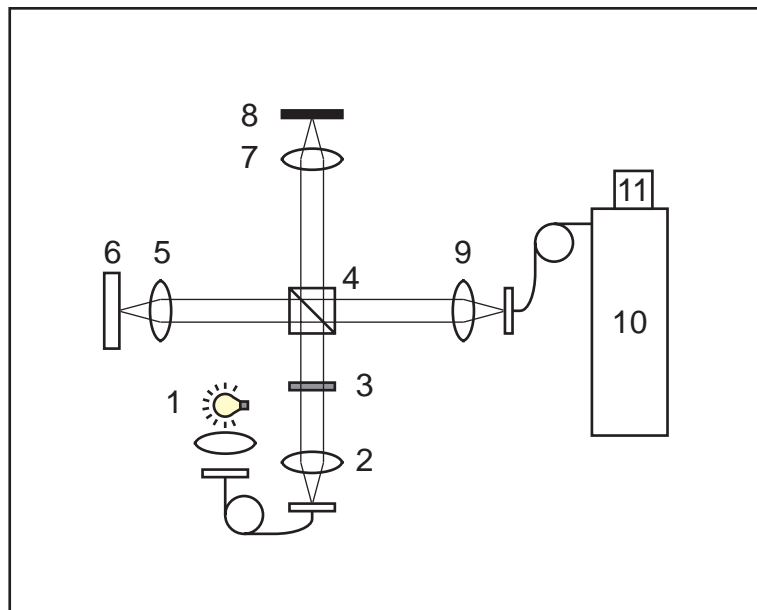


Figure 4.32: Description reflectivity set-up

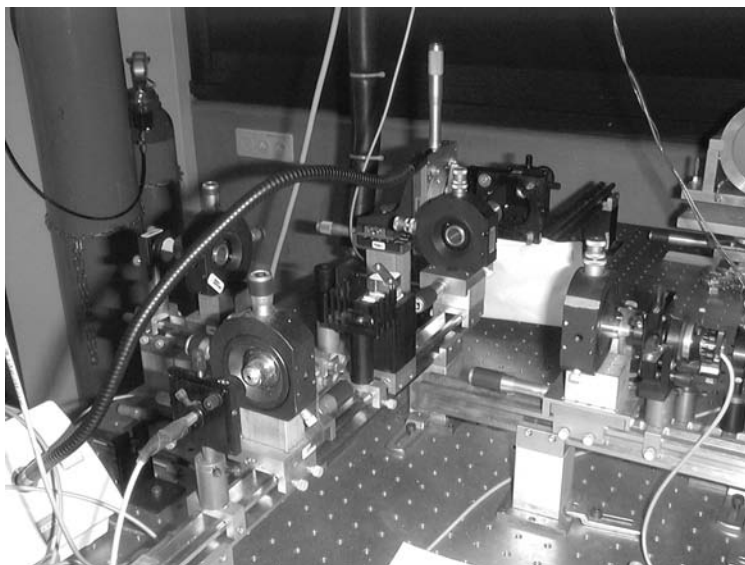


Figure 4.33: Photograph of the reflectivity set-up

Depending on the wavelength range, either a Spectrum One 1024 x 128 Si CCD or a Spectrum One InGaAs linear array detector is used, both operating at a temperature of 140 – 150 K. The silicon detector is normally used in the wavelength range from 650 to 1050 nm, the InGaAs detector between 700 and 1400 nm. Figures 4.34 and 4.35 show the typical spectral response curves for the two types of detectors issued by Jobin Yvon Horiba. A halogen lamp was chosen as white light source, since it exhibits a smooth spectral curve over a large wavelength range without any spectral peaks, a stable output and a long lifetime. The typical spectral irradiance of a quartz tungsten halogen lamp is shown in figure 4.36. Protected gold mirrors generally show a reflectivity superior to 96 % from 650 to 1700 nm, as can be seen in figure 4.37.

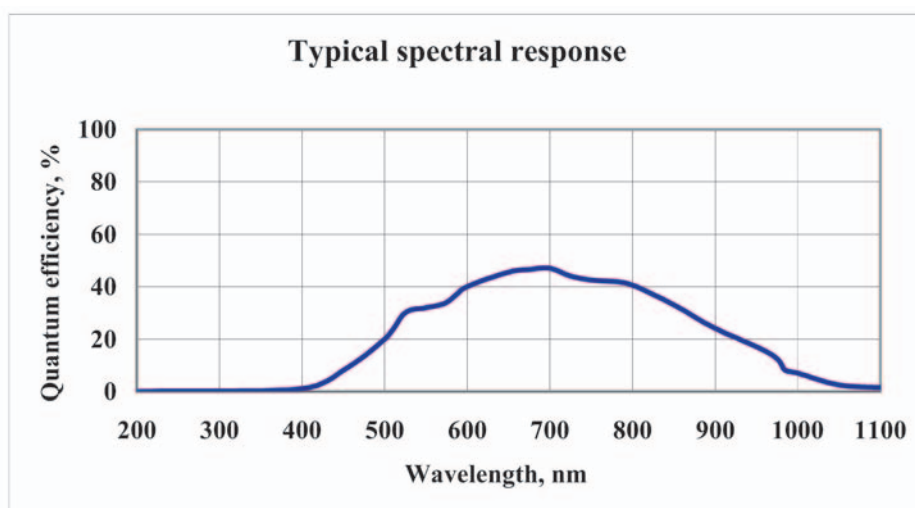


Figure 4.34: Typical spectral response of Si CCD at 25 °C (by Jobin Yvon)

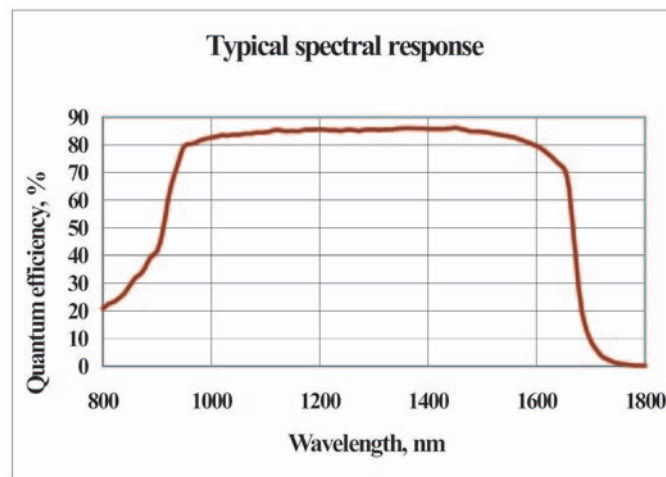


Figure 4.35: Typical spectral response of InGaAs array detector at 25 °C (by Jobin Yvon)

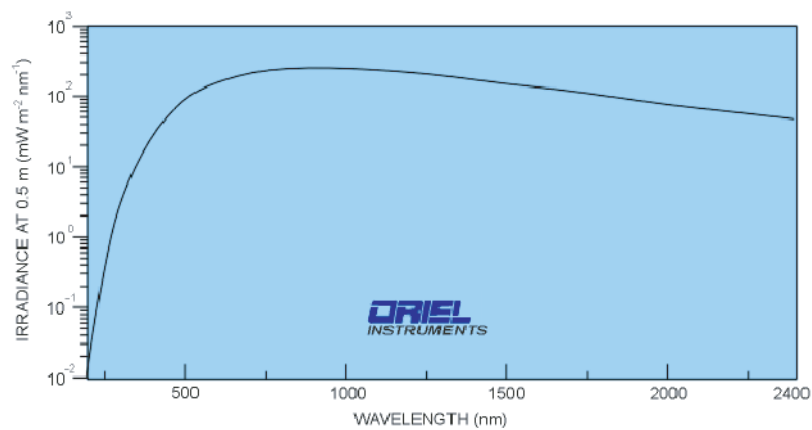


Figure 4.36: Typical spectral irradiance of a 1000 W Quartz Tungsten Halogen lamp (by ORIEL)

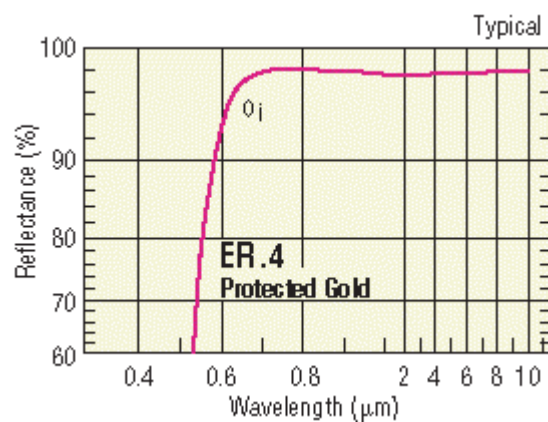


Figure 4.37: Typical reflectance vs. wavelength of protected gold mirrors (by Newport)

Figures 4.38 and 4.39 contain the reflectivity spectra of the different structures after growth, measured with the Si CCD. As the structure S1905 was not processed by us it wasn't characterized together with the other structures. The measurements are compared with the simulated spectra. The simulations show a discontinuity at 870 nm related to the absorption band edge of GaAs at this wavelength. For every structure the simulation matches quite well with the measurement, therefore it can be assumed that the layer thicknesses and compositions correspond to the designed structures. The reflectivity spectra of the semiconductor DBR structures show the stopband and the Fabry-Perot cavity peak, whereas the reflectivity of the oxide DBR structures before oxidation is too low to form a cavity.

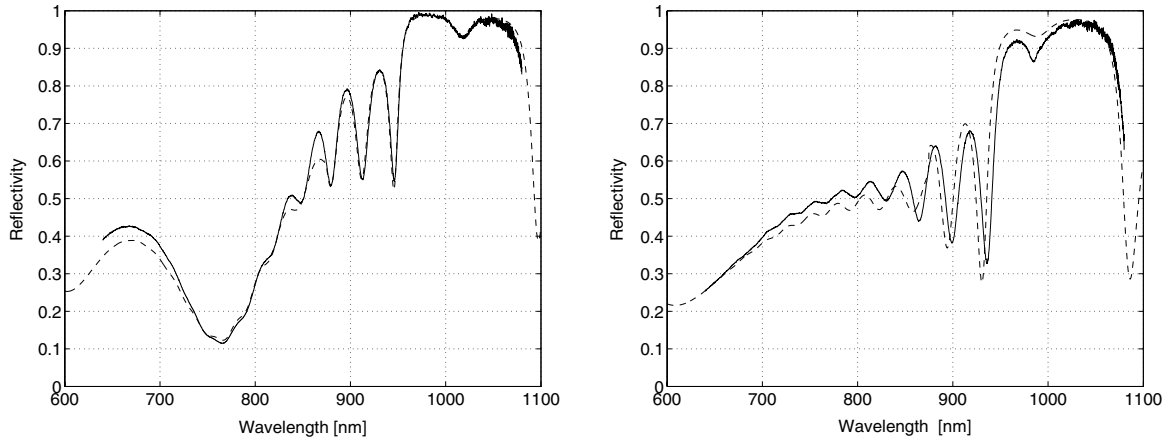


Figure 4.38: Reflectivity spectra of structure S1904 (left) and S1910 (right); comparison measurement with Si CCD (solid line) and simulation (dashed line)

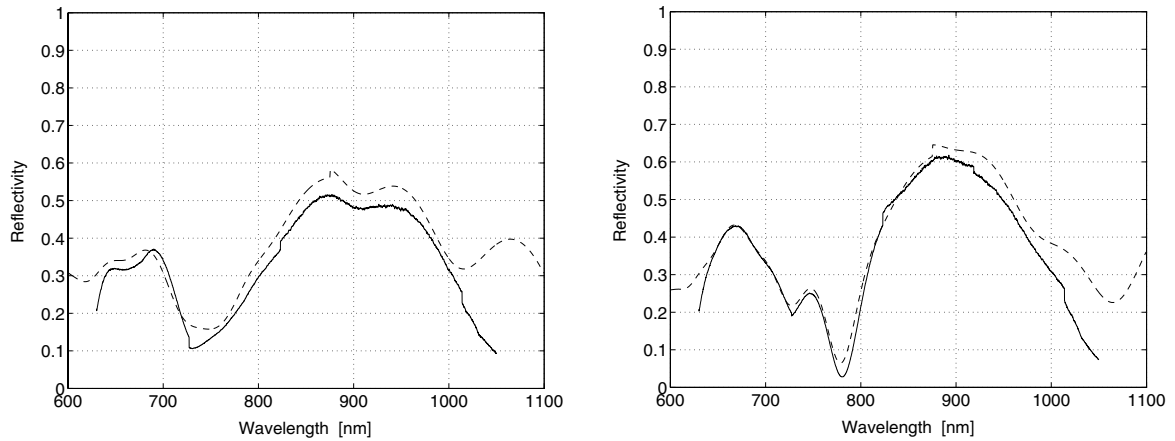


Figure 4.39: Reflectivity spectra of structure S1907 (left) and S1908 (right); comparison measurement with Si CCD (solid line) and simulation (dashed line)

4.5.2 Characterization of the Processed Devices

TLM Measurements

The Transmission Line Model (TLM) is explained in detail in section 3.5.1. Square test patterns are used with dimensions slightly varying between the two mask sets deployed. In case of the semiconductor DBR devices the contact areas are $100 \times 100 \mu\text{m}^2$, with contact spacings of 2, 4, 6, 8, 12 and $16 \mu\text{m}$. On the mask set for the oxide DBR devices the contact areas are $150 \times 150 \mu\text{m}^2$, with contact spacings of 4, 6, 10, 20, 50 and $150 \mu\text{m}$. The measurements are carried out by means of an HP4156A Semiconductor Parameter Analyzer. The I–V characteristics for the different contact spacings are recorded with a four point probe set-up. Two probes serve for applying a voltage and sweeping it over a certain range while the other two are used to measure the resulting current.

As for the bottom emitting devices, the sheet resistance and the contact resistivity of the used Ni/AuGe/Ni/Au n-contacts could not be determined since a non-ohmic behavior was measured for these contacts. Table 4.8 shows the sheet resistances R_{sh} and contact resistivities ρ_c of the p-contacts of the different samples obtained from the TLM measurements. The values are somewhat higher than earlier results on similar structures [239]. This might be related to the slightly lower cap doping levels. Similar contact resistivities are obtained for the non-alloyed gold contacts and the alloyed Ti/Pt/Au contacts. The non-alloyed Ti/Au and Ti/Pt/Au contacts of the oxide DBR devices on the other hand show values that are an order of magnitude higher than for the standard contacts.

Table 4.8: Contact parameters p-contacts

Sample	Contact	Alloying [°C]	R_{sh} [Ω/\square]	ρ_c [Ωcm^2]
S1904 na	Au	-	990	1.4×10^{-4}
S1904 a	Ti/Pt/Au	380	870	1.4×10^{-4}
S1910 na	Au	-	2300	3.1×10^{-4}
S1910 a	Ti/Pt/Au	380	2400	2.0×10^{-4}
S1905 D	Ti/Pt/Au	-	1900	9.8×10^{-3}
S1907 B	Ti/Au	-	1900	1.8×10^{-2}
S1907 D	Ti/Pt/Au	-	750	1.5×10^{-3}
S1908 B	Ti/Au	-	1400	3.1×10^{-3}
S1908 D	Ti/Pt/Au	-	770	1.2×10^{-3}

L–I–V Measurements

The devices are characterized by detailed light, current and voltage (L–I–V) measurements. The set-up consists of a calibrated large area silicon photodiode (Hamamatsu S1337-1010BR) and a HP 4145A Semiconductor Parameter Analyzer which is used as DC voltage source, current monitor and photocurrent monitor simultaneously (see figure 4.40). All measurements are taken in cw (continuous wave) mode and at room temperature. The device is contacted with two prober needles connected via coaxial cables. A voltage is applied to the diode and is varied over a certain range while the resulting diode forward current and the photocurrent generated in the photodiode are recorded. The photodiode is biased at 0 V in order to minimize its dark current.

Bottom emitting devices are measured simply by placing them on the photodiode. As the surface of the photodiode of 1 cm^2 is large compared to the device sizes, it can be assumed that all the emitted light is captured by the photodiode. For top emitting devices on the other hand the photodiode is mounted on a cantilever connected to a xyz-translation stage. After contacting the device with the prober needles the photodiode is centered on the device and then lowered as close as possible. The needles are kept as horizontal as possible but nevertheless the minimal distance between the device and the photodiode is about 2 – 3 mm. This corresponds to a collection angle of approximately 65° . A schematic of the photodiode set-up is shown in figure 4.41; figure 4.42 contains a photograph of the set-up for top emission measurements.

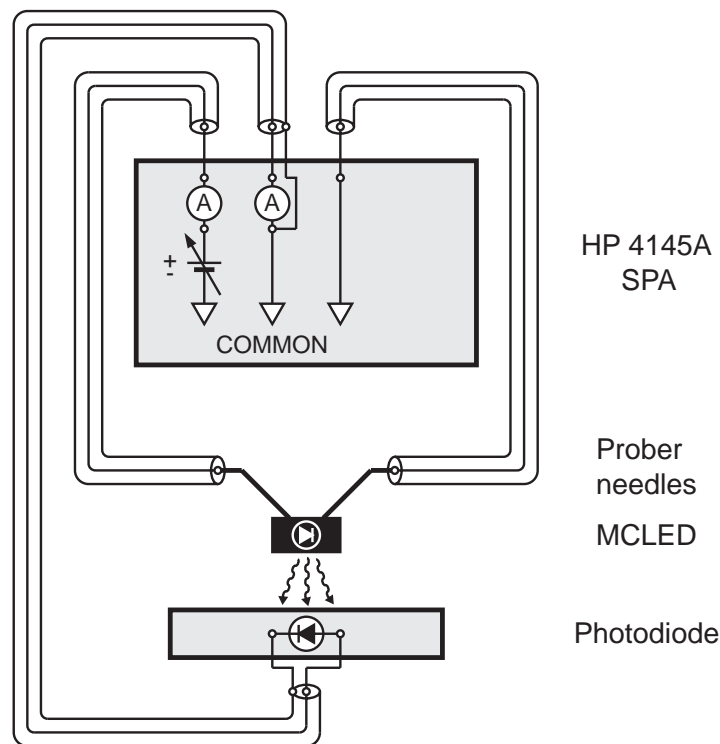


Figure 4.40: Schematic representation electrical circuit L–I–V measurement set-up

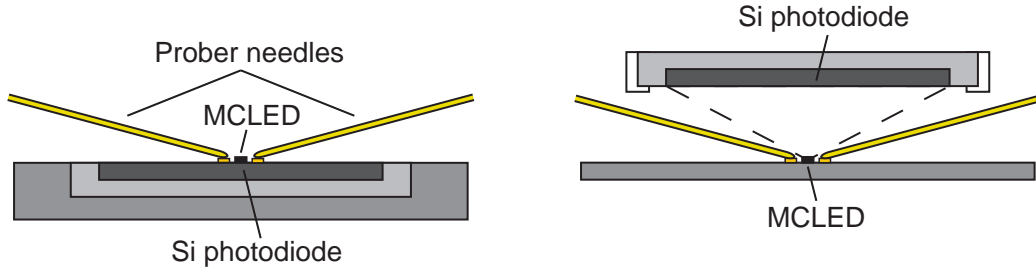


Figure 4.41: Light collection bottom (left) and top emission (right) set-up

A large part the light is emitted within the 65° collection cone. In case of a device optimized for maximum efficiency into air the emission is maximal on an annulus with a half angle of approximately 45° . The measured data are corrected with a geometry factor ζ_{geom} , corresponding to the estimated fraction of collected light. This value is estimated to be 0.9.

The external quantum efficiency η_{ext} is defined as the ratio of the externally emitted photon flux, $\Phi_{\text{opt}}^{\text{out}}$, to the total injected electron flux, $\Phi_{\text{el}}^{\text{tot}}$ (see section 2.5.1)

$$\eta_{\text{ext}} = \frac{\Phi_{\text{opt}}^{\text{out}}}{\Phi_{\text{el}}^{\text{tot}}} = \frac{e}{h\nu} \frac{P_{\text{opt}}}{I} \quad (4.2)$$

where $h\nu$ denotes the energy of the emitted photons, e the electron charge, P_{opt} the optical output power and I the injected current [37]. The external quantum efficiency is therefore calculated as follows:

$$\eta_{\text{ext}} = \frac{\lambda[\mu\text{m}]}{1.24} \frac{I_{PD}}{\zeta_{\text{geom}} R_{PD} I_F} \quad (4.3)$$

R_{PD} corresponds to the photo sensitivity of the photodiode, which is expressed in units

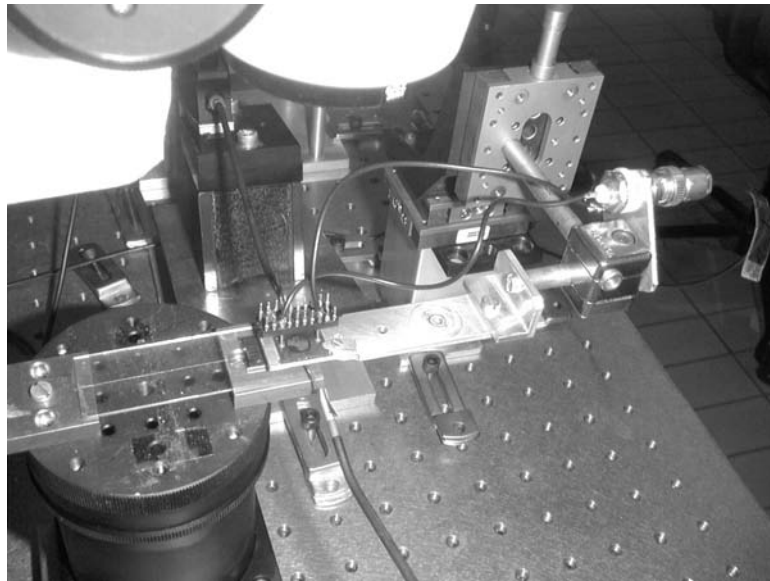


Figure 4.42: Photograph L-I-V top emission set-up

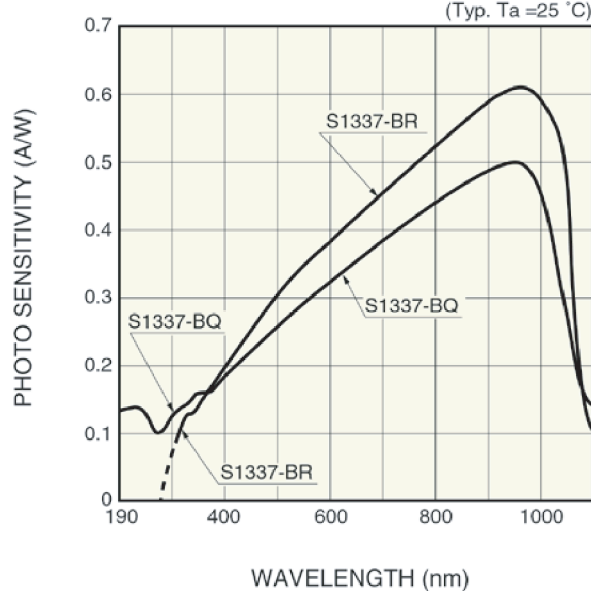


Figure 4.43: Typical spectral response large area photodiodes by Hamamatsu

of A/W. The typical spectral response of the photodiodes S1337-1010 BR given by Hamamatsu is shown in figure 4.43. The measurements were carried out with a photodiode S1337-1010BR, which had been calibrated by the Swiss Federal Office of Metrology and Accreditation (METAS). The calibration results are listed in appendix D.1.

The external quantum efficiency of the photodetector, which corresponds to the product $1.24R_{PD}/\lambda[\mu m]$, is equal to 0.786 at 970nm. The detector efficiency is assumed to be independent of the angle of incidence. Therefore with a geometry factor ζ_{geom} of 0.9 the overall conversion factor for top emitting devices is equal to 0.7. This leads to the following expression for η_{ext}

$$\eta_{\text{ext}} = \frac{1}{0.7} \frac{I_{PD}}{I_F} \quad (4.4)$$

As the LED characteristics at low current densities give a good indication of the electrical and optical quality of the device, the current–voltage curves are plotted on a semilogarithmic scale ($\log(I)$ – V) and the external quantum efficiency is plotted versus the logarithm of the current density (η_{ext} – $\log(J)$).

The emission into epoxy is simulated by immersing the device in a roughly hemispherical droplet of glycerol. Anhydrous glycerol has a refractive index of 1.4746 at 589 nm and 20 °C [208], which is close to the refractive index of epoxy of 1.5. In addition glycerol does not wet GaAs very well, hence it forms a droplet similar to the shape of a hemispherical epoxy dome. However glycerol is hygroscopic and with increasing water content the refractive index decreases towards 1.33. Plus if the curvature of the droplet is not high enough the amount of light coupled out is lower as well.

The measured I–V characteristics and external quantum efficiencies as a function of drive current density ($\eta_{\text{ext}}\text{--}J$) for the **semiconductor DBR devices** are shown in figures 4.44–4.47. The curves of the devices with non-alloyed and alloyed p-contacts and each time without and with a p-contact grid are compared. The ideality factors of the I–V curves are summarized in table 4.9. n_{ideal} is approximately 1.7 for sample S1904 and ≈ 2 for sample S1910.

For the devices S1904 na not only the emission into air but as well the emission into glycerol was measured. As the contact pads are in the vicinity of the device, the proper needles are often immersed in the glycerol droplet as well. This leads to a significant increase of the leakage currents at low bias, as can be seen for sample S1904 na. However this effect does not seem to influence the efficiencies measured at higher current densities. Since the measured efficiencies are significantly lower for sample S1904 a, these devices were not measured in glycerol. The maximum external quantum efficiencies measured for the different types of devices are listed in table 4.10.

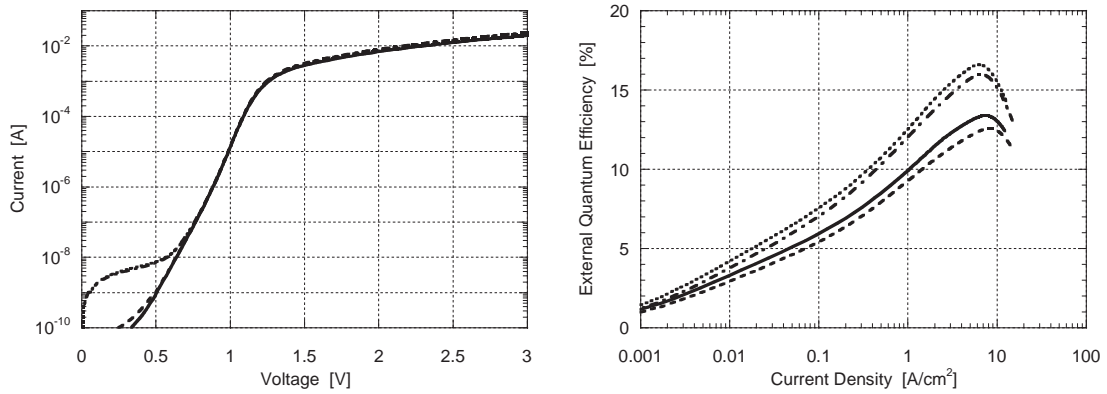


Figure 4.44: I–V characteristic and external quantum efficiency vs. drive current density of 400 μm MCLEDs from sample S1904 na; emission into air without (solid line) and with grid (dashed line), emission into glycerol without (dotted line) and with grid (dash-dot line)

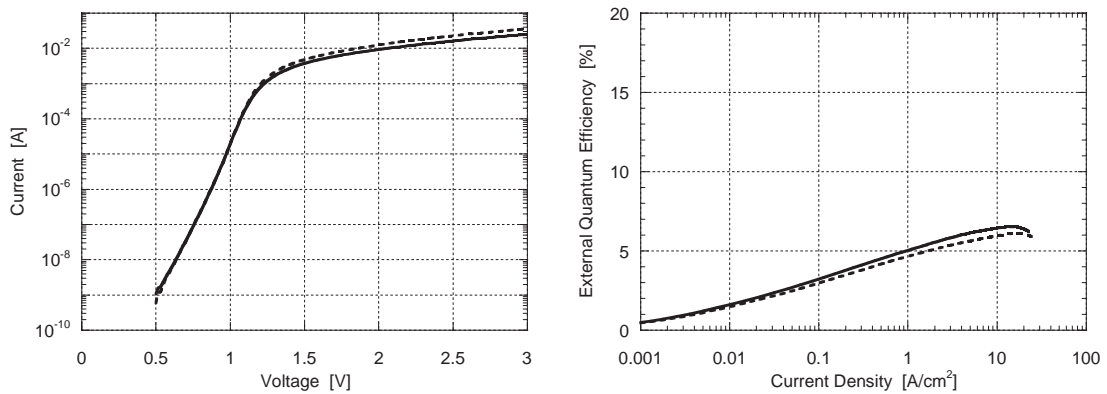


Figure 4.45: I–V characteristic and external quantum efficiency vs. drive current density of 400 μm MCLEDs from sample S1904 a; emission into air without (solid line) and with grid (dashed line)

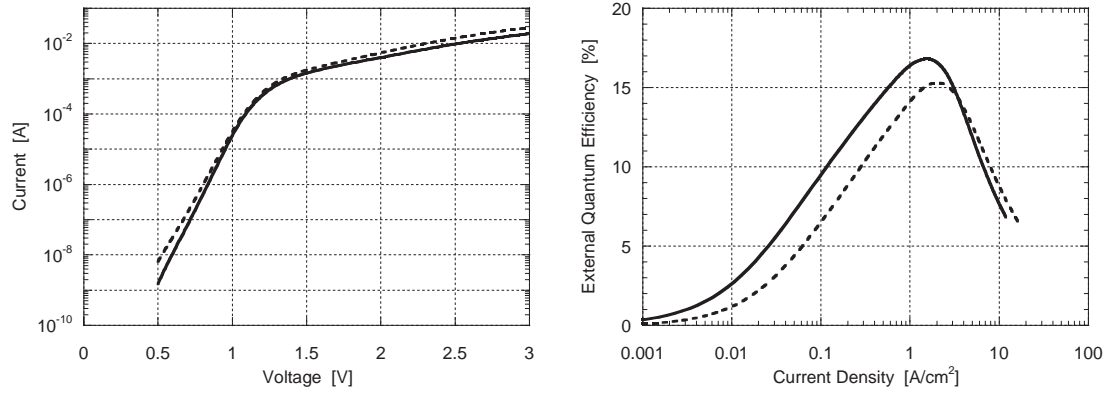


Figure 4.46: I–V characteristic and external quantum efficiency vs. drive current density of $400\ \mu\text{m}$ MCLEDs from sample S1910 na; emission into air without (solid line) and with grid (dashed line)

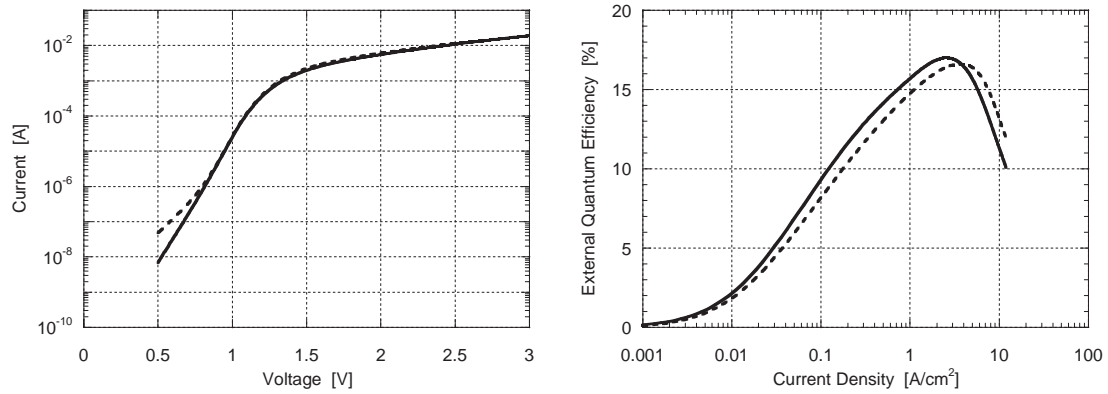


Figure 4.47: I–V characteristic and external quantum efficiency vs. drive current density of $400\ \mu\text{m}$ MCLEDs from sample S1910 a; emission into air without (solid line) and with grid (dashed line)

Table 4.9: Ideality factors I–V characteristics semiconductor DBR devices

Sample	no grid	grid
S1904 na	1.70	1.69
S1904 a	1.67	1.67
S1910 na	2.0	2.2
S1910 a	2.2	2.2

Table 4.10: Maximum external quantum efficiencies of the semiconductor DBR devices, measured with a large area photodiode

Sample	Simulation		Measurements				
	air	epoxy	dia-meter [μm]	air		glycerol	
	[%]	[%]		no grid [%]	grid [%]	no grid [%]	grid [%]
S1904 na	10	34	400	12.4	11.9	16.6	16.0
S1904 a	10	34	400	6.5	6.1	-	-
S1910 na	24	31	400	16.8	15.3	-	-
S1910 a	24	31	400	17.0	16.6	-	-

For every device type the efficiency slightly decreases with the use of a p-contact grid. Apparently the additional shadowing due to the grid is more important than the improved current injection. The significantly lower values for the devices from sample S1904 a indicate that this sample was damaged during the processing. In the case of structure S1910 the use of an alloyed contact leads to a slight improvement in efficiency, especially for the devices with a p-contact grid. It seems that the use of an alloyed Ti/Pt/Au p-contact leads to an improved current injection compared to a non-alloyed gold contact. The efficiency increase due to the droplet of glycerol for S1904 na is not as high as expected, probably the shape of the droplet was not appropriate. Furthermore the glycerol might have a reduced refractive index due to water absorption.

Figures 4.48–4.53 contain the I–V characteristics and external quantum efficiencies as a function of drive current density for the **oxide DBR devices**. The values of the ideality factors of the I–V characteristics vary between 1.8 and 1.9, as can be seen in table 4.11. The efficiency for emission into glycerol was measured only for the devices from sample S1907 B and S1908 B. Table 4.12 shows the maximum measured external quantum efficiencies for the different oxide DBR device types for emission into air and epoxy. On sample S1905 D only a few devices were actually emitting light. They show significantly lower efficiencies than the MCLEDs from sample S1905 A.

Table 4.11: Ideality factors I–V characteristics oxide DBR devices

Sample	no grid	grid
S1905 A	1.79	-
S1905 D	1.85	1.85
S1907 B	1.82	1.82
S1907 D	1.86	1.77
S1908 B	-	1.82
S1908 D	-	1.92

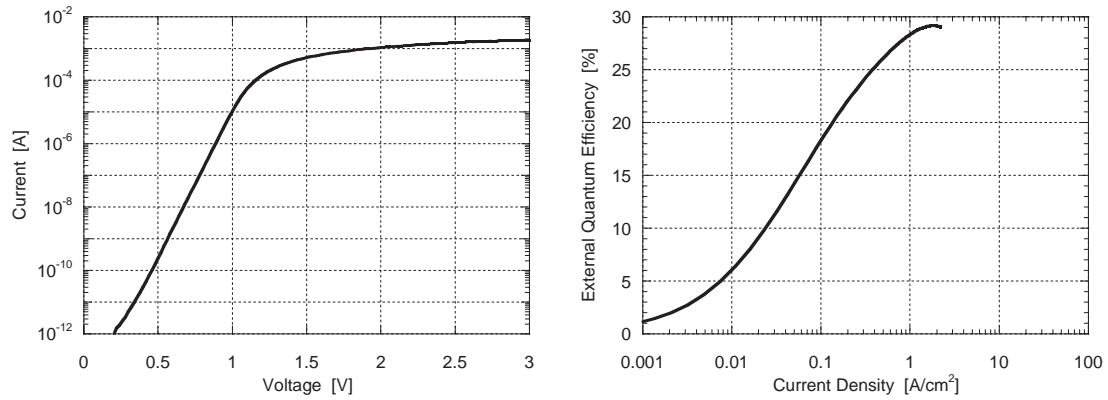


Figure 4.48: I-V characteristic and external quantum efficiency vs. drive current density of a 350 μm MCLED without grid from sample S1905 A; emission into air

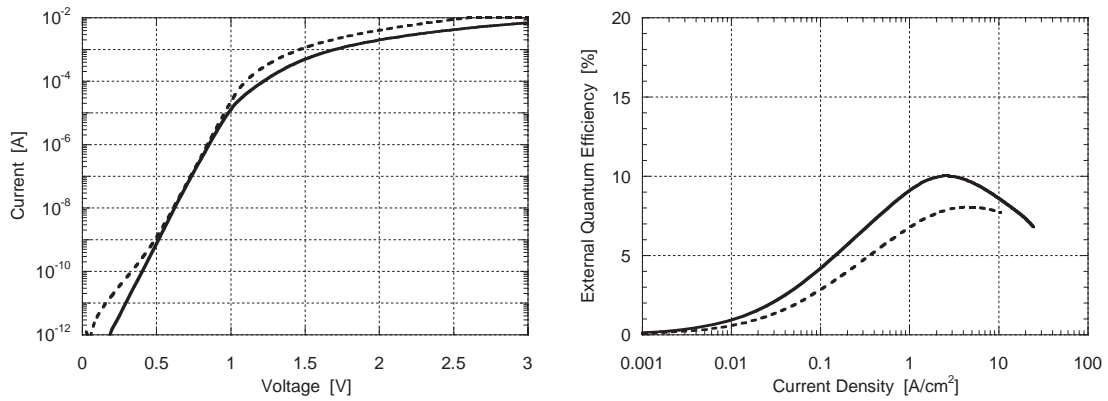


Figure 4.49: I-V characteristic and external quantum efficiency vs. drive current density of 350 μm MCLEDs from sample S1905 D; emission into air without (solid line) and with grid (dashed line)

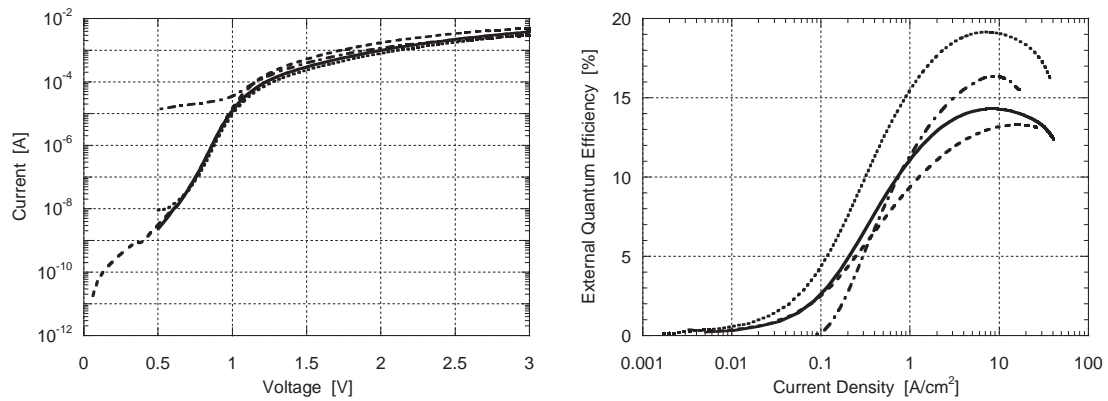


Figure 4.50: I-V characteristic and external quantum efficiency vs. drive current density of 200 μm MCLEDs from sample S1907 B; emission into air without (solid line) and with grid (dashed line), emission into glycerol without (dotted line) and with grid (dash-dot line)

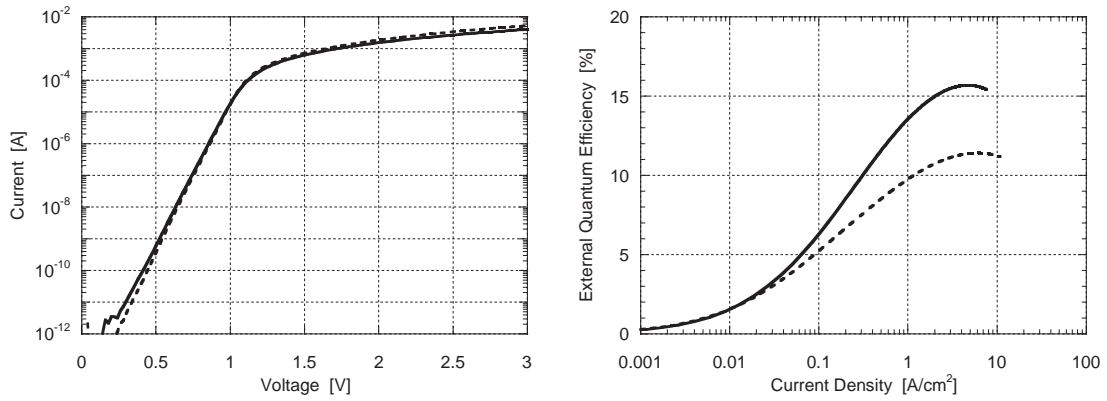


Figure 4.51: I-V characteristic and external quantum efficiency vs. drive current density of 350 μm MCLEDs from sample S1907 D; emission into air without (solid line) and with grid (dashed line)

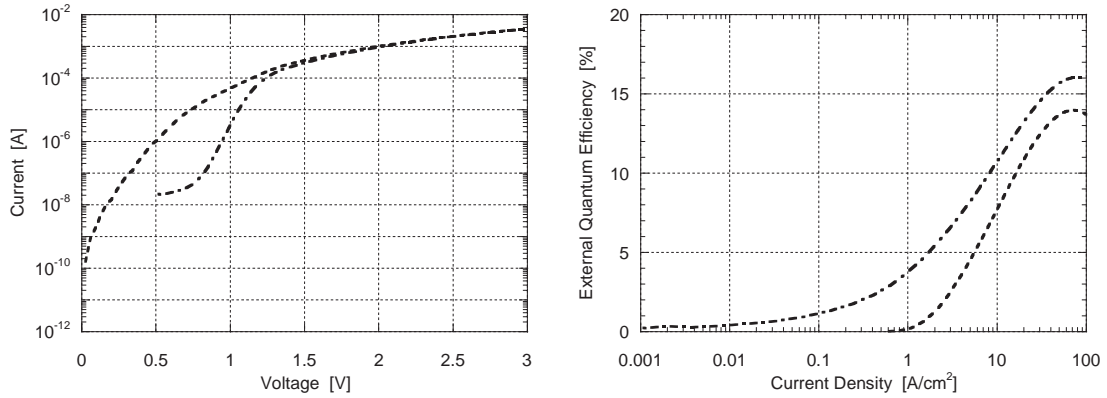


Figure 4.52: I-V characteristic and external quantum efficiency vs. drive current density of a 100 μm MCLED with grid from sample S1908 B; emission into air (dashed line) and glycerol (dash-dot line)

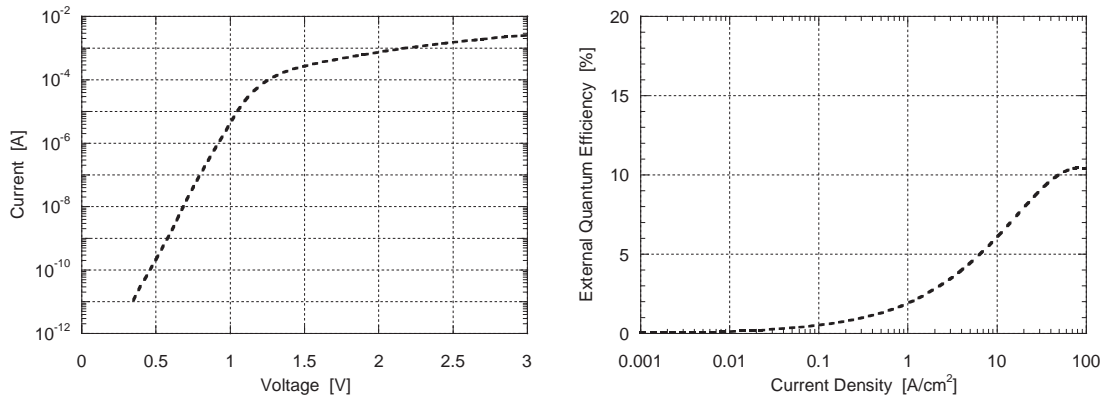


Figure 4.53: I-V characteristic and external quantum efficiency vs. drive current density of a 100 μm MCLED with grid from sample S1908 D; emission into air

Table 4.12: Maximum external quantum efficiencies of the oxide DBR devices, measured with a large area photodiode

Sample	Simulation		Measurements				
	air	epoxy	dia- meter [μm]	air		glycerol	
	[%]	[%]		no grid [%]	grid [%]	no grid [%]	grid [%]
S1905 A	29	34	350	29.2	-	-	-
S1905 D	29	34	350	10.0	8.1	-	-
S1907 B	30	35	200	14.3	13.3	19.2	16.4
S1907 D	30	35	350	15.7	11.4	-	-
S1908 B	18	38	100	-	14.0	-	16.0
S1908 D	18	38	100	-	10.4	-	-

The few working devices from sample S1905 D show a significantly lower efficiency than the ones from sample S1905 A, indicating that either the second processing was not ideal or the structures degraded during storage. Apart from sample S1905 A all the measured efficiencies are significantly lower than the simulated values. As for the semiconductor DBR devices the efficiencies slightly decrease with the implementation of a p-contact grid. The 100 μm devices only come with a p-contact grid, therefore no comparison is possible for the devices with structure S1908. Devices of larger diameter on samples S1908 B and S1908 D show lower efficiencies. The glycerol encapsulation lead to slightly higher increases in efficiency than for the semiconductor DBR devices, however the values are still far away from the simulated ones.

The maximum external quantum efficiencies for the different kind of top emitting near infrared structures are summarized in table 4.13.

Table 4.13: Maximum external quantum efficiencies of TE MCLEDs emitting at 970 nm for emission into air and glycerol, measured with a large area photodiode

Structure	Simulation		Measurements	
	air [%]	epoxy [%]	air [%]	glycerol [%]
S1904	10	34	12	17
S1910	24	31	17	-
S1905	29	34	29	-
S1907	30	35	16	19
S1908	18	38	14	16

L–I–V Measurements with Integrating Sphere

For precise absolute efficiency measurements of top emitting diodes the devices need to be measured with an integrating sphere. By placing the emitter inside the sphere virtually all the light emitted in the top hemisphere is collected; the measurement is independent of the orientation of the device and the detector [240]. The light is collected by the highly reflective interior coating and uniformly reflected and scattered around the sphere's interior. The output is then a uniform, spatially integrated beam, which is insensitive to the spatial, angular and polarization changes of the input.

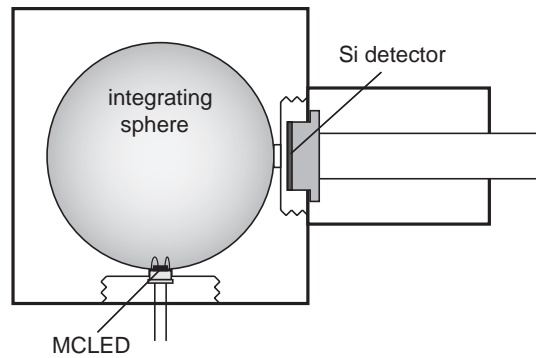


Figure 4.54: Schematic cross-section integrating sphere

In order to be able to insert the devices into the sphere they need to be cleaved, mounted on TO-18 transistor headers and bonded. The bonding wires should be placed in a way they shadow the emission the least. The sphere used (UDT Instruments Radiometry Model 2575 Laser Power Attenuator) features a 50 mm diameter, a 5 mm entrance aperture and an attenuation ratio of approximately 1000:1. A UDT Instruments Model 260 silicon sensor head with an effective aperture size of 0.44 cm^2 is attached to it. The ensemble had been calibrated by UDT Instruments. The calibration results are listed in appendix D.2. At 970 nm the external quantum efficiency of the detection system corresponds to 1.73×10^{-3} . As for the previous measurements the voltage applied to the device is controlled by a HP 4145A semiconductor parameter analyzer, which is used to measure the current and the photocurrent as well.

Figures 4.55 and 4.56 show the I–V characteristics and external quantum efficiencies as a function of drive current density for bonded devices from samples S1904 na and S1910 na, measured with the integrating sphere. In both cases the measured device is a $400 \mu\text{m}$ diameter device with a non-alloyed p-contact and without a p-contact grid. The device from sample S1910 na was only measured in air, the one from sample 1904 na in in air and glycerol.

A $350 \mu\text{m}$ diode without p-contact grid from sample S1905 A was bonded and measured in air in the integrating sphere as well. Unfortunately the diode or more likely the bonding wires broke before the measurement curve could be recorded. The external quantum efficiency maximum measured is 28.0 %. Since the devices with structures S1907 and S1908 show significantly lower efficiencies than expected they were not measured in the integrating sphere. The maximum efficiencies measured with the integrating sphere are listed in table 4.14.

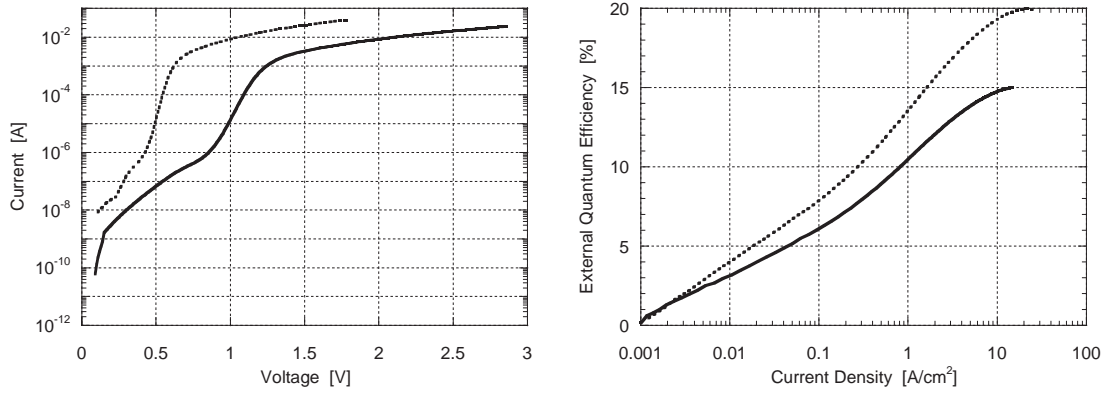


Figure 4.55: I–V characteristic and external quantum efficiency vs. drive current density of a $400\ \mu\text{m}$ MCLED from sample S1904 na without grid, measured with an integrating sphere; emission into air (solid line) and glycerol (dotted line)

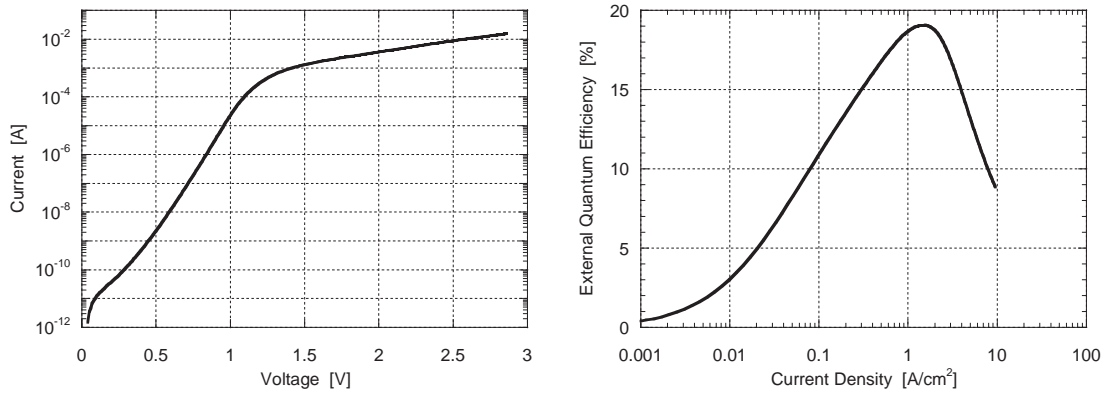


Figure 4.56: I–V characteristics and external quantum efficiency vs. drive current density of a $400\ \mu\text{m}$ MCLED from sample S1910 na without grid, measured with an integrating sphere; emission into air

Table 4.14: Maximum external quantum efficiencies of TE MCLEDs emitting at 970 nm measured with an integrating sphere

Structure	Simulation		Measurements	
	air [%]	epoxy [%]	air [%]	glycerol [%]
S1904	10	34	15.0	20.0
S1910	24	31	19.1	-
S1905	29	34	28.0	-

The external quantum efficiency of 19 % for a $400 \times 400\ \mu\text{m}^2$ device with structure S1910 represents the highest efficiency reported for semiconductor DBR MCLEDs so far. This result has been presented by Ross Stanley at ISCS'02 [134]. The 28 % for a $350\ \mu\text{m}$ diameter device with structure S1905 is the highest ever reported external quantum efficiency for a MCLED and has been published by Maxime Rattier [241].

Device Reflectivity

By comparing the simulated and the measured reflectivity spectrum of a MCLED the accuracy of the final device can be controlled and deviations from the nominal structure arisen during the growth or the fabrication can easily be spotted. This verification is especially important for MCLEDs with metal mirrors or oxide DBRs, for which the cavity is only created during the processing.

The details concerning the reflectivity measurement set-up are given in section 4.5.1. In order to be able to measure the reflectivity of an individual device the beam has to be centered on the light aperture. This is done by imaging the transmission through the sample with a CCD camera placed behind the device or by using a flip mirror and imaging the reflection. The gold reference spectrum can be recorded by placing the beam on a large gold feature on the sample next to the emission region. The spot size on the sample is estimated to be between 50 and 200 μm in diameter, depending on the microscope objective used.

Reflectivity measurements of processed devices were carried out on the samples with an oxide bottom DBR and for comparison on the sample S1910 a as well. The measured reflectivities of more than 100 % in some cases are assigned to intensity variations due to scattering, which are more pronounced for the small spot sizes used for these measurements. However this should not influence the spectral characteristics. Figures 4.57–4.60 show the reflectivity spectra of MCLEDs of varying diameter with structures S1910, S1905, S1907 and S1908. When the Fabry-Perot cavity peak is separated from the QW emission at 970 nm, the emission peak can be noticed as a small dip in reflectivity due to the absorption in the QW.

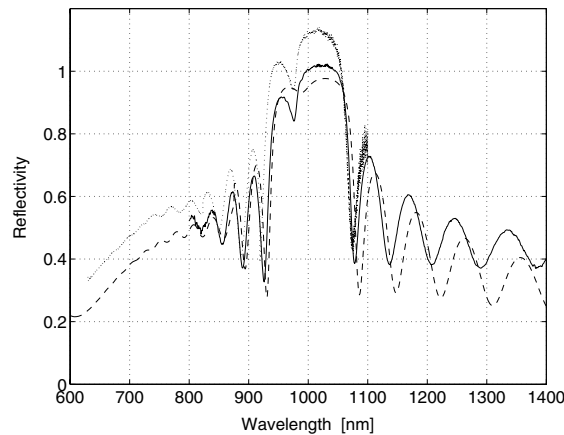


Figure 4.57: Reflectivity spectrum of a 400 μm MCLED from sample S1910 a; comparison measurement with Si CCD (dotted line), InGaAs array detector (solid line) and simulation (dashed line)

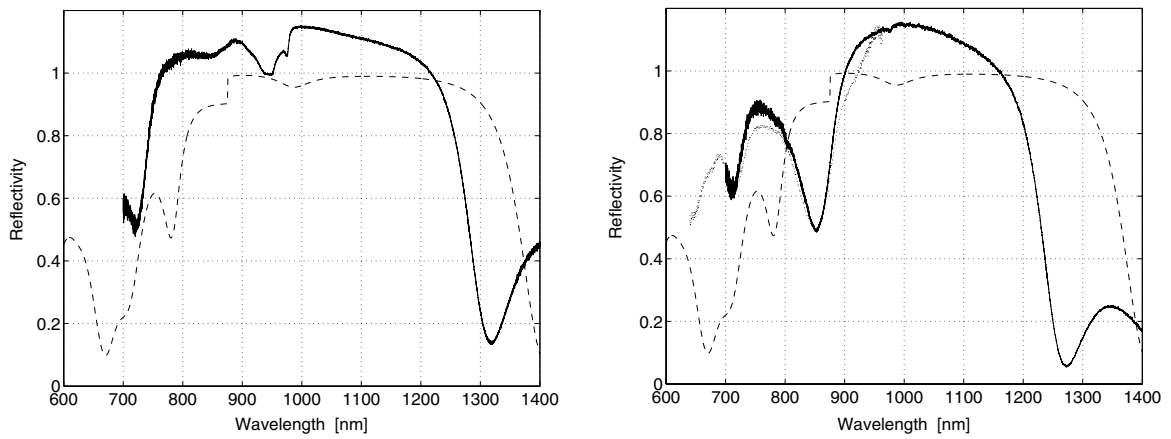


Figure 4.58: Reflectivity spectrum of a 350 μm MCLED from sample S1905 A (left) and a 200 μm MCLED from sample S1905 D (right); comparison measurement with Si CCD (dotted line), InGaAs array detector (solid line) and simulation (dashed line)

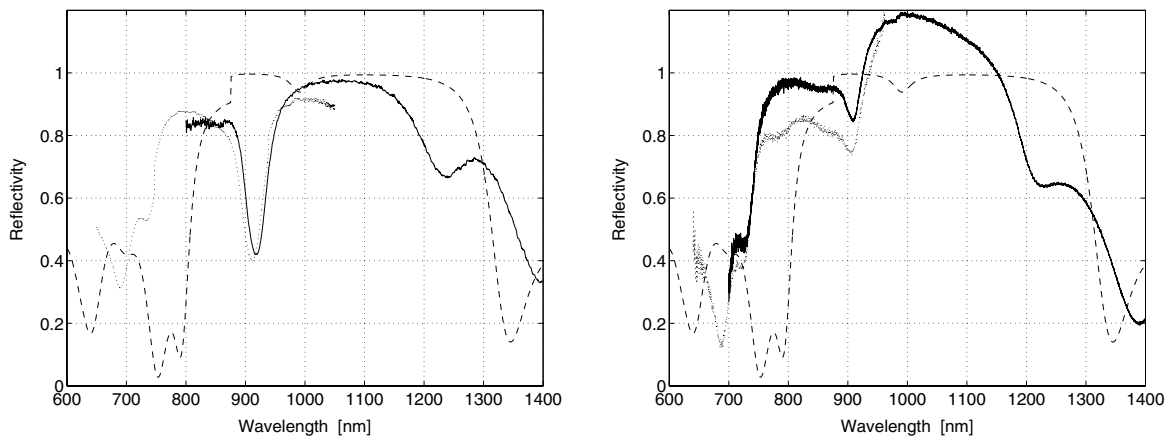


Figure 4.59: Reflectivity spectrum of a 200 μm MCLED from sample S1907 B (left) and a 200 μm MCLED from sample S1907 D (right); comparison measurement with Si CCD (dotted line), InGaAs array detector (solid line) and simulation (dashed line)

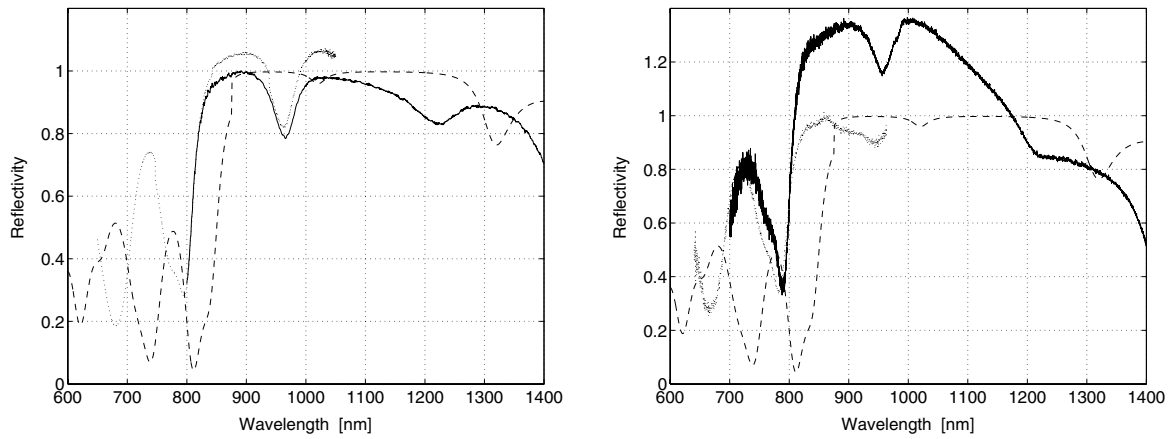


Figure 4.60: Reflectivity spectrum of a 200 μm MCLED from sample S1908 B (left) and a 100 μm MCLED from sample S1908 D (right); comparison measurement with Si CCD (dotted line), InGaAs array detector (solid line) and simulation (dashed line)

The reflectivity curve of the device from sample S1910 a agrees quite well with the simulated spectrum. In case of the device of type S1905 D the Fabry-Perot cavity peak seems to be located around 850 nm, however at these wavelength the characteristics are strongly influenced by the absorption in the GaAs. The devices with structure S1907 and S1908 clearly show a distinct blue-shift of the cavity peak. This shows that after processing the cavity lengths of these oxide DBR devices are much shorter than designed and that the detunings are not negative but highly positive. The calculated and measured Fabry-Perot cavity peaks are compiled in table 4.15, together with the results from the reflectivity measurements directly after growth for the semiconductor DBR structures.

Table 4.15: Designed and measured Fabry-Perot cavity peak positions of TE MCLEDs emitting at 970 nm

Sample	Design [nm]	Measurements [nm]	Shift [nm]
S1904 as grown	1018	1018	0
S1910 as grown	988	985	-3
S1910 a	988	976	-12
S1905 A	987	940 – 950	-42
S1905 D	987	850 – 855	-134
S1907 B	991	912 – 918	-76
S1907 D	991	905 – 908	-85
S1908 B	1021	962 – 966	-57
S1908 D	1021	945 – 956	-71

Far-Field Emission

The determination of the far-field radiation pattern of a MCLED allows the verification of the detuning of the device after processing. Devices with an optimal detuning for emission into air should show a maximum emission at an angle of 45° from the normal in air. Since the angular emission is very sensitive to the detuning, the comparison of the far-field radiation pattern with the simulation is a simple means of identifying cavity length deviations.

A silicon photodiode is mounted on a rotating arm driven by a motorized actuator. The actuator is controlled via a stepping motor (ORIEL Instruments DC Encoder MikeTM Controller Model 18011). The detector is placed at a distance of approximately 15 cm from the diode and can be rotated by 360° . The emitted light at a certain angle is collected with a diaphragm of variable diameter and focussed on the photodiode with two lenses (see figure 4.61). Assuming a diaphragm aperture diameter of 4 mm and a distance of 6 cm between the device and the diaphragm, the angular resolution corresponds to 2° . Figure 4.62 shows an image of the measurement set-up.

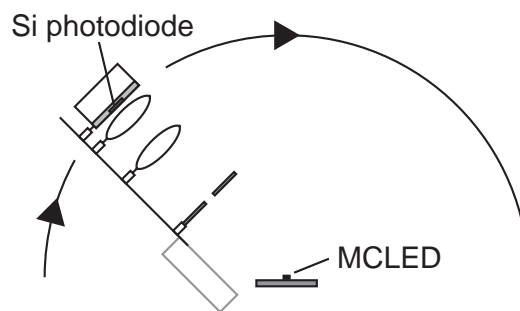


Figure 4.61: Description far-field emission measurement set-up

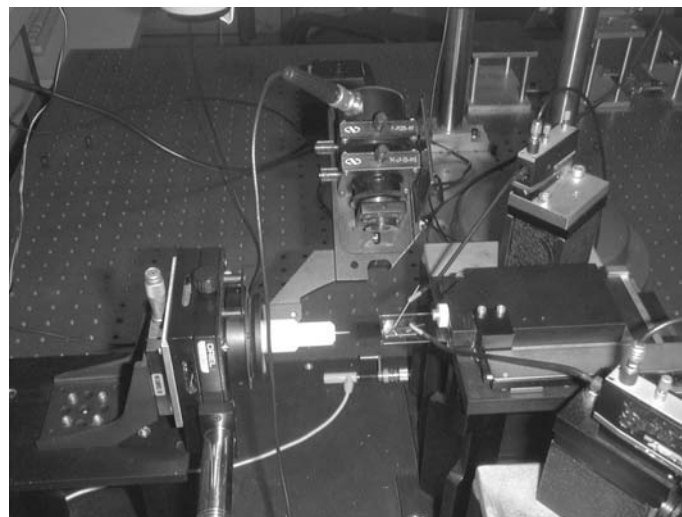


Figure 4.62: Image far-field emission measurement set-up

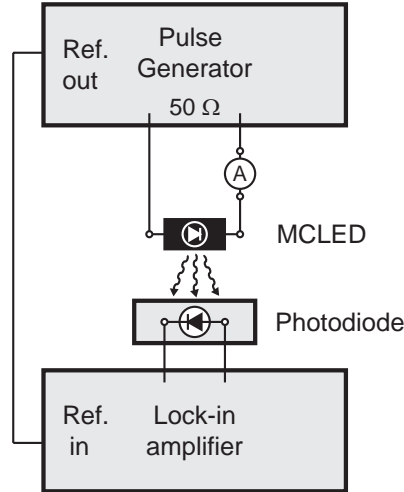


Figure 4.63: Schematic far-field emission measurement set-up

The device is contacted with two probe needles. A square wave AC voltage with a frequency of 10 kHz is applied using a HAMEG HM 8035 Pulse Generator. The device is driven at a peak current corresponding to the current at maximum efficiency determined previously from the L-I-V measurements. The current is monitored with a Digital Multimeter M3900. The photodiode current is detected by means of a Stanford Research Systems SR510 Lock-in Amplifier, which is synchronized with the pulse generator. A schematic of the set-up is depicted in figure 4.63.

Figure 4.64 shows the measured and simulated far-field emission spectra of samples S1907 B and S1908 B. For both structures the measurement deviates drastically from the simulation, indicating zero or even a positive detuning. The structures as designed on the other hand show emission peaks at 36° and 61° off normal for structure S1907 and S1908, respectively.

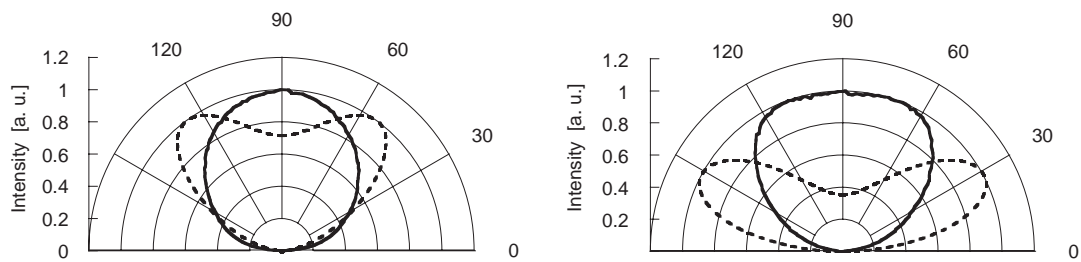


Figure 4.64: Far-field emission spectrum of a $200\ \mu\text{m}$ MCLED from sample S1907 B (left) and a $100\ \mu\text{m}$ MCLED from sample S1908 B (right); comparison between measurement (solid line) and simulation (dashed line)

Electroluminescence

The spectral emission of a device depends mainly on three parameters, the collection angle, the device current and the device temperature. In general two different peaks can be distinguished (as long as they are not coinciding). One is corresponding to the QW emission, the other one to the cavity resonance.

By increasing the collection angle the cavity resonance peak is blue-shifting as the optical length of the cavity is decreasing with increasing angle due to Bragg's law:

$$n\lambda = 2d\sin\theta \quad (4.5)$$

n being the order of reflection, λ the wavelength, d corresponds in this case to the cavity length and θ to the incident angle which corresponds to 90° in the growth direction. In the case of an ideal negative detuning the cavity resonance wavelength is larger than the quantum well emission at 0° (0° being the normal direction) but coincides with the emission peak at a collection angle of 45° .

Increasing the current density leads to a broader quantum well emission spectrum. Consequently the overlap of the quantum well emission and the cavity resonance improves with increasing current density. This leads to an increase in the cavity resonance peak intensity relative to the quantum well emission.

Changing the temperature allows to shift the quantum well emission peak, since the bandgap of the active layer is much more temperature-sensitive than the refractive indices of the cavity layers [242]. The gap energy decreases with increasing temperature as following

$$E_g = E_g(0K) - \frac{\alpha T^2}{T + \beta} \quad (4.6)$$

Therefore the QW emission red-shifts with increasing temperature. In the case of a positive detuning at room temperature the quantum well emission could therefore be decreased below the cavity resonance by cooling the device. However this would have to be done under vacuum to avoid condensation.

The emission spectra are recorded with an ANDO AQ-6135A Optical Spectrum Analyzer. A constant voltage is applied to the device with a HP 4145A Semiconductor Parameter Analyzer, which serves as current meter as well. The bare end of an optical fiber connected to the optical spectrum analyzer is brought in close distance to the device.

Due to time limitations and experimental difficulties no temperature-dependent measurements were carried out within the scope of this thesis. The dependence of the electroluminescence on the collection angle as well as on the device current was studied for a $200\ \mu\text{m}$ device from sample S1907 B and a $100\ \mu\text{m}$ device from sample S1908 B. The results are shown in figures 4.65 and 4.66.

For the variation of the collection angle the device was driven at a constant current corresponding to the current at maximum efficiency determined previously from the L-I-V measurements. The normal to the device surface is defined as 0° . As can be seen in figure 4.65, the QW emission peak can be identified at 970 nm and for larger angles the cavity resonance peak is visible at lower wavelengths. These measurements confirm therefore that for both devices the detuning is either zero or positive already

at 0° , which shows that the cavities of these devices are too short.

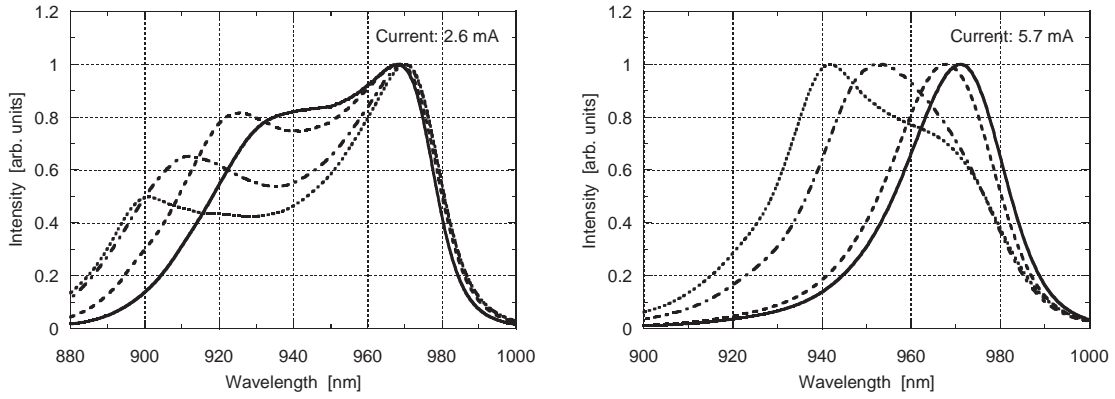


Figure 4.65: Electroluminescence for different collection angles of a $200\ \mu\text{m}$ MCLED from sample S1907 B at 2.6 mA (left) and a $100\ \mu\text{m}$ MCLED from sample S1908 B at 5.7 mA (right); 0° (solid line), 25° (dashed line), 45° (dash-dot line) and 60° (dotted line)

The spectra at different device currents were taken at an angle of 0° for sample S1907 B and 45° for sample S1908 B. The increase of the cavity resonance peak intensity relative to the quantum well emission with increasing current can clearly be seen in figure 4.66 for both structures.

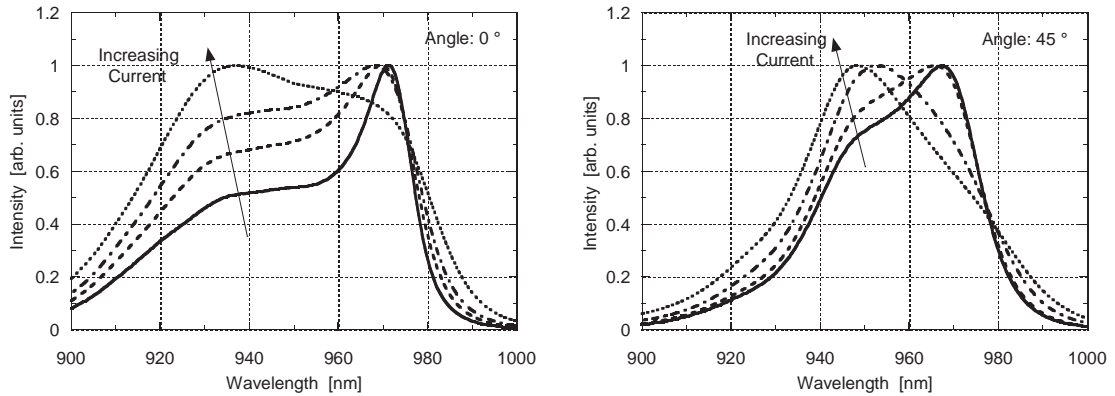


Figure 4.66: Electroluminescence for different drive currents of a $200\ \mu\text{m}$ MCLED from sample S1907 B at 0° (left) and a $100\ \mu\text{m}$ MCLED from sample S1908 B at 45° (right); 0.1, 1.0, 2.6, and 10 mA (left); 0.4, 1.0, 5.7, and 11 mA (right)

Figure 4.67 shows the simulated cavity resonances for different collection angles of structures S1907 and S1908 as designed. The resonance wavelength decreases with increasing collection angle. For cavity resonance wavelengths larger than the QW emission wavelength (970 nm in this case) the maximum measured intensity is centered at 0° and its intensity simply decreases with increasing wavelength.

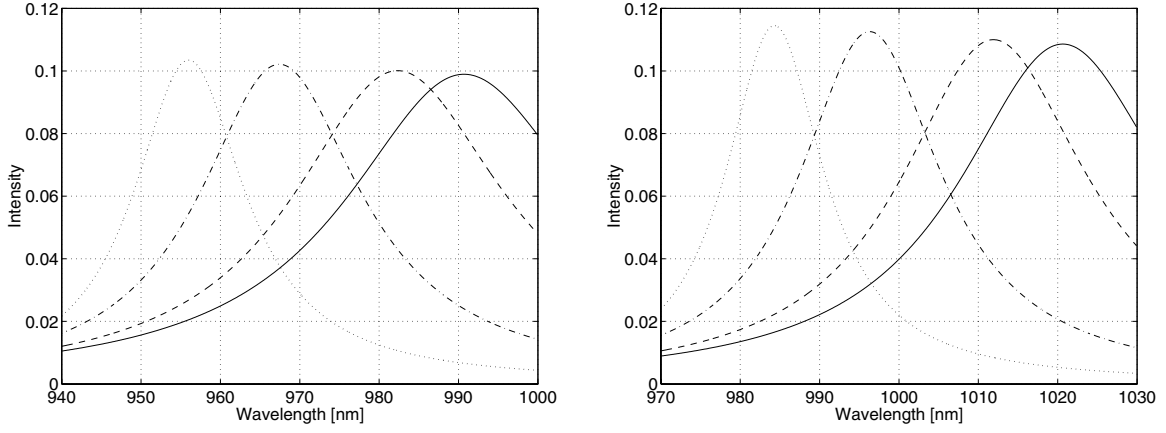


Figure 4.67: Simulation based on design parameters of cavity resonance for different collection angles for structures S1907 (left) and S1908 (right); 0° (solid line), 25° (dashed line), 45° (dash-dot line) and 60° (dotted line)

The simulation results are compared with the measurements in table 4.16 and 4.17. For smaller angles the cavity peak value can only be approximated from the measurements, as the peak coalesces with the emission peak. This effect is more pronounced in case of sample S1908 B.

At 45° the detuning should be zero for structure S1907 and around -25 nm for structure S1908, as it is optimized for emission into epoxy. However, from the measurements values of $+60$ and $+15$ nm can be deduced for samples S1907 B and S1908 B, respectively. Hence these observations indicate a blue-shift of the Fabry-Perot cavity resonance of approximately 60 nm for sample S1907 B and 40 nm for sample S1908 B.

Table 4.16: Cavity resonance peaks at different collection angles for a $200\ \mu\text{m}$ device from sample S1907 B

Angle [$^\circ$]	Simulation [nm]	Measurement [nm]
0	991	≈ 935
25	982	926
45	967	912
60	956	902

Table 4.17: Cavity resonance peaks at different collection angles for a $100\ \mu\text{m}$ device from sample S1908 B

Angle [$^\circ$]	Simulation [nm]	Measurement [nm]
0	1021	-
25	1012	-
45	996	≈ 954
60	984	942

4.6 Discussion

4.6.1 Semiconductor DBR Devices

The semiconductor DBR devices show efficiencies for emission into air which are quite close to the theoretical values. According to the reflectivity measurements the stopband and the Fabry-Perot cavity peak are more or less situated at the designed wavelengths. The fact that for the devices of type S1904 an efficiency for emission into air was measured which is significantly higher than the simulated one can have two different origins. It is possible that the cavity is slightly shorter than designed and has therefore an extraction efficiency curve shifted to lower wavelengths. This would considerably increase the overlap of the QW emission and the extraction efficiency curve (see figure 4.4), which means a higher potential extraction into air. In addition a significant amount of photon recycling can be assumed to take place in these devices since they are comparatively large [117]. This assumption is affirmed by the rapidly decreasing efficiency with decreasing device size (values not shown).

The TLM measurements show very similar contact resistivities for the devices with a non-alloyed gold contact and the ones with an alloyed Ti/Pt/Au contact. Comparable efficiencies were measured for the two types of devices in case of structure S1910. The low efficiencies measured for devices from sample S1904 can only be explained with a deterioration of this sample during the processing steps after the p-contact deposition. It is assumed that the vicinity of the p-side oxide aperture to the top p-contact leads to additional stresses and maybe even partial delamination near the active region during the p-contact alloying. Figure 4.45 shows that the efficiency curve is slightly displaced to higher current densities for these devices, a sign of additional non-radiative recombination.

The comparison between the devices without and with p-contact grid shows that for both structures the implementation of a grid leads to a slight decrease in efficiency. The additional shadowing by the grid seems to be more important than its ameliorative effect on the uniformity of the current injection. However the reduction is smaller for the devices with an alloyed p-contact. This might be due to the fact that the metal diffusion under the grid lines can be reduced by the use of an alloyed contact which would lead to slightly less shadowing. The sheet resistivity of the cap layer seems to be low enough to achieve a homogeneous current injection with the use of just a p-contact ring.

The limited extraction into glycerol can be explained with a droplet shape which is much flatter than the ideal hemispherical geometry and a reduced refractive index of the glycerol due to water absorption.

Simulations show that with phase-shift MCLED structures with semiconductor DBRs emitting in the near infrared significantly higher external quantum efficiencies than for standard MCLEDs are achievable. Up to 24 % for emission into air and 34 % for emission into epoxy are theoretically possible. Preliminary devices with different kind of p-contacts have been realized. Efficiencies of 19 % for emission into air and 20 % for emission into glycerol, a liquid with a similar refractive index as epoxy have been measured for $400 \times 400 \mu\text{m}^2$ oxide aperture devices [134]. The highest efficiencies for top emitting semiconductor DBR MCLEDs published beforehand were 10 % by Carlin et al. [123].

4.6.2 Oxide DBR Devices

Apart from sample S1905 A the oxide DBR devices show efficiencies which are significantly lower than expected. The reflectivity curves as well as the angular and spectral emission characteristics of devices from samples S1907 B and S1908 B all show that the cavities are too short. Instead of a negative detuning the devices show a highly positive detuning. This means a directional emission but a reduced extraction efficiency.

Similarly to the semiconductor DBR devices the use of a p-contact grid leads to a reduction in efficiency. Apparently for this device type as well the additional shadowing is more important than the improved current injection. The contact resistivities of the p-contacts used for these devices are one to two orders of magnitude higher than for the more standard contacts used for the semiconductor DBR devices. Nevertheless the I–V characteristics are comparable.

The fact that on both samples with structure S1908 the highest efficiencies are found for the $100\mu\text{m}$ devices implies that there is a problem related to the electrical properties of this structure. In addition the efficiency curves are shifted to higher current densities by at least one order of magnitude, as can be seen in figures 4.52 and 4.53. The TLM measurements yield similar sheet resistivities for the p^+ -cap layer. A possible explanation could be that the doping of the n-intracavity contact layer or its thickness after etching are insufficient.

All the additional measurements carried out on the devices from samples S1907 B and S1908 B indicate a positive detuning after processing and hence a cavity which is too short. The reflectivity measurements of the structures as grown on the other hand indicate that the cavity length before processing is correct. Based on these results the defects that appeared during the device processing of samples S1907 B and S908 B (see figures 4.27 and 4.28) are assumed to be due to a punctiform lateral oxidation of the $\text{p-Al}_{0.90}\text{Ga}_{0.10}\text{As}$ layer in the top DBR pair starting from tiny holes in the structure, such as misfit dislocations or threading dislocations. An oxidation of this layer leads to a higher index contrast top DBR and hence an increased confinement and a reduced cavity length. In the case of these MCLED structures, both effects lead to a reduced external quantum efficiency, the first one due to a reduced extraction efficiency and the second one due to a inappropriate detuning. In addition the lack of an interface grading of the oxidation layers might result in a bad quality of the GaAs–oxide interface and can even lead to the formation of voids at the interface.

The reflectivity, far-field and electroluminescence measurement curves could be fitted quite well assuming a complete oxidation of the $\text{p-Al}_{0.90}\text{Ga}_{0.10}\text{As}$ layer in the top DBR and a partial transformation to air of the GaAs next to the oxidation layers. These thicknesses were estimated to be 8 nm in the n-GaAs intracavity contact layer and 10 nm in the GaAs bottom DBR layers. The simulation results are shown in figures 4.68–4.70.

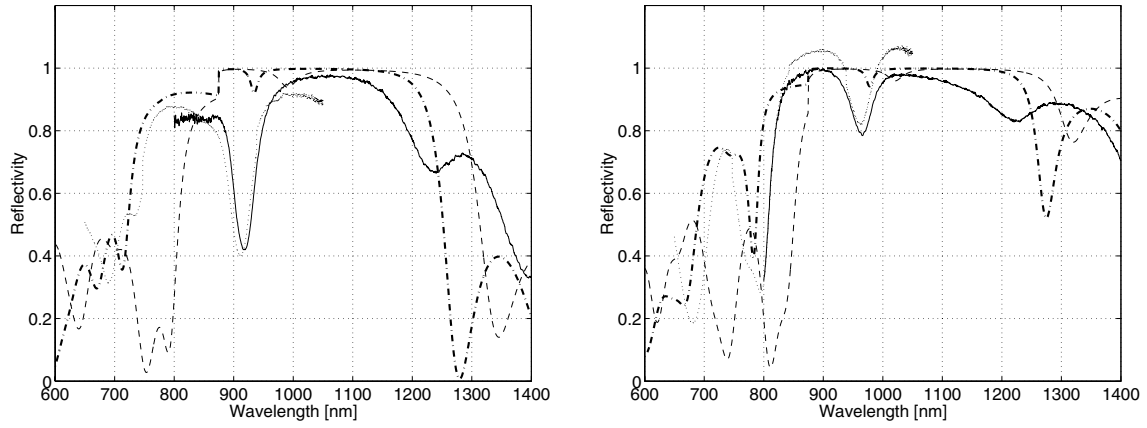


Figure 4.68: Fitted simulation reflectivity spectrum compared with measurements of a 200 μm MCLED from sample S1907 B (left) and a 200 μm MCLED from sample S1908 B (right); measurement with Si CCD (dotted line), InGaAs array detector (solid line), simulation structure as designed (dashed line) and simulation corrected structure (dash-dot line)

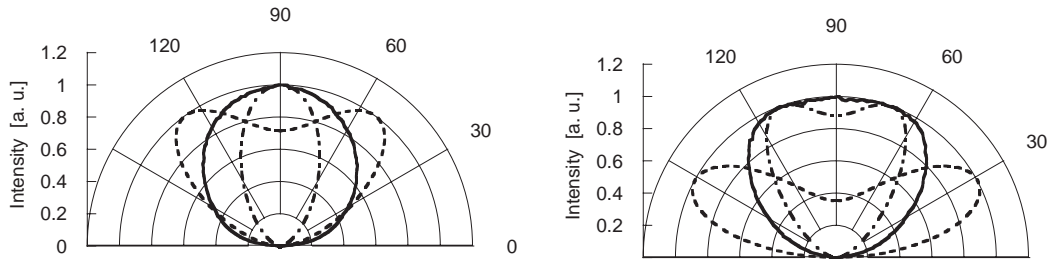


Figure 4.69: Corrected simulation far-field emission spectrum compared with measurements of a 200 μm MCLED from sample S1907 B (left) and a 200 μm MCLED from sample S1908 B (right); measurement (solid line), simulation structure as designed (dashed line) and simulation corrected structure (dash-dot line)

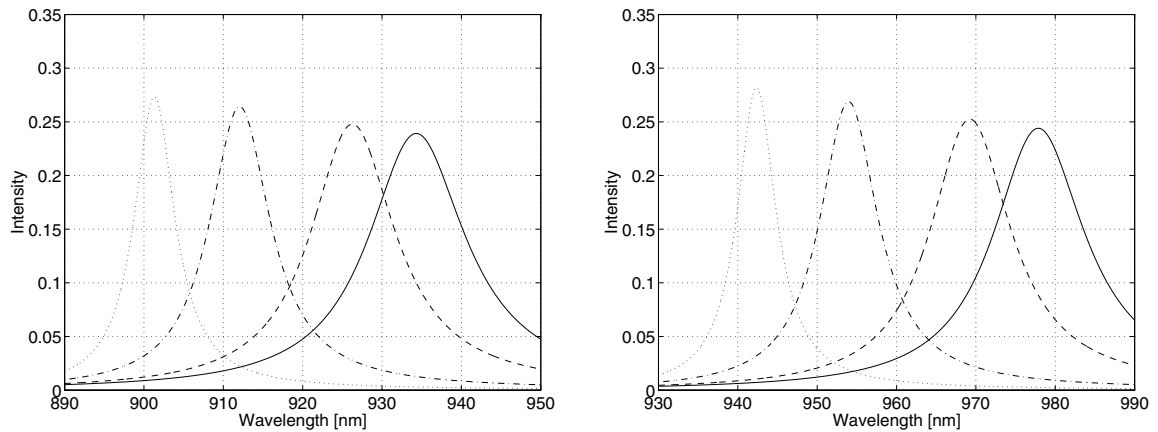


Figure 4.70: Corrected simulation cavity resonance for different collection angles for structure S1907 (left) and structure S1908 (right); 0° (solid line), 25° (dashed line), 45° (dash-dot line) and 60° (dotted line)

As can be seen in tables 4.18 and 4.19 the cavity resonance simulations match very well with the electroluminescence measurements. However the fit is not as good for the far-field emission and the reflectivity measurements. This can be explained with the only partial oxidation of the p-Al_{0.90}Ga_{0.10}As layer, hence the measured spectra correspond to a superposition of the structure with and without oxidation of this layer. The simulation results for the structures with a non-oxidized p-Al_{0.90}Ga_{0.10}As layer are close to the ones for the designed structure, as the cavity is only slightly shortened by the void formation at the semiconductor–air interface. As the defect density is lower on sample S1908 B, the measurements differ more from the simulation including an oxidation of the p-Al_{0.90}Ga_{0.10}As layer.

Table 4.18: Cavity resonance peaks at different collection angles for a 200 μm device from sample S1907 B

Angle [°]	Simulation		Measurement [nm]
	design [nm]	corrected [nm]	
0	991	934	≈ 935
25	982	926	926
45	967	912	912
60	956	901	902

Table 4.19: Cavity resonance peaks at different collection angles for a 100 μm device from sample S1908 B

Angle [°]	Simulation		Measurement [nm]
	design [nm]	corrected [nm]	
0	1021	978	-
25	1012	969	-
45	996	954	≈ 954
60	984	942	942

The corrected simulations of the extraction efficiency for monochromatic emission and the estimated external quantum efficiencies for the corrected structures are presented in figure 4.71 and tables 4.20 and 4.21. The latter ones show the calculated external quantum efficiencies for the structures with a non-oxidized p-Al_{0.90}Ga_{0.10}As top DBR layer as well (extraction efficiency curves not shown). Obviously the structural changes lead to a drastically decreased overlap between the intrinsic emission and the extraction efficiency in case of structure S1907 for emission into air and epoxy. Without the parasitic oxidation of the top DBR layer on the other hand the characteristics are quite close to the designed ones. The measurement results are somewhere in between, indicating that approximately half of the device surface the p-Al_{0.90}Ga_{0.10}As layer is oxidized.

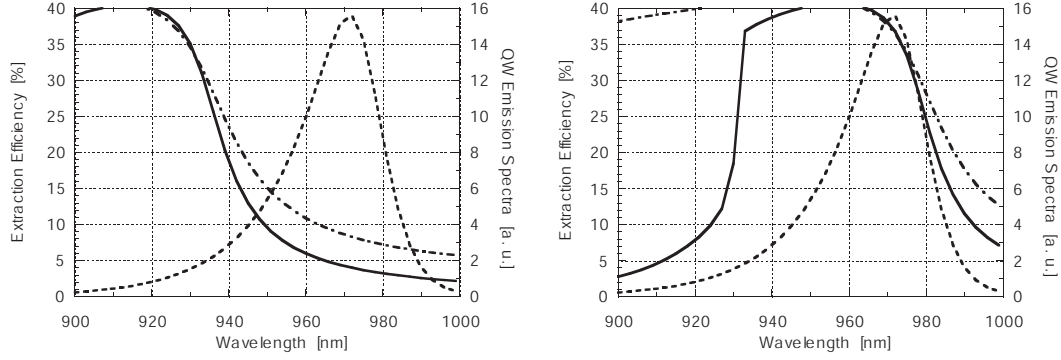


Figure 4.71: Corrected simulation extraction efficiency for structure S1907 (left) and S1908 (right); emission into air (solid line) and epoxy (dash-dot line) plus intrinsic emission spectrum (dashed line)

Table 4.20: Theoretical external quantum efficiencies for structure S1907 compared with measurement results

	Design [%]	Corrected		Measurements [%]
		with ox. [%]	without ox. [%]	
$\eta_{\text{ext}}(\text{air})$	30	8	25	14
$\eta_{\text{ext}}(\text{epoxy})$	35	12	28	19

Table 4.21: Theoretical external quantum efficiencies for structure S1908 compared with measurement results

	Design [%]	Corrected		Measurements [%]
		with ox. [%]	without ox. [%]	
air	17	34	25	14
epoxy	38	37	36	16

In case of S1908 on the other hand the shift leads to a significant increase of the external quantum efficiency for emission into air, whereas the one for emission into epoxy does not seem to be affected by the different modifications. The fact that the measured efficiencies are much lower is explained with the poor electrical properties of these devices. Increased resistivities can lead to additional heating within the device which in turn can cause an even more positive detuning by red-shifting the QW emission.

The low external quantum efficiencies of the oxide DBR devices can therefore be explained by a partial parasitic oxidation of the p- $\text{Al}_{0.90}\text{Ga}_{0.10}\text{As}$ layer in the top DBR and a delamination and void formation at the GaAs-oxide interfaces. The parasitic oxidation of the p- $\text{Al}_{0.90}\text{Ga}_{0.10}\text{As}$ layer is believed to start from dislocations in the top layers. The refractive index change from 3.5 to 1.6 leads to a significant reduction of the optical length of the cavity. These point defects could be avoided by optimizing the epitaxial growth conditions.

The assumption of an interface degradation in the bottom DBR is based on several reports showing that abrupt interfaces lead to weak and porous GaAs–oxide interfaces [210,223,224,243,244]. According to a transmission electron microscope (TEM) analysis by Guha et al. [243] porosities at the interface extend to a few hundred angstroms on either side of the interface. This void formation leads to an additional cavity length reduction and to a blue-shift of the bottom DBR stopband. The successful realization of VCSELs with oxide DBRs shows that these problems can be avoided by an alloy grading at the interfaces between the high aluminum content and the GaAs layers [218,223,245,246]. For VCSELs the interface grading is used as well to reduce the electrical resistance of the DBRs [195,247,248].

The structure S1905 contains no additional top DBR pair and is therefore not susceptible to the above mentioned parasitic oxidation. The fact that the good results from sample S1905 A could not be reproduced is explained in part with a degradation of the GaAs–Al_{0.98}Ga_{0.02}As interface with time by being exposed to air. The sample S1905 A has been processed soon after the growth whereas the other samples were processed 1.5–3 years later. As structure S1905 is optimized for emission into air, its external quantum efficiency for emission into air is quite sensitive to cavity length changes. Simulations show that an interface degradation similar to the one estimated for structures S1907 and S1908 reduces the theoretical external quantum efficiency to 22 % for emission into air. The large blue-shift of the Fabry-Perot cavity peak for the devices from sample S1905 D might be related to a more pronounced interface degradation than for S1907 B and S1908 B. This would explain as well why only a few devices are working on this sample.

By incorporating the insights from this batch efficiencies greater than 30% should be attainable with structures with an interface grading of the oxidation layer and optimal epitaxial growth conditions. Due to time constraints it was not possible to fabricate new optimized oxide DBR devices within the framework of this thesis.

4.7 Conclusions

Different types of high-efficiency top emitting near infrared MCLEDs have been realized. The structures consist of a phase-shift cavity and a high reflectivity bottom DBR. The top GaAs–air interface is used as a weak outcoupling reflector. With semiconductor DBR devices record external quantum efficiencies for this type of 19 % have been demonstrated. Oxide DBR devices showed efficiencies up to 28 %, which corresponds to the highest ever reported efficiency for a MCLED.

The implementation of an oxide bottom DBR to phase-shift MCLEDs increases the limit for the attainable external quantum efficiencies. Simulations predict values of approximately 30 % for emission into air and nearly 40 % for emission into epoxy. Thanks to the higher index contrast the penetration depth is much smaller, which means a reduced effective cavity length. On the other hand the device design and the fabrication become more complicated and the devices more fragile. This is related to a degradation of the GaAs–oxide interface and a parasitic oxidation of other high aluminum content AlGaAs layers in the structure. A grading of the interfaces in the oxide DBR layers is therefore crucial for a good device performance.

Chapter 5

Top Emitting MCLEDs at 650 nm

5.1 Introduction

Red emitting LEDs are commercially interesting, as they have a broad range of possible applications, from general lighting to indicators, traffic lights or break lights. The high brightness of red MCLEDs makes them interesting for applications, where the light has to be coupled into an optical system with a given numerical aperture, like plastic optical fibers (POFs), optical scanners, printers or even displays.

POFs are becoming increasingly popular for low-cost short-haul communication systems or local area networks (LANs), e.g. for communication within a building, an airplane or a car [23–25]. They are inexpensive, robust and easy to align. The losses of plastic fibers however are about 10^3 times higher than in silica fibers. Figure 5.1 shows the attenuation of a poly(methyl methacrylate) (PMMA) step-index plastic optical fiber [9]. The preferred communication window is at 650 nm, where the losses are of the order of 0.15 dB/m. The attenuation decreases even further with decreasing wavelength, but the material dispersion increases at the same time.

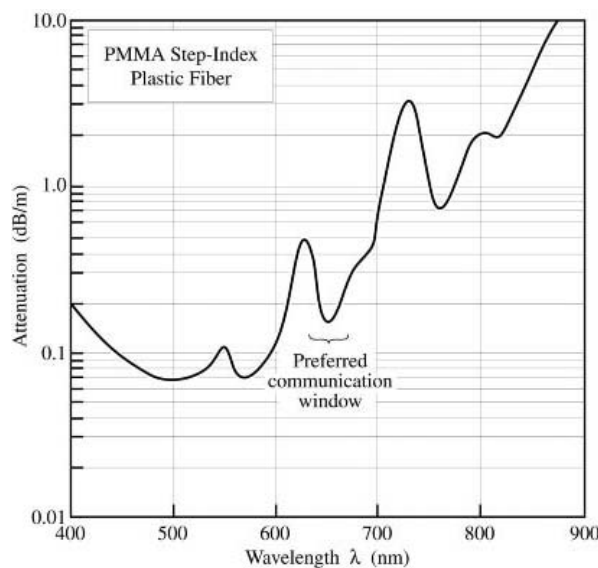


Figure 5.1: Attenuation of a PMMA step-index plastic optical fiber [9]

Red MCLEDs are especially interesting as light sources for POF communication since they show a higher brightness and modulation bandwidth than conventional LEDs [249,250]. The advantages compared to red VCSELs are lower fabrication costs, higher yield and reliability, a threshold-less operation and a better thermal behavior [251].

AlGaInP has become the material system of choice for red LEDs and has led to record efficiencies [16]. The design of GaInP/AlGaInP MCLEDs however is more challenging than for the near infrared InGaAs/GaAs system [195,249,252]. The QW confinement potentials are significantly smaller, resulting in an increased carrier leakage. The larger thermal resistivity (W) and the high electrical resistivity for p-type material of the high Al-content AlGaInP confinement layers leads to an increased sensitivity to Joule heating [253,254]. Less restrictive is the limited current spreading in high Al-content p-AlGaInP layers due to a low hole mobility [255,256] and limited p-doping levels, as it can be circumvented with the use of a p-AlGaAs current spreading layer.

Table 5.1: Physical heterostructure parameters for InGaAs/AlGaAs and GaInP/AlGaInP lattice-matched (LM) and strained quantum well (SQW) heterostructures [252]

Parameter	$\text{In}_x\text{Ga}_{1-x}\text{As}/\text{Al}_{0.4}\text{Ga}_{0.6}\text{As}$	$\text{In}_x\text{Ga}_{1-x}\text{P}/\text{Al}_{0.5}\text{Ga}_{0.5}\text{InP}$
ΔE_C	350 meV for $x = 0$ (LM) 480 meV for $x = 0.2$ (SQW)	≈ 165 meV for $x = 0.5$ (LM) ≈ 225 meV for $x = 0.6$ (SQW)
ΔE_V	220 meV for $x = 0$ (LM) 290 meV for $x = 0.2$ (SQW)	≈ 110 meV for $x = 0.5$ (LM) ≈ 150 meV for $x = 0.6$ (SQW)
W	$2 < W < 10 \text{ cm}^\circ\text{C}/\text{W}$	$W > 19 \text{ cm}^\circ\text{C}/\text{W}$

The fact that GaAs is absorbing in the visible wavelength range leads to several restrictions. In order for the AlGaAs layers to be transparent, their aluminum content needs to be at least 50 %. In a MCLED structure with a bottom intracavity contact (similar to the one in the previous chapter) this aggravates the formation of an ohmic contact on the AlGaAs intracavity contact layer as well as the parasitic vertical oxidation of this layer during the lateral wet oxidation of the low index DBR layers. A GaAs cap layer to inhibit an exposure to air and oxidation of the underlying AlGaAs layer is unavoidable, however its thickness needs to be kept as thin as possible. Furthermore the light cannot be extracted efficiently through the substrate, therefore the structure has to be either top emitting or the substrate needs to be removed.

In addition this leads to a further reduction of the refractive index contrast for $\text{Al}_x\text{Ga}_{1-x}\text{As}/\text{AlAs}$ DBRs, $\Delta n = 0.38$ at 650 nm for $x = 0.5$. An alternative material system for DBRs is $\text{Al}_{0.51}\text{In}_{0.49}\text{P}/(\text{Al}_y\text{Ga}_{1-y})_{0.51}\text{In}_{0.49}\text{P}$ [257,258]. However in that case the minimum Al-content is 20 % at 650 nm, which leads to an even smaller refractive index contrast of $\Delta n = 0.27$. This type of DBR becomes interesting for lower emission wavelengths, in the orange or green [257,259,260]. As for the near-IR DBRs, the refractive index contrast can be drastically increased with the use of oxide DBRs, either using low Al-content AlGaAs as high index material [261] or AlGaInP [262–265].

Top emitting AlGaInP MCLEDs with a bottom AlGaAs/ AlO_x DBR, AlGaAs current injection and spreading layers and the interface GaAs/air as top mirror were fabricated. The performance of devices without and with a p-contact grid is compared.

5.2 Structure

The red MCLED structure presented in this chapter is based on the near infrared structure with a bottom oxide DBR treated in the previous chapter, with the difference that in this case the phase-shift cavity principle cannot be applied. Due to the lower confinement potentials the barriers cannot be kept as thin. This structure thus contains a standard 2λ cavity, similar to the one used in MCLED structures by OSRAM already previously [119,266]. The p-current spreading layer and the n-intracavity contact layer do not consist of GaAs but of $\text{Al}_{0.7}\text{Ga}_{0.3}\text{As}$ in order to minimize the optical absorption in the cavity. For the same reason the GaAs cap layer is very thin.

The bottom DBR contains 3.5 pairs of undoped $\text{Al}_{0.5}\text{Ga}_{0.5}\text{As}/\text{Al}_{0.98}\text{Ga}_{0.02}\text{As}$ with thick $\text{Al}_{0.95}\text{Ga}_{0.05}\text{As}$ intermediate grading layers. The 2λ cavity is made up of a single compressively strained GaInP QW surrounded by $\lambda/4$ $(\text{Al}_{0.5}\text{Ga}_{0.5})_{0.5}\text{In}_{0.5}\text{P}$ barrier layers and $(\text{Al}_{0.7}\text{Ga}_{0.3})_{0.5}\text{In}_{0.5}\text{P}$ confinement layers. The latter are doped with tellurium or magnesium for n- or p-doping, respectively. On the n-side a Te-doped $\lambda/4$ $\text{Al}_{0.7}\text{Ga}_{0.3}\text{As}$ intermediate layer and a highly Te-doped $\lambda/4$ $\text{Al}_{0.7}\text{Ga}_{0.3}\text{As}$ n-intracavity contact layer are added. The top p-side contains a $\lambda/2$ carbon-doped $\text{Al}_{0.7}\text{Ga}_{0.3}\text{As}$ current spreading layer and a thin highly C-doped GaAs p-contact and surface protection layer with a thickness of 10 nm.

The epitaxial structure was designed by Maxime Rattier (Ecole Polytechnique, Paris) and Christian Karnutsch (OSRAM Opto Semiconductors), based on the near infrared oxide DBR structures from the previous chapter by Ross Stanley. This structure is labelled K1439 and was grown by metalorganic vapor phase epitaxy (MOVPE) by Christian Karnutsch at the OSRAM Opto Semiconductors R&D lab in Regensburg, Germany. An n-doped 4 inch (100) GaAs wafer tilted by 6° towards $\langle 111 \rangle_A$ is used as substrate. This allows to suppress an atomic ordering of the indium and gallium (or aluminum) atoms in the GaInP and AlGaInP layers along the (111) crystal planes [10,267,268]. Otherwise this superlattice formation would result in a significantly reduced bandgap energy and wider PL linewidths [269]. The refractive index profile of the structure is displayed in figure 5.2, the detailed structure can be found in appendix B.

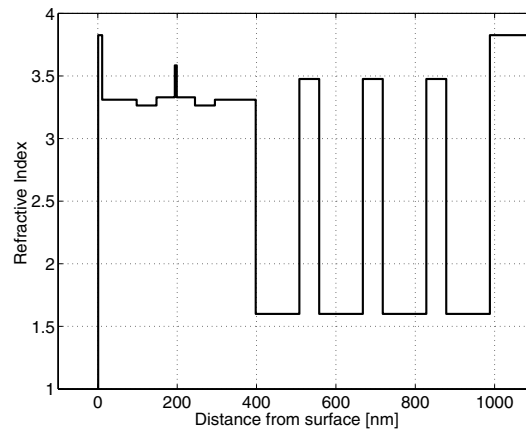


Figure 5.2: Refractive index profile of structure K1439

5.3 Simulation

The light extraction properties of the structure are calculated with the simulation program described in section 3.3. The refractive index calculation is based on the data by Adachi [162] for AlGaAs and on the analytical model presented by Moser et al. [270] for AlGaInP. The refractive index of AlO_x is assumed to be 1.6 over the whole wavelength range of interest [138–141] and the vertical contraction during the oxidation is estimated to be 8 % [140,141,219].

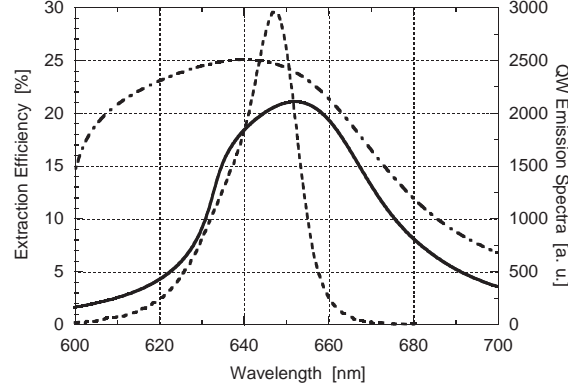


Figure 5.3: Simulated extraction efficiency of structure K1439; emission into air (solid line) and epoxy (dash-dot line) plus intrinsic emission spectrum (dashed line)

Figure 5.3 shows the extraction efficiency of structure K1439 as a function of wavelength, calculated for monochromatic emission into air and epoxy. The QW emission spectrum used for the integration is displayed as well. Table 5.2 shows the distribution of the emission in the different modes at 650 nm, for emission into air and epoxy.

Table 5.2: Fractions of emission in the various kinds of modes for structure K1439 at 650nm, for emission into air and epoxy

	extracted [%]	leaky [%]	guided [%]
air	24	15	61
epoxy	27	10	62

The external quantum efficiencies attained for this structure by integration of the extraction efficiency spectrum with the QW electroluminescence spectrum are 18 % for emission into air and 24 % for emission into epoxy (see table 5.3).

Table 5.3: Theoretical external quantum efficiencies of structure K1439 for emission into air and epoxy

	$\eta_{\text{ext}}(\text{air})$ [%]	$\eta_{\text{ext}}(\text{epoxy})$ [%]
design	18	24

5.4 Fabrication

The fabrication of the red top emitting MCLEDs with an oxide DBR is similar to the fabrication of the near infrared top emitting devices with an oxide bottom reflector. The same mask set is used. However the top GaAs layer is not thick enough to protect the underlying $\text{Al}_{0.7}\text{Ga}_{0.3}\text{As}$ layer from surface oxidation during the bottom DBR oxidation. Hence the surface needs to be covered with a protection layer during the oxidation. Common materials are silicon dioxide (SiO_2) and silicon nitride (Si_3N_4). They can both be deposited via plasma enhanced chemical vapor deposition (PECVD). It was decided to use the latter one, as it is believed to be more dense than the SiO_2 deposited with the PECVD machine in the cleanroom of the institute. As the stoichiometry of the layers deposited with this machine is not very well known, the deposited silicon nitride will be labelled as SiN_x ; it might even be an oxynitride. The surface protection layer is deposited prior to the oxidation trench etch and needs to be etched separately. Dry and wet etching solutions exist for silicon nitride. The deployed photoresist does not adhere very well to the surface of the silicon nitride, therefore an adhesion promoter, hexamethyldisilazane (HMDS), is deposited on the sample surface prior to the resist spinning.

5.4.1 Etching

Silicon Nitride Etch

The silicon nitride needs to be etched with a high selectivity versus GaAs in order to preserve the intended cavity length.

Si_3N_4 is known to be etched by hydrofluoric acid (HF) [271]. HF does not attack GaAs at a noticeable rate, however its etching rate increases drastically with Al-content in $\text{Al}_x\text{Ga}_{1-x}\text{As}$ [67,272,273]. Therefore HF can be used to etch the silicon nitride layer, as long as the GaAs cap layer protects the underlying $\text{Al}_{0.70}\text{Ga}_{0.30}\text{As}$. In the present case the SiN_x was etched with a buffered hydrofluoric acid solution (BHF), called buffered oxide etch (BOE) as well. It is a pH buffered solution consisting of ammonium fluoride (NH_4F) and hydrofluoric acid in the ratio 7:1.

Several dry etching methods have been proposed as well for Si_3N_4 [271]. The SiN_x used for the fabrication of the red MCLEDs discussed in this chapter was found to be etched with a high rate and a high selectivity versus GaAs with a CF_4/O_2 Plasma.

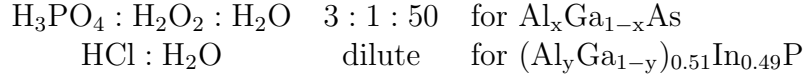
Selective Wet Mesa Etch

For the mesa etching a selective etch solution had to be found in order to stop on the n- $\text{Al}_{0.7}\text{Ga}_{0.3}\text{As}$ intracavity contact layer. This is a difficult task as the common AlGaInP etchants etch AlGaAs as well. Selective etching of GaInP or AlInP over GaAs can be obtained with several solutions, as well as for AlInP over GaInP . The standard wet etchants for AlGaInP are hot sulfuric acid (H_2SO_4) and dilute hydrochloric acid (HCl), both are selective with composition [274]. Selective wet etching of GaInP versus GaAs is achieved with HCl [275], $\text{H}_3\text{PO}_4 : \text{HCl} : \text{H}_2\text{O}$ [276] and $\text{HCl} : \text{CH}_3\text{COOH} : \text{H}_2\text{O}_2$ for an appropriate H_2O_2 content [277,278]. AlInP is etched selectively over GaAs with dilute HCl [279], HI , HF and citric acid ($\text{C}_6\text{H}_8\text{O}_7$) [280]. In addition HCl [279], H_3PO_4 ,

H_2SO_4 , HI, HF and citric acid show much higher etch rates for AlInP than for GaInP [280].

Hence HCl was chosen as etchant for AlGaInP, although it is only selective over GaAs and not $\text{Al}_{0.7}\text{Ga}_{0.3}\text{As}$. It has been shown that the $\text{Al}_x\text{Ga}_{1-x}\text{As}$ etch rate of HCl increases with Al-content [175]. However, as the $(\text{Al}_y\text{Ga}_{1-y})_{0.51}\text{In}_{0.49}\text{P}$ etch rates of HCl increase drastically with Al-content [274], HCl should nevertheless show a small selectivity for $(\text{Al}_{0.7}\text{Ga}_{0.3})_{0.5}\text{In}_{0.5}\text{P}$ over $\text{Al}_{0.7}\text{Ga}_{0.3}\text{As}$. Extensive etch tests indicated that it is possible to stop in the n-doped intermediate $\text{Al}_{0.7}\text{Ga}_{0.3}\text{As}$ layer and preserve the highly doped n-intracavity contact layer, even if the selectivity is not very high. The concentrated phosphoric acid solution consisting of phosphoric acid (H_3PO_4), hydrogen peroxide (H_2O_2) and water, which is not selective between GaAs and $\text{Al}_x\text{Ga}_{1-x}\text{As}$, on the other hand was found to be highly selective versus $(\text{Al}_{0.7}\text{Ga}_{0.3})_{0.5}\text{In}_{0.5}\text{P}$.

Consequently the GaAs and $\text{Al}_{0.7}\text{Ga}_{0.3}\text{As}$ layers have been selectively etched with a concentrated phosphoric acid (H_3PO_4) solution and the $(\text{Al}_y\text{Ga}_{1-y})_{0.51}\text{In}_{0.49}\text{P}$ and $\text{Ga}_{0.51}\text{In}_{0.49}\text{P}$ layers with dilute HCl (approximately 19 w/o).



For convenience the same solutions were used to etch the deep trenches down into the substrate in order to expose the low index layers of the bottom DBR prior to the mirror oxidation.

5.4.2 Contacts

As GaAs is not transparent at 650nm, the n-contact needs to be formed on $\text{Al}_{0.7}\text{Ga}_{0.3}\text{As}$. The difficulties related to the formation of an ohmic contact to $\text{Al}_x\text{Ga}_{1-x}\text{As}$ are known to increase with aluminum content [189], which is in part due to the increasing readiness of $\text{Al}_x\text{Ga}_{1-x}\text{As}$ to oxidize in air [190]. Nevertheless, ohmic behavior on n-doped $\text{Al}_x\text{Ga}_{1-x}\text{As}$ has been shown with Au-Ge-Ni alloys [189,281,282]. Therefore it was decided to use the standard alloyed Ni/Ge/Au/Ni/Au metallization to contact the n^+ - $\text{Al}_{0.7}\text{Ga}_{0.3}\text{As}$ layer, as with this contact good results had been obtained on GaAs previously. However the n-intracavity contact layer could not be deoxidized prior to the metallization, as both standard etchants, HCl and HF, etch high Al-content $\text{Al}_x\text{Ga}_{1-x}\text{As}$ and do not show the same selectivity as versus GaAs. The residual oxide layer might therefore hamper the current injection.

A standard non-alloyed Ti/Au contact was deposited on the top p^+ -GaAs. Due to the small thickness of the GaAs cap layer, the metallization might interact mainly with the underlying $\text{p-Al}_{0.7}\text{Ga}_{0.3}\text{As}$ current spreading layer. Luo et al. [237] showed that a Ti/Pt/Au contact on $\text{p-Al}_{0.2}\text{Ga}_{0.8}\text{As}$ shows a Schottky behavior without alloying, but becomes ohmic after an adequate rapid thermal annealing (RTA) step. All the same it was decided not to anneal the p-contact in order to minimize the thermal stress in the structure from temperature treatments after the mirror oxidation.

5.4.3 Lateral Oxidation

AlGaInP Oxidation

High Al-content $(\text{Al}_x\text{Ga}_{1-x})_{0.51}\text{In}_{0.49}\text{P}$ can be oxidized in a similar way as $\text{Al}_x\text{Ga}_{1-x}\text{As}$ and forms a stable and insulating oxide with a similar refractive index [283,284]. Its current-blocking characteristics have been demonstrated in oxide-defined stripe-geometry laser diodes [285]. However the oxidation rates are significantly lower compared to the ones of $\text{Al}_x\text{Ga}_{1-x}\text{As}$ layers with a similar Al-content and higher temperatures are required for the $(\text{Al}_x\text{Ga}_{1-x})_{0.51}\text{In}_{0.49}\text{P}$ oxidation. Therefore at typical $\text{Al}_x\text{Ga}_{1-x}\text{As}$ oxidation temperatures, the $\text{Al}_x\text{Ga}_{1-x}\text{As}$ oxidation is nevertheless highly selective even versus high Al-content $(\text{Al}_x\text{Ga}_{1-x})_{0.51}\text{In}_{0.49}\text{P}$ layers [262]. This has been confirmed with detailed oxidation tests on the particular structure used in this work.

Parasitic Vertical Oxidation AlGaAs Intracavity Contact Layer

The use of an $\text{Al}_{0.7}\text{Ga}_{0.3}\text{As}$ n-intracavity contact layer has implications on the oxidation process as well. Even though the oxidation rate strongly decreases with decreasing aluminum content [221,227,228], the vertical oxidation of lower Al-content layers adjacent to high Al-content oxidation layers cannot be neglected due to the large length to thickness ratio. For the oxidation of standard GaAs/ $\text{Al}_x\text{Ga}_{1-x}\text{As}$ ($x \geq 0.97$) near infrared DBRs with graded interfaces this is only a minor problem, as it just leads to a slight blue-shift of the resonance wavelength with progressive vertical oxidation of the grading layers [223,224]. This effect is even exploited to form tapered current confinement apertures in VCSELs, in order to reduce scattering losses [286–290]. Another application is the tuning of the cavity resonance wavelength of a VCSEL after epitaxial growth, by partial vertical oxidation of a thick $\text{Al}_x\text{Ga}_{1-x}\text{As}$ ($x \approx 0.7 - 0.9$) tuning layer [291–293].

In the present MCLED structure, however, this leads to an unwanted vertical oxidation of the n- $\text{Al}_{0.7}\text{Ga}_{0.3}\text{As}$ intracavity contact layer which is on top of a bottom DBR oxide layer. This parasitic oxidation limits the maximum oxidation time, as a complete oxidation of the n-intracavity contact layer under the n-contact would lead to an isolation of the device. Hence the bottom mirror of the 350 and 200 μm diameter devices could only be partially oxidized. The parasitic vertical oxidation is schematically shown in figure 5.4. The same effect is taking place in the high index $\text{Al}_{0.5}\text{Ga}_{0.5}\text{As}$ bottom DBR layers to a lesser extent. In order to preserve clarity, this is not shown in the schematic.

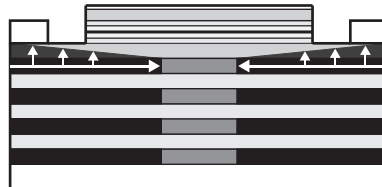


Figure 5.4: Schematic illustration parasitic vertical oxidation n-intracavity contact layer

5.4.4 Fabrication Red Emitting Oxide DBR MCLEDs

The main processing steps are:

- Silicon Nitride Surface Protection Layer Deposition
- Trench Etch in Silicon Nitride
- Trench Etch in Semiconductor
- Lateral Oxidation of Low Index DBR Layers
- Silicon Nitride Removal
- Mesa Etch
- Recess Etch
- N-Contact Deposition
- Dielectric Coating
- P-Contact Deposition

The different steps are described in detail below and are illustrated with schematic cross-sections and top views in figures 5.5–5.15. Different processing runs were carried out with this structure. The sequence of the first run, labelled *K1439 A*, corresponds to the one described in the following, with a wet etching of the silicon nitride. For the second one, *K1439 B*, the mesa etch was done prior to the surface protection layer deposition and the mirror oxidation, and the oxidation times were reduced. As the results of the devices on this sample are inferior they will not be presented. The third run was carried out as a reference without surface protection layer and mirror oxidation, *K1439 C*. The last sample, *K1439 D*, was processed the same way as the first one, except that the silicon nitride was etched via plasma etching and the oxidation temperature was reduced in an attempt to minimize the parasitic vertical oxidation of the n-intracavity contact layer. Tests carried out beforehand indicated that the amount of vertical oxidation can be reduced by decreasing the oxidation temperature from 450 to 410 °C, in accordance with Fiore et al., who reported a dependence of the amount of vertical oxidation on the oxidation temperature [292]. The removal of the silicon nitride layer via wet etching on sample K1439 A lead to sporadic defects, hence it was decided to adopt a plasma etching solution that had proven to be highly selective in precedent tests.

On both oxidized samples, K1439 B and K1439 D, the oxidation layers of the bottom DBR of the 350 and 200 μm diameter devices are only partially oxidized, with larger residual non-oxidized apertures on the latter sample. However, the vertical oxidation could be reduced on the sample K1439 D. Therefore the smaller devices can still be contacted on this sample, since they are not isolated from the n-contact.

In case of the 350 and 200 μm diameter devices, the performance of devices without and with a p-contact grid is compared. This is not possible for the smaller devices, as they all come with p-contact grids.

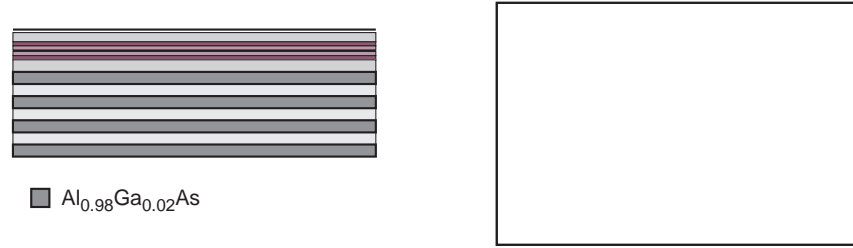


Figure 5.5: Schematic layer structure after growth

Silicon Nitride Surface Protection Layer Deposition

- i. Surface cleaning
- ii. Surface deoxidation with diluted HCl
- iii. PECVD surface protection layer:

K1439 A: SiN_x 200 nm
 K1439 D: SiN_x 500 nm

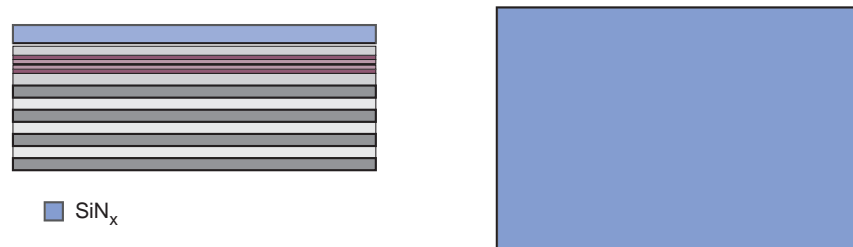


Figure 5.6: Silicon nitride surface protection layer deposition by PECVD

Trench Etch in Silicon Nitride

- i. Adhesion promoter (HMDS) deposition
- ii. Lithography
- iii. Surface deoxidation with diluted HCl
- iv. Selective etching of trenches in SiN_x :

K1439 A: Selective wet etching with BHF
 K1439 D: Selective dry etching with CF_4/O_2 plasma

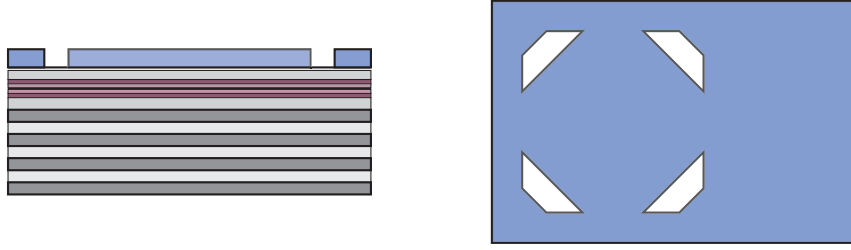


Figure 5.7: Trench etch in silicon nitride

Trench Etch in Semiconductor

- i. Surface deoxidation with diluted HCl
- ii. Selective wet etching of trenches in semiconductor with concentrated phosphoric acid solution for AlGaAs layers and diluted HCl for AlGaInP layers.

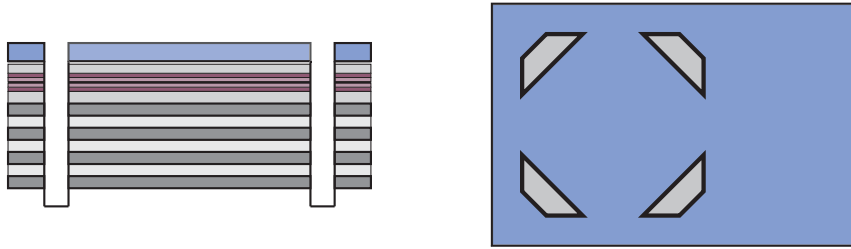


Figure 5.8: Trench etch in semiconductor

Lateral Oxidation of Low Index DBR Layers

Lateral wet oxidation of exposed $\text{Al}_{0.98}\text{Ga}_{0.02}\text{As}$ layers in bottom DBR was carried out until the concomitant vertical oxidation of the n-intracavity contact $\text{Al}_{0.7}\text{Ga}_{0.3}\text{As}$ layer approached the inner boundary of the n-contact area. Due to that the DBR of the 350 and 200 μm diameter devices could not be completely oxidized.

Table 5.4: Oxidation parameters K1439 A and K1439 D

Sample	temperature	time	oxidation depth	aperture diameter
	[°C]	[min]	[μm]	200 μm devices [μm]
K1439 A	450	120	110	≈ 65
K1439 D	410	225	60	≈ 160

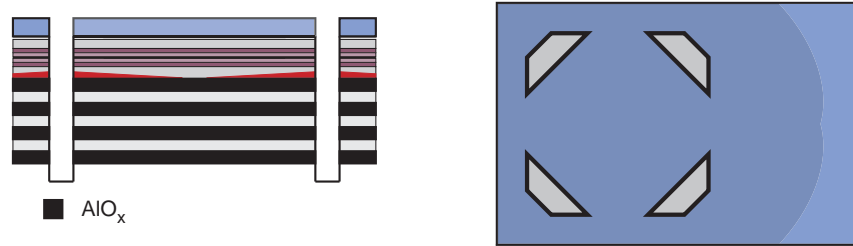


Figure 5.9: Lateral wet oxidation of low index DBR layers (parasitic vertical oxidation of n-intracavity contact $\text{Al}_{0.7}\text{Ga}_{0.3}\text{As}$ layer schematically indicated in red)

Silicon Nitride Removal

Selective etching of SiN_x :

- K1439 A: Selective wet etching with BHF
- K1439 D: Selective dry etching with CF_4/O_2 plasma

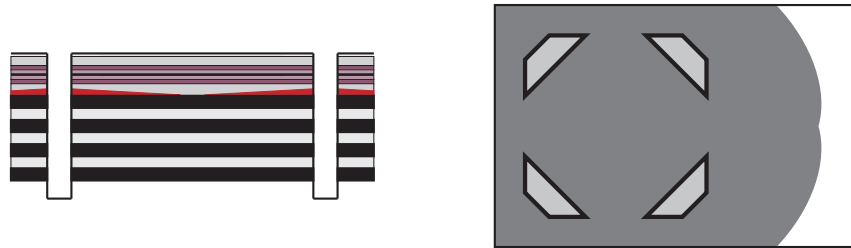


Figure 5.10: Silicon nitride removal

Mesa Etch

- i. Lithography
- ii. Surface deoxidation with diluted HCl
- iii. Selective wet etching of circular mesas of varying diameter; through cavity, down to n- $\text{Al}_{0.7}\text{Ga}_{0.3}\text{As}$ intracavity contact layer. Concentrated phosphoric acid solution for AlGaAs layers and diluted HCl for AlGaInP layers.

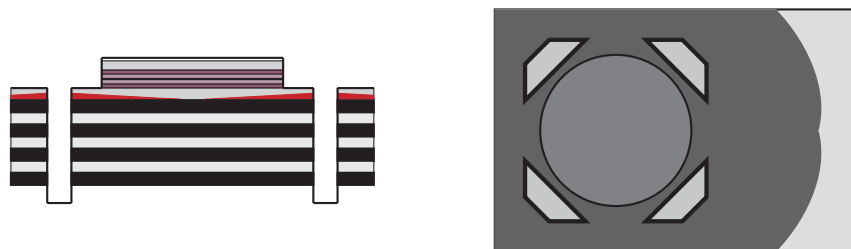


Figure 5.11: Mesa etch

Recess Etch

- i. Lithography
- ii. Surface deoxidation with diluted HCl
- iii. Selective wet etching of ring-shaped recess; down to p-(Al_{0.7}Ga_{0.3})_{0.5}In_{0.5}P confinement layer. Removal of p-doped GaAs and Al_{0.7}Ga_{0.3}As layer with concentrated phosphoric acid solution.

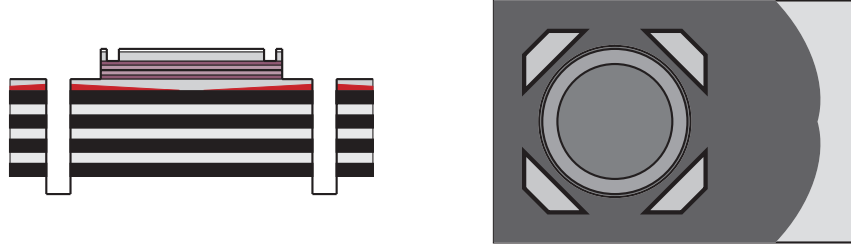


Figure 5.12: Recess etch

N-Contact Deposition

- i. Lithography
- ii. No surface deoxidation
- iii. E-beam evaporation n-contact layer sequence:

Ni/Ge/Au/Ni/Au 10/25/50/20/100 nm

- iv. Lift-off in acetone
- v. N-contact alloying at 380 °C in forming gas atmosphere (ramps 5 °C/min)

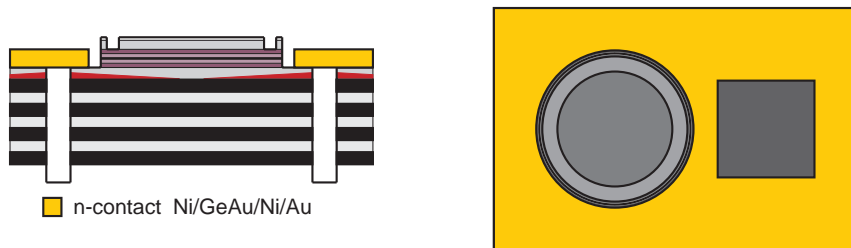


Figure 5.13: N-contact deposition

Dielectric Coating

- i. Polyimide spinning (thickness $1\ \mu\text{m}$)
- ii. Polyimide soft bake
- iii. Lithography
- iv. Polyimide etching
- v. Polyimide curing at $250\ ^\circ\text{C}$ for 2 h in air (ramps $5\ ^\circ\text{C}/\text{min}$)

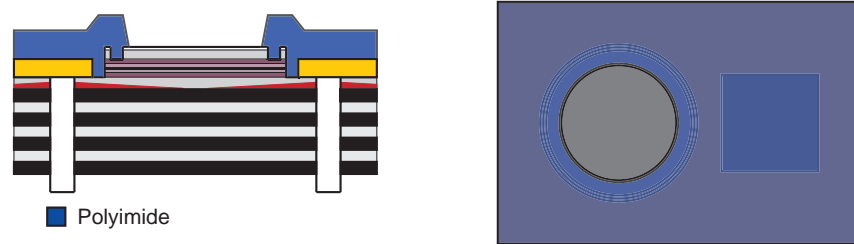


Figure 5.14: Dielectric coating with polyimide

P-Contact Deposition

- i. Lithography
- ii. Surface deoxidation with diluted HCl
- iii. E-beam evaporation p-contact layer sequence:

K1439 A: Ti/Au 10/250 nm
K1439 D: Ti/Au 20/200 nm

- iv. Lift-off in acetone
- v. No alloying

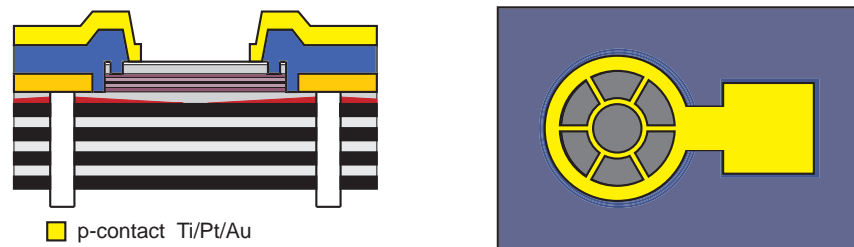


Figure 5.15: P-contact deposition

Final Samples

The extent of the oxidation of the low index bottom DBR layers for the 200 and 350 μm diameter devices on sample K1439 A can be seen in figure 5.16. The areas where the n-intracavity contact layer is completely oxidized due to its parasitic vertical oxidation can be distinguished as well.

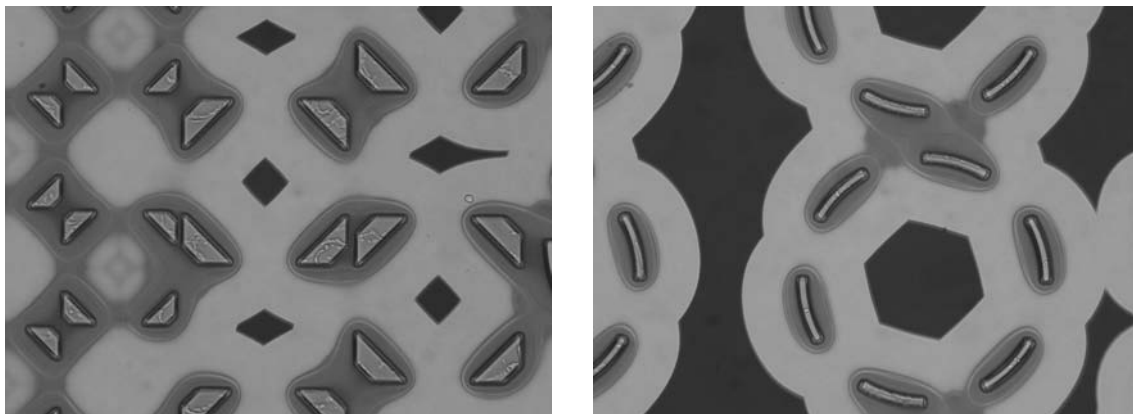


Figure 5.16: K1439 A after oxidation: 200 μm device area (left) and 350 μm device area (right); oxidation fronts of the mirror oxidation and the oxidation of the n-intracavity contact layer are clearly distinguishable

Figure 5.17 shows the defects that appeared on sample K1439 A after the silicon nitride removal with BHF. It is assumed that the hydrofluoric acid penetrated through the GaAs cap layer via defects such as misfit dislocations or threading dislocations and locally attacked the underlying $\text{Al}_{0.7}\text{Ga}_{0.3}\text{As}$ current spreading layer. The dark spots at the surface of the n-intracavity $\text{Al}_{0.7}\text{Ga}_{0.3}\text{As}$ layer after the mesa etch are presumably due to an increased surface roughness, caused by the preferential oxidation in air.

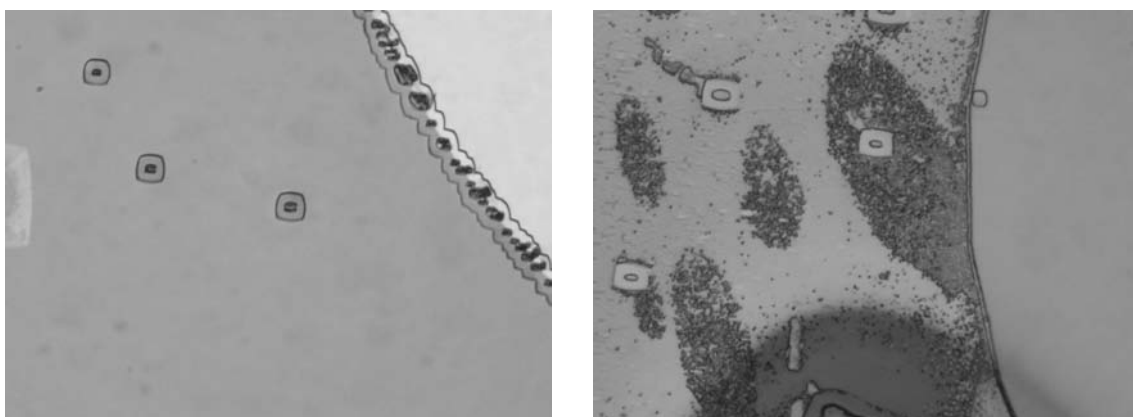


Figure 5.17: K1439 A after after silicon nitride wet etch (left) and after mesa etch (right); defects appearing after silicon nitride wet etch and enlarging after mesa etch

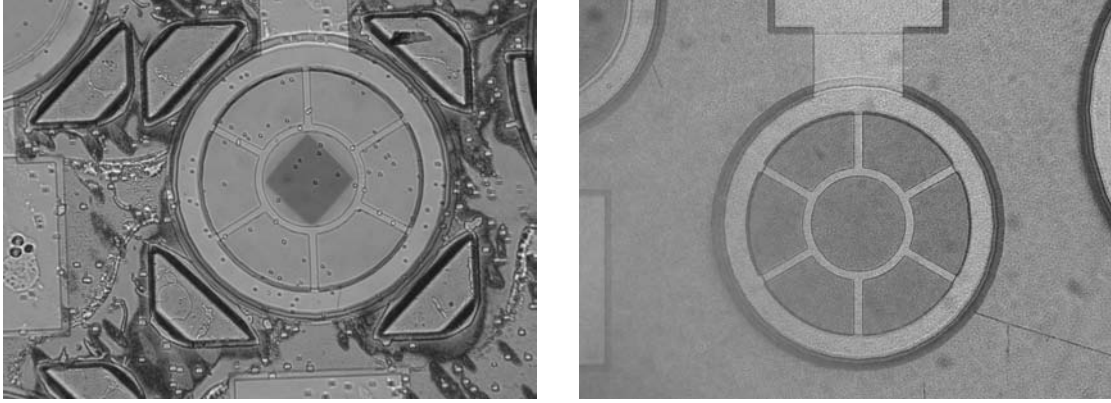


Figure 5.18: 200 μm device with p-contact grid of sample K1439 A (left) and K1439 C (right)

Final devices from the different samples are compared in figures 5.18 and 5.19. The first figure shows 200 μm diameter devices from sample K1439 A and K1439 C. The device from sample K1439 C, which was not oxidized, shows no defects at all. Hence the defects on the devices from sample K1439 A can be attributed to either the deposition and etching of the silicon nitride surface protection layer or the lateral wet oxidation of the bottom DBR. The devices from sample K1439 D, shown in figure 5.19, show nearly no defects either, which indicates that the plasma etching is better suited for the selective etching of the silicon nitride layer. Note the smaller oxidation extent for sample K1439 D.

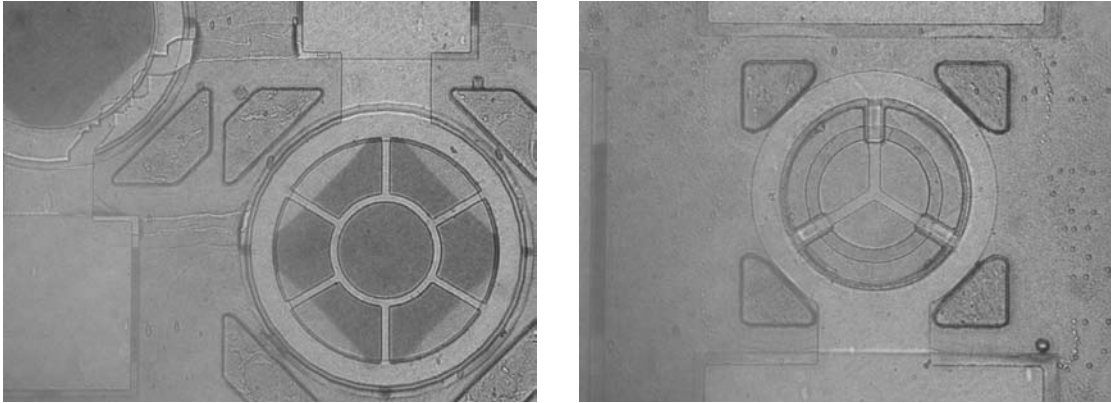


Figure 5.19: 200 μm device with p-contact grid (left) and 50 μm device (right) of sample K1439 D

5.5 Experimental Results

5.5.1 Characterization after Epitaxial Growth

Photoluminescence

The photoluminescence spectrum of structure K1439 after growth has a maximum at 651 nm, as can be seen in figure 5.20. As at that stage the bottom DBR is not oxidized yet and its reflectivity is quite low, the emission spectrum should not be significantly influenced by the presence of the microcavity.

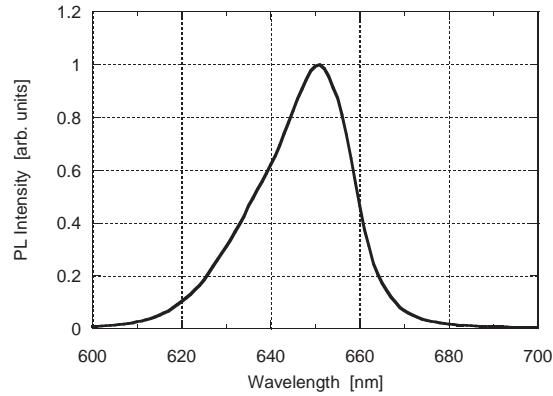


Figure 5.20: Photoluminescence spectrum of structure K1439 after growth

Reflectivity

The reflectivity measurement set-up is explained in detail in section 4.5.1. Figure 5.21 shows the reflectivity spectrum of structure K1439 after growth, measured with the silicon CCD. At wavelengths below 550 nm the measured intensity amplitudes are not

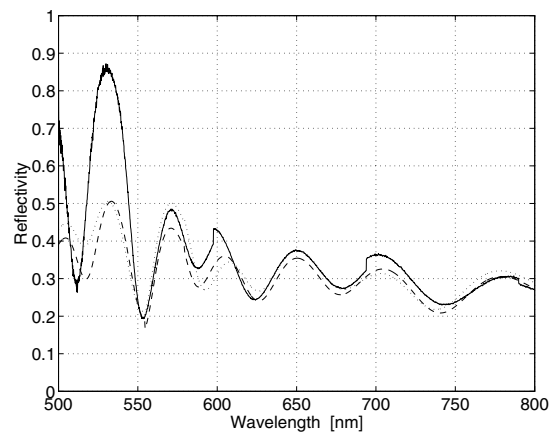


Figure 5.21: Reflectivity spectrum of structure K1439; comparison measurement with Si CCD (solid line) and simulation design (dotted line) and nominal values (dashed line)

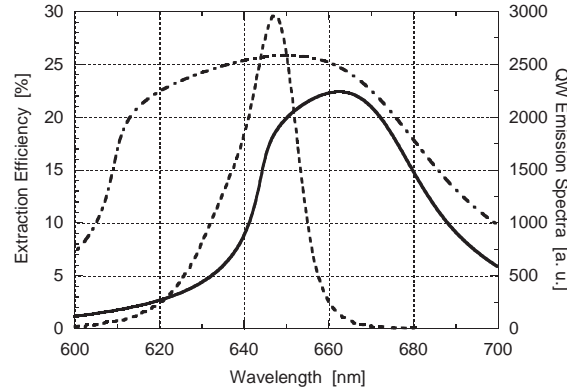


Figure 5.22: Simulated extraction efficiency of structure K1439 as grown; emission into air (solid line) and epoxy (dash-dot line) plus intrinsic emission spectrum (dashed line)

accurate due to the fact that the reflectance of the gold reference mirror is drastically decreasing, as can be seen in figure 4.37 in section 4.5.1. However the spectral positions still seem to be correct.

Christian Karnutsch, who grew the structure at OSRAM, derived the nominal thicknesses from their reflectivity measurements with the aid of a simulation program. These values are listed in appendix B, together with the design values. In figure 5.21 the simulation based on the design as well as on the nominal thickness values is shown, however by eye no significant difference can be noted, as at this stage the reflectivity of the bottom DBR is quite low.

The nominal thicknesses found by this means differ slightly from the design values, the cap layer is a few nanometers thinner, whereas all the other layers in the cavity are a few nanometers thicker. Thus the cavity is slightly longer than designed, which means that its extraction properties are changed. Figure 5.22 shows that the extraction efficiency curve of structure K1439 based on these nominal thicknesses is red-shifted compared to the initial curve (see figure 5.3). The theoretical external quantum efficiencies of the structure as grown are listed in table 5.5 and are compared with the values of the structure as designed. The efficiency into air is drastically reduced due to a smaller overlap with the QW emission curve, the emission into epoxy on the other hand is more or less the same for both cases.

Table 5.5: Theoretical external quantum efficiencies for emission into air and epoxy of structure K1439 as designed and as grown

	$\eta_{\text{ext}}(\text{air})$ [%]	$\eta_{\text{ext}}(\text{epoxy})$ [%]
design	18	24
as grown	13	25

5.5.2 Characterization of the Processed Devices

TLM Measurements

TLM measurements are explained in detail in section 3.5.1. The contact areas of the square test patterns are $150 \times 150 \mu\text{m}^2$, with contact spacings of 4, 6, 10, 20, 50 and $150 \mu\text{m}$. An HP4156A Semiconductor Parameter Analyzer is used for these measurements. The I–V characteristics for the different contact spacings are recorded with a four point probe set-up. Two probes serve for applying a voltage and sweeping it over a certain range while the other two are used to measure the resulting current.

Similar to the near infrared devices, the Ni/AuGe/Ni/Au n-contacts show a non-ohmic behavior, which is assigned to interdiffusion during the alloying and the small intracavity layer thickness. In the case of the red MCLEDs, the Ti/Au p-contacts show a clear Schottky behavior. It is assumed that the GaAs cap layer is either too thin or not doped high enough and hence the contact is formed on the underlying $\text{Al}_{0.7}\text{Ga}_{0.3}\text{As}$ layer. A Schottky behavior of non-alloyed Ti/Pt/Au contacts on $\text{Al}_{0.2}\text{Ga}_{0.8}\text{As}$ has been reported previously already [237]. Figure 5.23 shows the I–V characteristic measured over an extended voltage range for different contact pad spacings. These curves have been measured with a two point probe setup and a HP4145A Semiconductor Parameter Analyzer.

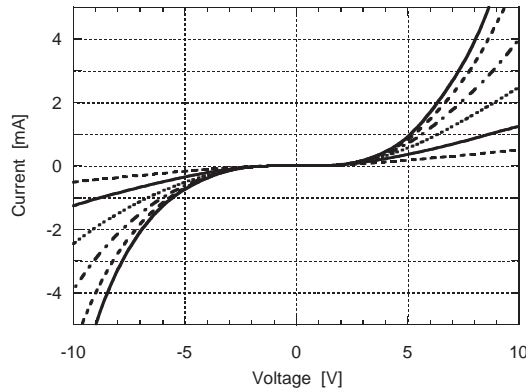


Figure 5.23: Two point probe I–V characteristics of p-contact TLM pads as a function of contact spacing; 4 (solid line), 6 (dashed line), 10 (dash-dot line), 20 (dotted line), 50 (solid line) and $150 \mu\text{m}$ (dashed line)

L–I–V Measurements

The devices are characterized by detailed light, current and voltage (L–I–V) measurements. The set-up consists of a calibrated large area silicon photodiode (Hamamatsu S1337-1010BR) and a HP 4145A Semiconductor Parameter Analyzer, which is used as DC voltage source, current monitor and photocurrent monitor simultaneously. All measurements are taken in cw (continuous wave) mode and at room temperature. The device is contacted with two probe needles connected via coaxial cables. A voltage is applied to the diode and is varied over a certain range while the resulting diode forward current and the photocurrent generated in the photodiode are recorded. The photodiode is biased at 0 V in order to minimize its dark current. The measurement setup for top emitting devices is explained in detail in section 4.5.2.

At 650 nm the same conversion factor as for 970 nm can be used since the external quantum efficiency of the photodiode, which is equal to the product $1.24R_{PD}/\lambda[\mu m]$, is very similar for the two wavelengths. R_{PD} corresponds to the photo sensitivity of the photodiode which is expressed in units of A/W. The typical spectral response of the photodiode S1337-1010 BR given by Hamamatsu is shown in figure 5.24. The measurements were carried out with a photodiode S1337-1010BR, which had been calibrated by the Swiss Federal Office of Metrology and Accreditation (METAS). The calibration results are listed in appendix D.1.

As the LED characteristics at low current densities give a good indication of the electrical and optical quality of the device, the current–voltage curves are plotted on a semilogarithmic scale ($\log(I)$ – V) and the external quantum efficiency is plotted versus the logarithm of the current density (η_{ext} – $\log(J)$).

The emission into epoxy is simulated by immersing the device in a roughly hemispherical droplet of glycerol. Anhydrous glycerol has a refractive index of 1.4746 at 589 nm and 20 °C [208], which is close to the refractive index of epoxy of 1.5. In addition glycerol does not wet GaAs very well, hence it forms a droplet similar to the shape

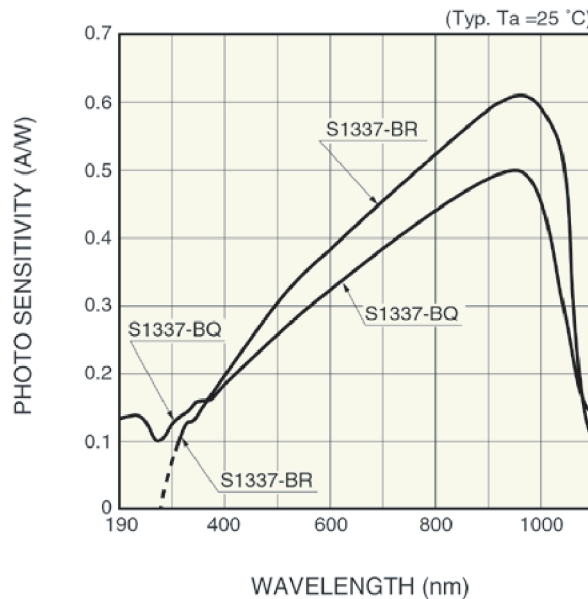


Figure 5.24: Spectral response photodiode Hamamatsu S1337-1010BR

of a hemispherical epoxy dome. However glycerol is hygroscopic and with increasing water content the refractive index is decreases towards 1.33. If the curvature of the droplet is not high enough the amount of light coupled out is lower as well.

The measured I–V characteristics and external quantum efficiencies as a function of drive current density for the devices from the different samples are shown in figures 5.25–5.27. No current could be injected in the devices with a diameter of 100 μm or smaller on sample K1439 A. It is assumed that this is due to an isolation of the devices from the n-contact, caused by a complete vertical oxidation of the n- $\text{Al}_{0.7}\text{Ga}_{0.3}\text{As}$ intracavity contact layer underneath. Therefore only the results of the 200 μm diameter devices are presented. On sample K1439 D the most interesting devices are the 50 μm diameter MCLEDs, as they have a completely oxidized DBR. The larger devices on sample K1439 D show significantly lower efficiencies due to the reduced oxidation extent and the values for the 20 μm diameter devices are lower due to the increased shadowing by the top p-contact. For comparison the results of the non-oxidized 200 and 50 μm diameter devices from sample K1439 C are shown as well.

In case of the 200 μm diameter MCLEDs the curves of the devices without and with a p-contact grid are compared. For the devices from sample K1439 A not only the emission into air but as well the emission into glycerol was measured. The fabricated red MCLEDs do not show the typical diode I–V characteristic. It is assumed that this is related to the non-ohmic behavior of the p-contact, the reduced thickness of the n- $\text{Al}_{0.7}\text{Ga}_{0.3}\text{As}$ intracavity contact layer due to its partial vertical oxidation and the surface oxide on this layer that could not be removed prior to the metallization. Only the non-oxidized devices from sample K1439 C show an exponential behavior at injection currents below 10^{-4} A with an ideality factor around 2. In figure 5.27 the I–V characteristics of two 50 μm diameter devices from sample K1439 D with identical geometry are compared. It can be seen that they differ significantly, although the two diodes show a similar efficiency. The maximum measured external quantum efficiencies of the different device types are listed in table 5.6, together with the simulation results for the structure as grown.

Table 5.6: Maximum external quantum efficiencies of the red MCLEDs with oxide DBR, measured with a large area photodiode

Sample	Simulation		Measurements				
	air	epoxy	dia- meter [μm]	air		glycerol	
	[%]	[%]		no grid [%]	grid [%]	no grid [%]	grid [%]
K1439 A	13	25	200	10.9	12.3	11.4	14.9
K1439 C	2	5	200	0.9	1.2	-	-
	2	5	50		1.6		-
K1439 D	13	25	50		9.4		-

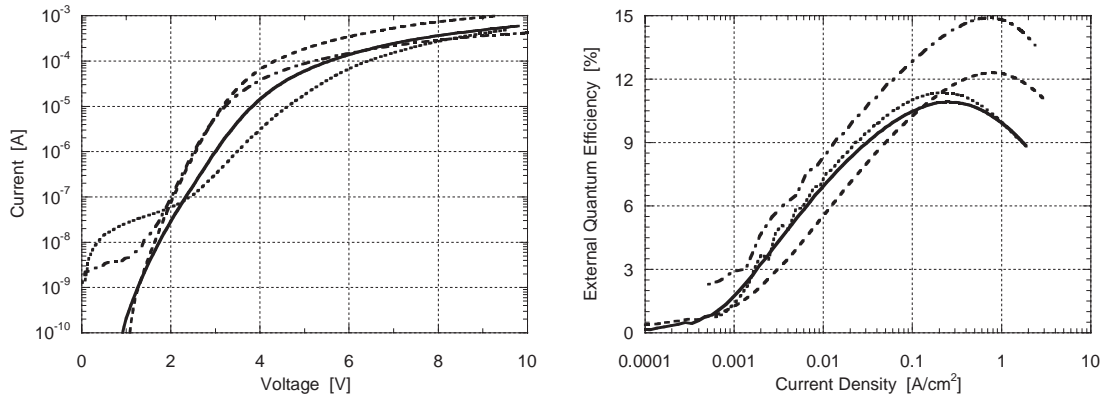


Figure 5.25: I–V characteristic and external quantum efficiency vs. drive current density of 200 μm MCLEDs from sample K1439 A; emission into air without (solid line) and with p-contact grid (dashed line), emission into glycerol without (dotted line) and with grid (dash-dot line)

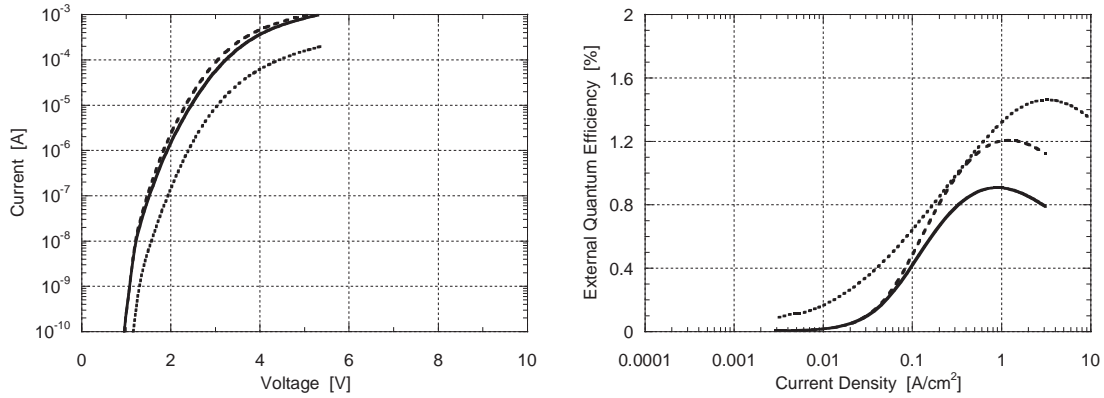


Figure 5.26: I–V characteristic and external quantum efficiency vs. drive current density of MCLEDs from sample K1439 C (non-oxidized mirror) for emission into air; 200 μm diameter device without (solid line) and with p-contact grid (dashed line) and 50 μm diameter device (dotted line)

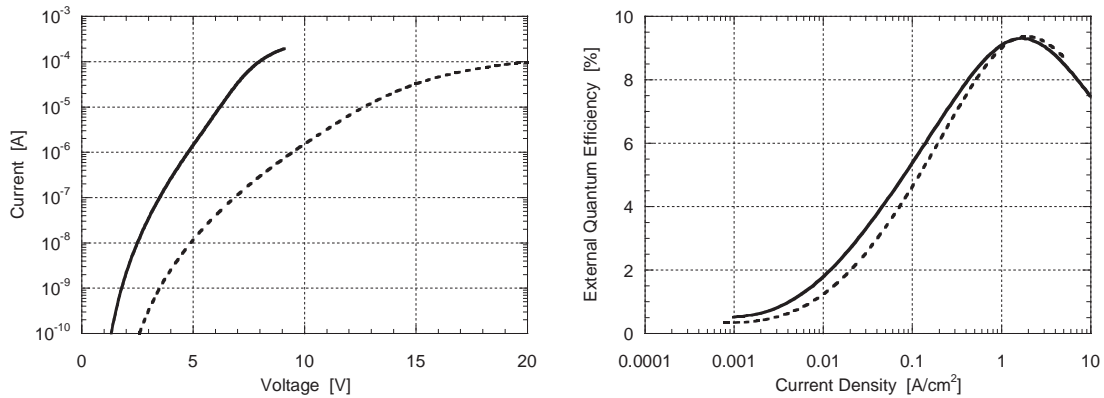


Figure 5.27: I–V characteristic and external quantum efficiency vs. drive current density of two different 50 μm MCLEDs from sample K1439 D for emission into air

Contrary to the near infrared devices, the introduction of a p-contact grid leads to a significant increase in external quantum efficiency for the red MCLEDs. It seems like the current spreading is more critical in these devices and therefore the beneficial effect of the grid is more important. Furthermore thanks to the more homogeneous current injection the efficiency roll-over is shifted to higher current densities. The $50\mu\text{m}$ diameter devices all have a p-contact grid, hence this observation could not be verified on the smaller devices. The measured efficiency for emission into air of the $200\mu\text{m}$ diameter devices with a p-contact grid from sample K1439 A is close to the theoretical value, which is surprising considering the fact that the bottom DBR is not completely oxidized. However the efficiencies measured for emission into glycerol are significantly lower than the simulated ones. The values of the smaller devices are lower due to the increased shadowing by the top contact.

Table 5.7: Maximum measured external quantum efficiencies, compared with the simulation results

	$\eta_{\text{ext}}(\text{air})$ [%]	$\eta_{\text{ext}}(\text{epoxy})$ [%]
design	18	24
as grown	13	25
measurements	12	15

Near-Field Emission

The near-field emission of the devices from sample K1439 A and K1439 D has been imaged onto a CCD camera by means of a microscope objective. In order not to saturate the CCD camera, the light intensity was reduced with the use of metallic neutral density filters. The devices were driven at a fixed current, corresponding to the current at maximum external quantum efficiency.

It can clearly be seen that for the 200 μm diameter devices from sample K1439 A with a only partially oxidized bottom DBR the emission in the oxidized area is much stronger than in the non-oxidized center region. The bright areas close to the p-contact indicate a current crowding effect, which obviously can be reduced with the use of a p-contact grid. In case of the 50 μm diameter MCLED on the other hand the emission seems to be uniform. For comparison, near field emission pictures of near infrared MCLEDs with a semiconductor DBR from sample S1910 a are shown as well. Note the more homogeneous current spreading for both devices, the one without and the one with a p-contact grid.

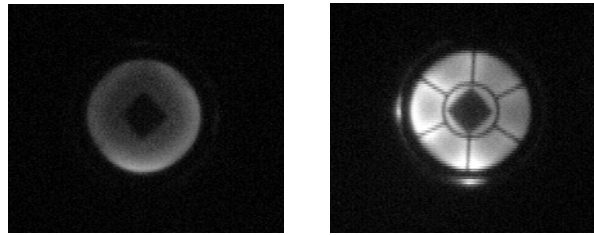


Figure 5.28: Near field emission of 200 μm diameter MCLEDs from sample K1439 A; without (left) and with p-contact grid (right)



Figure 5.29: Near field emission of a 50 μm diameter MCLED from sample K1439 D

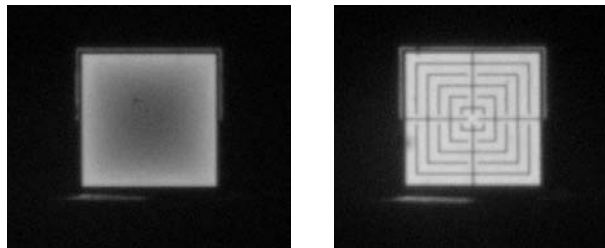


Figure 5.30: Near field emission of 400 μm diameter MCLEDs from sample s1910 a; without (left) and with p-contact grid (right)

Device Reflectivity

Figure 5.31 shows the reflectivity spectrum of a $200\text{ }\mu\text{m}$ diameter device without p-contact grid from sample K1439 A, measured with a Si CCD and a gold reference mirror. The devices with p-contact grid show a similar behavior, however the additional metal on the surface leads to a less accurate measurement. The low reflectivity of the stopband, especially at longer wavelengths, is assigned to the fact that part of the imaged bottom DBR is not oxidized. It can be seen that the Fabry-Perot peak is blue-shifted compared to the simulation of the nominal values determined from the reflectivity spectrum after growth. Hence the cavity length must have been reduced during the device fabrication. In fact the measurements indicate a cavity length even smaller than the one of the initially designed structure. With a FP-peak around 658 nm the detuning reduces to approximately 7 nm . Hence a reduced external quantum efficiency and a more directional emission compared to the designed structure can be expected.

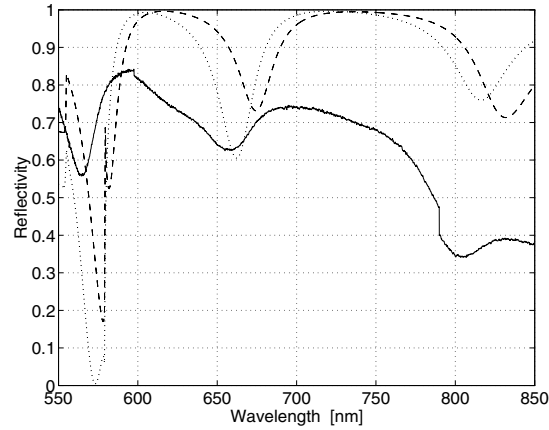


Figure 5.31: Reflectivity spectrum of a $200\text{ }\mu\text{m}$ MCLED with p-contact grid from sample K1439 A; comparison measurement with Si CCD (solid line) and simulation design (dotted line) and nominal values (dashed line)

Far-Field Emission

The far-field radiation pattern of 200 μm diameter devices from sample K1439 A was determined as described in section 4.5.2. The measured curves are very similar for the devices with and without a p-contact grid. In figure 5.32 the curve of a device with a p-contact grid is shown, representative for both types. Effectively, as suspected from the results of the device reflectivity measurements, the emission of these devices is much more directional than predicted. During the processing the cavity length appears to have been significantly reduced.

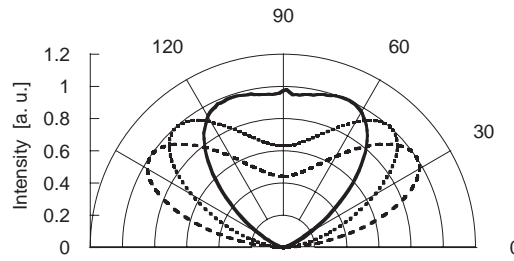


Figure 5.32: Far-field emission spectrum of a 200 μm MCLED without p-contact grid from sample K1439 A; comparison between measurement (solid line) and simulation design (dotted line) and nominal values (dashed line)

Electroluminescence

The electroluminescence spectra of 200 μm diameter devices without and with p-contact grid from sample K1439 A are displayed in figure 5.33. Both spectra were taken at an angle of 0° (0° being the normal direction). They are nearly identical, with a peak centered at 653 nm and a full width at half maximum (FWHM) around 48 meV. The fact that at 0° the QW emission and the cavity resonance are overlapping confirms that for these devices the detuning is nearly zero.

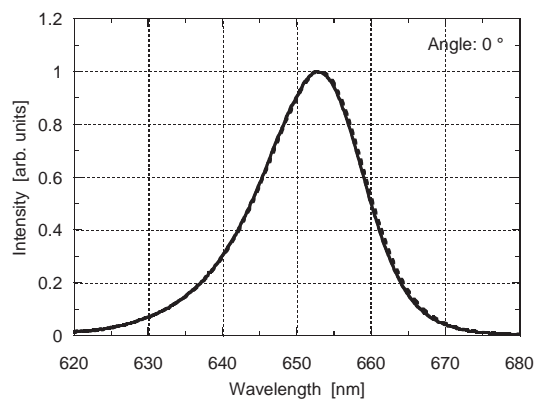


Figure 5.33: Electroluminescence of 200 μm diameter MCLEDs from sample K1439 A measured at a collection angle of 0° ; without (solid line) and with p-contact grid (dashed line)

Figure 5.34 shows the simulated cavity resonance of structure K1439 for different collection angles, for both, the structure as it was designed and based on the nominal values deduced from the reflectivity measurements. Obviously if the structure of the final devices resembled any of these two, the cavity resonance at a collection angle of 0° would not coincide with the QW emission and hence an additional peak at longer wavelengths could be distinguished. The resonance peaks at the different collection angles are summarized in table 5.8 for the two simulated structures and the measurement.

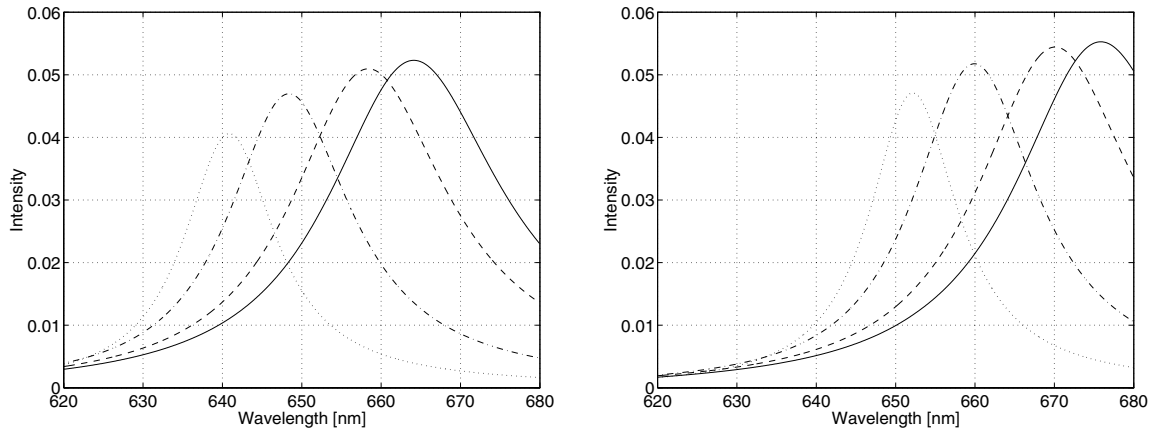


Figure 5.34: Simulation of cavity resonance of structure K1439 for different collection angles, based on structure as designed (left) and based on structure as grown (right); 0° (solid line), 25° (dashed line), 45° (dash-dot line) and 60° (dotted line)

Table 5.8: Cavity resonance peaks of structure K1439 for different collection angles

Angle [$^\circ$]	Simulation		Measurement [nm]
	design [nm]	as grown [nm]	
0	664	676	653
25	658	670	-
45	648	660	-
60	641	652	-

5.6 Discussion

In the case of these red MCLEDs the beneficial effect of the use of a p-contact grid prevails. It seems that the current spreading is more critical in the $\text{Al}_{0.7}\text{Ga}_{0.3}\text{As}$ and $(\text{Al}_x\text{Ga}_{1-x})_{0.51}\text{In}_{0.49}\text{P}$ layers compared to the GaAs layers in the near infrared devices discussed in the previous chapter. Thus with a p-contact grid higher efficiencies can be achieved thanks to a more homogeneous emission. In addition the efficiency roll-over is shifted to higher current densities, which is explained with the occurrence of carrier spill-over or heating effects at higher current densities only due to the more uniform injection.

No ohmic p-contact could be formed, in part due to the fact that an additional alloying step was avoided in order to minimize the thermal stress in the structure. The nature of the n-contact could not be determined. These non-ideal contacts lead to elevated turn-on voltages and atypical I–V characteristics. Nevertheless record efficiencies for small-sized red MCLEDs could be achieved.

The maximum external quantum efficiencies measured for the larger red MCLEDs with an only partially oxidized bottom DBR are surprisingly close to the simulated values based on the nominal thicknesses derived from reflectivity measurements after epitaxial growth. Nevertheless they are significantly lower than the theoretical values of the structure as designed initially. The grown microcavity was slightly longer than designed, which led to a too large detuning and hence a reduced theoretical external quantum efficiency. However the measurements of the processed devices indicate that their detuning is nearly zero. Therefore the cavity length must have been reduced at some point during the processing.

Plausible explanations for a cavity length reduction during processing are an etching of the top layer(s) or a parasitic vertical oxidation of the n- $\text{Al}_{0.7}\text{Ga}_{0.3}\text{As}$ intracavity contact layer. The concomitant refractive index change in the latter case from 3.1 to 1.6 leads to a considerable reduction of the optical length of the cavity. The p- $\text{Al}_{0.7}\text{Ga}_{0.3}\text{As}$ current spreading layer underneath the thin GaAs cap layer might have been etched with hydrofluoric acid or hydrochloric acid during a wet etching step. However it is not plausible that several tens of nanometers of this layer could be attacked without noticing it under the optical microscope. Hence it is concluded that the cavity length reduction must be caused by a partial vertical oxidation of the n-intracavity contact layer. This oxide has the form of a taper, with the thickness decreasing from the outside to the inside. Nonetheless, in a simplified approach, the extent of the vertical oxidation has been estimated assuming a uniform oxidation extent over the whole device. For the fitting, the reflectivity, far-field emission and electroluminescence measurements were taken into account. The best fit was found for a vertical oxidation of 25 nm of the n-intracavity contact layer, with the layer thicknesses corresponding to the nominal values based on reflectivity measurements after growth. The fitted curves are shown in figures 5.35–5.37 and the cavity resonance peaks at the different collection angles are listed in table 5.9. A slightly better fit could be obtained for the reflectivity spectrum with a vertical oxidation of only 20 nm, however the far-field and electroluminescence simulations match very well for 25 nm and differ substantially for 20 nm. These results seem to confirm the theory of a partial parasitic vertical oxidation of the n- $\text{Al}_{0.7}\text{Ga}_{0.3}\text{As}$ intracavity contact layer.

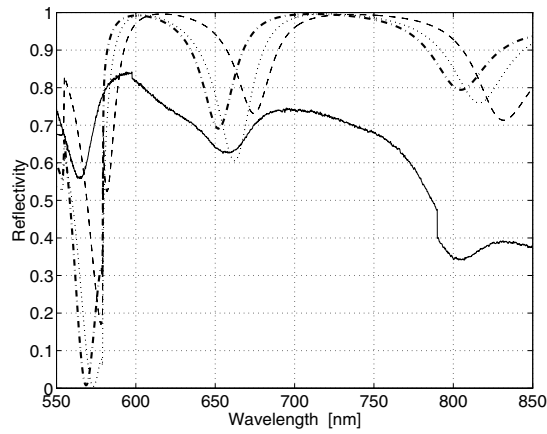


Figure 5.35: Fitted simulation reflectivity spectrum compared with the measurement of a 200 μm MCLED without p-contact grid from sample K1439 A; measurement with Si CCD (solid line), simulation design (dotted line), structure as grown (dashed line) and including a vertical oxidation of 25 nm (dash-dot line)

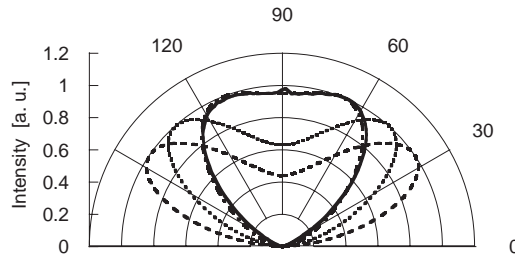


Figure 5.36: Corrected simulation far-field emission spectrum compared with the measurement of a 200 μm MCLED without p-contact grid from sample K1439 A; measurement (solid line), simulation design (dotted line), structure as grown (dashed line) and including a vertical oxidation of 25 nm (dash-dot line)

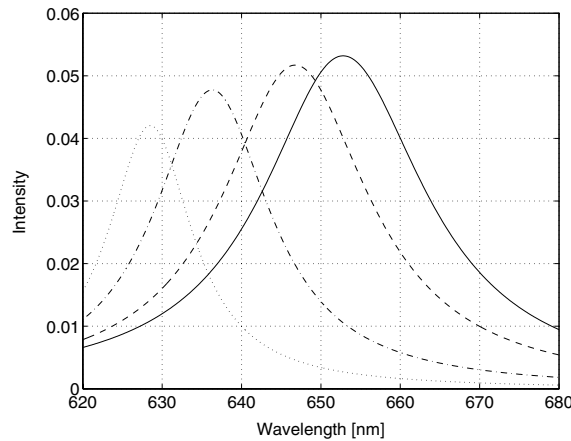
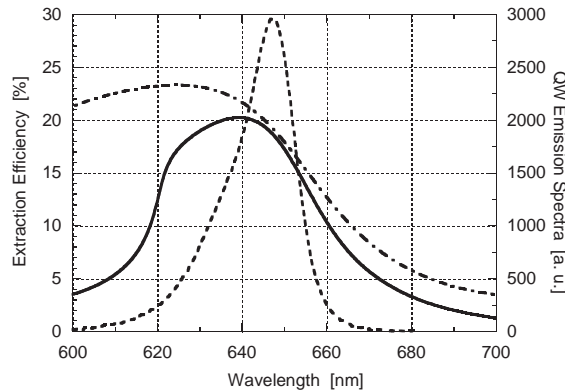


Figure 5.37: Corrected simulation cavity resonance of structure K1439 for different collection angles, based on structure as grown including a vertical oxidation of 25 nm; 0° (solid line), 25° (dashed line), 45° (dash-dot line) and 60° (dotted line)

Table 5.9: Cavity resonance peaks for different collection angles

Angle [°]	Simulation			Measurement [nm]
	design [nm]	as grown [nm]	vertical ox. [nm]	
0	664	676	653	653
25	658	670	647	-
45	648	660	636	-
60	641	652	629	-

The corrected simulations of the extraction efficiency as a function of wavelength and the estimated external quantum efficiencies are presented in figure 5.38 and table 5.10. Theoretical external quantum efficiencies similar to the ones for the designed structure have been estimated for this structure, even though it shows a positive detuning. Compared to the measurement results it seems reasonable to have achieved two thirds of the theoretical efficiency with devices with an only partially oxidized bottom DBR (approximately 90 % oxidized). Furthermore the efficiency can be expected to be reduced by shadowing from the top contact grid, a non-homogeneous current injection, carrier spill-over and heating effects.

**Figure 5.38:** Simulated extraction efficiency of structure K1439 as grown including a vertical oxidation of 25 nm of the n-intracavity contact layer; emission into air (solid line) and epoxy (dash-dot line) plus intrinsic emission spectrum (dashed line)**Table 5.10:** Theoretical external quantum efficiencies for emission into air and epoxy of structure K1439 as designed, as grown and including a vertical oxidation of 25 nm of the n-intracavity contact layer; compared with measurement results

	$\eta_{\text{ext}}(\text{air})$ [%]	$\eta_{\text{ext}}(\text{epoxy})$ [%]
design	18	24
as grown	13	25
vertical oxidation	18	20
measurements	12	15

In the present structure the Al-content of the $\text{Al}_x\text{Ga}_{1-x}\text{As}$ current spreading and injection layers is fixed to 70 %. It is believed that by reducing this value to 50 % the electrical properties as well as the oxidation behavior of this type of devices can be significantly improved without degrading its optical properties. Simulations show that with this type of structure efficiencies of 19 % and 25 % are achievable, for emission into air and epoxy, respectively.

The structure K1439 was regrown with an Al-content of only 50% in the $\text{Al}_x\text{Ga}_{1-x}\text{As}$ current spreading and injection layers (label K2362). It was grown by metalorganic vapor phase epitaxy (MOVPE) by Rainer Butendeich from OSRAM Opto Semiconductors. The new structure was processed similarly to sample K1439 D. Due to the lower Al-content in the n- $\text{Al}_x\text{Ga}_{1-x}\text{As}$ intracavity contact layer longer lateral wet oxidation times were possible. However no reasonably working device could be found on this sample. It is believed that the p-doping and the thickness of the top GaAs-layer in this structure are insufficient for an effective hole injection from a non-alloyed p-contact. This would explain the atypical I–V characteristics and limited drive current levels of the devices on this sample. Due to time constraints it was not possible to grow and fabricate another set of red MCLEDs.

5.7 Conclusions

MCLEDs with an AlGaInP cavity containing a single GaInP quantum well emitting at 650 nm and an AlGaAs/ AlO_x bottom DBR have been fabricated. To our knowledge, this is the first report on red MCLEDs with an oxide DBR. Record external quantum efficiencies for red MCLEDs of 12% at very low current densities have been achieved with preliminary devices, even though the top p-contact does not show an ohmic behavior and the bottom DBR is only partially oxidized. The highest external quantum efficiency for red MCLEDs published so far is 9.6% by Wirth et al. [119] for $300 \times 300 \mu\text{m}^2$ devices, corresponding to a wall-plug efficiency of 10%. For larger devices of the same type with a size of $700 \times 700 \mu\text{m}^2$ a wall-plug efficiency of 12 % was reported [65].

Due to the low refractive index contrast in AlGaAs-based semiconductor DBRs at 650 nm, the implementation of an AlGaAs/ AlO_x DBR enables a drastic increase in extraction efficiency. However the presence of AlGaAs current spreading layers complicates the device design and the device fabrication. A parasitic vertical oxidation of the n-intracavity contact layer is unavoidable and the formation of ohmic contacts on AlGaAs is a difficult task.

Nevertheless, by further optimizing the device design and the device fabrication, reliable devices with efficiencies close to 20 % for emission into air should be attainable with this device type, making red MCLEDs more attractive compared to other LED designs for specific applications such as optical communication for example.

Chapter 6

Thin-Film MCLEDs at 650 nm

6.1 Introduction

The maximum achievable efficiencies for standard red emitting MCLEDs are lower than for near infrared MCLEDs due to several reasons discussed in detail in the previous chapter. The GaInP/AlGaInP active region shows an increased carrier leakage and an increased sensitivity to heating, which in both cases leads to an onset of the roll-over of the external quantum efficiency at lower current densities. Transparent AlGaAs-based DBRs exhibit a lower refractive index contrast in this wavelength regime, which results in an increased penetration depth and therefore a larger effective cavity length. As the GaAs substrate is highly absorbing in the red, bottom emitting MCLEDs without a removal of the substrate would be limited to low efficiencies. Oxide DBRs lead to improved device performances for top emitting devices, however the device realization is further hampered by several aspects compared to near infrared emitting devices, as shown in the previous chapter.

The thin-film technology enables the removal of the absorbing substrate and the transfer of the epitaxially grown structure on a dielectric-coated metal mirror without the stringent process parameters of the semiconductor-to-semiconductor wafer bonding technique [60]. However, without further extraction methods, the light not extracted at the first incidence with the surface tends to be trapped in the waveguide formed by the hybrid mirror and the semiconductor-air interface. If the internal quantum efficiency is very high the trapped light is continuously re-absorbed in the active region and re-emitted and can therefore be ultimately extracted due to this photon recycling mechanism, but otherwise a large part of the light will be lost due to non-radiative recombination. Common extraction enhancement methods for thin-film LEDs are surface texturing [69,71–73], buried micro-reflectors [65,76] or the combination of both [72,73]. They all lead to a drastic reduction of the mean photon path length for extraction by an angular randomization of the totally reflected light. With these approaches high external quantum efficiencies have been achieved in the red and in the near infrared (see chapter 2.6.2).

Due to the angular randomization, these device types show a non-directional emission despite their single facet emission. To achieve high directionality, MCLEDs are ideal candidates [249,250]; however, the maximum achievable efficiencies in the red are limited. A self-evident approach for the realization of directional emitters in the red

with reasonable efficiencies is therefore the combination of the resonant cavity concept with the thin-film technology. Due to the highly reflective bottom hybrid mirror with a large spectral and angular stopband and the waveguide structure formed with the semiconductor-air interface, **thin-film MCLEDs** can be expected to exhibit small effective cavity lengths and have the potential for high photon recycling factors. Therefore higher external quantum efficiencies than for standard red MCLEDs can be expected from these red thin-film MCLEDs.

Devices of this type were grown and fabricated by OSRAM Opto Semiconductors and have been characterized in detail. They consist of an AlGaInP cavity, a bottom hybrid mirror and a top AlGaAs outcoupling DBR. The hybrid mirror is made up of an omnidirectional reflector (ODR, see chapter 2.8.3) and a single AlGaAs DBR pair. The angular and spectral emission properties specific to this device type will be presented and the effect of photon recycling and in-plane superluminescence on the far-field radiation pattern will be discussed. To our knowledge these devices represent the first realization of thin-film MCLEDs.

6.2 Structure

The epitaxial structure of the thin-film MCLEDs consists of a 1- λ AlGaInP cavity, a 6 pair n-Al_{0.53}Ga_{0.47}As/Al_{0.95}Ga_{0.05}As outcoupling DBR and a single pair of p-type Al_{0.53}Ga_{0.47}As/Al_{0.95}Ga_{0.05}As. The active region is made up of 5 compressively strained GaInP QWs with (Al_{0.47}Ga_{0.53})_{0.51}In_{0.49}P barrier layers, surrounded by Al_{0.51}In_{0.49}P confinement layers. On the extraction side a several micron thick Al_{0.80}Ga_{0.20}As current spreading layer and an (Al_{0.55}Ga_{0.45})_{0.51}In_{0.49}P etch stop layer enabling the substrate removal are added.

During device fabrication an omnidirectional reflector (ODR), consisting of a low index semiconductor layer and a gold layer, is added on the p-side in order to complete the high reflectivity hybrid mirror. On the extraction side a silicon nitride anti-reflection coating is deposited on the etch stop layer after the substrate removal. This should minimize the parasitic reflections within the waveguide structure.

The structure was designed by Wolfgang Schmid from OSRAM Opto Semiconductors and is labelled K2552. It was grown by metalorganic vapor phase epitaxy (MOVPE) by Rainer Butendeich at the OSRAM Opto Semiconductors R&D lab in Regensburg, Germany. The refractive index profile of the structure is displayed in figure 6.1, the detailed structure can be found in appendix B.

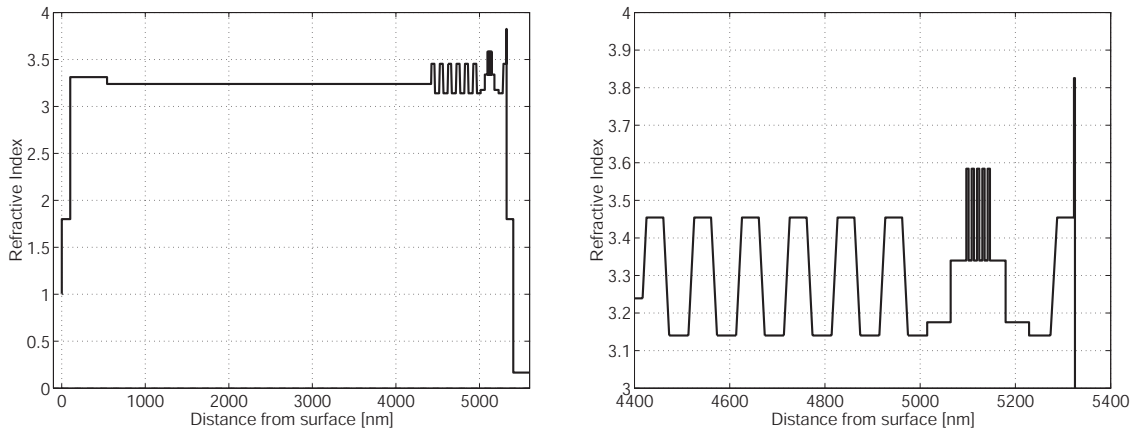


Figure 6.1: Refractive index profile of structure K2552 (left) with a close-up of the cavity region (right)

6.3 Simulation

The light extraction properties of the structure are calculated with the simulation program described in section 3.3. The refractive index calculation is based on the data by Adachi [162] for AlGaAs and on the analytical model presented by Moser et al. [270] for AlGaInP. The refractive index of gold is estimated to be $0.166 + 3.15i$ around 650 nm based on the data by Palik et al. [163].

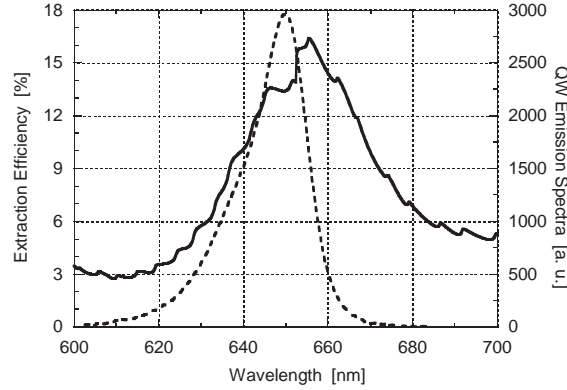


Figure 6.2: Simulated extraction efficiency of structure K2552; emission into air (solid line) plus intrinsic emission spectrum (dashed line)

Figure 6.2 shows the extraction efficiency of structure K2552 as a function of wavelength, calculated for monochromatic emission into air. The QW emission spectrum used for the integration is displayed as well. Table 6.1 shows the distribution of the emission in the different modes at 650 nm. The outcoupling DBR shows a narrow angular stopband, since its refractive index contrast is quite low. This explains the high leaky mode fraction. However this fraction is not lost as the original absorbing substrate is removed during the fabrication. This light is totally internally reflected at the interface semiconductor–air and thus laterally guided in the waveguide formed by the hybrid mirror and the top interface. Therefore in the case of structures of this type the leaky mode fraction can be counted as guided modes as well.

Table 6.1: Fractions of emission in the various kinds of modes for structure K2552 at 650 nm and for emission into air. Leaky mode fraction guided in thin-film waveguide.

	extracted [%]	(leaky) [%]	guided [%]
air	14	74	11

An external quantum efficiency of the order of 12% can thus be expected to achieve with this structure for. A discontinuity in the simulation around 652 nm related to the absorption band edge of GaInP at this wavelength leads to a high relative error of the simulation result on the order of 10 to 20%. It was not possible to simulate the emission into epoxy for this structure. In addition it has to be noted that this simulation does not include any photon recycling.

6.4 Fabrication

The chip processing of these thin-film MCLEDs has been done in the wafer fab of OSRAM Opto Semiconductors in Regensburg, Germany and can therefore not be compared with the fabrication of the other MCLEDs treated in this thesis. Device fabrication begins with the deposition of a dielectric on the central device area on the p-side in order to avoid light generation beneath the final n-contact bond pad. Subsequently the omnidirectional reflector and solder metallizations are added. The wafer is then bonded onto a new carrier and the GaAs substrate is removed by selective etching. An anti-reflection coating (ARC) deposited on the etch stop layer minimizes parasitic reflections within the waveguide structure formed by the bottom reflector and the semiconductor-air interface. The ARC is removed in the central area and replaced by a standard bond pad. Finally the wafer is sawn into $300 \times 300 \mu\text{m}^2$ chips which are then mounted on TO18 headers for characterization. Some of the devices are furthermore encapsulated in epoxy.

The main processing steps are:

- Current Blocking Dielectric, ODR and P-Contact Deposition
- Wafer Bonding and Substrate Removal
- Anti-Reflection Coating and N-Contact Deposition
- Wafer Sawing, Bonding and Encapsulation

The different steps are described below and are illustrated with schematic cross-sections in figures 6.3–6.6. However the description is not as detailed as in the previous chapters, as the chip processing was done by OSRAM.

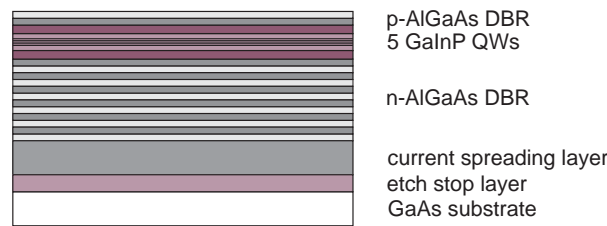


Figure 6.3: Schematic layer structure after growth

Current Blocking Dielectric, ODR and P-Contact Deposition

- i. Insulator pad deposition: SiN_x (opposite of n-contact pad to be deposited later)
- ii. Low refractive index semiconductor layer deposition
- iii. Gold mirror and p-contact layer deposition

6.5 Experimental Results

6.5.1 L–I–V Measurements

Figure 6.7 shows the dc output characteristics of the red thin-film MCLEDs, measured with an integrating sphere, as determined by OSRAM Opto Semiconductors. These devices show a maximum external quantum efficiency of 18 % and 23 % for non-encapsulated and epoxy-encapsulated devices, respectively. The corresponding output powers are 3.4 mW and 5.4 mW. The efficiency maxima occur at a drive current of 10 mA, translating to a current density of approximately 11 A/cm², and at a voltage of 2.5 V. Since the backside mirror contact and the associated semiconductor interface are not yet optimized from an electrical point of view, the series resistance is still quite high in these devices, leading to wall-plug efficiencies slightly lower than the external quantum efficiencies.

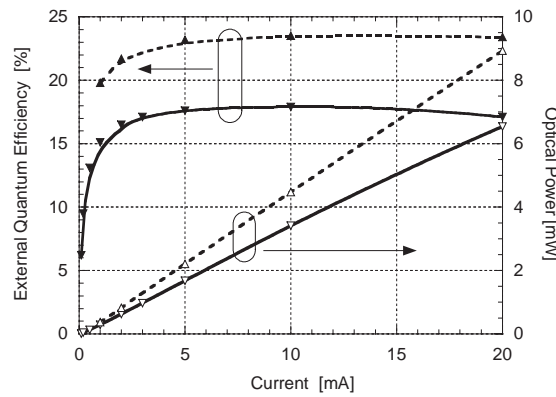


Figure 6.7: External quantum efficiency (solid symbols) and optical power (empty symbols) vs. drive current of thin-film MCLEDs from sample K2552, measured with an integrating sphere; without (solid line) and with epoxy encapsulation (dashed line). Measurements carried out by OSRAM Opto Semiconductors.

The devices are further characterized by more detailed light, current and voltage (L–I–V) measurements over a larger current range and with a smaller step width. The emitted light is collected either with a large area silicon photodiode or with an integrating sphere.

L–I–V Measurements with Large Area Photodiode

The set-up consists of a calibrated large area silicon photodiode (Hamamatsu S1337-1010BR) and a HP 4145B Semiconductor Parameter Analyzer, which is used as DC voltage source, current monitor and photocurrent monitor simultaneously. All measurements are taken in cw (continuous wave) mode and at room temperature. The bonded devices are attached to a transistor socket. A voltage is applied to the diode and is varied over a certain range while the resulting diode forward current and the photocurrent generated in the photodiode are recorded. The photodiode is biased at 0 V in order to minimize its dark current. The measurement setup for top emitting devices is explained in detail in section 4.5.2. At 650 nm the external quantum efficiency

of the photodiode is 0.783. This value corresponds to the product $1.24R_{PD}/\lambda[\mu m]$ with R_{PD} being the calibrated photo sensitivity of the photodiode in units of A/W. The calibration values are listed in appendix D.1.

As the LED characteristics at low current densities give a good indication of the electrical and optical quality of the device, the current–voltage curves are plotted on a semilogarithmic scale ($\log(I)$ – V) and the external quantum efficiency is plotted versus the logarithm of the current density (η_{ext} – $\log(J)$). The measured I–V characteristic and external quantum efficiency as a function of drive current density are shown in figure 6.8. The efficiency is maximal at a current of 5 mA, corresponding to a current density of 7 A/cm^2 . The ideality factor of the I–V characteristic can be determined in the 10^{-8} to the 10^{-5} A current range and is approximately 2.2.

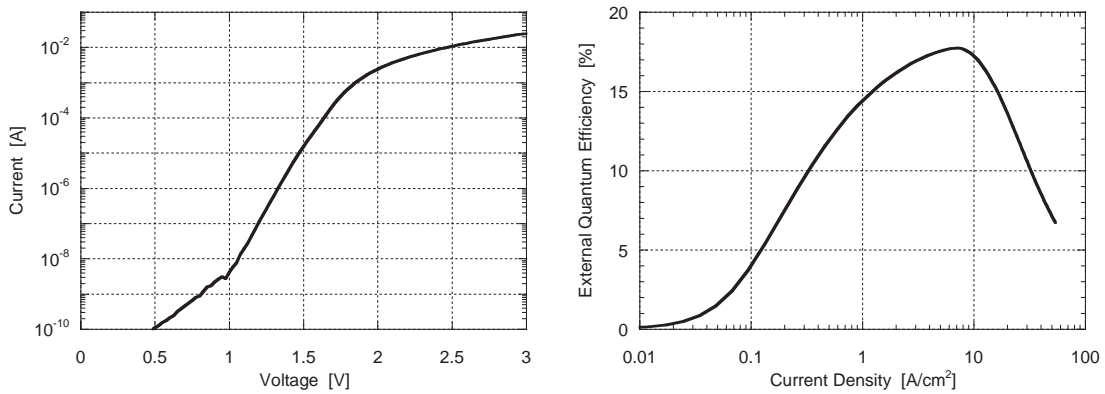


Figure 6.8: I–V characteristic and external quantum efficiency vs. drive current density of thin-film MCLEDs from sample K2552; emission into air

L–I–V Measurements with Integrating Sphere

This set-up consists of a calibrated integrating sphere (UDT Instruments Radiometry Model 2575 Laser Power Attenuator with a Model 260 silicon sensor head attached to it) and a HP 4145B Semiconductor Parameter Analyzer, which is used as DC voltage source, current monitor and photocurrent monitor simultaneously. All measurements are taken in cw (continuous wave) mode and at room temperature. The bonded devices are attached to a transistor socket. The measurement conditions are the same as for the previous setup; measurements with an integrating sphere are described in detail in section 4.5.2. According to the calibration sheet in appendix D.2 the external quantum efficiency of the ensemble sphere – photodetector corresponds to 1.45×10^{-3} at 650 nm.

In figure 6.9 the current–voltage curve and the external quantum efficiency versus the current density of the thin-film MCLEDs measured with the integrating sphere are plotted. Compared to the measurement with the large area detector the efficiency maximum is located at a higher current density, 11 A/cm^2 , and the roll-over is smoother and less steep. This phenomenon will be discussed later on.

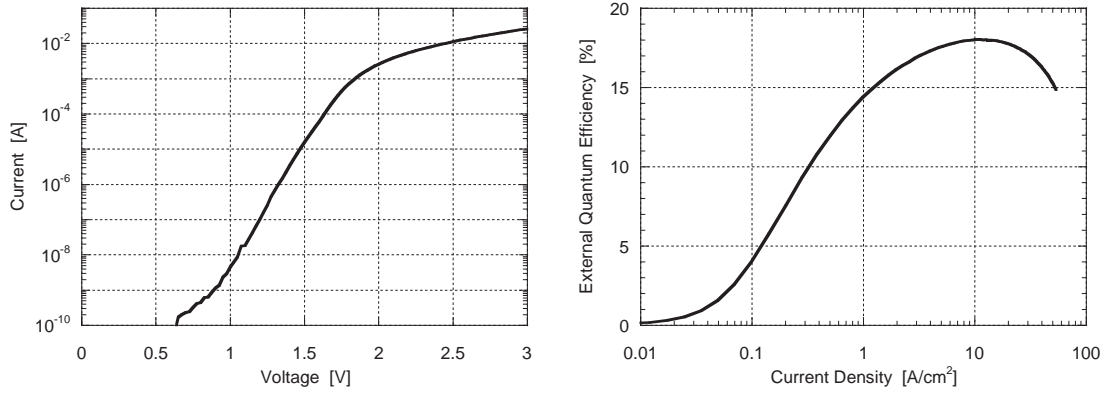


Figure 6.9: I–V characteristic and external quantum efficiency vs. drive current density of thin–film MCLEDs from sample K2552, measured with an integrating sphere; emission into air

6.5.2 Far–Field Emission

The far–field emission of the red thin–film MCLEDs from sample K2552 was determined as described in section 4.5.2. The structure as designed with the intended negative detuning for a maximum external quantum efficiency should show an emission peak at an angle of 45° from the normal. However the measurements show a directional emission centered around the normal, as can be seen in figure 6.10 for the measurements carried out by OSRAM Opto Semiconductors. This emission profile indicates a detuning of approximately zero, i.e. a shorter cavity length than designed. Furthermore an increase in temperature did not lead to a change of the emission pattern but only to a decrease in intensity, as would be expected for a positive detuning (measurements carried out by OSRAM Opto Semiconductors, not shown).

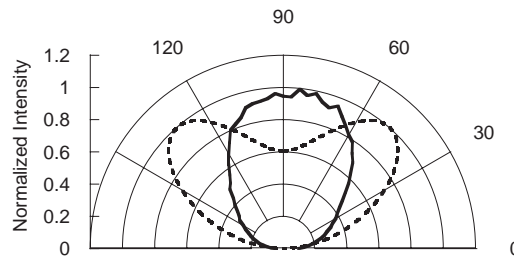


Figure 6.10: Far–field emission spectrum of thin–film MCLEDs from sample K2552 at a current of 10mA; comparison between measurement (solid line) and simulation (dashed line). Measurement carried out by OSRAM Opto Semiconductors.

The evolution of the far-field radiation pattern with injection current density was studied. Figure 6.11 shows the emission spectra for different drive currents. Up to 5 mA, corresponding to the current density for which the maximum in efficiency was measured with the large area detector, a general broadening of the emission spectrum can be noted. Between 5 and 50 mA however the relative emission significantly increases for large angles from the normal but decreases for small angles. This intensity shift is more obvious in the linear plot in figure 6.12.

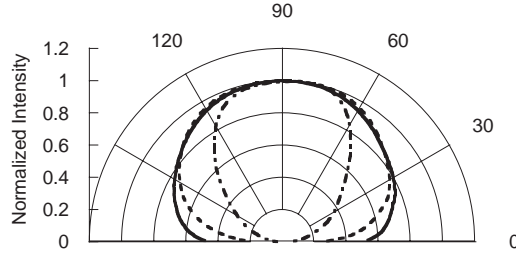


Figure 6.11: Far-field emission spectrum of thin-film MCLEDs from sample K2552 as a function of injection current; 0.1 mA (dash-dot line), 5 mA (dashed line), and 50 mA (solid line)

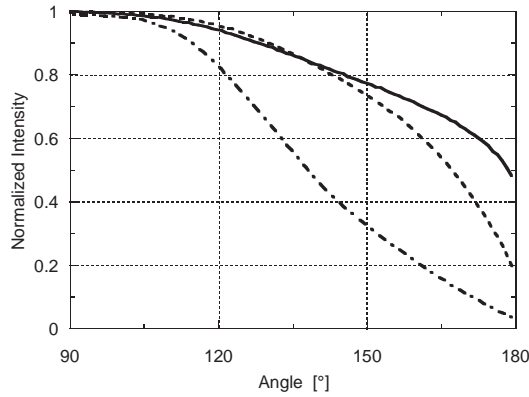


Figure 6.12: Linear plot of the far-field emission spectrum of thin-film MCLEDs from sample K2552 as a function of injection current; 0.1 mA (dash-dot line), 5 mA (dashed line), and 50 mA (solid line)

6.5.3 Electroluminescence

The thin-film MCLEDs realized show an emission peak centered around 655 nm with a full width at half maximum (FWHM) of 34 meV at room temperature and in the normal direction. With increasing collection angle the cavity resonance shifts to shorter wavelengths, as can be seen in figure 6.13. In addition the emission into secondary resonances related to the thick waveguide is increasing with collection angle. The corresponding simulated spectra based on the design parameters, integrated with a typical QW emission spectrum, are shown in figure 6.14. The comparison of the measured spectra with the simulations indicates a blue-shift of the cavity resonances.

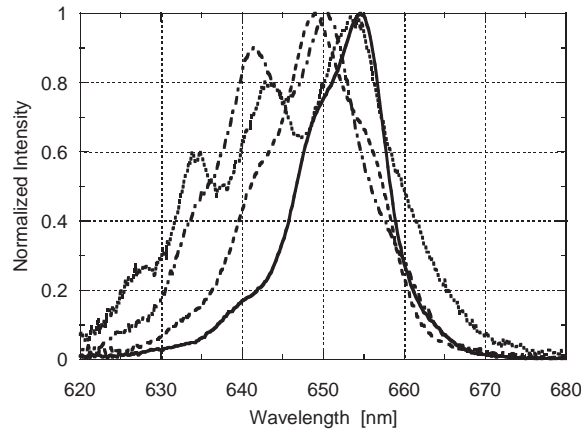


Figure 6.13: Electroluminescence for different collection angles of thin-film MCLEDs from sample K2552 at a current of 10 mA; 0° (solid line), 30° (dashed line), 45° (dash-dot line) and 60° (dotted line)

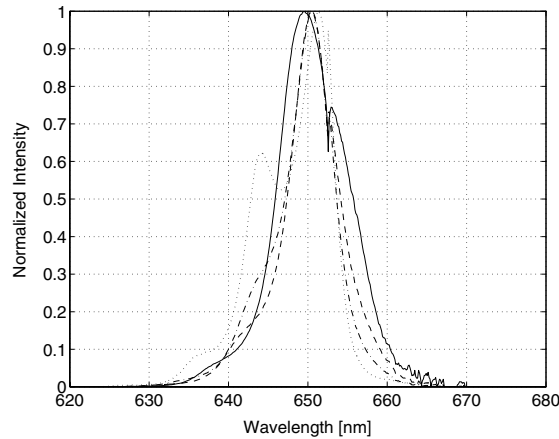


Figure 6.14: Simulation based on design parameters of cavity resonance for different collection angles for structure K2552, integrated with a typical QW emission spectrum; 0° (solid line), 30° (dashed line), 45° (dash-dot line) and 60° (dotted line)

6.6 Discussion

The incorporation of a thin-film structure leads to a significant increase in performance of red MCLEDs. Despite a non-optimized backside contact and an obviously inadequate detuning the thin-film MCLEDs realized show significantly higher external quantum efficiencies than standard red MCLEDs.

6.6.1 Cavity Thickness and Detuning

The measured far-field emission and electroluminescence spectra show that the resonant cavity in these thin-film MCLEDs is shorter than designed, leading to a detuning of approximately zero. Reflectivity measurements carried out after the epitaxial growth by OSRAM Opto Semiconductors (not shown) indicate that the $\text{Al}_{0.53}\text{Ga}_{0.47}\text{As}$ high index layer in the p-DBR pair is too thin. Furthermore it is believed that the low refractive index semiconductor layer in the bottom hybrid reflector is partially attacked during the device fabrication.

By reducing the thicknesses of these two layers by a total of 0.1λ , a reasonable overlap can be found between measurement and simulation for the far-field emission and the electroluminescence as a function of collection angle. The simulation results are shown in figures 6.15 and 6.16. It seems as if the internal emission spectrum at a

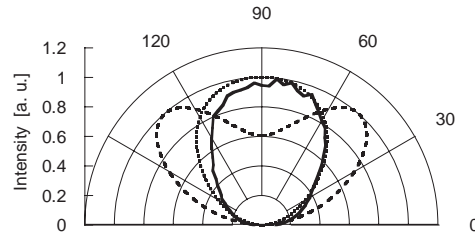


Figure 6.15: Corrected simulation angular emission spectrum compared with the measurement of thin-film MCLEDs; measurement (solid line), simulation structure as designed (dashed line) and simulation corrected structure (dash-dot line)

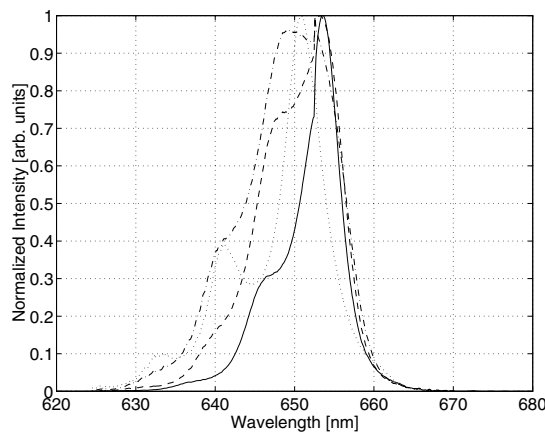


Figure 6.16: Corrected simulation cavity resonance of structure K2552 for different collection angles; 0° (solid line), 30° (dashed line), 45° (dash-dot line) and 60° (dotted line)

current of 10 mA is wider than the one used for the electroluminescence simulations, nevertheless the individual curves match quite well.

Further processing runs were carried out with different parameters or sequences, in order to avoid a cavity thickness reduction during fabrication by an attack of the ODR semiconductor layer. However, all thin-film MCLEDs realized to date show a near normal emission suggesting a detuning around zero.

6.6.2 Photon Recycling and In-Plane Superluminescence

Apart from the reduced effective cavity length and the reduced absorption an important part of the efficiency increase in red thin-film MCLEDs compared to standard red MCLEDs is attributed to photon recycling. Photon recycling denotes the re-absorption in the active region of photons that would not normally escape (i.e. guided modes) and the subsequent re-emission of some of these photons into the escape cone. This effect is discussed in more detail in section 2.7.3.

The simulation of the structure with the non-optimal detuning leads to a similar external quantum efficiency for emission into air as for the designed structure, a value of the order of 12 %. Therefore by comparing this value with the measured 18 %, the photon recycling factor can be estimated to be approximately 1.5 for this thin-film MCLED structure. Neither any shadowing effects by the top contact nor any current crowding effects are included in this simple estimation.

In the present structure the guided mode fraction is very high, up to 80 %. Due to the waveguide formed by the hybrid reflector and the semiconductor-air interface and the absence of an absorbing substrate, no leaky modes occur in this thin-film MCLED structure. Hence, apart from a small fraction that is absorbed in the metal mirror layer, all the light trapped in the device is emitted into guided modes. The internal quantum efficiency can be assumed to be at least 80 %. Thus for devices with dimensions larger than the typical characteristic absorption length, which is of the order of 100 μm , it is not surprising to find recycling factors significantly higher than unity.

Photon recycling only takes place if the absorption in the active region is non-negligible. However the absorption coefficient decreases with increasing carrier density and at some point population inversion and gain occurs. Therefore, at transparency, the photon recycling mechanism collapses and **superluminescence** in the lateral direction within the waveguide formed by the hybrid reflector and the semiconductor-air interface sets in. This leads to a redirection of a large part of the emission from the vertical Fabry-Perot mode to lateral guided modes.

Effect on External Quantum Efficiency Characteristic

In the case where transparency occurs at a lower current density than the roll-over of the internal quantum efficiency caused by thermal effects or carrier spill-over, the occurrence of photon recycling and in-plane superluminescence can be visualized by comparing the emission in the vertical direction and in the lateral direction. In figure 6.17 the external quantum efficiency characteristics measured with an integrating sphere and with a large area Si photodiode situated on top of the device are plotted. With the large area detector over the device only the vertical emission is measured whereas the integrating sphere collects light emitted in all directions, including any

lateral emission. It can be seen that, if only the emission in the vertical direction is taken into account, the efficiency starts to decrease at a lower current density and with a steeper slope compared to the efficiency for the overall emission. This can therefore be explained by a gradual re-distribution of the emission from the vertical to the lateral direction due to the disappearance of photon recycling and the onset of in-plane superluminescence at a lower current density than the overall efficiency roll-over.

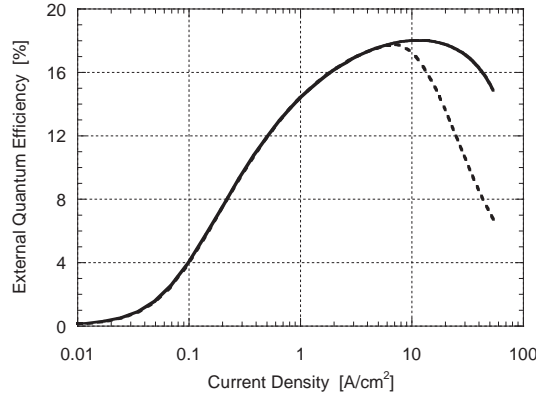


Figure 6.17: External quantum efficiency vs. drive current density of thin-film MCLEDs from sample K2552; measured with an integrating sphere (solid line) and with a large area photodiode (dashed line)

Effect on Far-Field Radiation Pattern

The transition from photon recycling to in-plane superluminescence with increasing current density can be visualized as well by tracing the far-field emission of the thin-film MCLEDs as a function of current density. The current-dependence of the radiation pattern has been shown in figures 6.11 and 6.12. The general broadening of the emission up to 5 mA, the current density for which the maximum in efficiency was measured with the large area detector, can be explained with a spectral broadening of the internal emission, leading to a wider spatial emission pattern. Between 5 and 50 mA however the relative intensity at large angles drastically increases, at the expense of the relative intensity for angles smaller than 45° from the normal. This effect is ascribed to the successive redirection of the emission from the vertical to the lateral direction above transparency as a result of a switch from enhanced vertical emission due to photon recycling to enhanced lateral emission due to in-plane superluminescence.

6.7 Conclusions

A new type of high-brightness LEDs is presented, which is based on the combination of resonant cavities and thin-film structures. To our knowledge, this is the first realization of thin-film MCLEDs. With this device design significantly higher external quantum efficiencies compared to standard MCLEDs can be achieved in the red. This is related to the absence of an absorbing substrate and the presence of a waveguide structure with high angle-averaged reflectivities and minor penetration depths. The large guided mode fraction in this type of devices leads to a significant amount of photon recycling, causing an additional efficiency enhancement. Red emitting thin-film MCLEDs with an AlGaInP-based cavity surrounded by an AlGaAs/AlAs outcoupling reflector and a high reflectivity hybrid mirror have been realized by OSRAM Opto Semiconductors. Even though these devices show a non-optimal detuning, external quantum efficiencies of 23 % and 18 % with and without encapsulation, respectively, have been achieved. Due to a detuning of virtually zero, these emitters show a highly directional emission with a narrow far-field around the normal. This makes these thin-film MCLEDs ideal for high brightness applications and in particular for optical communication, because of their increased fiber coupling efficiency as compared to other LED designs. With an optimum negative detuning a further increase in efficiency should be achievable.

The occurrence of photon recycling and in-plane superluminescence and their effect on the far-field radiation pattern of these thin-film MCLEDs is demonstrated. The transition from photon recycling to in-plane superluminescence at transparency causes a gradual redirection of part of the emission from the vertical to the lateral direction with increasing current density in that range.

Chapter 7

Conclusions and Perspectives

The need for high efficiency LEDs in order to achieve a further market penetration and to broaden the range of applications for LEDs has been emphasized in the introduction, together with the resulting beneficial effects on the economy and the environment. In modern semiconductor LEDs internal quantum efficiencies close to unity can be achieved. High injection efficiencies are possible due to an optimized bandgap engineering and high radiative efficiencies are achieved with advanced epitaxial growth techniques. Therefore the external quantum efficiency of a semiconductor LED is mainly limited by its extraction efficiency. Due to the high refractive index of common III-V semiconductor materials only a small fraction of the light generated internally is extracted from a standard planar device and the extraction efficiencies are limited to very low values.

Several methods have been developed in order to circumvent this problem, either by optimizing the device geometry in order to increase the escape cones or by incorporating a resonant structure in order to force the emission into the existing escape cones. The latter approach is called microcavity LED (MCLED) or resonant cavity LED (RCLED). In a MCLED the spontaneous internal emission is controlled by placing the emitter inside an optical cavity with a thickness of the order of the emission wavelength. The resulting interference effects increase the part of the emission that can be extracted. Contrary to the other approaches this is possible without changing the device geometry and thus without additional costly back-end processing steps. The control of the far-field radiation pattern makes these devices particularly interesting for high brightness applications demanding highly directional emitters, such as printing, bar code reading, large area displays or optical communication.

7.1 Summary of results

The extraction efficiency of standard MCLEDs is limited by several technological aspects. Even though an optical cavity thickness of $\lambda/2$ would be ideal for optical purposes, λ cavities are generally used. For smaller sized cavities either the carrier injection or the radiative recombination efficiency in the quantum well would be compromised. Furthermore due to the limited refractive index contrast in the semiconductor distributed Bragg reflectors (DBRs) the penetration depth of the optical field into these reflectors is large compared to the actual cavity length. This leads to high effective cav-

ity lengths and thus decreased external quantum efficiencies, as the extraction efficiency of a MCLED structure is inversely proportional to the effective cavity length.

Thanks to the implementation of novel concepts the extraction properties of different types of MCLEDs are further enhanced by decreasing their effective cavity length. The phase-shift cavity principle whilst maintaining the electrical properties of a standard λ cavity achieves optical properties close to a $\lambda/2$ cavity. The use of AlO_x instead of AlAs as the low refractive index component in the distributed Bragg reflectors (DBRs) leads to smaller penetration depths and therewith a reduction in the effective cavity length. Another means of reducing the effective cavity length of a standard MCLED is to combine it with a thin-film structure.

The beneficial effect of these structure modifications is studied for two different emission regions. For near infrared emitting devices high quality InGaAs/GaAs QWs are available (peak wavelength 970–980 nm). Red emitting devices with GaInP/AlGaInP active regions (peak wavelength 650 nm) are of commercial interest. For red emitting MCLEDs the attainable efficiencies are lower than for near infrared devices due to several reasons. The lower confinement potentials lead to an increased carrier leakage and the larger thermal and electrical resistivities cause an increased sensitivity to Joule heating. In addition the lower refractive index contrast of the AlGaAs-based DBRs leads to larger penetration depths and thus increased effective cavity lengths. Since thicker barrier layers are needed due to the lower confinement potentials, the phase-shift cavity concept cannot be applied to red emitting AlGaInP MCLEDs. However due to the lower refractive index contrast for the semiconductor DBRs the use of an oxide DBR leads to a larger efficiency increase than in the near infrared. The latter is also true for the implementation of a thin-film structure.

For near infrared bottom emitting MCLEDs with a phase-shift cavity and a device diameter of $150\mu\text{m}$ values of 18% for emission into air and 24% for emission into glycerol were measured at a very low current density of 10 A/cm^2 . Simulations show that with a further device optimization values above 20% into air and 30% into epoxy are possible. These devices include a top gold contact and a recess etch of the top p-doped layers for an efficient lateral current confinement; the substrate is thinned and coated with an anti-reflection layer. The highest external quantum efficiencies reported prior to this work for similar bottom emitting MCLEDs with a standard λ cavity are 17% and 23% for small devices (diameter $85\mu\text{m}$) and large area devices (contact diameter 1.5 mm), respectively [118].

Near infrared MCLEDs with semiconductor DBRs and designed for top emission based on the phase-shift cavity principle show maximum external quantum efficiencies of 19% for emission into air. The light aperture defined by an oxide current confinement measures $400 \times 400\mu\text{m}^2$. According to the simulations up to 24% for emission into air and 34% for emission into epoxy are theoretically possible. The efficiency of standard top emitting semiconductor DBR MCLEDs is limited to 10% [123].

With the additional incorporation of a high reflectivity GaAs/ AlO_x bottom DBR the performance of this device type can be further enhanced. The external quantum efficiency of 28% measured for a $350\mu\text{m}$ diameter top emitting oxide DBR MCLED corresponds to the highest ever reported efficiency for a MCLED. Simulations predict values of 30% for emission into air and nearly 40% for emission into epoxy. The previously published record value for oxide DBR devices was a differential external quantum

efficiency of 27 % [124], corresponding to an absolute external quantum efficiency of approximately 23 %. However the introduction of an oxide DBR leads to a more complicated device design and device fabrication, mainly related to a degradation of the semiconductor-oxide interface. A grading of the interfaces in the oxide DBR layers is missing in the present devices but is considered crucial for a good and reliable device performance.

Preliminary red emitting MCLEDs with a single GaInP QW in an AlGaInP cavity, surrounded by AlGaAs current spreading layers and an AlGaAs/ AlO_x bottom DBR were realized. The structure was grown by OSRAM Opto Semiconductors and is based on a design developed in collaboration between the Ecole Polytechnique in Paris, OSRAM Opto Semiconductors and EPFL. These devices show an external quantum efficiency of 12 %. The maximum external quantum efficiency achieved for standard red emitting MCLEDs with semiconductor DBRs is 9.6 % [119]. For larger device sizes ($700 \times 700 \mu\text{m}^2$ instead of $300 \times 300 \mu\text{m}^2$) the wall-plug efficiency of these MCLEDs increases from 10 to 12 % [65]. In order for the AlGaAs layers to be transparent around 650 nm, the aluminum content needs to be at least 50 %. This condition significantly complicates the device design and device fabrication for red MCLEDs with an oxide DBR, since a partial parasitic vertical oxidation of the high index AlGaAs DBR layers and of the n-AlGaAs intracavity contact layer on top of the bottom DBR is inevitable. A change in the optical properties as well as a reduced current injection are the result of this parasitic oxidation. Nevertheless with an optimized device design and fabrication efficiencies close to 20 % for emission into air should be attainable with this device type.

The problems related to the incorporation of an oxide DBR into a red emitting MCLED structure can be avoided by combining the resonant cavity with a thin-film structure instead. With the bottom hybrid mirror, formed by a metal mirror, a low refractive index semiconductor layer and a single DBR pair, a high angle-averaged reflectivity and a small penetration depth can be achieved. Thanks to the substrate removal the absorption losses are minimal. Thus with devices of this type significantly higher efficiencies than for standard red emitting MCLEDs can be achieved. First non-optimized devices were fabricated by OSRAM Opto Semiconductors and have been characterized in detail. To our knowledge, this corresponds to the first realization of thin-film MCLEDs. Even though their detuning is not optimal, these devices show an external quantum efficiency of 18 % for emission into air and 23 % for emission into epoxy. It is assumed that a significant fraction of the high external quantum efficiency of these devices is related to a strong photon recycling effect, favored by the presence of the waveguide structure formed by the bottom hybrid mirror and the top interface semiconductor-air. Furthermore a study of the far-field radiation pattern of these thin-film MCLEDs as a function of injection current shows that gain occurs in the quantum wells at high injection levels, causing the disappearance of photon recycling and the on-set of lateral in-plane superluminescence. This change from one mechanism to the other manifests itself as a re-direction of part of the emission from the vertical to the lateral direction with increasing current injection.

It has been shown that with an optimization of the microcavity design the limits in terms of efficiency can be pushed to higher values. In the near infrared the external quantum efficiencies of bottom emitting MCLEDs with a phase-shift cavity seem to be limited to 20 and 30 % before and after encapsulation, respectively. For top emission

the values are slightly higher, 25 and 35%. With an oxide DBR in addition top emitting phase-shift cavity MCLEDs might reach up to 30 % for emission into air and 40 % for emission into epoxy. In the case of red emitting MCLEDs the implementation of an oxide DBR leads to a theoretical value for unencapsulated devices close to 20 %. By combining a standard resonant cavity with a thin-film structure instead it should be possible to surpass the 20 % limit for red emitting devices.

In all the presented cases the implementation of novel concepts led to an enlargement of the efficiency levels available with MCLEDs. However these values are still far below the maximum efficiencies demonstrated with other, geometrical approaches. Nevertheless it is hoped that this work contributes to an enlargement of the field of applications for MCLEDs thanks to their increased efficiencies.

7.2 The Future of MCLEDs

The devices presented in this work represent prototypes, which require a further optimization in terms of device design and fabrication. This should lead to an additional increase in external quantum efficiency for these types of MCLEDs. The combination with a thin-film structure is applicable to any other material system and is especially interesting for wavelength ranges that still lack high refractive index contrast DBRs with a reasonable conductivity, such as for example III-nitride based devices. Once a viable substrate lift-off technique is found for this latter material system, high efficiencies can be expected for thin-film MCLEDs of this type.

In order to surpass the efficiency limits for MCLEDs mentioned previously, a further evolution of the epitaxial growth techniques is necessary. With a better control of the doping profiles and the availability of high refractive index contrast reflectors that can be grown epitaxially, the effective cavity lengths could be further reduced. Finally once it is possible to grow high aluminum content epitaxial layers with a low defect density, such as AlAs with a similar quality as GaAs for example, it will be possible to realize low index $\lambda/2$ cavities without any guided modes. However the problem of an efficient carrier injection into these high bandgap cavities still needs to be addressed.

From a realistic point of view, the above stated limits for different types of MCLEDs probably represent the highest efficiencies achievable with a reasonable effort. Only for hybrid forms such as thin-film MCLEDs there still seems to be a large potential for improvement. The use of classic MCLEDs will therefore presumably remain limited to high brightness applications.

Maybe it is rather the general approach towards MCLEDs which needs to be reconsidered. Detailed and extensive simulations have shown that a high extraction efficiency is currently impossible to achieve for a single sided extraction from a planar geometry. However if this latter condition of single sided emission and high brightness was dropped and ways were explored to include the guided mode in the overall emission, very high extraction efficiencies can be expected. In the absence of any leaky modes the extraction would only be limited by the optical absorption within the cavity and the reflectors. For this approach again thin-film MCLEDs seem to be the most promising candidates.

Appendix A

Material Parameters

A.1 Bandgap Energy

Figure A.1 shows the energy gap of several III–V semiconductors as a function of the lattice constant (not shown is the GaInN material system). The bandgap energy E_g and the bandgap wavelength λ_g are related via the following expression [37]

$$\lambda_g[\mu\text{m}] = \frac{hc}{eE_g} = \frac{1.24}{E_g[\text{eV}]} \quad (\text{A.1})$$

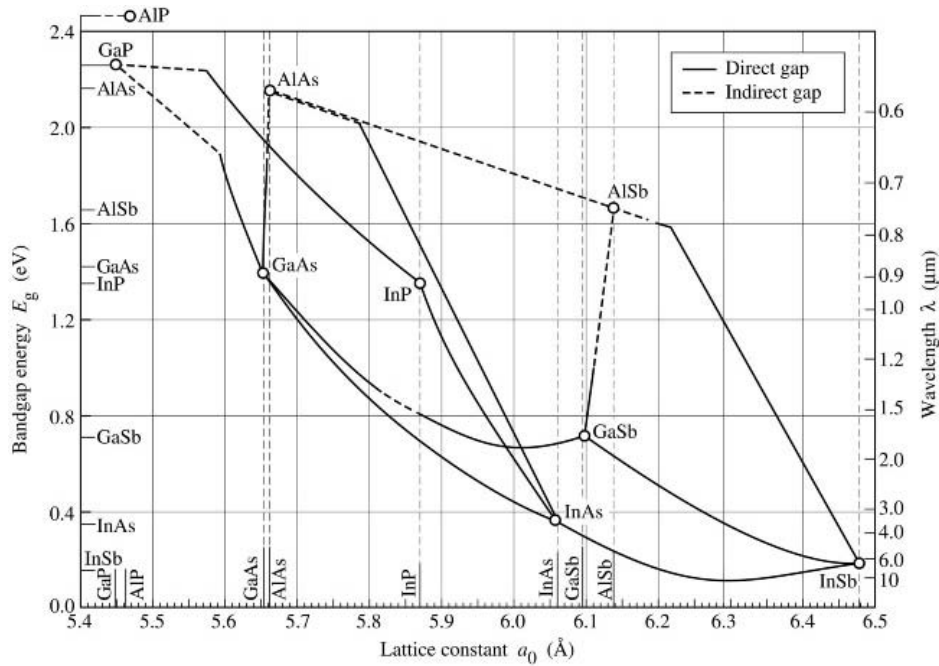


Figure A.1: Bandgap energy and corresponding wavelength versus lattice constant of various III–V semiconductors at room temperature [9]

A.1.1 The AlGaAs material system

$\text{Al}_x\text{Ga}_{1-x}\text{As}$ is a direct bandgap semiconductor for $x < 0.45$. The bandgap energy of $\text{Al}_x\text{Ga}_{1-x}\text{As}$ versus the Al mole fraction is shown in figure A.2. Its direct bandgap energy $E_{g\Gamma}$ can be analytically expressed as [9,294]

$$E_{g\Gamma}/\text{eV} = 1.424 + 1.247x \quad (0 \leq x \leq 0.45) \quad (\text{A.2})$$

Figure A.3 shows in addition the intrinsic absorption coefficient of $\text{Al}_x\text{Ga}_{1-x}\text{As}$ near the intrinsic absorption edge as a function of photon energy for different values of x [295]. From these two figures it can be seen that in order to be transparent in the red ($\lambda \approx 650 \text{ nm}$, $E_g \approx 1.9 \text{ eV}$) the Al-content has to be larger than 35 % at least.

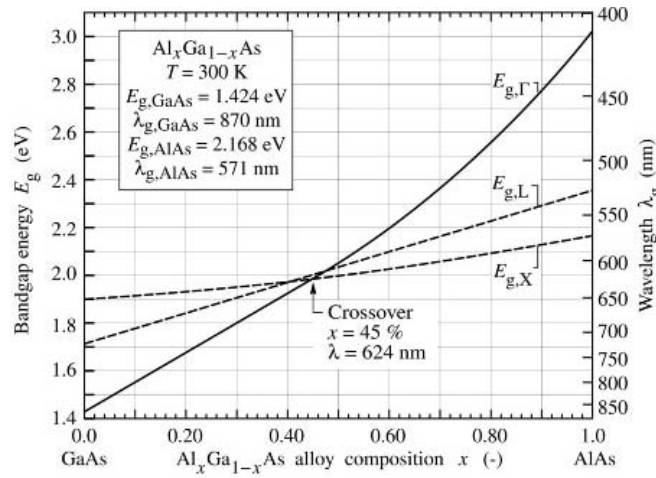


Figure A.2: Bandgap energy and emission wavelength of $\text{Al}_x\text{Ga}_{1-x}\text{As}$ at room temperature. $E_{g\Gamma}$ denotes the direct gap at the Γ point and E_{gL} and E_{gX} denote the indirect gap at the L and X point of the Brillouin zone, respectively [9,294].

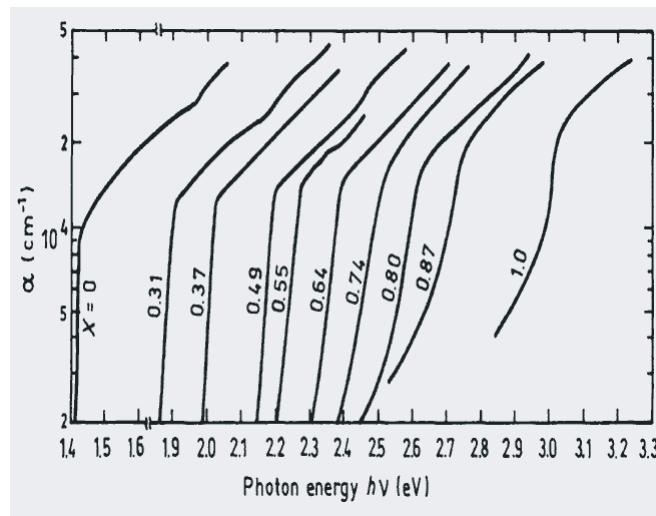


Figure A.3: Intrinsic absorption coefficient of $\text{Al}_x\text{Ga}_{1-x}\text{As}$ near the intrinsic absorption edge versus photon energy for different values of x at room temperature [295]

A.1.2 The AlGaInP material system

Figure A.4 shows the energy gap and the corresponding wavelength versus the lattice constant of $(\text{Al}_x\text{Ga}_{1-x})_y\text{In}_{1-y}\text{P}$. $\text{Ga}_{0.51}\text{In}_{0.49}\text{P}$ is lattice matched to GaAs (cf. figure A.1) and since Al and Ga have very similar atomic radii $(\text{Al}_x\text{Ga}_{1-x})_{0.51}\text{In}_{0.49}\text{P}$ is lattice matched to GaAs as well.

$(\text{Al}_x\text{Ga}_{1-x})_{0.51}\text{In}_{0.49}\text{P}$ has a direct bandgap for $x < 0.53$. Figure A.5 shows the bandgap energy of unordered $(\text{Al}_x\text{Ga}_{1-x})_{0.51}\text{In}_{0.49}\text{P}$ lattice-matched to GaAs. The following analytical expression was found for the direct bandgap energy [9,10]

$$E_{g\Gamma}/\text{eV} = 1.91 + 0.61x \quad (0 \leq x \leq 0.53) \quad (\text{A.3})$$

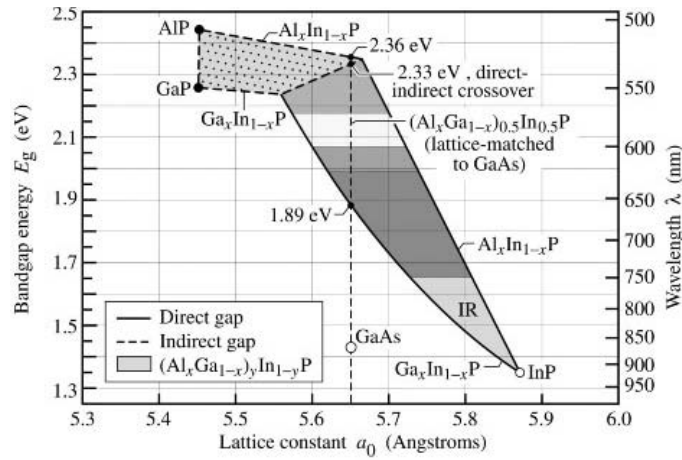


Figure A.4: Bandgap energy and corresponding wavelength versus lattice constant of $(\text{Al}_x\text{Ga}_{1-x})_y\text{In}_{1-y}\text{P}$ at room temperature. The dashed vertical line shows $(\text{Al}_x\text{Ga}_{1-x})_{0.51}\text{In}_{0.49}\text{P}$ lattice matched to GaAs [9,10].

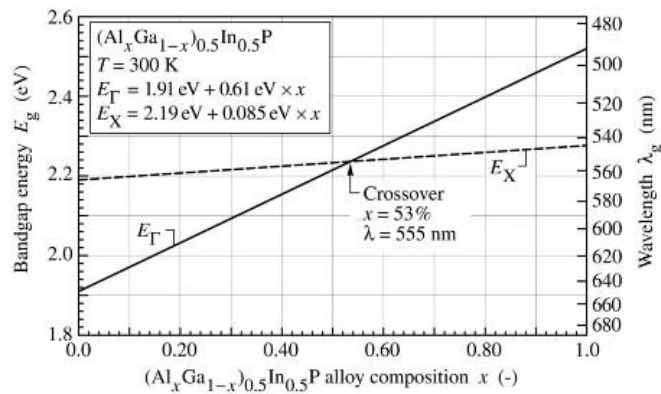


Figure A.5: Bandgap energy and emission wavelength of unordered $(\text{Al}_x\text{Ga}_{1-x})_{0.51}\text{In}_{0.49}\text{P}$ lattice-matched to GaAs at room temperature. $E_{g\Gamma}$ denotes the direct gap at the Γ point and E_{gX} denotes the indirect gap the X point of the Brillouin zone [9,10].

A.2 Indices of refraction

The refractive index calculation is based on the data by Adachi [162] for $\text{Al}_x\text{Ga}_{1-x}\text{As}$ and on the analytical model presented by Moser et al. [270] for $(\text{Al}_x\text{Ga}_{1-x})_{0.51}\text{In}_{0.49}\text{P}$. Table A.1 shows the values as a function of aluminum content at 970 and 650 nm for $\text{Al}_x\text{Ga}_{1-x}\text{As}$ and 650 nm for $(\text{Al}_x\text{Ga}_{1-x})_{0.51}\text{In}_{0.49}\text{P}$.

Table A.1: Calculated refractive indices of $\text{Al}_x\text{Ga}_{1-x}\text{As}$ at 970 nm and 650 nm (based on [162]) and of $(\text{Al}_x\text{Ga}_{1-x})_{0.51}\text{In}_{0.49}\text{P}$ at 650 nm (based on [270])

Al-content x	$\text{Al}_x\text{Ga}_{1-x}\text{As}$				$(\text{Al}_x\text{Ga}_{1-x})_{0.51}\text{In}_{0.49}\text{P}$	
	970 nm		650 nm		650 nm	
	n	k	n	k	n	k
0	3.5228		3.8254	0.1808	3.5842	0.1004
10	3.4770		3.7784	0.2383	3.5009	
20	3.4229		3.7044	0.1694	3.4464	
30	3.3662		3.6609	0.1231	3.4033	
40	3.3100		3.5793	0.0004	3.3649	
50	3.2502		3.4759		3.3294	
60	3.1928		3.4006		3.2959	
70	3.1349		3.3101		3.2639	
80	3.0791		3.2391		3.2333	
90	3.0295		3.1858		3.2038	
93	3.0070		3.1585		3.1952	
95	2.9920		3.1403		3.1895	
98	2.9695		3.1130		3.1810	
100	2.9545		3.0953		3.1754	

Appendix B

Epitaxial Structures

The structures grown and processed during this work are listed in the following tables. Table B.1 shows a general overview of the different structures. The ones emitting in the near infrared are labelled "S" and were grown at EPFL by molecular beam epitaxy (MBE). The structures emitting in the red are labelled "K" and were grown by metal organic chemical vapor deposition (MOCVD) by OSRAM Opto-Semiconductors, Regensburg, Germany.

Table B.1: Overview MCLED structures

Structure	Type	Emission wavelength	Cavity length	Emission optimization	Carrier confinement
S1892	SE MCLED	970	$\lambda/8$ PS	air	oxide aperture
S1904	TE MCLED	970	$\lambda/8$ PS	epoxy	oxide aperture
S1905	TE MCLED	970	$\lambda/8$ PS	air	recess etch
S1907	TE MCLED	970	$\lambda/8$ PS	air	recess etch
S1908	TE MCLED	970	$\lambda/8$ PS	epoxy	recess etch
S1910	TE MCLED	970	$\lambda/8$ PS	air	oxide aperture
K1439	TE MCLED	650	2λ	air	recess etch
K2552	TF MCLED	650	1λ	air	current blocking

Except for S1892 all structures are top emitting (TE), whereas S1892 is substrate emitting (SE). K2552 corresponds to a thin-film (TF) MCLED structure. The infrared MCLEDs all consist of a bottom DBR and a $\lambda/8$ phase-shift (PS) cavity with a single $\text{In}_{0.16}\text{Ga}_{0.84}\text{As}$ quantum well and a squeezed GRINSCH-like confinement region. The top mirror consists either simply of the interface GaAs–air or has an additional DBR pair. The detailed mirror compositions are listed in table B.2, the individual epitaxial structures are presented subsequently. The metal mirror for structure S1892 and the ODR for K2552 are deposited during the device fabrication subsequent to the epitaxial growth.

Structures S1892 and S2062 contain an $\text{Al}_{0.98}\text{Ga}_{0.02}\text{As}$ layer in order to form an oxide aperture for lateral current confinement, in case of the structures S1904 and S1910 the $\text{Al}_{0.98}\text{Ga}_{0.02}\text{As}$ layer in the top DBR and the top $\text{Al}_{0.98}\text{Ga}_{0.02}\text{As}$ layer in the bottom DBR can be selectively oxidized by only exposing these layers by selective wet etching. In

Table B.2: Different MCLED structures as grown and processed

Structure	Bottom Reflector			Top Reflector		
	pairs	n_h	n_l	pairs	n_h	n_l
S1892	3.5	GaAs	$\text{Al}_{0.93}\text{Ga}_{0.07}\text{As}$	0	-	gold
S1904	16.5	GaAs	$\text{Al}_{0.98}\text{Ga}_{0.02}\text{As}$	1	GaAs	$\text{Al}_{0.98}\text{Ga}_{0.02}\text{As}$
S1905	3.5	GaAs	AlO_x	0	GaAs	air
S1907	3.5	GaAs	AlO_x	1	GaAs	$\text{Al}_{0.90}\text{Ga}_{0.10}\text{As}$
S1908	3.5	GaAs	AlO_x	1	GaAs	$\text{Al}_{0.90}\text{Ga}_{0.10}\text{As}$
S1910	+1	GaAs	$\text{Al}_{0.90}\text{Ga}_{0.10}\text{As}$	0	GaAs	air
	15.5	GaAs	$\text{Al}_{0.98}\text{Ga}_{0.02}\text{As}$			
K1439	3.5	$\text{Al}_{0.5}\text{Ga}_{0.5}\text{As}$	AlO_x	0	GaAs	air
K2552	-	ODR	-	6	$\text{Al}_{0.53}\text{Ga}_{0.47}\text{As}$	$\text{Al}_{0.95}\text{Ga}_{0.05}\text{As}$
	+1	$\text{Al}_{0.53}\text{Ga}_{0.47}\text{As}$	$\text{Al}_{0.95}\text{Ga}_{0.05}\text{As}$			

the other structures the current is confined by a selective recess etch of the top p-doped GaAs layers and the top DBR pair, if present. The thin-film MCLEDs with structure K2552 feature a dielectric current blocking layer on the p-side opposite to the n-contact pad.

S1905, S1907 and S1908 contain a 3.5 pair GaAs/ $\text{Al}_{0.98}\text{Ga}_{0.02}\text{As}$ bottom DBR designated for lateral oxidation. By transforming the $\text{Al}_{0.98}\text{Ga}_{0.02}\text{As}$ layers to AlO_x a similar reflectivity as for the semiconductor DBRs with a significantly higher number of DBR pairs can be achieved.

In case of the substrate emitting devices with structure S1892 the substrate is thinned after the device processing and an anti-reflection coating is deposited on the substrate side.

The red MCLED structure K1439 consists of an $\text{Al}_{0.5}\text{Ga}_{0.5}\text{As}/\text{AlO}_x$ bottom DBR and a standard 2λ cavity with a single GaInP quantum well, AlGaInP barrier and confinement layers and AlGaAs current spreading and contact layers. The GaAs top p-contact layer is kept as thin as possible in order to minimize absorption. The mirror oxidation layers are surrounded by thick $\text{Al}_{0.95}\text{Ga}_{0.05}\text{As}$ intermediate grading layers.

The thin-film MCLED devices based on structure K2552 contain a $1-\lambda$ cavity with 5 GaInP QWs. An omnidirectional reflector (ODR) consisting of a gold and a proprietary semiconductor layer in combination with a single pair of p-type $\text{Al}_{0.53}\text{Ga}_{0.47}\text{As}/\text{Al}_{0.95}\text{Ga}_{0.05}\text{As}$ represent the bottom hybrid mirror. The outcoupling reflector consists of a 6 pair n- $\text{Al}_{0.53}\text{Ga}_{0.47}\text{As}/\text{Al}_{0.95}\text{Ga}_{0.05}\text{As}$ DBR, in both DBRs the interfaces are graded linearly. After the epitaxial growth the bottom ODR is deposited, before the wafer is bonded onto a new carrier and the substrate is removed by epitaxial lift-off. With an anti-reflection coating deposited on the etch stop layer the parasitic reflections within the waveguide structure are minimized.

Table B.3: Epitaxial structure S1892

Compound	Doping	Thickness [nm]	Comments
GaAs	n-Si		substrate and buffer
Al _{0.93} Ga _{0.07} As	n-Si	91	3.5 pair bottom DBR
GaAs	n-Si	64	
Al _{0.93} Ga _{0.07} As	n-Si	91	
GaAs	n-Si	64	
Al _{0.93} Ga _{0.07} As	n-Si	91	n-intracavity contact layer
GaAs	n-Si	64	
Al _{0.98} Ga _{0.02} As	n-Si	91	oxide aperture layer
GaAs	n-Si	65	
Al _{0.93} Ga _{0.07} As	n-Si	30	3-step GRINSCH
Al _{0.50} Ga _{0.50} As		20	
Al _{0.10} Ga _{0.90} As		15	
GaAs		10	
In _{0.16} Ga _{0.84} As		7.5	barrier layer
GaAs		10	QW emitting at 970 nm
Al _{0.10} Ga _{0.90} As		15	barrier layer
Al _{0.50} Ga _{0.50} As		20	3-step GRINSCH
Al _{0.93} Ga _{0.07} As		30	
GaAs	p-Be	84	current spreading layer
GaAs	p ⁺ -Be	20	p-contact layer
air			

Table B.4: Epitaxial structure S1904

Compound	Doping	Thickness [nm]	Comments
GaAs	n-Si		substrate and buffer
Al _{0.98} Ga _{0.02} As	n-Si	82	16.5 pair bottom DBR
GaAs	n-Si	76.4	
Al _{0.98} Ga _{0.02} As	n-Si	82	
GaAs	n-Si	76.4	
Al _{0.98} Ga _{0.02} As	n-Si	82	
GaAs	n-Si	76.4	
Al _{0.98} Ga _{0.02} As	n-Si	82	
GaAs	n-Si	76.4	
Al _{0.98} Ga _{0.02} As	n-Si	82	
⋮	⋮	⋮	
Al _{0.98} Ga _{0.02} As	n-Si	82	n-intracavity contact layer oxide aperture layer
GaAs	n-Si	76.4	
Al _{0.98} Ga _{0.02} As	n-Si	82	3-step GRINSCH barrier layer QW emitting at 970 nm barrier layer 3-step GRINSCH
GaAs	n-Si	77	
Al _{0.90} Ga _{0.10} As	n-Si	24	
Al _{0.90} Ga _{0.10} As		24	
Al _{0.50} Ga _{0.50} As		10	
Al _{0.10} Ga _{0.90} As		5	
GaAs		10	
In _{0.16} Ga _{0.84} As		7.5	
GaAs		10	
Al _{0.10} Ga _{0.90} As		5	
Al _{0.50} Ga _{0.50} As		10	oxide aperture layer 1 pair top DBR
Al _{0.90} Ga _{0.10} As		24	
Al _{0.90} Ga _{0.10} As	p-Be	24	
GaAs	p-Be	75	
Al _{0.98} Ga _{0.02} As	p-Be	82	p-contact layer
GaAs	p-Be	54	
GaAs	p ⁺ -Be	20	
air			

Table B.5: Epitaxial structure S1905

Compound	Doping	Thickness [nm]	Comments
GaAs	n-Si		substrate and buffer
Al _{0.98} Ga _{0.02} As	n-Si	120	3.5 pair GaAs/AlO_x bottom DBR
GaAs	n-Si	88	
Al _{0.98} Ga _{0.02} As	n-Si	120	
GaAs	n-Si	88	
Al _{0.98} Ga _{0.02} As	n-Si	120	
GaAs	n-Si	94	
Al _{0.98} Ga _{0.02} As	n-Si	120	
GaAs	n-Si	78.5	n-intracavity contact layer
Al _{0.90} Ga _{0.10} As	n-Si	20	3-step GRINSCH
Al _{0.50} Ga _{0.50} As		20	
Al _{0.10} Ga _{0.90} As		15	
GaAs		10	barrier layer
In _{0.16} Ga _{0.84} As		7.5	QW emitting at 970 nm
GaAs		10	barrier layer
Al _{0.10} Ga _{0.90} As		15	3-step GRINSCH
Al _{0.50} Ga _{0.50} As		20	
Al _{0.90} Ga _{0.10} As	p-Be	20	
GaAs	p-Be	53.6	current spreading layer
GaAs	p ⁺ -Be	20	p-contact layer
air			

Table B.6: Epitaxial structure S1907

Compound	Doping	Thickness [nm]	Comments
GaAs	n-Si		substrate and buffer
Al _{0.98} Ga _{0.02} As	n-Si	120	3.5 pair GaAs/AlO_x bottom DBR
GaAs	n-Si	88	
Al _{0.98} Ga _{0.02} As	n-Si	120	
GaAs	n-Si	88	
Al _{0.98} Ga _{0.02} As	n-Si	120	
GaAs	n-Si	94	
Al _{0.98} Ga _{0.02} As	n-Si	120	
GaAs	n-Si	78.5	n-intracavity contact layer
Al _{0.90} Ga _{0.10} As	n-Si	20	3-step GRINSCH
Al _{0.50} Ga _{0.50} As		20	
Al _{0.10} Ga _{0.90} As		15	
GaAs		10	
In _{0.16} Ga _{0.84} As		7.5	QW emitting at 970 nm
GaAs		10	barrier layer
Al _{0.10} Ga _{0.90} As		15	3-step GRINSCH
Al _{0.50} Ga _{0.50} As		20	
Al _{0.90} Ga _{0.10} As		20	
GaAs		76	
Al _{0.90} Ga _{0.10} As	p-Be	76	1 pair top DBR
GaAs	p-Be	56	
GaAs	p ⁺ -Be	20	
air			

Table B.7: Epitaxial structure S1908

Compound	Doping	Thickness [nm]	Comments
GaAs	n-Si		substrate and buffer
Al _{0.98} Ga _{0.02} As	n-Si	140	3.5 pair GaAs/AlO_x bottom DBR
GaAs	n-Si	96	
Al _{0.98} Ga _{0.02} As	n-Si	140	
GaAs	n-Si	96	
Al _{0.98} Ga _{0.02} As	n-Si	140	
GaAs	n-Si	84	
Al _{0.98} Ga _{0.02} As	n-Si	140	1 pair bottom DBR
GaAs	n-Si	77.6	
Al _{0.90} Ga _{0.10} As	n-Si	82.3	n-intracavity contact layer 3-step GRINSCH barrier layer QW emitting at 970 nm barrier layer 3-step GRINSCH
GaAs	n-Si	74.6	
Al _{0.90} Ga _{0.10} As	n-Si	24	
Al _{0.90} Ga _{0.10} As		24	
Al _{0.50} Ga _{0.50} As		10	
Al _{0.10} Ga _{0.90} As		5	
GaAs		10	
In _{0.16} Ga _{0.84} As		7.5	
GaAs		10	
Al _{0.10} Ga _{0.90} As		5	
Al _{0.50} Ga _{0.50} As		10	1 pair top DBR
Al _{0.90} Ga _{0.10} As		24	
Al _{0.90} Ga _{0.10} As	p-Be	24	p-contact layer
GaAs	p-Be	75	
Al _{0.90} Ga _{0.10} As	p-Be	80.5	
GaAs	p-Be	55	
GaAs	p ⁺ -Be	20	
air			

Table B.8: Epitaxial structure S1910

Compound	Doping	Thickness [nm]	Comments
GaAs	n-Si		substrate and buffer
Al _{0.98} Ga _{0.02} As	n-Si	89.1	15.5 pair bottom DBR
GaAs	n-Si	67.6	
Al _{0.98} Ga _{0.02} As	n-Si	89.1	
GaAs	n-Si	67.6	
Al _{0.98} Ga _{0.02} As	n-Si	89.1	
GaAs	n-Si	67.6	
Al _{0.98} Ga _{0.02} As	n-Si	89.1	
GaAs	n-Si	67.6	
Al _{0.98} Ga _{0.02} As	n-Si	89.1	
⋮	⋮	⋮	
Al _{0.98} Ga _{0.02} As	n-Si	89.1	n-intracavity contact layer oxide aperture layer
GaAs	n-Si	67.6	
Al _{0.98} Ga _{0.02} As	n-Si	89.1	3-step GRINSCH barrier layer QW emitting at 970 nm barrier layer 3-step GRINSCH current spreading layer p-contact layer
GaAs	n-Si	78.5	
Al _{0.90} Ga _{0.10} As	n-Si	15	
Al _{0.90} Ga _{0.10} As		15	
Al _{0.50} Ga _{0.50} As		10	
Al _{0.10} Ga _{0.90} As		10	
GaAs		10	
In _{0.16} Ga _{0.84} As		7.5	
GaAs		10	
Al _{0.10} Ga _{0.90} As		10	
Al _{0.50} Ga _{0.50} As		10	
Al _{0.90} Ga _{0.10} As		15	
Al _{0.90} Ga _{0.10} As	p-Be	15	
GaAs	p-Be	55.7	
GaAs	p ⁺ -Be	20	
air			

Table B.9: Epitaxial structure K1439

Compound	Doping	Thickness		Comments
		design [nm]	nominal [nm]	
GaAs				substrate and buffer
Al _{0.95} Ga _{0.05} As		45		3.5 pair Al_{0.5}Ga_{0.5}As/AlO_x bottom DBR with Al _{0.95} Ga _{0.05} As grading layers
Al _{0.98} Ga _{0.02} As		20	110.3	
Al _{0.95} Ga _{0.05} As		45		
Al _{0.5} Ga _{0.5} As		50	47.7	
Al _{0.95} Ga _{0.05} As		45		
Al _{0.98} Ga _{0.02} As		20	110.3	
Al _{0.95} Ga _{0.05} As		45		
Al _{0.5} Ga _{0.5} As		50	47.7	
Al _{0.95} Ga _{0.05} As		45		
Al _{0.98} Ga _{0.02} As		20	110.3	
Al _{0.95} Ga _{0.05} As		45		
Al _{0.5} Ga _{0.5} As		50	47.7	
Al _{0.95} Ga _{0.05} As		45		
Al _{0.98} Ga _{0.02} As		20	110.3	
Al _{0.95} Ga _{0.05} As		45		
Al _{0.7} Ga _{0.3} As	n ⁺ -Te	53	103.1	n-intracavity contact layer
Al _{0.7} Ga _{0.3} As	n-Te	50		intermediate layer
(Al _{0.7} Ga _{0.3}) _{0.5} In _{0.5} P	n-Te	50	54.8	confinement layer
(Al _{0.5} Ga _{0.5}) _{0.5} In _{0.5} P		46	48.7	barrier layer
GaInP		5	4.6	QW emitting at 650 nm
(Al _{0.5} Ga _{0.5}) _{0.5} In _{0.5} P		46	48.7	barrier layer
(Al _{0.7} Ga _{0.3}) _{0.5} In _{0.5} P	p-Mg	50	54.8	confinement layer
Al _{0.7} Ga _{0.3} As	p-C	87	88.4	current spreading layer
GaAs	p ⁺ -C	10	6.4	p-contact layer
air				

Table B.10: Epitaxial structure K2552

Compound	Doping	Thickness [nm]	Comments
GaAs	n		substrate and buffer
$(\text{Al}_{0.55}\text{Ga}_{0.45})_{0.51}\text{In}_{0.49}\text{P}$	n	440	etch stop layer
$\text{Al}_{0.80}\text{Ga}_{0.20}\text{As}$	n	3875	current spreading layer
$\text{Al}_x\text{Ga}_{1-x}\text{As}$	n	12.4	6 pair top DBR with linear grading
$\text{Al}_{0.53}\text{Ga}_{0.47}\text{As}$	n	35.3	
$\text{Al}_x\text{Ga}_{1-x}\text{As}$	n	12.4	
$\text{Al}_{0.95}\text{Ga}_{0.05}\text{As}$	n	40.2	
$\text{Al}_x\text{Ga}_{1-x}\text{As}$	n	12.4	
$\text{Al}_{0.53}\text{Ga}_{0.47}\text{As}$	n	35.3	
$\text{Al}_x\text{Ga}_{1-x}\text{As}$	n	12.4	
$\text{Al}_{0.95}\text{Ga}_{0.05}\text{As}$	n	40.2	
\vdots	\vdots	\vdots	
$\text{Al}_{0.95}\text{Ga}_{0.05}\text{As}$	n	40.2	
$\text{Al}_x\text{Ga}_{1-x}\text{As}$	n	12.4	
$\text{Al}_{0.53}\text{Ga}_{0.47}\text{As}$	n	35.3	
$\text{Al}_x\text{Ga}_{1-x}\text{As}$	n	12.4	
$\text{Al}_{0.95}\text{Ga}_{0.05}\text{As}$	n	40.2	
$\text{Al}_{0.51}\text{In}_{0.49}\text{P}$	n	49.3	confinement layer
$(\text{Al}_{0.47}\text{Ga}_{0.53})_{0.51}\text{In}_{0.49}\text{P}$		32.9	barrier layer
GaInP		4.9	QW emitting at 650 nm
$(\text{Al}_{0.47}\text{Ga}_{0.53})_{0.51}\text{In}_{0.49}\text{P}$		6.3	barrier layer
GaInP		4.9	QW emitting at 650 nm
$(\text{Al}_{0.47}\text{Ga}_{0.53})_{0.51}\text{In}_{0.49}\text{P}$		6.3	barrier layer
GaInP		4.9	QW emitting at 650 nm
$(\text{Al}_{0.47}\text{Ga}_{0.53})_{0.51}\text{In}_{0.49}\text{P}$		6.3	barrier layer
GaInP		4.9	QW emitting at 650 nm
$(\text{Al}_{0.47}\text{Ga}_{0.53})_{0.51}\text{In}_{0.49}\text{P}$		6.3	barrier layer
GaInP		4.9	QW emitting at 650 nm
$(\text{Al}_{0.47}\text{Ga}_{0.53})_{0.51}\text{In}_{0.49}\text{P}$		32.9	barrier layer
$\text{Al}_{0.51}\text{In}_{0.49}\text{P}$	p	49.3	confinement layer
$\text{Al}_{0.95}\text{Ga}_{0.05}\text{As}$	p	45	1 pair
$\text{Al}_x\text{Ga}_{1-x}\text{As}$	p	14	bottom DBR
$\text{Al}_{0.53}\text{Ga}_{0.47}\text{As}$	p	35.2	with linear grading
GaAs	p ⁺	2	p-contact layer
air			

Appendix C

Lithography Masks

C.1 Mask Substrate Emitting Devices

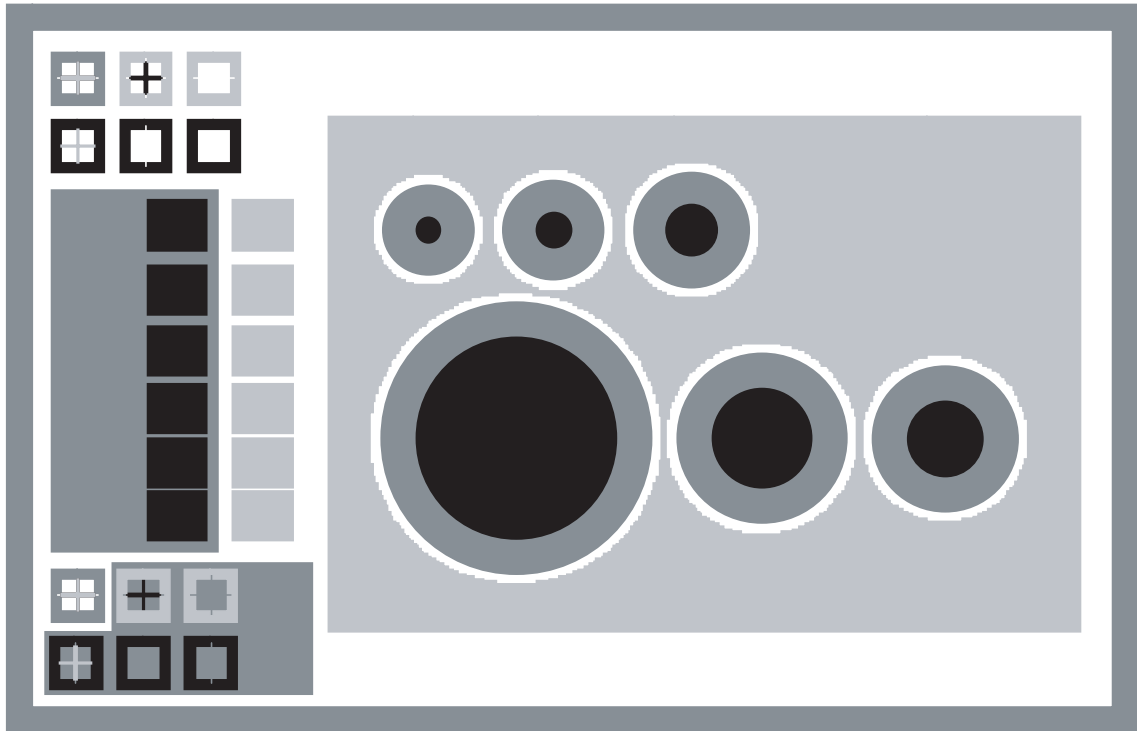


Figure C.1: Schematic of mask set used for substrate emitting MCLEDs; mesas (dark gray), n-contact (light gray) and p-contact (black). The device sizes are defined by the p-contact areas and vary from $400\ \mu\text{m}$ to $50\ \mu\text{m}$ in diameter.

C.2.1 Mask Semiconductor DBR Devices

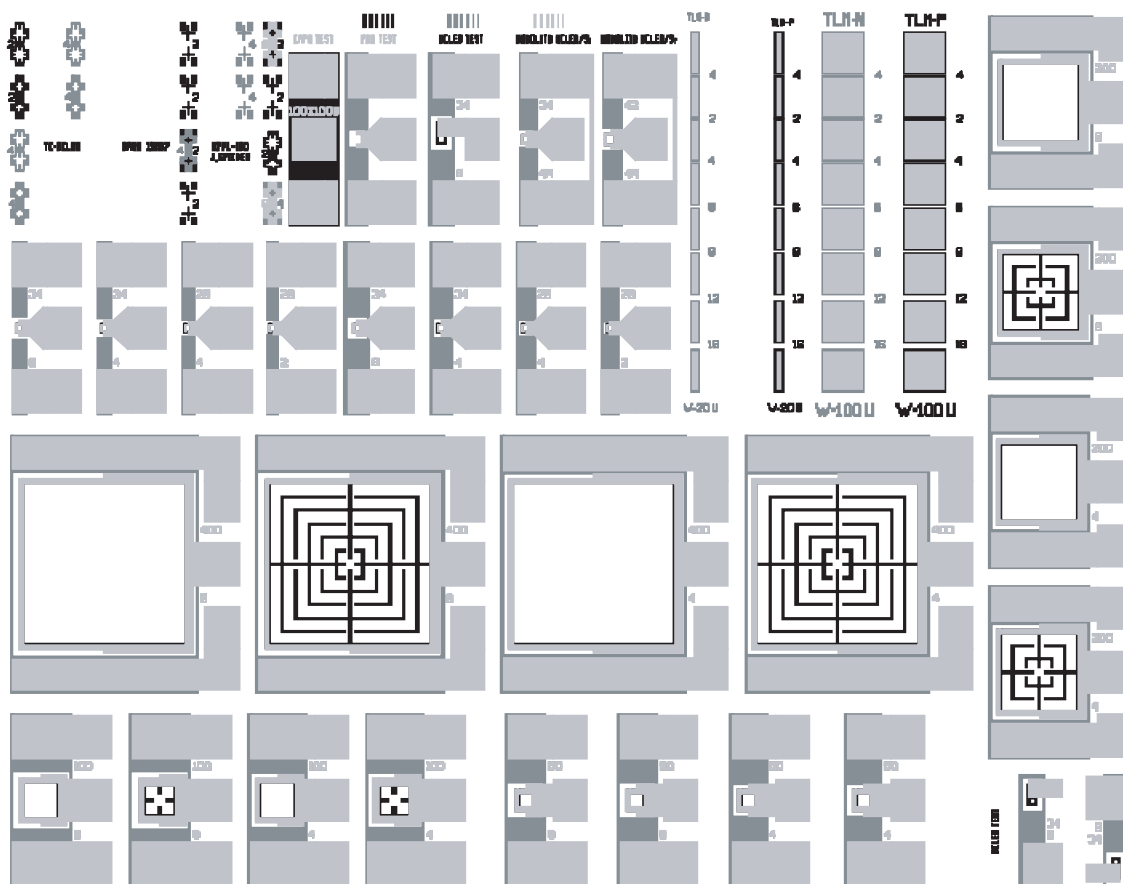


Figure C.2: Schematic of mask set used for top emitting MCLEDs with a semiconductor bottom DBR; n-contact (dark gray), p-contact (black) and contact pads (light gray). The device sizes are defined by the light aperture within the outer p-contact ring and range from $400 \times 400 \mu\text{m}^2$ to $28 \times 28 \mu\text{m}^2$.

C.2.2 Mask Oxide DBR Devices

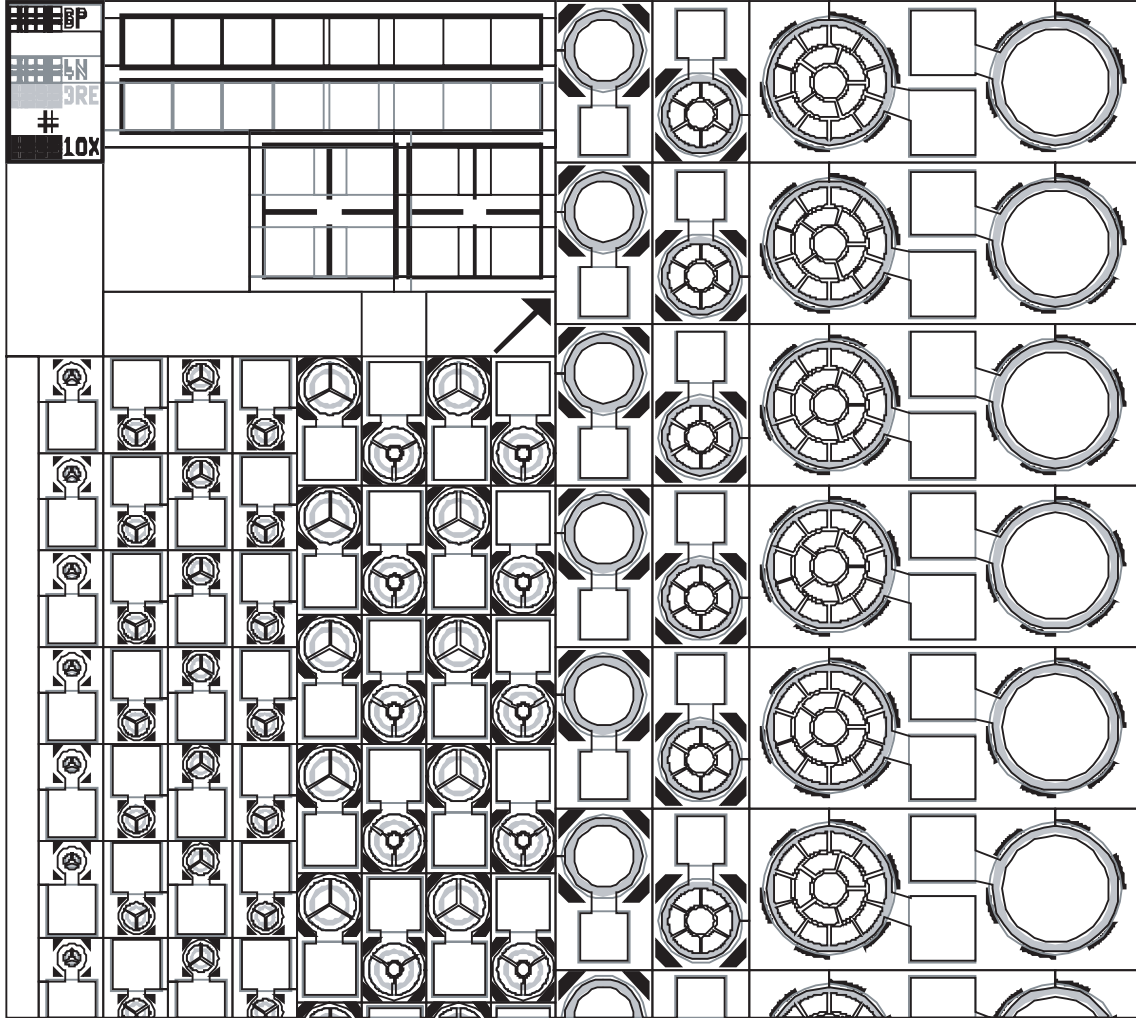


Figure C.3: Schematic of mask set used for top emitting MCLEDs with an oxide bottom DBR; oxidation trenches (black, filled), recess etch (light gray, filled), n-contact (dark gray, empty) and p-contact (black, empty). The device sizes are defined by the light aperture within the outer p-contact ring and vary from $350\ \mu\text{m}$ to $20\ \mu\text{m}$ in diameter.

Appendix D

Detector Calibration

D.1 Large Area Photodiodes

The large area silicon photodiodes used for the L–I–V measurements in this thesis had been calibrated beforehand by the Swiss Federal Office of Metrology and Accreditation (METAS) in Bern, Switzerland. The absolute spectral sensitivity of four different photodiodes was determined. The photocurrent generated by the photodiode was compared with the optical power displayed by the reference detectors EAM4, EAM5 and EAM6 for the same monochromatic collimated light beam. The electric current was measured with a pico-ampere meter METAS 2240.

Two different types of photodiodes were evaluated, Hamamatsu S1337-1010BR and Hamamatsu S1337-1010BQ. The photodiodes S1337-1010BQ have a quartz window instead of a resin coating and show therefore an increased sensitivity below 400 nm but a reduced sensitivity for larger wavelengths. The typical spectral response of the photodiodes given by Hamamatsu is shown in figure D.1. The four different photodiodes

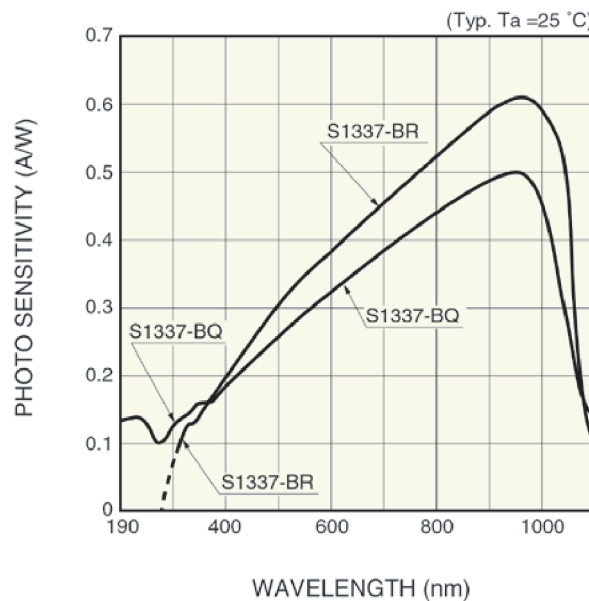


Figure D.1: Typical spectral response large area photodiodes by Hamamatsu

Table D.1: Calibrated large area photodiodes

Label	Type	Calibration range
“B”	S1337-1010BR	310 - 1000 nm, step width 10 nm
“C”	S1337-1010BR	400, 450, 500, 600, 650, 700, 900, 950 and 1000 nm
“D”	S1337-1010BQ	270 - 1000 nm, step width 10 nm
“E”	S1337-1010BQ	300, 400, 450, 500, 600, 650, 700, 900, 950 and 1000 nm

are labelled “B”, “C”, “D” and “E”, the first two being of type S1337-1010BR and the latter two of type S1337-1010BQ. Photodiode “B” was calibrated from 310nm to 1000nm with a step width of 10 nm; photodiode “D” from 270 nm to 1000 nm with the same step width. The two photodiodes “C” and “E” were calibrated only at certain specific wavelengths which are listed in table D.1. The photodiodes of type S1337-1010BR could not be calibrated between 270 nm and 310 nm as the dark current noise was too high.

Table D.2: Spectral sensitivities of the different Hamamatsu large area photodiodes (METAS calibration certificate No 116-0096)

Wavelength [nm]	“B”	“D”	“C”	“E”
	$\varepsilon(\lambda)$ [A/W]	$\varepsilon(\lambda)$ [A/W]	$\varepsilon(\lambda)$ [A/W]	$\varepsilon(\lambda)$ [A/W]
270		0.1226		
280		0.1183		
290		0.1241		
300		0.1343		0.1325
310	0.1036	0.1421		
320	0.1194	0.1467		
330	0.1298	0.1501		
340	0.1384	0.1526		
350	0.1444	0.1531		
360	0.1463	0.1494		
370	0.1527	0.1489		
380	0.1699	0.1601		
390	0.1884	0.1734		
400	0.2031	0.1840	0.2019	0.1827
410	0.2159	0.1933		
420	0.2275	0.2018		
430	0.2379	0.2096		
440	0.2476	0.2170		
450	0.2570	0.2240	0.2563	0.2228
460	0.2660	0.2308		
470	0.2745	0.2375		
480	0.2828	0.2438		
490	0.2910	0.2501		
500	0.2990	0.2563	0.2985	0.2552

Wavelength [nm]	$\varepsilon(\lambda)$ [A/W]	$\varepsilon(\lambda)$ [A/W]	$\varepsilon(\lambda)$ [A/W]	$\varepsilon(\lambda)$ [A/W]
510	0.3070	0.2625		
520	0.3148	0.2684		
530	0.3225	0.2745		
540	0.3300	0.2805		
550	0.3376	0.2863		
560	0.3450	0.2921		
570	0.3525	0.2981		
580	0.3600	0.3037		
590	0.3672	0.3094		
600	0.3743	0.3153	0.3741	0.3143
610	0.3818	0.3209		
620	0.3889	0.3266		
630	0.3962	0.3320		
640	0.4035	0.3378		
650	0.4103	0.3433	0.4102	0.3425
660	0.4175	0.3490		
670	0.4245	0.3545		
680	0.4317	0.3601		
690	0.4386	0.3656		
700	0.4458	0.3713	0.4455	0.3704
710	0.4526	0.3767		
720	0.4596	0.3823		
730	0.4666	0.3878		
740	0.4733	0.3932		
750	0.4800	0.3987		
760	0.4871	0.4042		
770	0.4940	0.4097		
780	0.5009	0.4152		
790	0.5078	0.4207		
800	0.5147	0.4261		
810	0.5215	0.4318		
820	0.5281	0.4370		
830	0.5352	0.4426		
840	0.5418	0.4479		
850	0.5487	0.4533		
860	0.5553	0.4588		
870	0.5615	0.4647		
880	0.5684	0.4700		
890	0.5752	0.4753		
900	0.5807	0.4809	0.5805	0.4803
910	0.5869	0.4863		
920	0.5945	0.4917		
930	0.6007	0.4969		
940	0.6077	0.5016		

Wavelength [nm]	$\varepsilon(\lambda)$ [A/W]	$\varepsilon(\lambda)$ [A/W]	$\varepsilon(\lambda)$ [A/W]	$\varepsilon(\lambda)$ [A/W]
950	0.6125	0.5048	0.6126	0.5047
960	0.6151	0.5070		
970	0.6145	0.5067		
980	0.6098	0.5031		
990	0.6000	0.4942		
1000	0.5826	0.4802	0.5825	0.4818

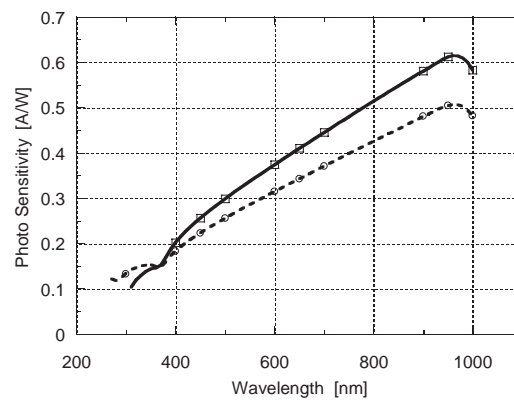


Figure D.2: Spectral response of the large area photodiodes by Hamamatsu; “B” (solid line), “D” (dashed line), “C” (squares) and “D” (circles)

D.2 Integrating Sphere

The integrating sphere used for the absolute L–I–V measurements in this thesis had been calibrated by the manufacturer, UDT Instruments, Baltimore, USA. The detector labelled “S2575 S/N 8U087” was calibrated as a whole, integrating sphere (UDT Instruments Radiometry Model 2575 Laser Power Attenuator) together with the photodiode (UDT Instruments Model 260 silicon sensor head), using the laboratory standards that are traceable to the National Institute of Standards and Technology (NIST). The ensemble was calibrated from 400 nm to 1100 nm with a step width of 10 nm.

Table D.3: Spectral response of the UDT integrating sphere S2575 S/N 8U087 (UDT calibration certificate No 90198)

Wavelength [nm]	Response [10^{-3} A/W]	Response [%]
400	0.694	39.4
410	0.757	43.0
420	0.818	46.5
430	0.866	49.2
440	0.908	51.6
450	0.953	54.1
460	0.993	56.4
470	1.031	58.6
480	1.069	60.7
490	1.103	62.7
500	1.138	64.7
510	1.172	66.6
520	1.204	68.4
530	1.231	69.9
540	1.259	71.5
550	1.283	72.9
560	1.305	74.1
570	1.325	75.3
580	1.344	76.4
590	1.361	77.3
600	1.376	78.2
610	1.393	79.1
620	1.408	80.0
630	1.423	80.9
640	1.435	81.5
650	1.448	82.3
660	1.459	82.9
670	1.471	83.6
680	1.485	84.4
690	1.499	85.2
700	1.513	86.0

Wavelength [nm]	Response [10^{-3} A/W]	Response [%]
710	1.530	86.9
720	1.550	88.1
730	1.570	89.2
740	1.590	90.3
750	1.608	91.4
760	1.625	92.3
770	1.642	93.3
780	1.656	94.1
790	1.668	94.8
800	1.679	95.4
810	1.688	95.9
820	1.696	96.4
830	1.703	96.8
840	1.713	97.3
850	1.720	97.7
860	1.727	98.1
870	1.735	98.6
880	1.742	99.0
890	1.748	99.3
900	1.754	99.7
910	1.759	99.9
920	1.760	100.0
930	1.744	99.1
940	1.749	99.4
950	1.744	99.1
960	1.740	98.9
970	1.731	98.4
980	1.723	97.9
990	1.704	96.8
1000	1.675	95.2
1010	1.626	92.4
1020	1.554	88.3
1030	1.459	82.9
1040	1.328	75.5
1050	1.179	67.0
1060	1.009	57.3
1070	0.8560	48.6
1080	0.7400	42.0
1090	0.6290	35.7
1100	0.5260	29.9

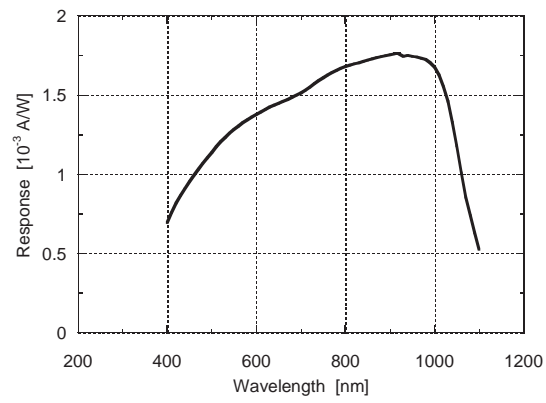


Figure D.3: Spectral response of the UDT integrating sphere S2575 S/N 8U087

Bibliography

- [1] http://www.aceee.org/ogeece/ch2_index.htm, “American Council for an Energy-Efficient Economy”, 2004.
- [2] <http://library.iea.org/dbtw-wpd/Textbase/stats/surveys/mes.pdf>, “International Energy Agency (IEA), Monthly Electricity Survey”, July 2004.
- [3] http://www.eere.energy.gov/buildings/info/documents/pdfs/oida_led-oled_rpt.pdf, “The Promise of Solid State Lighting for General Illumination”, Conclusions and Recommendations from OIDA Technology Roadmaps Co-sponsored by DOE (BTS) and OIDA.
- [4] H. J. Round, “A note on carborundum”, *Electrical World*, vol. 19, pp. 309, 1907.
- [5] O. V. Losev, “Behavior of contact detectors; the effect of temperature on the generating current (in Russian)”, *Telegrafia i telefonija bez provodov (TiTbp)*, vol. 18, pp. 45–62, 1923.
- [6] E. E. Loebner, “Subhistories of the Light Emitting Diode”, *IEEE Transactions on Electron Devices*, vol. 23, no. 7, pp. 675–699, 1976.
- [7] K. Lehovec, “New Photoelectric Devices Utilizing Carrier Injection”, *Proceedings of the Institute of Radio Engineers*, vol. 40, no. 11, pp. 1407–1409, 1952.
- [8] W. Shockley, “The theory of p-n junctions in semiconductors and p-n junction transistors”, *Bell System Technical Journal*, vol. 28, no. 3, pp. 435–489, 1949.
- [9] E. F. Schubert, *Light-Emitting Diodes*, Cambridge University Press, Cambridge, 2003.
- [10] G. B. Stringfellow and M. G. Craford, Eds., *High Brightness Light Emitting Diodes*, vol. 48 of *Semiconductors and Semimetals*, Academic Press, San Diego, 1997.
- [11] H. Kroemer, “A Proposed Class of Heterojunction Injection Lasers”, *Proceedings of the IEEE*, vol. 51, no. 12, pp. 1782–1783, 1963.
- [12] G. B. Stringfellow, *Organometallic vapor-phase epitaxy: theory and practice*, Academic Press, San Diego, 1999.
- [13] M. B. Panish, “Molecular Beam Epitaxy”, *Science*, vol. 208, no. 4446, pp. 916–922, 1980.
- [14] A. Y. Cho, “How molecular beam epitaxy (MBE) began and its projection into the future”, *Journal of Crystal Growth*, vol. 202, pp. 1–7, 1999.

- [15] F. A. Kish, F. M. Steranka, D. C. DeFever, D. A. Vanderwater, K. G. Park, C. P. Kuo, T. D. Osentowski, M. J. Peanasky, J. G. Yu, R. M. Fletcher, D. A. Steigerwald, M. G. Craford, and V. M. Robbins, "Very high-efficiency semiconductor wafer-bonded transparent-substrate $(\text{Al}_x\text{Ga}_{1-x})_{0.5}\text{In}_{0.5}\text{P}/\text{GaP}$ light-emitting diodes", *Applied Physics Letters*, vol. 64, no. 21, pp. 2839–2841, 1994.
- [16] M. R. Krames, M. Ochiai-Holcomb, G. E. Höfler, C. Carter-Coman, E. I. Chen, I.-H. Tan, P. Grillot, N. F. Gardner, H. C. Chui, J.-W. Huang, S. A. Stockman, F. A. Kish, M. G. Craford, T. S. Tan, C. P. Kocot, M. Hueschen, J. Posselt, B. Loh, G. Sasser, and D. Collins, "High-power truncated-inverted-pyramid $(\text{Al}_x\text{Ga}_{1-x})_{0.5}\text{In}_{0.5}\text{P}/\text{GaP}$ light-emitting diodes exhibiting $> 50\%$ external quantum efficiency", *Applied Physics Letters*, vol. 75, no. 16, pp. 2365–2367, 1999.
- [17] T. Whitaker, "Backlights, airports and vehicles boost LED market", *Compound Semiconductor*, vol. 9, no. 11, pp. 20–22, 2003.
- [18] B. Kennedy, "Any color, as long as it's white", *Compound Semiconductor*, vol. 9, no. 11, pp. 27–29, 2003.
- [19] S. Muthu, F. J. P. Schuurmans, and M. D. Pashley, "Red, green, and blue LEDs for white light illumination", *IEEE Journal of Selected Topics in Quantum Electronics*, vol. 8, no. 2, pp. 333–338, 2002.
- [20] C. W. Tang and S. A. van Slyke, "Organic Electroluminescent Diodes", *Applied Physics Letters*, vol. 51, no. 12, pp. 913–915, 1987.
- [21] J. H. Burroughes, D. D. C. Bradley, A. R. Brown, R. N. Marks, K. Mackay, R. H. Friend, P. L. Burns, and A. B. Holmes, "Light-Emitting-Diodes Based on Conjugated Polymers", *Nature*, vol. 347, no. 6293, pp. 539–541, 1990.
- [22] N. K. Patel, S. Cina, and J. H. Burroughes, "High-efficiency organic light-emitting diodes", *IEEE Journal of Selected Topics in Quantum Electronics*, vol. 8, no. 2, pp. 346–361, 2002.
- [23] I. E. Bergman, "Plastic optical fiber: A short-haul solution", *Optics and Photonics News*, vol. 9, no. 2, pp. 29–31, 1998.
- [24] R. Wirth, "Resonators provide LEDs with laser-like performance", *Compound Semiconductor*, vol. 8, no. 1, pp. 49–53, 2002.
- [25] T. Freeman, "Plastic optical fibre tackles automotive requirements", *FibreSystems Europe in association with LIGHTWAVE Europe*, vol. 1, no. 4, pp. 14–16, 2004.
- [26] T. Whitaker, "Lighting the future with LEDs (Strategies in Light Conference Report)", *Compound Semiconductor*, vol. 7, no. 3, pp. 51–57, 2001.
- [27] B. Steele, "HB-LEDs: the market drive towards solid-state lighting", *Compound Semiconductor*, vol. 9, no. 11, pp. 23–24, 2003.
- [28] T. Whitaker, "Innovations push white LEDs towards new applications", *Compound Semiconductor*, vol. 9, no. 5, pp. 29–32, 2003.
- [29] <http://www.lightuptheworld.org>, "Light Up The World Foundation", 2004.

- [30] D. McGraw, "LEDs light up medical diagnostics", *Compound Semiconductor*, vol. 7, no. 3, pp. 76–81, 2001.
- [31] K. W. Woodburn, S. W. Young, F. Qing, D. R. Miles, and P. Thiemann, "Light-emitting diode versus laser irradiation phototherapy with lutetium texaphyrin (PCI-0123)", in *Photonics West 97 - Optical Methods for Tumor Treatment and Detection: Mechanisms and Techniques in Photodynamic Therapy VI*, T. J. Dougherty, Ed., San Jose, 1997, vol. 2972, pp. 46–53, SPIE.
- [32] R. W. Ignatius, T. S. Martin, R. J. Bula, R. C. Morrow, and T. W. Tibbitts, "Method and Apparatus for Irradiation of Plants using Optoelectronic Devices", United States Patent 5,012,609.
- [33] <http://www1.msfc.nasa.gov/NEWSROOM/background/facts/advasc5.html>, "Soybean Chemical Composition Study using ADVANCED ASTROCULTURE² (ADVASC) - Expedition Five", 2004.
- [34] <http://www.scipoc.com/videochron.html>, "Time-lapse image of soybean plants aboard Space Station", 2004.
- [35] <http://www.nasdaq.com/about/marketsitetowervideo.aspx>, "MarketSite Live Webcam", 2004.
- [36] T. Whitaker, "Lighting community outlines challenges for LED industry", *Compound Semiconductor*, vol. 10, no. 2, pp. 20–22, 2004.
- [37] B. E. A. Saleh and M. C. Teich, *Fundamentals of Photonics*, John Wiley & Sons, New York, 1991.
- [38] R. Windisch, P. Altieri, R. Butendeich, S. Illek, P. Stauss, W. Stein, W. Wegleiter, R. Wirth, H. Zull, and K. Streubel, "InGaAlP thin film LEDs with high luminous efficiency", in *Proc. SPIE Light-Emitting Diodes: Research, Manufacturing, and Applications VIII*, S. A. Stockman, W. T. Yao, and E. F. Schubert, Eds. 2004, vol. 5366, pp. 43–52, The International Society for Optical Engineering.
- [39] N. E. J. Hunt, E. F. Schubert, D. L. Sivco, A. Y. Cho, and G. J. Zydzik, "Power and Efficiency Limits in Single-Mirror Light Emitting Diodes with Enhanced Intensity", *Electronics Letters*, vol. 28, no. 23, pp. 2169–2171, 1992.
- [40] J. Singh, *Optoelectronics - An introduction to materials and devices*, McGraw-Hill International Editions, New York, 1996.
- [41] M. Born and E. Wolf, *Principles of optics: electromagnetic theory of propagation, interference and diffraction of light*, Cambridge University Press, Cambridge, 7th expanded ed. edition, 1999.
- [42] P. Royo, *Light extraction from microcavity based light emitting diodes: optimization and characterization of high-brightness AlGaInP-based devices*, Ph.D. thesis, Swiss Federal Institute of Technology, Lausanne (EPFL), 2000.
- [43] L. A. Coldren and S. W. Corzine, *Diode lasers and photonic integrated circuits*, John Wiley & Sons, New York, 1995.

- [44] K. Czotscher, S. Weisser, E. C. Larkins, J. Fleissner, J. D. Ralston, A. Schönfelder, J. Rosenzweig, and I. Esquivias, “Structural and carrier density dependence of carrier lifetime in InGaAs/GaAs multiple-quantum-well lasers”, *Applied Physics Letters*, vol. 69, no. 21, pp. 3158–3160, 1996.
- [45] A. P. Ongstad, M. L. Tilton, E. J. Bochove, and G. C. Dente, “Carrier spillover at 300, 195, and 77 K in InGaAs and GaAs single quantum wells”, *Journal of Applied Physics*, vol. 80, no. 5, pp. 2866–2872, 1996.
- [46] C. H. Henry, R. A. Logan, and F. R. Merritt, “Origin of $n \approx 2$ Injection Current in $\text{Al}_x\text{Ga}_{1-x}\text{As}$ Heterojunctions”, *Applied Physics Letters*, vol. 31, no. 7, pp. 454–456, 1977.
- [47] C. H. Henry, R. A. Logan, and F. R. Merritt, “The Effect of Surface Recombination on Current in $\text{Al}_x\text{Ga}_{1-x}\text{As}$ Heterojunctions”, *Journal of Applied Physics*, vol. 49, no. 6, pp. 3530–3542, 1978.
- [48] S. Y. Hu, S. W. Corzine, K. K. Law, D. B. Young, A. C. Gossard, L. A. Coldren, and J. L. Merz, “Lateral Carrier Diffusion and Surface Recombination in InGaAs/AlGaAs Quantum-Well Ridge-Waveguide Lasers”, *Journal of Applied Physics*, vol. 76, no. 8, pp. 4479–4487, 1994.
- [49] J. W. Scott, R. S. Geels, S. W. Corzine, and L. A. Coldren, “Modeling Temperature Effects and Spatial Hole Burning to Optimize Vertical-Cavity Surface-Emitting Laser Performance”, *IEEE Journal of Quantum Electronics*, vol. 29, no. 5, pp. 1295–1308, 1993.
- [50] R. S. Geels, B. J. Thibeault, S. W. Corzine, J. W. Scott, and L. A. Coldren, “Design and Characterization of $\text{In}_{0.2}\text{Ga}_{0.8}\text{As}$ MQW Vertical-Cavity Surface-Emitting Lasers”, *IEEE Journal of Quantum Electronics*, vol. 29, no. 12, pp. 2977–2987, 1993.
- [51] C. J. Nuese, J. J. Tietjen, J. J. Gannon, and H. F. Gossenberger, “Optimization of Electroluminescent Efficiencies for Vapor-Grown $\text{GaAs}_{1-x}\text{P}_x$ Diodes”, *Journal of the Electrochemical Society*, vol. 116, no. 2, pp. 248–253, 1969.
- [52] W. N. Carr, “Photometric Figures of Merit for Semiconductor Luminescent Sources Operating in Spontaneous Mode”, *Infrared Physics*, vol. 6, no. 1, pp. 1–19, 1966.
- [53] D. A. Vanderwater, I.-H. Tan, G. E. Höfler, D. C. DeFever, and F. A. Kish, “High-Brightness AlGaInP Light Emitting Diodes”, *Proceedings of the IEEE*, vol. 85, no. 11, pp. 1752–1764, 1997.
- [54] W. N. Carr and G. E. Pittman, “One-Watt GaAs p-n Junction Infrared Source”, *Applied Physics Letters*, vol. 3, no. 10, pp. 173–175, 1963.
- [55] A. R. Franklin and R. Newman, “Shaped Electroluminescent GaAs Diodes”, *Journal of Applied Physics*, vol. 35, no. 4, pp. 1153–1155, 1964.
- [56] N. F. Gardner, H. C. Chui, E. I. Chen, M. R. Krames, J. W. Huang, F. A. Kish, S. A. Stockman, C. P. Kocot, T. S. Tan, and N. Moll, “1.4x efficiency improvement in transparent-substrate $(\text{Al}_x\text{Ga}_{1-x})_{0.5}\text{In}_{0.5}\text{P}$ light-emitting diodes with thin (≤ 2000 Å) active regions”, *Applied Physics Letters*, vol. 74, no. 15, pp. 2230–2232, 1999.

- [57] C. P. Kuo, R. M. Fletcher, T. D. Osentowski, M. C. Lardizabal, M. G. Craford, and V. M. Robbins, "High Performance AlGaInP Visible Light-Emitting Diodes", *Applied Physics Letters*, vol. 57, no. 27, pp. 2937–2939, 1990.
- [58] K. H. Huang, J. G. Yu, C. P. Kuo, R. M. Fletcher, T. D. Osentowski, L. J. Stinson, M. G. Craford, and A. S. H. Liao, "Twofold Efficiency Improvement in High-Performance AlGaInP Light-Emitting Diodes in the 555-620 nm Spectral Region Using a Thick GaP Window Layer", *Applied Physics Letters*, vol. 61, no. 9, pp. 1045–1047, 1992.
- [59] F. A. Kish, D. A. Vanderwater, D. C. DeFever, D. A. Steigerwald, G. E. Hofler, K. G. Park, and F. M. Steranka, "Highly reliable and efficient semiconductor wafer-bonded AlGaInP/GaP light-emitting diodes", *Electronics Letters*, vol. 32, no. 2, pp. 132–134, 1996.
- [60] I. Schnitzer, E. Yablonovitch, C. Caneau, and T. J. Gmitter, "Ultrahigh Spontaneous Emission Quantum Efficiency, 99.7% Internally and 72% Externally, from AlGaAs/GaAs/AlGaAs Double Heterostructures", *Applied Physics Letters*, vol. 62, no. 2, pp. 131–133, 1993.
- [61] W. Schmid, M. Scherer, C. Karnutsch, A. Plossl, W. Wegleiter, S. S. Schad, B. Neubert, and K. Streubel, "High-efficiency red and infrared light-emitting diodes using radial outcoupling taper", *IEEE Journal of Selected Topics in Quantum Electronics*, vol. 8, no. 2, pp. 256–263, 2002.
- [62] R. Wirth, S. Illek, C. Karnutsch, I. Pietzonka, A. Plössl, P. Stauss, W. Stein, W. Wegleiter, R. Windisch, H. Zull, and K. Streubel, "Recent progress of AlGaInP thin-film light-emitting diodes", in *Proc. SPIE Light-Emitting Diodes: Research, Manufacturing, and Applications VII*, E. F. Schubert, W. T. Yao, K. J. Linden, and D. J. McGraw, Eds. 2003, vol. 4996, pp. 1–9, The International Society for Optical Engineering.
- [63] C. Rومان, S. De Jonge, C. Karnutsch, K. Streubel, M. Kuijk, B. Dutta, G. Borghs, and P. Heremans, "Wafer-bonded thin-film surface-roughened light-emitting diodes", in *Proc. SPIE Light-Emitting Diodes: Research, Manufacturing, and Applications VII*, E. F. Schubert, W. T. Yao, K. J. Linden, and D. J. McGraw, Eds. 2003, vol. 4996, pp. 40–45, The International Society for Optical Engineering.
- [64] E. F. Schubert, Y.-H. Wang, A. Y. Cho, L.-W. Tu, and G. J. Zydzik, "Resonant cavity light-emitting diode", *Applied Physics Letters*, vol. 60, no. 8, pp. 921–923, 1992.
- [65] K. Streubel, N. Linder, R. Wirth, and A. Jaeger, "High brightness AlGaInP light-emitting diodes", *IEEE Journal of Selected Topics in Quantum Electronics*, vol. 8, no. 2, pp. 321–332, 2002.
- [66] T. Gessmann and E. F. Schubert, "High-efficiency AlGaInP light-emitting diodes for solid-state lighting applications", *Journal of Applied Physics*, vol. 95, no. 5, pp. 2203–2216, 2004.
- [67] E. Yablonovitch, T. Gmitter, J. P. Harbison, and R. Bhat, "Extreme Selectivity in the Lift-Off of Epitaxial GaAs Films", *Applied Physics Letters*, vol. 51, no. 26, pp. 2222–2224, 1987.
- [68] H. W. Deckman, C. R. Wronski, H. Witzke, and E. Yablonovitch, "Optically Enhanced Amorphous Silicon Solar Cells", *Applied Physics Letters*, vol. 42, no. 11, pp. 968–970, 1983.

- [69] I. Schnitzer, E. Yablonovitch, C. Caneau, T. J. Gmitter, and A. Scherer, “30% external quantum efficiency from surface textured, thin film light-emitting diodes”, *Applied Physics Letters*, vol. 63, no. 16, pp. 2174–2176, 1993.
- [70] H. W. Deckman and J. H. Dunsmuir, “Natural Lithography”, *Applied Physics Letters*, vol. 41, no. 4, pp. 377–379, 1982.
- [71] R. Windisch, C. Rومان, S. Meinschmidt, P. Kiesel, D. Zipperer, G. H. Dohler, B. Dutta, M. Kuijk, G. Borghs, and P. Heremans, “Impact of texture-enhanced transmission on high-efficiency surface-textured light-emitting diodes”, *Applied Physics Letters*, vol. 79, no. 15, pp. 2315–2317, 2001.
- [72] R. Windisch, C. Rومان, S. De Jonge, C. Karnutsch, K. Streubel, M. Kuijk, B. Dutta, G. Borghs, and P. Heremans, “Thin-film surface-textured LEDs with current injection through a rear reflector”, in *Proc. SPIE Light-Emitting Diodes: Research, Manufacturing, and Applications VI*, E. F. Schubert and W. T. Yao, Eds. 2002, vol. 4641, pp. 13–18, The International Society for Optical Engineering.
- [73] C. Rومان, R. Windisch, M. D’Hondt, B. Dutta, P. Modak, P. Mijlemans, G. Borghs, R. Vounckx, I. Moerman, M. Kuijk, and P. Heremans, “High-efficiency thin-film light-emitting diodes at 650 nm”, *Electronics Letters*, vol. 37, no. 13, pp. 852–853, 2001.
- [74] N. Linder, S. Kugler, P. Stauss, K. P. Streubel, R. Wirth, and H. Zull, “High-brightness AlGaInP light-emitting diodes using surface texturing”, in *Proc. SPIE Light Emitting Diodes: Research, Manufacturing, and Applications V*. 2001, vol. 4278, pp. 19–25, The International Society for Optical Engineering.
- [75] N. Linder, S. Kugler, P. Stauss, R. Wirth, H. Zull, and K. P. Streubel, “Surface texturing boosts light emission in new-generation AlInGaP LED chips”, *Compound Semiconductor*, vol. 7, no. 4, pp. 59–60, 2001.
- [76] S. Illek, “Buried micro-reflectors boost performance of AlGaInP LEDs”, *Compound Semiconductor*, vol. 8, no. 1, pp. 39–42, 2002.
- [77] W. Schmid, M. Scherer, R. Jäger, P. Strauss, K. Streubel, and K. J. Ebeling, “Efficient light-emitting diodes with radial outcoupling taper at 980 and 630 nm emission wavelength”, in *Proc. SPIE Light-Emitting Diodes: Research, Manufacturing, and Applications V*, W. T. Yao and E. F. Schubert, Eds. 2001, vol. 4278, pp. 109–118, The International Society for Optical Engineering.
- [78] E. F. Schubert, N. E. J. Hunt, M. Micovic, R. J. Malik, D. L. Sivco, A. Y. Cho, and G. J. Zydzik, “Highly Efficient Light-Emitting Diodes with Microcavities”, *Science*, vol. 265, no. 5174, pp. 943–945, 1994.
- [79] H. Yokoyama, “Physics and Device Applications of Optical Microcavities”, *Science*, vol. 256, no. 5053, pp. 66–70, 1992.
- [80] R. E. Slusher, “Optical Processes in Microcavities”, *Semiconductor Science and Technology*, vol. 9, no. 11, pp. 2025–2030, 1994.
- [81] K. J. Vahala, “Optical microcavities”, *Nature*, vol. 424, no. 6950, pp. 839–846, 2003.
- [82] E. M. Purcell, “Spontaneous Emission Probabilities at Radio Frequencies”, *Physical Review*, vol. 69, no. 11-1, pp. 681, 1946.

- [83] R. E. Kunz and W. Lukosz, "Changes in Fluorescence Lifetimes Induced by Variable Optical Environments", *Physical Review B*, vol. 21, no. 10, pp. 4814–4828, 1980.
- [84] W. Lukosz, "Theory of Optical-Environment-Dependent Spontaneous-Emission Rates for Emitters in Thin Layers", *Physical Review B*, vol. 22, no. 6, pp. 3030–3038, 1980.
- [85] F. De Martini, G. Innocenti, G. R. Jacobovitz, and P. Mataloni, "Anomalous Spontaneous Emission Time in a Microscopic Optical Cavity", *Physical Review Letters*, vol. 59, no. 26, pp. 2955–2958, 1987.
- [86] M. Suzuki, H. Yokoyama, S. D. Brorson, and E. P. Ippen, "Observation of Spontaneous Emission Lifetime Change of Dye-Containing Langmuir-Blodgett Films in Optical Microcavities", *Applied Physics Letters*, vol. 58, no. 10, pp. 998–1000, 1991.
- [87] E. Yablonovitch, T. J. Gmitter, and R. Bhat, "Inhibited and Enhanced Spontaneous Emission from Optically Thin AlGaAs/GaAs Double Heterostructures", *Physical Review Letters*, vol. 61, no. 22, pp. 2546–2549, 1988.
- [88] H. Yokoyama, K. Nishi, T. Anan, H. Yamada, S. D. Brorson, and E. P. Ippen, "Enhanced Spontaneous Emission from GaAs Quantum Wells in Monolithic Microcavities", *Applied Physics Letters*, vol. 57, no. 26, pp. 2814–2816, 1990.
- [89] E. F. Schubert, A. M. Vredenberg, N. E. J. Hunt, Y. H. Wong, P. C. Becker, J. M. Poate, D. C. Jacobson, L. C. Feldman, and G. J. Zydzik, "Giant Enhancement of Luminescence Intensity in Er-Doped Si/SiO₂ Resonant Cavities", *Applied Physics Letters*, vol. 61, no. 12, pp. 1381–1383, 1992.
- [90] T. Nakayama, Y. Itoh, and A. Kakuta, "Organic Photoluminescent and Electroluminescent Devices with Double Mirrors", *Applied Physics Letters*, vol. 63, no. 5, pp. 594–595, 1993.
- [91] A. Dodabalapur, L. J. Rothberg, and T. M. Miller, "Color Variation with Electroluminescent Organic Semiconductors in Multimode Resonant Cavities", *Applied Physics Letters*, vol. 65, no. 18, pp. 2308–2310, 1994.
- [92] C. Fabry and A. Perot, "Théorie et applications d'une nouvelle méthode de spectroscopie interférentielle", *Annales de Chimie et de Physique*, vol. 16, pp. 115–144, 1899.
- [93] R. P. Stanley, R. Houdré, C. Weisbuch, U. Oesterle, and M. Illegems, "Cavity-polariton photoluminescence in semiconductor microcavities: Experimental evidence", *Physical Review B*, vol. 53, no. 16, pp. 10995–11007, 1996.
- [94] C. Weisbuch, M. Nishioka, A. Ishikawa, and Y. Arakawa, "Observation of the Coupled Exciton-Photon Mode Splitting in a Semiconductor Quantum Microcavity", *Physical Review Letters*, vol. 69, no. 23, pp. 3314–3317, 1992.
- [95] H. Benisty, H. De Neve, and C. Weisbuch, "Impact of planar microcavity effects on light extraction - Part I: Basic concepts and analytical trends", *IEEE Journal of Quantum Electronics*, vol. 34, no. 9, pp. 1612–1631, 1998.
- [96] H. Benisty, H. De Neve, and C. Weisbuch, "Impact of Planar Microcavity Effects on Light Extraction - Part II: Selected Exact Simulations and Role of Photon Recycling", *IEEE Journal of Quantum Electronics*, vol. 34, no. 9, pp. 1632–1643, 1998.

- [97] H. Benisty, R. Stanley, and M. Mayer, "Method of source terms for dipole emission modification in modes of arbitrary planar structures", *Journal of the Optical Society of America A-Optics Image Science and Vision*, vol. 15, no. 5, pp. 1192–1201, 1998.
- [98] K. A. Neyts, "Simulation of light emission from thin-film microcavities", *Journal of the Optical Society of America A-Optics Image Science and Vision*, vol. 15, no. 4, pp. 962–971, 1998.
- [99] J. A. E. Wasey and W. L. Barnes, "Efficiency of spontaneous emission from planar microcavities", *Journal of Modern Optics*, vol. 47, no. 4, pp. 725–741, 2000.
- [100] D. Delbeke, R. Bockstaele, P. Bienstman, R. Baets, and H. Benisty, "High-efficiency semiconductor resonant-cavity light-emitting diodes: A review", *IEEE Journal of Selected Topics in Quantum Electronics*, vol. 8, no. 2, pp. 189–206, 2002.
- [101] R. G. Baets, D. Delbeke, R. Bockstaele, and P. Bienstman, "Resonant-cavity light-emitting diodes: a review", in *Proc. SPIE Light-Emitting Diodes: Research, Manufacturing, and Applications VII*, E. F. Schubert, W. T. Yao, K. J. Linden, and D. J. McGraw, Eds. 2003, vol. 4996, pp. 74–86, The International Society for Optical Engineering.
- [102] D. Ochoa, *Diodes électroluminescentes planaires à haut rendement d'extraction lumineuse*, Ph.D. thesis, Swiss Federal Institute of Technology, Lausanne (EPFL), 2001.
- [103] A. Kastler, "Atomes à l'intérieur d'un Interféromètre Perot-Fabry", *Applied Optics*, vol. 1, no. 1, pp. 17–24, 1962.
- [104] W. Lukosz, "Light Emission by Multipole Sources in Thin-Layers. I. Radiation Patterns of Electric and Magnetic Dipoles", *Journal of the Optical Society of America*, vol. 71, no. 6, pp. 744–754, 1981.
- [105] D. Delbeke, P. Bienstman, R. Bockstaele, and R. Baets, "Rigorous electromagnetic analysis of dipole emission in periodically corrugated layers: the grating-assisted resonant-cavity light-emitting diode", *Journal of the Optical Society of America A-Optics Image Science and Vision*, vol. 19, no. 5, pp. 871–880, 2002.
- [106] I. Abram, I. Robert, and R. Kuszelewicz, "Spontaneous emission control in semiconductor microcavities with metallic or Bragg mirrors", *IEEE Journal of Quantum Electronics*, vol. 34, no. 1, pp. 71–76, 1998.
- [107] J. M. Gérard and B. Gayral, "Strong Purcell effect for InAs quantum boxes in three-dimensional solid-state microcavities", *Journal of Lightwave Technology*, vol. 17, no. 11, pp. 2089–2095, 1999.
- [108] J. P. van der Ziel and M. Ilegems, "Multilayer GaAs-Al_{0.3}Ga_{0.7}As Dielectric Quarter Wave Stacks Grown by Molecular Beam Epitaxy", *Applied Optics*, vol. 14, no. 11, pp. 2627–2630, 1975.
- [109] D. I. Babic and S. W. Corzine, "Analytic Expressions for the Reflection Delay, Penetration Depth, and Absorptance of Quarter-Wave Dielectric Mirrors", *IEEE Journal of Quantum Electronics*, vol. 28, no. 2, pp. 514–524, 1992.
- [110] A. Yariv, *Quantum electronics*, John Wiley & Sons, New York, 1989.

- [111] H. A. Macleod, *Thin-film optical filters*, Adam Hilger Ltd, Bristol, 2nd edition edition, 1986.
- [112] P. Yeh, *Optical Waves in Layered Media*, John Wiley & Sons, New York, 1988.
- [113] G. Björk, Y. Yamamoto, and H. Heitmann, “Spontaneous Emission Control in Semiconductor Microcavities”, in *Confined Electrons and Photons*, E. Burstein and C. Weisbuch, Eds., vol. NATO ASI series. Series B, Physics vol. 340, pp. 467–502. Plenum Press, New York, 1995.
- [114] Z. Huang, C. C. Lin, and D. G. Deppe, “Spontaneous Lifetime and Quantum Efficiency in Light-Emitting Diodes Affected by a Close Metal Mirror”, *IEEE Journal of Quantum Electronics*, vol. 29, no. 12, pp. 2940–2949, 1993.
- [115] D. Ochoa, R. Houdré, R. P. Stanley, C. Dill, U. Oesterle, and M. Ilegems, “Device simultaneous determination of the source and cavity parameters of a microcavity light-emitting diode”, *Journal of Applied Physics*, vol. 85, no. 5, pp. 2994–2996, 1999.
- [116] T. Baba, R. Watanabe, K. Asano, F. Koyama, and K. Iga, “Theoretical and experimental estimations of photon recycling effect in light emitting devices with a metal mirror”, *Japanese Journal of Applied Physics Part 1-Regular Papers Short Notes & Review Papers*, vol. 35, no. 1A, pp. 97–100, 1996.
- [117] H. De Neve, J. Blondelle, P. Van Daele, P. Demeester, R. Baets, and G. Borghs, “Recycling of guided mode light emission in planar microcavity light emitting diodes”, *Applied Physics Letters*, vol. 70, no. 7, pp. 799–801, 1997.
- [118] J. Blondelle, H. De Neve, G. Borghs, P. Van Daele, P. Demeester, and R. Baets, “High Efficiency (> 20%) Microcavity LEDs”, in *Semiconductor Optical Microcavity Devices and Photonic Bandgaps*, *IEE Colloquium on*, 1996.
- [119] R. Wirth, C. Karnutsch, S. Kugler, and K. Streubel, “High-efficiency resonant-cavity LEDs emitting at 650 nm”, *IEEE Photonics Technology Letters*, vol. 13, no. 5, pp. 421–423, 2001.
- [120] R. Bockstaele, J. Derluyn, C. Sys, S. Verstuyft, I. Moerman, P. Van Daele, and R. Baets, “Realisation of highly efficient 850 nm top emitting resonant cavity light emitting diodes”, *Electronics Letters*, vol. 35, no. 18, pp. 1564–1565, 1999.
- [121] P. Sipilä, M. Saarinen, V. Vilokkinen, S. Orsila, P. Melanen, P. Savolainen, M. Toivonen, M. Dumitrescu, and M. Pessa, “Resonant cavity LEDs at 655 nm and 880 nm wavelengths”, in *Proc. SPIE Light Emitting Diodes: Research, Manufacturing, and Applications IV*, W. T. Yao, I. T. Ferguson, and E. F. Schubert, Eds. 2000, vol. 3938, pp. 82–89, The International Society for Optical Engineering.
- [122] J. F. Carlin, P. Royo, M. Ilegems, B. Gerard, X. Marcadet, and J. Nagle, “High-efficiency top-emitting microcavity LEDs on GaAs and GaAs/Si substrate”, *Journal of Crystal Growth*, vol. 201/202, pp. 994–998, 1999.
- [123] J. F. Carlin, P. Royo, R. P. Stanley, R. Houdré, J. Spicher, U. Oesterle, and M. Ilegems, “Design and characterization of top-emitting microcavity light-emitting diodes”, *Semiconductor Science and Technology*, vol. 15, no. 2, pp. 145–154, 2000.

- [124] J. J. Wierer, D. A. Kellogg, and N. Holonyak Jr., "Tunnel contact junction native-oxide aperture and mirror vertical-cavity surface-emitting lasers and resonant-cavity light-emitting diodes", *Applied Physics Letters*, vol. 74, no. 7, pp. 926–928, 1999.
- [125] B. Depreter, I. Moerman, R. Baets, P. Van Daele, and P. Demeester, "InP-based 1300 nm microcavity LEDs with 9% quantum efficiency", *Electronics Letters*, vol. 36, no. 15, pp. 1303–1304, 2000.
- [126] B. Depreter, S. Verstuyft, I. Moerman, R. Baets, and P. Van Daele, "InP-based microcavity light emitting diodes emitting at 1.3 μm and 1.55 μm ", in *Proc. of the 11th International Conference on InP and related materials (IPRM)*, Davos, Switzerland, 1999, pp. 227–230.
- [127] E. Hadji, J. Bleuse, N. Magnea, and J. L. Pautrat, "3.2 μm Infrared Resonant Cavity Light Emitting Diode", *Applied Physics Letters*, vol. 67, no. 18, pp. 2591–2593, 1995.
- [128] E. Hadji, J. Bleuse, N. Magnea, and J. L. Pautrat, "Resonant cavity light emitting diodes for the 3-5 μm range", *Solid-State Electronics*, vol. 40, no. 1-8, pp. 473–476, 1996.
- [129] E. Hadji, E. Picard, C. Roux, E. Molva, and P. Ferret, "3.3- μm microcavity light emitter for gas detection", *Optics Letters*, vol. 25, no. 10, pp. 725–727, 2000.
- [130] J. P. Zanatta, F. Noel, P. Ballet, N. Hdadach, A. Million, G. Destefanis, E. Mottin, C. Kopp, E. Picard, and E. Hadji, "HgCdTe molecular beam epitaxy material for microcavity light emitters: Application to gas detection in the 2-6 μm range", *Journal of Electronic Materials*, vol. 32, no. 7, pp. 602–607, 2003.
- [131] S. T. Wilkinson, N. M. Jokerst, and R. P. Leavitt, "Resonant-cavity-enhanced thin-film AlGaAs/GaAs/AlGaAs LED's with metal mirrors", *Applied Optics*, vol. 34, no. 36, pp. 8298–8302, 1995.
- [132] B. Corbett, L. Considine, S. Walsh, and W. M. Kelly, "Resonant Cavity Light Emitting Diode and Detector Using Epitaxial Liftoff", *IEEE Photonics Technology Letters*, vol. 5, no. 9, pp. 1041–1043, 1993.
- [133] M. C. Larson and J. S. Harris, "Broadly-Tunable Resonant-Cavity Light-Emitting Diode", *IEEE Photonics Technology Letters*, vol. 7, no. 11, pp. 1267–1269, 1995.
- [134] R. P. Stanley, P. Royo, U. Oesterle, R. Joray, and M. Ilegems, "Novel Microcavity Light Emitting Diodes", in *Institute of Physics Conference Series - 29th International Symposium on Compound Semiconductors*, M. Ilegems, G. Weimann, and J. Wagner, Eds., Lausanne, Switzerland, 2002, vol. 174, pp. 359–362, Institute of Physics.
- [135] R. P. Stanley, R. Joray, J. F. Carlin, and M. Ilegems, "Phase-Shift Microcavities for Light-Emitting Diodes", *unpublished*, 2001.
- [136] J. M. Dallesasse, P. Gavrilovic, N. Holonyak, R. W. Kaliski, D. W. Nam, E. J. Vesely, and R. D. Burnham, "Stability of AlAs in $\text{Al}_x\text{Ga}_{1-x}\text{As}$ -AlAs-GaAs Quantum Well Heterostructures", *Applied Physics Letters*, vol. 56, no. 24, pp. 2436–2438, 1990.
- [137] J. M. Dallesasse, N. Holonyak Jr., A. R. Sugg, T. A. Richard, and N. El-Zein, "Hydrolyzation oxidation of $\text{Al}_x\text{Ga}_{1-x}\text{As}$ -AlAs-GaAs quantum well heterostructures and superlattices", *Applied Physics Letters*, vol. 57, no. 26, pp. 2844–2846, 1990.

- [138] A. R. Sugg, E. I. Chen, N. Holonyak Jr., K. C. Hsieh, J. E. Baker, and N. Finnegan, "Effects of low-temperature annealing on the native oxide of $\text{Al}_x\text{Ga}_{1-x}\text{As}$ ", *Journal of Applied Physics*, vol. 74, no. 6, pp. 3880–3885, 1993.
- [139] M. H. MacDougal, H. Zhao, P. D. Dapkus, M. Ziari, and W. H. Steier, "Wide-Bandwidth Distributed Bragg Reflectors Using Oxide GaAs Multilayers", *Electronics Letters*, vol. 30, no. 14, pp. 1147–1149, 1994.
- [140] K. J. Knopp, R. P. Mirin, D. H. Christensen, K. A. Bertness, A. Roshko, and R. A. Synowicki, "Optical constants of $(\text{Al}_{0.98}\text{Ga}_{0.02})_x\text{O}_y$ native oxides", *Applied Physics Letters*, vol. 73, no. 24, pp. 3512–3514, 1998.
- [141] A. Bek, A. Aydinli, J. G. Champlain, R. Naone, and N. Dagli, "A study of wet oxidized $\text{Al}_x\text{Ga}_{1-x}\text{As}$ for integrated optics", *IEEE Photonics Technology Letters*, vol. 11, no. 4, pp. 436–438, 1999.
- [142] M. H. MacDougal, P. D. Dapkus, V. Pudikov, H. Zhao, and G. M. Yang, "Ultralow threshold current vertical-cavity surface-emitting lasers with AlAs oxide-GaAs distributed Bragg reflectors", *IEEE Photonics Technology Letters*, vol. 7, no. 3, pp. 229–31, 1995.
- [143] T. Gessmann, E. F. Schubert, J. W. Graff, K. Streubel, and C. Karnutsch, "Omnidirectional reflective contacts for light-emitting diodes", *IEEE Electron Device Letters*, vol. 24, no. 11, pp. 683–685, 2003.
- [144] W. L. Barnes, A. Dereux, and T. W. Ebbesen, "Surface plasmon subwavelength optics", *Nature*, vol. 424, no. 6950, pp. 824–830, 2003.
- [145] J. Moreland, A. Adams, and P. K. Hansma, "Efficiency of Light-Emission from Surface-Plasmons", *Physical Review B*, vol. 25, no. 4, pp. 2297–2300, 1982.
- [146] W. L. Barnes, "Electromagnetic Crystals for Surface Plasmon Polaritons and the Extraction of Light from Emissive Devices", *Journal of Lightwave Technology*, vol. 17, no. 11, pp. 2170–2182, 1999.
- [147] P. T. Worthing and W. L. Barnes, "Efficient coupling of surface plasmon polaritons to radiation using a bi-grating", *Applied Physics Letters*, vol. 79, no. 19, pp. 3035–3037, 2001.
- [148] P. A. Hobson, J. A. E. Wasey, I. Sage, and W. L. Barnes, "The role of surface plasmons in organic light-emitting diodes", *IEEE Journal of Selected Topics in Quantum Electronics*, vol. 8, no. 2, pp. 378–386, 2002.
- [149] W. L. Barnes and P. T. Worthing, "Spontaneous emission and metal-clad microcavities", *Optics Communications*, vol. 162, no. 1-3, pp. 16–20, 1999.
- [150] I. Gontijo, M. Boroditsky, E. Yablonovitch, S. Keller, U. K. Mishra, and S. P. DenBaars, "Coupling of InGaN quantum-well photoluminescence to silver surface plasmons", *Physical Review B*, vol. 60, no. 16, pp. 11564–11567, 1999.
- [151] J. Vuckovic, M. Loncar, and A. Scherer, "Surface Plasmon Enhanced Light-Emitting Diode", *IEEE Journal of Quantum Electronics*, vol. 36, no. 10, pp. 1131–1144, 2000.

- [152] R. P. Stanley and M. Liley, *GoldiLEDs: Gold Microparticle Enhanced Light Emitting Diodes*, Technical report, CSEM Centre Suisse d'Electronique et de Microtechnique SA, 2003.
- [153] T. Klar, M. Perner, S. Grosse, G. Von Plessen, W. Spirk, and J. Feldmann, "Surface-plasmon resonances in single metallic nanoparticles", *Physical Review Letters*, vol. 80, no. 19, pp. 4249–52, 1998.
- [154] O. Wada, S. Yamakoshi, M. Abe, Y. Nishitani, and T. Sakurai, "High Radiance In-GaAsP/InP Lensed LED's for Optical Communication Systems at 1.2-1.3 μm ", *IEEE Journal of Quantum Electronics*, vol. 17, no. 2, pp. 174–178, 1981.
- [155] E. M. Strzelecka, G. D. Robinson, L. A. Coldren, and E. L. Hu, "Fabrication of refractive microlenses in semiconductors by mask shape transfer in reactive ion etching", *Microelectronic Engineering*, vol. 35, no. 1-4, pp. 385–388, 1997.
- [156] P. Heremans, J. Genoe, M. Kuijk, R. Vounckx, and G. Borghs, "Mushroom microlenses: Optimized microlenses by reflow of multiple layers of photoresist", *IEEE Photonics Technology Letters*, vol. 9, no. 10, pp. 1367–1369, 1997.
- [157] F. W. Ostermayer, P. A. Kohl, and R. H. Burton, "Photoelectrochemical Etching of Integral Lenses on InGaAsP/InP Light-Emitting Diodes", *Applied Physics Letters*, vol. 43, no. 7, pp. 642–644, 1983.
- [158] Z. I. Alferov, V. M. Andreev, B. V. Egorov, and A. V. Syrbu, "Heterojunction Light-Emitting Al-Ga-As Diodes Formed by Negative Profiling of Substrate", *Soviet Physics Semiconductors*, vol. 11, no. 10, pp. 1123–1127, 1977.
- [159] O. Hasegawa, R. Namazu, M. Abe, and Y. Toyama, "Coupling of Spherical-Surfaced LED and Spherical-Ended Fiber", *Journal of Applied Physics*, vol. 51, no. 1, pp. 30–36, 1980.
- [160] Y. S. Kim, J. Kim, J. S. Choe, Y. G. Roh, H. Jeon, and J. C. Woo, "Semiconductor microlenses fabricated by one-step wet etching", *IEEE Photonics Technology Letters*, vol. 12, no. 5, pp. 507–509, 2000.
- [161] K. Iga, T. Kambayashi, K. Wakao, C. Kitahara, and K. Moriki, "GaInAsP/InP Double-Heterostructure Planar LED's", *IEEE Transactions on Electron Devices*, vol. 26, no. 8, pp. 1227–1230, 1979.
- [162] S. Adachi, Ed., *Properties of Aluminium Gallium Arsenide*, INSPEC, London, 1993.
- [163] E. D. Palik, *Handbook of Optical Constants of Solids*, Academic Press, San Diego, 1998.
- [164] P. Royo, R. P. Stanley, M. Ilegems, K. Streubel, and K. H. Gulden, "Deconvolution of the intrinsic spontaneous spectrum of vertical-cavity surface-emitting devices", *Applied Physics Letters*, vol. 77, no. 24, pp. 3899–3901, 2000.
- [165] R. Williams, *Modern GaAs Processing Methods*, Artech House, Boston, 1990.
- [166] Z. Song, S. Shogen, M. Kawasaki, and I. Suemune, "X-Ray Photoelectron Spectroscopic and Atomic Force Microscopic Study of GaAs Etching with a HCl Solution", *Applied Surface Science*, vol. 82-3, pp. 250–256, 1994.

- [167] M. G. Kang, S. H. Sa, H. H. Park, K. S. Suh, and K. H. Oh, "The characterization of etched GaAs surface with HCl or H₃PO₄ solutions", *Thin Solid Films*, vol. 308, pp. 634–642, 1997.
- [168] M. G. Kang and H. H. Park, "Effect of GaAs surface treatments using HCl or (NH₄)₂S_x solutions on the interfacial bonding states induced by deposition of Au", *Thin Solid Films*, vol. 332, no. 1-2, pp. 437–443, 1998.
- [169] S. Adachi and D. Kikuchi, "Chemical etching characteristics of GaAs(100) surfaces in aqueous HF solutions", *Journal of the Electrochemical Society*, vol. 147, no. 12, pp. 4618–4624, 2000.
- [170] S. Salimian, C. B. Cooper, R. Norton, and J. Bacon, "Reactive Ion Etch Process with Highly Controllable GaAs-to-AlGaAs Selectivity Using SF₆ and SiCl₄", *Applied Physics Letters*, vol. 51, no. 14, pp. 1083–1085, 1987.
- [171] A. A. Ketterson, E. Andideh, I. Adesida, T. L. Brock, J. Baillargeon, J. Laskar, K. Y. Cheng, and J. Kolodzey, "Selective Reactive Ion Etching for Short-Gate-Length GaAs/AlGaAs/InGaAs Pseudomorphic Modulation-Doped Field-Effect Transistors", *Journal of Vacuum Science & Technology B*, vol. 7, no. 6, pp. 1493–1496, 1989.
- [172] M. Tong, D. G. Ballegeer, A. Ketterson, E. J. Roan, K. Y. Cheng, and I. Adesida, "A Comparative Study of Wet and Dry Selective Etching Processes for GaAs/AlGaAs/InGaAs Pseudomorphic MODFETs", *Journal of Electronic Materials*, vol. 21, no. 1, pp. 9–15, 1992.
- [173] Y. Mori and N. Watanabe, "A New Etching Solution System, H₃PO₄-H₂O₂-H₂O, for GaAs and Its Kinetics", *Journal of the Electrochemical Society*, vol. 125, no. 9, pp. 1510–1514, 1978.
- [174] K. Bacher and J. S. Harris, "A Wet Etching Technique for Accurate Etching of GaAs/AlAs Distributed Bragg Reflectors", *Journal of the Electrochemical Society*, vol. 142, no. 7, pp. 2386–2388, 1995.
- [175] W. P. Dumke, J. M. Woodall, and V. L. Rideout, "GaAs-GaAlAs Heterojunction Transistor for High Frequency Operation", *Solid-State Electronics*, vol. 15, no. 12, pp. 1339–1343, 1972.
- [176] R. A. Logan and F. K. Reinhart, "Optical Waveguides in GaAs-AlGaAs Epitaxial Layers", *Journal of Applied Physics*, vol. 44, no. 9, pp. 4172–4176, 1973.
- [177] K. Kenefick, "Selective Etching Characteristics of Peroxide/Ammonium-Hydroxide Solutions for GaAs/Al_{0.16}Ga_{0.84}As", *Journal of the Electrochemical Society*, vol. 129, no. 10, pp. 2380–2382, 1982.
- [178] Y. Uenishi, H. Tanaka, and H. Ukita, "Characterization of AlGaAs Microstructure Fabricated by AlGaAs/GaAs Micromachining", *IEEE Transactions on Electron Devices*, vol. 41, no. 10, pp. 1778–1783, 1994.
- [179] M. Otsubo, T. Oda, H. Kumabe, and H. Miki, "Preferential Etching of GaAs through Photoresist Masks", *Journal of the Electrochemical Society*, vol. 123, no. 5, pp. 676–680, 1976.

- [180] C. Juang, K. J. Kuhn, and R. B. Darling, "Selective Etching of GaAs and $\text{Al}_{0.30}\text{Ga}_{0.70}\text{As}$ with Citric Acid/Hydrogen Peroxide Solutions", *Journal of Vacuum Science & Technology B*, vol. 8, no. 5, pp. 1122–1124, 1990.
- [181] G. C. DeSalvo, W. F. Tseng, and J. Comas, "Etch Rates and Selectivities of Citric Acid/Hydrogen Peroxide on GaAs, $\text{Al}_{0.3}\text{Ga}_{0.7}\text{As}$, $\text{In}_{0.2}\text{Ga}_{0.8}\text{As}$, $\text{In}_{0.53}\text{Ga}_{0.47}\text{As}$, $\text{In}_{0.52}\text{Al}_{0.48}\text{As}$, and InP", *Journal of the Electrochemical Society*, vol. 139, no. 3, pp. 831–835, 1992.
- [182] B. Y. Mao, J. A. Nielsen, R. A. Friedman, and G. Y. Lee, "The Applications of Citric Acid/Hydrogen Peroxide Etching Solutions in the Processing of Pseudomorphic MOD-FETs", *Journal of the Electrochemical Society*, vol. 141, no. 4, pp. 1082–1085, 1994.
- [183] H. J. Lee, M. S. Tse, K. Radhakrishnan, K. Prasad, J. Weng, S. F. Yoon, X. Zhou, H. S. Tan, S. K. Ting, and Y. C. Leong, "Selective wet etching of a GaAs/ $\text{Al}_x\text{Ga}_{1-x}\text{As}$ heterostructure with citric acid-hydrogen peroxide solutions for pseudomorphic GaAs/ $\text{Al}_x\text{Ga}_{1-x}\text{As}$ / $\text{In}_y\text{Ga}_{1-y}\text{As}$ heterojunction field effect transistor fabrication", *Materials Science and Engineering B-Solid State Materials for Advanced Technology*, vol. 35, no. 1-3, pp. 230–233, 1995.
- [184] J. H. Kim, D. H. Lim, and G. M. Yang, "Selective etching of AlGaAs/GaAs structures using the solutions of citric acid/ H_2O_2 and de-ionized H_2O /buffered oxide etch", *Journal of Vacuum Science & Technology B*, vol. 16, no. 2, pp. 558–560, 1998.
- [185] E. A. Moon, J. L. Lee, and H. M. Yoo, "Selective wet etching of GaAs on $\text{Al}_x\text{Ga}_{1-x}\text{As}$ for AlGaAs/InGaAs/AlGaAs pseudomorphic high electron mobility transistor", *Journal of Applied Physics*, vol. 84, no. 7, pp. 3933–3938, 1998.
- [186] H. J. Ueng, N. P. Chen, D. B. Janes, K. J. Webb, D. T. McInturff, and M. R. Melloch, "Temperature-dependent behavior of low-temperature-grown GaAs nonalloyed ohmic contacts", *Journal of Applied Physics*, vol. 90, no. 11, pp. 5637–5641, 2001.
- [187] N. Braslau, J. B. Gunn, and J. L. Staples, "Metal-Semiconductor Contacts for GaAs Bulk Effect Devices", *Solid-State Electronics*, vol. 10, no. 5, pp. 381–383, 1967.
- [188] O. Madelung, Ed., *Landolt-Börnstein*, vol. New Series IV/5, Springer-Verlag, Berlin, 1991.
- [189] V. L. Rideout, "Review of Theory and Technology for Ohmic Contacts to Group III-V Compound Semiconductors", *Solid-State Electronics*, vol. 18, no. 6, pp. 541–550, 1975.
- [190] V. G. Keramidas, "Metallurgical Interactions at Metallization-Compound Semiconductor Interfaces", *Thin Solid Films*, vol. 96, no. 4, pp. 347–363, 1982.
- [191] H. J. Bühlmann and M. Ilegems, "Characterization of AuGe/Ni/Au Contacts on GaAs/AlGaAs Heterostructures for Low-Temperature Applications", *Journal of the Electrochemical Society*, vol. 138, no. 9, pp. 2795–2798, 1991.
- [192] S. J. Chua and S. H. Lee, "Contact Resistivity Dependence on Ge:Ni Ratio in AuNiAuGe Metallization on n-GaAs", *Japanese Journal of Applied Physics Part 1-Regular Papers Short Notes & Review Papers*, vol. 33, no. 1A, pp. 66–69, 1994.
- [193] Y. C. Shih, M. Murakami, E. L. Wilkie, and A. C. Callegari, "Effects of Interfacial Microstructure on Uniformity and Thermal Stability of AuNiGe Ohmic Contact to n-type GaAs", *Journal of Applied Physics*, vol. 62, no. 2, pp. 582–590, 1987.

- [194] H. J. Lee, M. S. Tse, K. Radhakrishnan, K. Prasad, J. Weng, S. F. Yoon, X. Zhou, and H. S. Tan, "Characterization of Ni/Ge/Au/Ni/Au contact metallization on Al-GaAs/InGaAs heterostructures for pseudomorphic heterojunction field effect transistor application", *Materials Science and Engineering B-Solid State Materials for Advanced Technology*, vol. 35, no. 1-3, pp. 234–238, 1995.
- [195] W. W. Chow, K. D. Choquette, M. H. Crawford, K. L. Lear, and G. R. Hadley, "Design, fabrication, and performance of infrared and visible vertical-cavity surface-emitting lasers", *IEEE Journal of Quantum Electronics*, vol. 33, no. 10, pp. 1810–1824, 1997.
- [196] W. G. Spitzer and J. M. Whelan, "Infrared Absorption and Electron Effective Mass in n-Type Gallium Arsenide", *Physical Review*, vol. 114, no. 1, pp. 59–63, 1959.
- [197] W. Shockley, "Research and investigation of inverse epitaxial UHF power transistors", Tech. Rep. AI-TOR-64-207, Air Force Atomic Laboratory, September 1964.
- [198] H. Murrmann and D. Widmann, "Current Crowding on Metal Contacts to Planer Devices", *Digest of technical papers / IEEE International Solid-State Circuits Conference (ISSCC)*, vol. 12, pp. 162–163, 1969.
- [199] H. Murrmann and D. Widmann, "Measurement of Contact Resistance between Metal and Diffusion Layer in Si Planar Elements", *Solid-State Electronics*, vol. 12, no. 11, pp. 879–886, 1969.
- [200] H. Murrmann and D. Widmann, "Current Crowding on Metal Contacts to Planar Devices", *IEEE Transactions on Electron Devices*, vol. ED-16, no. 12, pp. 1022–1024, 1969.
- [201] H. H. Berger, "Contact Resistance on Diffused Resistors", *Digest of technical papers / IEEE International Solid-State Circuits Conference (ISSCC)*, vol. 12, pp. 160–161, 1969.
- [202] I. F. Chang, "Contact Resistance in Diffused Resistors", *Journal of the Electrochemical Society*, vol. 117, no. 3, pp. 368–372, 1970.
- [203] W. Kellner, "Planar Ohmic Contacts to N-Type GaAs: Determination of Contact Parameters Using the Transmission Line Model", *Siemens Forschungs- und Entwicklungsberichte*, vol. 4, no. 3, 1975.
- [204] G. K. Reeves and H. B. Harrison, "Obtaining the Specific Contact Resistance from Transmission Line Model Measurements", *IEEE Electron Device Letters*, vol. 3, no. 5, pp. 111–113, 1982.
- [205] G. K. Reeves and H. B. Harrison, "An Analytical Model for Alloyed Ohmic Contacts Using a Trilayer Transmission Line Model", *IEEE Transactions on Electron Devices*, vol. 42, no. 8, pp. 1536–1547, 1995.
- [206] M. Ogawa, "Alloying Behavior of Ni/Au-Ge Films on GaAs", *Journal of Applied Physics*, vol. 51, no. 1, pp. 406–412, 1980.
- [207] D. C. Miller, "Alloying of Gold and Gold Alloy Ohmic Contact Metallizations with Gallium Arsenide", *Journal of the Electrochemical Society*, vol. 127, no. 2, pp. 467–475, 1980.

- [208] D. R. Lide, *CRC Handbook of Chemistry and Physics*, CRC Press, Boca Raton, 82st edition, 2001-2002.
- [209] D. E. Aspnes, "Recombination at Semiconductor Surfaces and Interfaces", *Surface Science*, vol. 132, no. 1-3, pp. 406-421, 1983.
- [210] J. A. Kash, B. Pezeshki, F. Agahi, and N. A. Bojarczuk, "Recombination in GaAs at the AlAs Oxide-GaAs Interface", *Applied Physics Letters*, vol. 67, no. 14, pp. 2022-2024, 1995.
- [211] S. S. Shi, E. L. Hu, J. P. Zhang, Y. I. Chang, P. Parikh, and U. Mishra, "Photoluminescence study of hydrogenated aluminum oxide-semiconductor interface", *Applied Physics Letters*, vol. 70, no. 10, pp. 1293-1295, 1997.
- [212] A. R. Pratt, T. Takamori, and I. Kamijoh, "Photoluminescence of InGaAs/GaAs single quantum well adjacent to a selectively oxidized AlAs layer", *Applied Physics Letters*, vol. 71, no. 10, pp. 1394-1396, 1997.
- [213] A. R. Pratt, T. Takamori, and T. Kamijoh, "Thermal quenching of the photoluminescence of InGaAs/GaAs single quantum wells adjacent to a selectively oxidized AlAs layer", *Japanese Journal of Applied Physics Part 2-Letters*, vol. 37, no. 3A, pp. L275-L277, 1998.
- [214] K. D. Choquette, Jr. Schneider, R. P., K. L. Lear, and K. M. Geib, "Low threshold voltage vertical-cavity lasers fabricated by selective oxidation", *Electronics Letters*, vol. 30, no. 24, pp. 2043-4, 1994.
- [215] K. L. Lear, K. D. Choquette, R. P. Schneider, S. P. Kilcoyne, and K. M. Geib, "Selectively Oxidized Vertical Cavity Surface Emitting Lasers with 50% Power Conversion Efficiency", *Electronics Letters*, vol. 31, no. 3, pp. 208-209, 1995.
- [216] K. L. Lear, A. Mar, K. D. Choquette, S. P. Kilcoyne, R. P. Schneider, and K. M. Geib, "High-frequency modulation of oxide-confined vertical cavity surface emitting lasers", *Electronics Letters*, vol. 32, no. 5, pp. 457-458, 1996.
- [217] T. R. Nelson, J. P. Prineas, G. Khitrova, H. M. Gibbs, J. D. Berger, E. K. Lindmark, J. H. Shin, H. E. Shin, Y. H. Lee, P. Tayebati, and L. Javniskis, "Room-temperature normal-mode coupling in a semiconductor microcavity utilizing native-oxide AlAl/GaAs mirrors", *Applied Physics Letters*, vol. 69, no. 20, pp. 3031-3033, 1996.
- [218] P. G. Newman, J. Pamulapati, H. Shen, M. Taysing-Lara, J. Liu, W. Chang, G. Simonis, B. Koley, M. Dagenais, S. Feld, and J. Loehr, "Molecular beam epitaxial growth of vertical cavity surface emitting lasers with digital alloys and digital gradings", *Journal of Vacuum Science & Technology B*, vol. 18, no. 3, pp. 1619-1622, 2000.
- [219] A. R. Sugg, N. Holonyak, J. E. Baker, F. A. Kish, and J. M. Dallesasse, "Native Oxide Stabilization of AlAs-GaAs Heterostructures", *Applied Physics Letters*, vol. 58, no. 11, pp. 1199-1201, 1991.
- [220] S. Adachi and K. Oe, "Chemical Etching Characteristics of (001)GaAs", *Journal of the Electrochemical Society*, vol. 130, no. 12, pp. 2427-2435, 1983.

- [221] K. D. Choquette, K. M. Geib, C. I. H. Ashby, R. D. Twesten, O. Blum, H. Q. Hou, D. M. Follstaedt, B. E. Hammons, D. Mathes, and R. Hull, "Advances in Selective Wet Oxidation of AlGaAs Alloys", *IEEE Journal of Selected Topics in Quantum Electronics*, vol. 3, no. 3, pp. 916–926, 1997.
- [222] K. D. Choquette, K. M. Geib, H. C. Chui, B. E. Hammons, H. Q. Hou, T. J. Drummond, and R. Hull, "Selective oxidation of buried AlGaAs versus AlAs layers", *Applied Physics Letters*, vol. 69, no. 10, pp. 1385–1387, 1996.
- [223] M. H. MacDougall and P. D. Dapkus, "Wavelength shift of selectively oxidized Al_xO_y -AlGaAs-GaAs distributed Bragg reflectors", *IEEE Photonics Technology Letters*, vol. 9, no. 7, pp. 884–886, 1997.
- [224] P. W. Evans, J. J. Wierer, and N. Holonyak, " $\text{Al}_x\text{Ga}_{1-x}\text{As}$ native-oxide-based distributed Bragg reflectors for vertical cavity surface emitting lasers", *Journal of Applied Physics*, vol. 84, no. 10, pp. 5436–5440, 1998.
- [225] D. L. Huffaker, D. G. Deppe, K. Kumar, and T. J. Rogers, "Native-oxide defined ring contact for low threshold vertical-cavity lasers", *Applied Physics Letters*, vol. 65, no. 1, pp. 97–99, 1994.
- [226] J. W. Mayer and S. S. Lau, *Electronic materials science: for integrated circuits in Si and GaAs*, Macmillan Publishing Company, New York, 1990.
- [227] K. M. Geib, K. D. Choquette, H. Q. Hou, and B. E. Hammons, "Fabrication issues of oxide-confined VCSELs", in *Vertical-Cavity Surface-Emitting Lasers*, K. D. Choquette and D. G. Deppe, Eds. 1997, vol. 3003, pp. 69–74, Proc. SPIE.
- [228] M. Brunner, *Design and characterization of single and dual cavity oxide-apertured VCSELs*, Ph.D. thesis, Swiss Federal Institute of Technology, Lausanne (EPFL), 2000.
- [229] C. I. H. Ashby, J. P. Sullivan, P. P. Newcomer, N. A. Missert, H. Q. Hou, B. E. Hammons, M. J. Hafich, and A. G. Baca, "Wet oxidation of $\text{Al}_x\text{Ga}_{1-x}\text{As}$: Temporal evolution of composition and microstructure and the implications for metal-insulator-semiconductor applications", *Applied Physics Letters*, vol. 70, no. 18, pp. 2443–2445, 1997.
- [230] C. I. H. Ashby, J. P. Sullivan, K. D. Choquette, K. M. Geib, and H. Q. Hou, "Wet oxidation of AlGaAs: the role of hydrogen", *Journal of Applied Physics*, vol. 82, no. 6, pp. 3134–3136, 1997.
- [231] T. Takamori, K. Takemasa, and T. Kamijoh, "Interface structure of selectively oxidized AlAs/GaAs", *Applied Physics Letters*, vol. 69, no. 5, pp. 659–661, 1996.
- [232] R. D. Twesten, D. M. Follstaedt, K. D. Choquette, and R. P. Schneider Jr., "Microstructure of laterally oxidized $\text{Al}_x\text{Ga}_{1-x}\text{As}$ layers in vertical-cavity lasers", *Applied Physics Letters*, vol. 69, no. 1, pp. 19–21, 1996.
- [233] G. W. Pickrell, J. H. Epple, K. L. Chang, K. C. Hsieh, and K. Y. Cheng, "Improvement of wet-oxidized $\text{Al}_x\text{Ga}_{1-x}\text{As}$ ($x \sim 1$) through the use of AlAs/GaAs digital alloys", *Applied Physics Letters*, vol. 76, no. 18, pp. 2544–2546, 2000.
- [234] G. Stareev, "Formation of Extremely Low Resistance Ti/Pt/Au Ohmic Contacts to p-GaAs", *Applied Physics Letters*, vol. 62, no. 22, pp. 2801–2803, 1993.

- [235] G. Stareev, H. Künzel, and G. Dortmann, “A Controllable Mechanism of Forming Extremely Low-Resistance Nonalloyed Ohmic Contacts to Group-III-V Compound Semiconductors”, *Journal of Applied Physics*, vol. 74, no. 12, pp. 7344–7356, 1993.
- [236] Y. Kitaura, T. Hashimoto, T. Inoue, K. Ishida, N. Uchitomi, and R. Nii, “Long-Term Reliability of Pt and Mo Diffusion Barriers in Ti-Pt-Au and Ti-Mo-Au Metallization Systems for GaAs Digital Integrated-Circuits”, *Journal of Vacuum Science & Technology B*, vol. 12, no. 5, pp. 2985–2991, 1994.
- [237] B. Luo, G. Dang, A. P. Zhang, F. Ren, J. Lopata, S. N. G. Chu, W. S. Hobson, and S. J. Pearton, “p-ohmic contact study for intracavity contacts in AlGaAs/GaAs vertical cavity surface-emitting lasers”, *Journal of the Electrochemical Society*, vol. 148, no. 12, pp. G676–G679, 2001.
- [238] S. S. Murtaza and J. C. Campbell, “Effects of Variations in Layer Thicknesses on the Reflectivity Spectra of Semiconductor Bragg Mirrors”, *Journal of Applied Physics*, vol. 77, no. 8, pp. 3641–3644, 1995.
- [239] C. Dill, *Fabrication and characterization of high efficiency microcavity light emitting diodes*, Ph.D. thesis, Swiss Federal Institute of Technology, Lausanne (EPFL), 1999.
- [240] S. Jennato and G. McKee, “Standardization helps LEDs measure up”, *Compound Semiconductor*, vol. 7, no. 3, pp. 73–75, 2001.
- [241] M. Rattier, H. Benisty, R. P. Stanley, J.-F. Carlin, R. Houdré, U. Oesterle, C. J. M. Smith, C. Weisbuch, and T. F. Krauss, “Toward ultrahigh-efficiency aluminum oxide microcavity light-emitting diodes: guided mode extraction by photonic crystals”, *IEEE Journal of Selected Topics in Quantum Electronics*, vol. 8, no. 2, pp. 238–247, 2002.
- [242] E. F. Schubert, N. E. J. Hunt, R. J. Malik, M. Micovic, and D. L. Miller, “Temperature and modulation characteristics of resonant-cavity light-emitting diodes”, *Journal of Lightwave Technology*, vol. 14, no. 7, pp. 1721–1729, 1996.
- [243] S. Guha, F. Agahi, B. Pezeshki, J. A. Kash, D. W. Kisker, and N. A. Bojarczuk, “Microstructure of AlGaAs-oxide heterolayers formed by wet oxidation”, *Applied Physics Letters*, vol. 68, no. 7, pp. 906–908, 1996.
- [244] J. C. Ferrer, Z. Liliental-Weber, H. Reese, Y. J. Chiu, and E. Hu, “Improvement of the interface quality during thermal oxidation of $\text{Al}_{0.98}\text{Ga}_{0.02}\text{As}$ layers due to the presence of low-temperature-grown GaAs”, *Applied Physics Letters*, vol. 77, no. 2, pp. 205–207, 2000.
- [245] M. H. MacDougal, P. D. Dapkus, A. E. Bond, C. K. Lin, and J. Geske, “Design and fabrication of VCSEL’s with Al_xO_y -GaAs DBR’s”, *IEEE Journal of Selected Topics in Quantum Electronics*, vol. 3, no. 3, pp. 905–915, 1997.
- [246] M. H. MacDougal, J. Geske, C. K. Lin, A. E. Bond, and P. D. Dapkus, “Low resistance intracavity-contacted oxide-aperture VCSEL’s”, *IEEE Photonics Technology Letters*, vol. 10, no. 1, pp. 9–11, 1998.
- [247] M. G. Peters, B. J. Thibeault, D. B. Young, J. W. Scott, F. H. Peters, A. C. Gossard, and L. A. Coldren, “Band-Gap Engineered Digital Alloy Interfaces for Lower Resistance Vertical-Cavity Surface-Emitting Lasers”, *Applied Physics Letters*, vol. 63, no. 25, pp. 3411–3413, 1993.

- [248] K. Tai, L. Yang, Y. H. Wang, J. D. Wynn, and A. Y. Cho, "Drastic Reduction of Series Resistance in Doped Semiconductor Distributed Bragg Reflectors for Surface-Emitting Lasers", *Applied Physics Letters*, vol. 56, no. 25, pp. 2496–2498, 1990.
- [249] M. M. Dumitrescu, M. J. Saarinen, M. D. Guina, and M. V. Pessa, "High-speed resonant cavity light-emitting diodes at 650 nm", *IEEE Journal of Selected Topics in Quantum Electronics*, vol. 8, no. 2, pp. 219–230, 2002.
- [250] K. Streubel and R. Stevens, "250 Mbit/s plastic fibre transmission using 660 nm resonant cavity light emitting diode", *Electronics Letters*, vol. 34, no. 19, pp. 1862–1863, 1998.
- [251] M. Dumitrescu, M. Saarinen, M. Guina, H. Komsa, and M. Pessa, "Modeling, design, growth and characterization of red wavelength range microcavity emitters for plastic optic fiber applications", *Optical and Quantum Electronics*, vol. 35, no. 6, pp. 589–613, 2003.
- [252] R. P. Schneider Jr., J. A. Lott, M. H. Crawford, and K. D. Choquette, "Epitaxial design and performance of AlGaInP red (650-690 nm) VCSEL's", *International Journal of High Speed Electronics and Systems Devices*, vol. 5, no. 4, pp. 625–666, 1994.
- [253] P. W. Epperlein, G. L. Bona, and P. Roentgen, "Local Mirror Temperatures of Red-Emitting (Al)GaInP Quantum-Well Laser Diodes by Raman Scattering and Reflectance Modulation Measurements", *Applied Physics Letters*, vol. 60, no. 6, pp. 680–682, 1992.
- [254] S. Adachi, "Lattice Thermal Resistivity of III-V Compound Alloys", *Journal of Applied Physics*, vol. 54, no. 4, pp. 1844–1848, 1983.
- [255] M. Ikeda and K. Kaneko, "Selenium and Zinc Doping in $\text{Ga}_{0.5}\text{In}_{0.5}\text{P}$ and $(\text{Al}_{0.5}\text{Ga}_{0.5})_{0.5}\text{In}_{0.5}\text{P}$ Grown by Metalorganic Chemical Vapor Deposition", *Journal of Applied Physics*, vol. 66, no. 11, pp. 5285–5289, 1989.
- [256] Y. Ohba, M. Ishikawa, H. Sugawara, M. Yamamoto, and T. Nakanisi, "Growth of High-Quality InGaAlP Epilayers by MOCVD Using Methyl Metalorganics and Their Application to Visible Semiconductor Lasers", *Journal of Crystal Growth*, vol. 77, no. 1-3, pp. 374–379, 1986.
- [257] R. P. Schneider and J. A. Lott, "InAlP/InAlGaP Distributed Bragg Reflectors for Visible Vertical Cavity Surface-Emitting Lasers", *Applied Physics Letters*, vol. 62, no. 22, pp. 2748–2750, 1993.
- [258] J. A. Lott, R. P. Schneider Jr., J. C. Zolper, and K. J. Malloy, "AlGaInP visible resonant cavity light-emitting diodes", *IEEE Photonics Technology Letters*, vol. 5, no. 6, pp. 631–633, 1993.
- [259] H. Sugawara, K. Itaya, H. Nozaki, and G. Hatakoshi, "High-Brightness InGaAlP Green Light-Emitting-Diodes", *Applied Physics Letters*, vol. 61, no. 15, pp. 1775–1777, 1992.
- [260] S. W. Chiou, C. P. Lee, C. K. Huang, and C. W. Chen, "Wide angle distributed Bragg reflectors for 590 nm amber AlGaInP light-emitting diodes", *Journal of Applied Physics*, vol. 87, no. 4, pp. 2052–2054, 2000.
- [261] M. J. Ries, N. Holonyak, E. I. Chen, S. A. Maranowski, M. R. Islam, A. L. Holmes, and R. D. Dupuis, "Visible-Spectrum ($\lambda = 650$ nm) Photopumped (pulsed, 300 K)

- Laser Operation of a Vertical-Cavity AlAs-AlGaAs/InAlP-InGaP Quantum-Well Heterostructure Utilizing Native Oxide Mirrors”, *Applied Physics Letters*, vol. 67, no. 8, pp. 1107–1109, 1995.
- [262] M. H. MacDougal, S. G. Hummel, P. D. Dapkus, H. M. Zhao, and Y. Cheng, “Epitaxial (Al,Ga)InP-Oxide Distributed Bragg Reflectors for Use in Visible-Wavelength Optical-Devices”, *IEEE Photonics Technology Letters*, vol. 7, no. 4, pp. 385–387, 1995.
- [263] A. L. Holmes, M. R. Islam, R. V. Chelakara, F. J. Ciuba, R. D. Dupuis, M. J. Ries, E. I. Chen, S. A. Maranowski, and N. Holonyak, “High-Reflectivity Visible-Wavelength Semiconductor Native Oxide Bragg Reflectors Grown by Metalorganic Chemical Vapor Deposition”, *Applied Physics Letters*, vol. 66, no. 21, pp. 2831–2833, 1995.
- [264] S. G. Hummel, M. H. Macdougall, and P. D. Dapkus, “Extremely Wide-Bandwidth Distributed Bragg Reflectors Using Chirped Semiconductor/Oxide Pairs”, *Electronics Letters*, vol. 31, no. 12, pp. 972–973, 1995.
- [265] J. A. Lott, L. V. Buydens, K. J. Malloy, K. Kobayashi, and S. Ishikawa, “Visible (630-650 nm) vertical cavity surface emitting lasers with Al-oxide/AlGaInP/AlGaAs distributed Bragg reflectors”, in *Institute of Physics Conference Series - 22nd International Symposium on Compound Semiconductors*, Cheju Island, Korea, 1996, vol. 145 of *Institute of Physics Conference Series*, pp. 973–976, Institute of Physics.
- [266] R. Wirth, C. Karnutsch, S. Kugler, S. Thaler, and K. Streubel, “Red and orange resonant-cavity LEDs”, in *Proc. SPIE Light-Emitting Diodes: Research, Manufacturing, and Applications V*. 2001, vol. 4278, pp. 41–49, The International Society for Optical Engineering.
- [267] A. Gomyo, T. Suzuki, K. Kobayashi, S. Kawata, I. Hino, and T. Yuasa, “Evidence for the Existence of an Ordered State in Ga_{0.5}In_{0.5}P Grown by Metalorganic Vapor Phase Epitaxy and Its Relation to Band-Gap Energy”, *Applied Physics Letters*, vol. 50, no. 11, pp. 673–675, 1987.
- [268] A. Gomyo, S. Kawata, T. Suzuki, S. Iijima, and I. Hino, “Large (6°) Off-Angle Effects on Sublattice Ordering and Band-Gap Energy in Ga_{0.5}In_{0.5}P Grown on (001) GaAs Substrates”, *Japanese Journal of Applied Physics Part 2-Letters*, vol. 28, no. 10, pp. L1728–L1730, 1989.
- [269] R. P. Schneider, R. P. Bryan, J. A. Lott, E. D. Jones, and G. R. Olbright, “MOVPE Growth of InAlGaP-Based Visible Vertical-Cavity Surface-Emitting Lasers”, *Journal of Crystal Growth*, vol. 124, no. 1-4, pp. 763–771, 1992.
- [270] M. Moser, R. Winterhoff, C. Geng, I. Queisser, F. Scholz, and A. Dörnen, “Refractive index of (Al_xGa_{1-x})_{0.5}In_{0.5}P grown by metalorganic vapor phase epitaxy”, *Applied Physics Letters*, vol. 64, no. 2, pp. 235–237, 1994.
- [271] M. Köhler, *Etching in microsystem technology*, Wiley-VCH, Weinheim, 1999.
- [272] M. Konagai, M. Sugimoto, and K. Takahashi, “High-Efficiency GaAs Thin Film Solar Cells by Peeled Film Technology”, *Journal of Crystal Growth*, vol. 45, no. 1, pp. 277–280, 1978.
- [273] X. S. Wu, L. A. Coldren, and J. L. Merz, “Selective Etching Characteristics of HF for Al_xGa_{1-x}As/GaAs”, *Electronics Letters*, vol. 21, no. 13, pp. 558–559, 1985.

- [274] T. R. Stewart and D. P. Bour, "Chemical etching of $(\text{Al}_x\text{Ga}_{1-x})_{0.5}\text{In}_{0.5}\text{P}$ using sulfuric and hydrochloric acids", *Journal of the Electrochemical Society*, vol. 139, no. 4, pp. 1217–1219, 1992.
- [275] J. W. Lee, S. J. Pearton, C. R. Abernathy, W. S. Hobson, F. Ren, and C. S. Wu, "Investigation of Wet Etching Solutions for $\text{In}_{0.5}\text{Ga}_{0.5}\text{P}$ ", *Solid-State Electronics*, vol. 38, no. 11, pp. 1871–1874, 1995.
- [276] J. R. Lothian, J. M. Kuo, F. Ren, and S. J. Pearton, "Plasma and Wet Chemical Etching of $\text{In}_{0.5}\text{Ga}_{0.5}\text{P}$ ", *Journal of Electronic Materials*, vol. 21, no. 4, pp. 441–445, 1992.
- [277] J. R. Flemish and K. A. Jones, "Selective wet etching of GaInP, GaAs and InP in solutions of HCl, CH_3COOH , and H_2O_2 ", *Journal of the Electrochemical Society*, vol. 140, no. 3, pp. 844–847, 1993.
- [278] D. Gregusova, P. Elias, L. Malacky, R. Kudela, and J. Skrinarirova, "Wet Chemical Mesa Etching of InGaP and GaAs with Solutions Based on HCl, CH_3COOH , and H_2O_2 ", *Physica Status Solidi A-Applied Research*, vol. 151, no. 1, pp. 113–118, 1995.
- [279] J. R. Lothian, J. M. Kuo, W. S. Hobson, E. Lane, F. Ren, and S. J. Pearton, "Wet and Dry Etching Characteristics of $\text{Al}_{0.5}\text{In}_{0.5}\text{P}$ ", *Journal of Vacuum Science & Technology B*, vol. 10, no. 3, pp. 1061–1065, 1992.
- [280] J. W. Lee, S. J. Pearton, C. R. Abernathy, W. S. Hobson, F. Ren, and C. S. Wu, "Wet Chemical Etching of $\text{Al}_{0.5}\text{In}_{0.5}\text{P}$ ", *Journal of the Electrochemical Society*, vol. 142, no. 6, pp. L100–L102, 1995.
- [281] K. K. Shih and J. M. Blum, "Contact Resistances of Au-Ge-Ni, Au-Zn and Al to III-V Compounds", *Solid-State Electronics*, vol. 15, no. 11, pp. 1177–1180, 1972.
- [282] N. Braslau, "Ohmic Contacts to GaAs and $\text{Ga}_x\text{Al}_{1-x}\text{As}$ ", *Journal of Vacuum Science & Technology B*, vol. 1, no. 3, pp. 700–701, 1983.
- [283] F. A. Kish, S. J. Caracci, N. Holonyak, J. M. Dallesasse, A. R. Sugg, R. M. Fletcher, C. P. Kuo, T. D. Osentowski, and M. G. Craford, "Native-Oxide Stripe-Geometry $\text{In}_{0.5}(\text{Al}_x\text{Ga}_{1-x})_{0.5}\text{P}$ - $\text{In}_{0.5}\text{Ga}_{0.5}\text{P}$ Heterostructure Laser Diodes", *Applied Physics Letters*, vol. 59, no. 3, pp. 354–356, 1991.
- [284] F. A. Kish, S. J. Caracci, N. Holonyak, K. C. Hsieh, J. E. Baker, S. A. Maranowski, A. R. Sugg, J. M. Dallesasse, R. M. Fletcher, C. P. Kuo, T. D. Osentowski, and M. G. Craford, "Properties and Use of $\text{In}_{0.5}(\text{Al}_x\text{Ga}_{1-x})_{0.5}\text{P}$ and $\text{Al}_x\text{Ga}_{1-x}\text{As}$ Native Oxides in Heterostructure Lasers", *Journal of Electronic Materials*, vol. 21, no. 12, pp. 1133–1139, 1992.
- [285] F. A. Kish, S. J. Caracci, N. Holonyak, S. A. Maranowski, J. M. Dallesasse, R. D. Burnham, and S. C. Smith, "Visible Spectrum Native-Oxide Coupled-Stripe $\text{In}_{0.5}(\text{Al}_x\text{Ga}_{1-x})_{0.5}\text{P}$ - $\text{In}_{0.5}\text{Ga}_{0.5}\text{P}$ Quantum Well Heterostructure Laser Arrays", *Applied Physics Letters*, vol. 59, no. 22, pp. 2883–2885, 1991.
- [286] O. Blum, K. L. Lear, H. Q. Hou, and M.E. Warren, "Buried refractive microlenses formed by selective oxidation of AlGaAs", *Electronics Letters*, vol. 32, no. 25, pp. 1406–1408, 1996.

- [287] R. L. Naone, E. R. Hegblom, B. J. Thibeault, and L. A. Coldren, "Oxidation of AlGaAs layers for tapered apertures in vertical-cavity lasers", *Electronics Letters*, vol. 33, no. 4, pp. 300–301, 1997.
- [288] E. R. Hegblom, B. J. Thibeault, R. L. Naone, and L. A. Coldren, "Vertical cavity lasers with tapered oxide apertures for low scattering loss", *Electronics Letters*, vol. 33, no. 10, pp. 869–871, 1997.
- [289] E. R. Hegblom, N. M. Margalit, A. Fiore, and L. A. Coldren, "Small efficient vertical cavity lasers with tapered oxide apertures", *Electronics Letters*, vol. 34, no. 9, pp. 895–897, 1998.
- [290] E. R. Hegblom, N. M. Margalit, A. Fiore, and L. A. Coldren, "High-performance small vertical-cavity lasers: A comparison of measured improvements in optical and current confinement in devices using tapered apertures", *IEEE Journal of Selected Topics in Quantum Electronics*, vol. 5, no. 3, pp. 553–560, 1999.
- [291] A. Fiore, Y. A. Akulova, J. Ko, E. R. Hegblom, and L. A. Coldren, "Multiple-wavelength vertical-cavity laser arrays based on postgrowth lateral-vertical oxidation of AlGaAs", *Applied Physics Letters*, vol. 73, no. 3, pp. 282–284, 1998.
- [292] A. Fiore, Y. A. Akulova, J. Ko, E. R. Hegblom, and L. A. Coldren, "Postgrowth tuning of semiconductor vertical cavities for multiple-wavelength laser arrays", *IEEE Journal of Quantum Electronics*, vol. 35, no. 4, pp. 616–623, 1999.
- [293] Y. G. Ju, D. Lofgreen, A. Fiore, S. Y. Hu, E. Hegblom, D. Louderback, O. Sjolund, A. Huntington, and L. A. Coldren, "Densely packed pie shaped vertical-cavity surface-emitting laser array incorporating a tapered one-dimensional wet oxidation", *IEEE Photonics Technology Letters*, vol. 12, no. 5, pp. 462–464, 2000.
- [294] H. C. Casey Jr. and M. B. Panish, *Heterostructure Lasers*, Academic Press, New York, 1978.
- [295] B. Monemar, K. K. Shih, and G. D. Pettit, "Some Optical Properties of the $\text{Al}_x\text{Ga}_{1-x}\text{As}$ Alloy System", *Journal of Applied Physics*, vol. 47, no. 6, pp. 2604–2613, 1976.

Curriculum vitae

Name: **Reto Joray**
Date of Birth: 13th of March, 1974
Place of Birth: Liestal (BL)
Nationality: Swiss
Marital Status: Single
E-mail: reto_j@yahoo.com

EDUCATION

1981 - 1986 Elementary School Ramllinsburg (BL)
1986 - 1990 Progymnasium Liestal (BL)
1990 - 1993 Gymnasium Liestal (BL)
1994 - 1999 Diploma in Materials Science at the Swiss Federal Institute of Technology, Zürich (ETHZ)
1998 - 1999 Diploma thesis carried out at the University of California, Santa Barbara (UCSB), USA
Title: "Optimization of Si_3N_4 Suspensions for Colloidal Iso-Press Forming"
2000 - 2005 Ph.D. at the Swiss Federal Institute of Technology, Lausanne (EPFL)
Title: "Microcavity Light-Emitting Diodes from the Red Visible to the Near Infrared Wavelength Range"
Supervisor: Prof. Marc Illegems, Semiconductor Device Physics Group, Institute of Quantum Electronics and Photonics (IPEQ)

Publications

Articles

- **R. Joray**, B. Yu, F. Lange and J. Pollinger, “Optimization of an Aqueous, Commercial Silicon Nitride Slurry for Colloidal Isopressing”, *Journal of the European Ceramic Society*, vol. 22, no. 7, pp. 1061–1066, 2002.
- W. Nakwaski, M. Wasiak, P. Mackowiak, W. Bedyk, M. Osinski, A. Passaseo, V. Tasco, M. T. Todaro, M. De Vittorio, **R. Joray**, J. X. Chen, R. P. Stanley and A. Fiore, “Oxidation kinetics of AlAs and (AlGa)As layers in GaAs-based diode laser structures: comparative analysis of available experimental data”, *Semiconductor Science and Technology*, vol. 19, no. 3, pp. 333–341, 2004.
- **R. Joray**, M. Ilegems, R. Stanley, W. Schmid, R. Butendeich, R. Wirth, A. Jaeger and K. Streubel, “Effect of Photon Recycling and In-Plane Superluminescence on the Far-Field Radiation Pattern of Red Emitting AlGaInP Thin-Film RCLEDs”, in preparation.
- **R. Joray**, R. Stanley, J. Dorsaz, U. Oesterle and M. Ilegems, “High Efficiency Substrate Emitting MCLEDs”, in preparation.

Conference Presentations and Proceedings

- **R. Joray**, J. Dorsaz, R. P. Stanley, M. Ilegems, M. Rattier, C. Karnutsch and K. Streubel, “High Extraction Efficiency AlGaInP Microcavity Light Emitting Diodes at 650 nm with AlGaAs–AlO_x DBR”, at the *29th International Symposium on Compound Semiconductors (ISCS)*, *Institute of Physics Conference Series*, Lausanne, Switzerland, vol. 174, M. Ilegems, G. Weimann and J. Wagner, Eds., pp. 363–366, 2002 (Oral Presentation).
- R. P. Stanley, P. Royo, U. Oesterle, **R. Joray** and M. Ilegems, “Novel Microcavity Light Emitting Diodes”, at the *29th International Symposium on Compound Semiconductors (ISCS)*, *Institute of Physics Conference Series*, Lausanne, Switzerland, vol. 174, M. Ilegems, G. Weimann and J. Wagner, Eds., pp. 359–362, 2002.
- **R. Joray**, M. Ilegems, R. Stanley, W. Schmid, R. Butendeich, R. Wirth, A. Jaeger and K. Streubel, “High brightness red emitting AlGaInP thin-film RCLEDs”, at *Optics East, Physics and Applications of Optoelectronic Devices*, *SPIE*, Philadelphia, PA, USA, in press, 2004 (Oral Presentation).